

Optimization of the pump spectral shape in a parametric down conversion process to generate multimode entangled states.

Thibault Michel



A thesis submitted for the degree of
Doctor of Philosophy at
The Australian National University

Sunday 18th July, 2021

© Copyright by Thibault Michel 2021
All Rights Reserved

Declaration

This thesis is an account of research undertaken between November 2016 and February 2021 at The Department of Quantum Science, Research School of Physics, The Australian National University, Canberra, Australia and at the *Laboratoire Kastler Brossel, Sorbonne Université*, Paris, France. This research was supervised by Prof. Ping Koy Lam (ANU), and Prof. Claude Fabre (*Sorbonne Université*). Unless otherwise indicated, the work present herein is my own. Except where acknowledged in the customary manner, the material presented in this thesis is, to the best of my knowledge, original and has not been submitted in whole or part for a degree in any university.

Some figures comprised in this thesis use ComponentLibrary, a vector graphics library for illustrations of optics experiments by Alexander Franzen, which is licensed under a Creative Commons Attribution-NonCommercial 3.0 Unported License, available at <http://www.gwoptics.org/ComponentLibrary/>.

Thibault Michel
February, 2021

Acknowledgements

This thesis is the accomplishment of more than 4 years of work and would not have been possible without all the people who contributed to it. Throughout my PhD, in France and Australia, I had the privilege of meeting some of the most remarkable people I know, many of whom have become good friends. Words are insufficient to express how grateful I feel but I ought to try.

First I would like to thank my jury for reviewing my thesis under short notice and for their corrections and insight on this work. I could tell from all your comments and corrections that you spent a significant time reviewing my thesis and I am very grateful for that.

I would also like to thank all my colleagues and friends from Australia who have welcomed me so warmly. First, all the people from admin who made my cotutelle a little less of an administrative nightmare, Lynne Christian and Liudmila Mangos in particular. Then, my supervisor, Ping Koy Lam, who managed to find the perfect balance between being supportive enough to help me with my work and professional perspective while still leaving me enough liberty to let me follow my scientific curiosity. I was very impressed and inspired by your overview and insight on all quantum sciences. I also owe some special thanks to all the people from the 1064 group who contributed a great deal to my work and scientific interrogations. Hao Jeng for the late night discussion about the foundation of quantum mechanics. Jing Yan Haw for his contribution to the work on quantum random number generators, I would not have fully understood the quantum information framework of QRNG without your help. Zhao Jie, for our discussion on details of OPO cavities. Your presence made long working hours in the lab far more pleasant. Plus you provided the best reliability tests for my cavity PHD locks. Baramée Charoensombutamon, Naomi Chaix, Lorcan Conlon and Biveen Shajilal, I had a great time collaborating with you, you brought some fresh blood to the group, and helped creating the best working environment. Thanks also for the jogging and optical ping pong sessions. I will never be grateful enough to Aaron Tranter for letting me use his wonderful machine learning code. It was essential to my work and Aaron was kind and patient enough to take the time to introduce me to his code and help me interface it. You are a great scientist and the best of friends and I will miss our motorbike trips. I want to thank Yosri Ben Aicha, having a fellow *francophone* in the group, helped me feel less homesick. For all the other scientific inputs and for the climbing, surfing, tarot, chess and hiking session, I also want to thank Oliver Thearle, Giovanni Guccionne, Sarah Lau, Karun Paul, Geoff Campbell, Pierre Vernazgris, Anthony Leung, Ida Melody, Jinyong Ma, Ruvi Lecamwasam and all the others from DQS. Last but not least, I would like to thank Syed Assad, my co-supervisor, and the most amazing scientist I have ever met. You have taught me the most valuable lessons of all: how to tackle new problems. As a junior PhD student, when I came to you with questions,

you would always take time to help me, even when you didn't have the answer. I learned a lot from watching how you handle new problems. I then realized that no problem is untrackable if you examine it with the correct attitude.

Having done a shared PhD between two laboratories, I met twice the amount of amazing people as I would have with a regular thesis. So I also ought to thank the people I met during my work in France. The working environment in the LKB Quantum Optics group was incredible. All the fun we had allowed to endure the tedious work hours in the lab when the experiment would act out with laser or electronic issues. Thanks to Adrien Dufour and Young-Sik Ra for teaching me all there is to know about the SPOPO set-up and for sticking together during the night shift photon subtraction measurements. To Paul Renault and Alex Davis thanks for handling most of the tedious work of rebuilding the set-up when I was away. Thanks to Francesco for initiating the pump shaping simulation and for his collaboration afterwards. To Ganael, our snake charmer, for his wonderful work on interfacing the set-up with python. To Tiphaine for sharing the painful experience of electronics design and thesis writing. To Francesca for the few tim tams she agreed to share. To Mathieu for not killing me when I stole most of his electronic filters in an emergency situation. Thanks also to Victor, David, Clementine, Mattia and Valentina, the atmosphere of the group would not be the same without you. Finally, I would like to thank my supervisors in France, Claude Fabre and Nicolas Treps. I will never be thankful enough for your support. In particular, thank you Nicolas for the unfathomable amount of time you spent reviewing this thesis.

*A mon père, ce héros au sourire si doux,
qui de la physique a su me donner le goût.*

Abstract

Quantum optics has been, from its beginning, a driving force both for the exploration of fundamental limits of the quantum world and for conceiving seminal ideas and applications of the so-called quantum technologies. The last 20 years have seen a rapid development of ideas and proof-of-principle experiments involving the fields of quantum communication, quantum computation, quantum metrology and quantum simulation.

The so-called continuous variable (CV) approach to quantum optics, which uses many photons in collective states, and information encoded in continuous observables, has many interesting properties, especially from a communications perspective. It is inherently broadband and compatible with standard Telecom infrastructures. Moreover, entanglement, one of the fundamental resources of quantum optics, can be generated deterministically.

One of the main challenges for all quantum information technologies is scalability, being able to generate and manipulate many quantum resources to achieve practical tasks efficiently. One approach to solve the issue of scalability is to use highly multimode quantum states. The quantum description of the electromagnetic field associates each photon (particle of light) with a mode (way for light to propagate). In a multimodal approach, we look at the quantum state bases and optical modes bases conjointly and tailor quantum fields not only in given modes, but also optimise the spatio-temporal shapes of the modes in which the state is defined. This opens wide perspectives for treating complex quantum states.

In particular, using ultra-fast pulses of light which contain many temporal/spectral modes, we are able to generate large entangled states of light using simple resources. In this thesis, we used an optical parametric oscillator pumped synchronously (SPOPO) with an optical frequency comb to generate multimode squeezed vacuum states. These can be used to form cluster states: the basic resource for Measurement Based Quantum Computation (MBQC). They can also be used in metrology or to simulate complex networks.

One of the advantages of this set-up is its tunability. Indeed, by changing the spectrum of the OPO pump with a pulse shaper, we can tailor the properties of the generated quantum state. In this work, we focus on the optimisation of the pump spectral shape to generate specific states. Using simulations based on Machine Learning Algorithms (MLA), we find optimal pump profile for typical target states. We then implement those shapes on the experimental set-up and measure the resulting quantum states using a multipixel homodyne detection. We also study intra-cavity dispersion effects. Dispersion inside the SPOPO cavity is indeed one of the main factors that limits the number of entangled modes in the generated quantum states. A systematic study of dispersion effects is therefore necessary to model the SPOPO output accurately. This work paves the way toward a fully tunable device that can be optimised in real time to generate specific quantum

resources.

Contents

Declaration	i
Acknowledgements	iii
Abstract	vii
Introduction	1
0.1 Thesis outline	4
I Theoretical background	7
1 Quantum light	9
1.1 Quantising the Electromagnetic (EM) field	9
1.1.1 The classical free EM field	9
1.1.2 The photon: a harmonic oscillator excitation	11
1.1.3 Quadrature operators and commutation relations	12
1.2 Quantum state representation	14
1.2.1 Discrete variable representation: the Fock basis	14
1.2.2 Continuous variables and Phase-Space representations	14
1.2.3 Statistical mixtures and the density operator	16
1.3 Importance of modes	16
1.3.1 Mode basis change	17
1.3.2 Intrinsically single-mode and multimode states	17
1.4 A zoo of quantum states	18
1.4.1 Fock states	18
1.4.2 Coherent states	18
1.4.3 Squeezed vacuum states	20
1.4.4 EPR states	23
2 Gaussian states and operations	25
2.1 Gaussian states, gaussian unitaries	26
2.1.1 Phase-space representation and covariance matrix	26
2.1.2 Example of Gaussian states	27
2.1.3 General Gaussian unitaries, Bogoliubov/Symplectic transformations	29
2.1.4 General mode basis change	30
2.2 Decompositions of Gaussian states and operations	30
2.2.1 Bloch-Messiah reduction	31

2.2.2	Williamson decomposition	32
2.2.3	One decomposition to rule them all	33
2.3	Gaussian measurements	33
2.3.1	Continuum of modes, two-mode formalism and envelope operators	33
2.3.2	Intensity measure	37
2.3.3	Homodyne detection	39
2.3.4	Squeezing and sideband noise correlations	41
II	Experimental tools	43
3	Ultrafast light	45
3.1	Optical frequency combs	45
3.1.1	The Mira laser	46
3.1.2	Single pulse of light	46
3.1.3	Spectral representation	47
3.1.4	Temporal representation	49
3.2	Dispersion effects	50
3.2.1	Spectral phase	50
3.2.2	Constant phase	51
3.2.3	Linear phase	51
3.2.4	Quadratic phase: chirp	52
3.3	Homodyne measurement with a frequency comb reference	53
4	Synchronous optical cavities	57
4.1	Ring cavity input-output relations	57
4.2	Synchronous cavities	60
4.2.1	Transmission of a frequency comb without CEO and partial resonances	60
4.2.2	CEO effects	63
4.2.3	Intra-cavity dispersion effects	65
5	The pulse shaper	67
5.1	General principle	67
5.1.1	Diffraction grating	68
5.1.2	SLM	69
5.2	Input output transformation	70
5.2.1	Simplified model: plane waves - pixel complexity	70
5.2.2	Effect of finite beam size - optical complexity	72
5.3	Effects of various misalignments	74
5.3.1	Input waist position	75
5.3.2	Grating rotation	75
5.3.3	Grating-cylindrical mirror distance	75
5.3.4	SLM-cylindrical mirror distance	77
6	Non linear optics	79
6.1	Introduction	79
6.2	Second harmonic generation	81
6.3	Parametric down conversion	85

6.3.1	Classical treatment for real signal envelopes	86
6.3.2	Complex signal envelope and quantum treatment	88
6.3.3	Pump spectral phase effects	89
6.4	SPOPO	91
6.4.1	SPOPO without dispersion, input-output relations.	91
6.4.2	Simulation of intra-cavity dispersion	93
III Pump-shape optimisation with machine-learning		97
7	Numerical optimisation of the pump spectrum	99
7.1	Introduction to machine learning	100
7.1.1	Reinforcement learning with projective simulation	100
7.1.2	Supervised learning with neural networks	102
7.2	Pump spectral shape optimisation	105
7.2.1	Previous results	105
7.2.2	Simulation parameters and details	107
7.3	Results	110
7.3.1	Maximising parametric gain	111
7.3.2	Maximising eigenvalue degeneracy	113
8	Covariance matrix reconstruction	121
8.1	Reconstruction from standard homodyne measurement	121
8.1.1	Principle	121
8.1.2	Fraxel modes and supermodes reconstruction	124
8.1.3	Mesurement details	124
8.2	Multipixel homodyne detection	126
8.2.1	Principle	126
8.2.2	Design	126
8.2.3	Mesurement details	129
8.3	Reconstruction from multipixel homodyne	130
8.3.1	Principle	130
8.3.2	Phase reconstruction	134
9	Experimental optimization of the pulse shaper	137
9.1	Flat pump	137
9.2	Optimising maximum squeezing	143
9.2.1	With amplitude shaping	143
9.2.2	With phase shaping	147
9.3	Optimising degenerate squeezing	150
Conclusion and outlook		157
A	Appendix	159
A.1	A squeezed state QRNG	159
A.2	Gaussian unitaries	175
A.3	Fourier transform definition and useful properties	178
A.4	Derivation of the non linear interaction equation from Maxwell's equations	178

A.5 Units, normalization and discretization	180
Bibliography	183

Introduction

Light is a fascinating thing. Human beings are naturally gifted with light detectors and it is our most direct way to interact with reality. Yet light eludes us and the journey towards a full understanding of its nature was long, full of surprises and would require the brightest minds of generations. Light has both been a tool and a catalyst, the actor and the director in this fiction superseding movie that is the history of modern physics. It was used to probe the inner workings of reality long before its own nature was fully understood. Indeed many revolutionary ideas in physics have lead to re-examine our understanding of light. Its status completely changed, from particles, to waves, to a quantum field, which is somewhat the modern synthesis of the two.

Since ancient times, people have been using lenses and mirrors to shape and control light. In the 17th century, Galileo, Kepler, Snell, Descartes and Newton among others, studied and (re)discovered the refraction and reflection properties of light. Using this knowledge, they designed powerful telescopes and microscopes that allowed to observe the world at small and large scales with unprecedented precision. Among those observation, the study of the movement of planets by Ticho Brahe, allowed Kepler to later formulate his famous laws, a cornerstone to Newton's Principia: the foundation of classical mechanics.

There was still no consensus about the nature of light then, Huygens proposed a wave theory of light, while Newton described light as made of particles. The debate was apparently solved by Young and Fresnel who designed experiments to show that light can produce interference effects, a signature of waves. Although, at the time, the exact nature of those waves remained unknown. It was later revealed, in an unexpected way, in 1865, when electricity and magnetism where unified by Maxwell under a single theory. Maxwell's equations predict that oscillations of the electric and magnetic fields can propagate as a wave, a wave that just happens to move at the speed of light. Therefore light is nothing but a propagating perturbation in the electromagnetic field. As these oscillations can happen at any frequency, even those undetectable by the human eye, a whole new spectrum of light was discovered, in the form of radio waves, microwaves, X-rays and others. Those same waves are now our main way to probe the early history of the universe with the cosmic microwave background. Light also had a pivotal role in the discovery of special relativity. The Michelson-Morley experiment, based on light interference, was attempting to probe the motion of earth relative to aether, the hypothetical propagation medium for electromagnetic waves. The negative results showed the speed of light was the same in all moving frames, in contradiction with the old principle of Galilean relativity. Solving this paradox would lead Einstein to revolutionise the concepts of time and space. Extending his ideas to non-inertial frames, Einstein then developed general relativity, which in turn predicted new behaviours for light, for example that it can be bended by large masses. Observations of the deviation of light from distant stars by the sun were one of the first

experimental confirmation of this new theory. Light can also be “stretched” as space expands, an effect that allows astronomers to study the history of expansion of the universe.

Finally light had a major role in the development of quantum physics as well. Three of the unexplained experimental facts that puzzled scientist in the early 19th century and lead to the foundations of quantum mechanics are associated with light: the ultraviolet catastrophe of black body radiation, the photoelectric effect and the discrete emission spectrum of atoms. Today, light is understood as a quantised electromagnetic field carrying one of the four fundamental interactions known by modern physics. Photons, the particles of light, are excitations of this field. A better understanding of the quantum properties of light and its interaction with matter lead to the invention of lasers [1], which now have countless applications in our everyday life. Lasers greatly improved our ability to control and measure quantum objects. It became an essential tool in fundamental research to probe new physics, to the point that it is now possible to carry out in the lab the “gedanken” experiments imagined a century ago by the founding fathers of quantum mechanics [2]. At the time, these thought experiments were simply ways to highlight and better apprehend the counter-intuitive behaviour of the quantum realm.

Entanglement is, without a doubt, the most intriguing property that quantum particles like photons can exhibit [3, 4]. Two entangled photons cannot be considered individually, but form a quantum state as a whole. This means that a measurement performed on one of the photons may influence the quantum state of the other photon regardless of their spatial separation, even when the two are spacelike separated and should not be able to causally influence each other. Locality and causality are closely bonded and this “spooky action at distance” was troubling for many physicists, especially for Einstein, Podolsky and Rosen [5], who thought this violation of locality could only mean that the quantum theory was incomplete. They exposed their idea with a thought experiment, now known as the EPR paradox. A heated debate ensued that divided the physicist community in two camps. Those who believed something had to be wrong in the theory and those who believed the theory was complete and rejected this paradox with metaphysical arguments on the concept of reality. This problem remained mostly ignored as an ontological one, until John Stuart Bell brought a new outlook on this paradox and formulated it in empirical terms with his famous inequality [6, 7]. Any hypothetical more complete and local theory would necessarily predict measurement results that satisfy the inequality. Later experiments [8–11] proved this inequality was indeed violated. This results is sometime thought of as a no hidden variable result although it is more accurate to think of it as a non-locality one. In any case, the old Einstein-Bohr debate was settled [12], no theory based on our common sense or natural intuition could account for the behaviour of quantum particles.

Entanglement is now at the core of the quantum technology revolutions. Using entanglement, quantum teleportation [13–18] has been achieved over large distances [19] and let us contemplate the quantum internet [20], a large quantum network ushering in a new era of communication. Quantum resources are already used in communication and cryptography with quantum key distribution [21–23] which was even achieved over a satellite to earth link [24]. Using quantum resources, the qubits, for information encoding and processing [25, 26], entirely new algorithms [27, 28] can be implemented that would improve the current computing capabilities by orders of magnitude. The ideal, universal quantum computer [25] is still far from being accessible and difficult (may be impossible?) challenges have to be overcome [29]. But imperfect implementations of quantum computers have already shown to supersede current classical computers on certain tasks [30, 31].

Algorithms are already proposed to use these imperfect quantum computers for practical tasks [32–36].

Entanglement is an important resource for quantum computers [37] and it has been shown [38] that any quantum computation can be done by building a large entangled resource called the cluster state (costly operation) and performing local single qubits measurements (“easy” operation). Entanglement is not limited to bipartite states and multipartite entangled photons can be produced by mixing single photons with linear optical components [39–43]. But this approach is not particularly appealing because of its limited scalability. Indeed, in the so called discrete variable regime, entanglement cannot be easily generated deterministically and post-selection analysis is necessary to rule out the unwanted contributions in the state. This post-selection makes the resource scarce when the number of entangled photons is scaled up.

Another intriguing property of the quantum realm is vacuum fluctuations. Even in vacuum, a quantum field exhibits some intrinsic fluctuations. The result is an intrinsic noise in the light field. This noise can be harnessed to produce unbiased random numbers [44]. But it also bounds the precision of conventional measurements to the so-called standard quantum limit [45]. However, this noise can be controlled and reduced in particular states of light called squeezed vacuum states [46], in order to enhance the precision of measurements [47]. This was done for example, in the VIRGO and LIGO gravity-wave detection experiment [48, 49]. The field fluctuations in two separated regions of space can also be correlated in a similar way to the EPR entangled particles. This type of entanglement is different from the one we mentioned for a discrete number of photons (discrete variable). Here the entanglement is carried by many photons, and the EPR correlation is present in variables, the field quadratures, that span a continuous range of values. Those states belong to the so-called continuous variable (CV) regime of quantum optics [50].

CV entanglement is also useful for quantum processing [51, 52] as multipartite CV cluster state can be produced and used for quantum computation [53, 54]. In the CV regime, that entanglement is generated deterministically [55, 56]. This makes the generation of large entangled resources more practical in CV. A standard way to generate CV EPR states is to first produce squeezed states with optical parametric oscillators (OPO) and use linear optics components to mix the various squeezed beams [57–59]. This way, large cluster states have already been created in the time and frequency domains [60–63].

Our research group focusses on using optical frequency combs (OFC) to generate such states. This type of laser source was developed in the 1980s [64, 65]. It produces ultra short pulses of light [66] (down to the attosecond regime [67–69]) and has various applications in non-linear optics, spectroscopy [70, 71], metrology [72, 73] and quantum optics. An OFC contains a large number of evenly spaced frequency modes. By synchronously pumping an optical parametric oscillator (SPOPO) cavity with an OFC it is possible to produce a complicated network of entangled frequency bands [74–76], i.e. a cluster state. We can measure arbitrary superposition of these frequencies which is effectively equivalent to mixing them with linear optics components. Depending on the frequency basis (modes) of the measurement, the state will either appear as a collection of independent squeezed states or a collection of entangled modes. This multimode state can be tuned by shaping the spectrum of the pump to the parametric down conversion process. This quantum resource is therefore reconfigurable and versatile. In general it is not possible to determine analytically what the pump spectrum should be for a desired output state and an optimization method must be used.

The main work conducted during my PhD concerned the optimisation of the structure of the SPOPO output quantum state by tuning the spectral shape of the pump. Two states were of particular relevance and interest: the first one is a state with a high degree of squeezing in one mode. This state is most relevant for metrology purposes. Indeed, it has been shown [77] that for single parameter estimation, the optimal way to maximize sensitivity is to put the most squeezed state available in a well defined light mode. The second state has identical squeezing in as many modes as possible. This state is the best approximation of an ideal large cluster state. The optimal pump shapes for these two states were obtained from simulations of the SPOPO cavity. The numerical optimisation was carried out with machine learning algorithms, in the hope that they could later be adapted to a live optimisation of the experimental set-up. Indeed, imperfections are present in the experiment and they have a non-trivial effect on the SPOPO output quantum state and its measurements.

The main results of this work are:

- the discovery of simple pump shapes by numerical optimization for the two aforementioned objective SPOPO outputs. The numerical optimization was carried out with a reduced number of degrees of freedom, this ensured obtained the pump shapes would be simple and therefore experimentally testable. Even so, significant changes in the SPOPO output state were predicted, both in terms of squeezing and supermode shapes. In some cases the supermodes had measurable spectra (not too broadband).
- the experimental testing of some of those shapes. For some pump shapes, the predicted effect on the supermodes spectra was confirmed. The effect on the squeezing levels was partially confirmed although limited by losses in the detection systems.
- the modelling of intracavity dispersion effects on the SPOPO output state. The first numerical optimization revealed that for some pump shapes it is important to take intracavity dispersion into account to predict the SPOPO output accurately. A simple model is used here and confirms what can be expected: The main effect of dispersion in our regime is a spectral filtering effect that reduces the bandwidth of the supermodes.

0.1 Thesis outline

The thesis is organised as follows. In the first part, we introduce the necessary theoretical background. Chapter 1 recalls the general basic principles of the quantum description of light, with emphasis on the continuous variable regime. It also introduces most of the notations used throughout this thesis. Chapter 2 presents the tools necessary for the analysis and measurement of multimode Gaussian states.

In the second part, we describe the various experimental devices we use. Chapter 3 presents our light source with emphasis on spectral phase effects as they play an important role in the SPOPO pump shape. Chapter 4 concerns synchronous cavities, how a cavity affects the spectral shape of a transmitted frequency comb. Chapter 5 describes the pulse shaper: the device that allows us to tune the pump spectral shape as well as our measurement basis. Chapter 6 concerns the modelling of multimode entanglement generation using a non-linear component. It gives the model used to simulate the SPOPO output

for a given pump spectral shape and contains the results of our simulation of intra-cavity dispersion effects.

In the last part, we detail the methods and results of machine-learning optimisation of the SPOPO pump. Chapter 7 presents the two machine learning algorithms we used and the corresponding optimal pump shapes obtained from simulation. Chapter 8 explains how various types of homodyne measurements can be used to reconstruct the multimode quantum state. Finally Chapter 9, gives the experimental results obtained with the optimal pump profiles.

Another significant part of the work done during this PhD concerned the generation of quantum random numbers from a squeezed state of light. It has no direct connection with the rest of this work and was already described in great details in a paper [78], we therefore choose to reproduce this paper in the appendix A.1.

Part I

Theoretical background

Chapter 1

Quantum light

Contents

1.1	Quantising the Electromagnetic (EM) field	9
1.1.1	The classical free EM field	9
1.1.2	The photon: a harmonic oscillator excitation	11
1.1.3	Quadrature operators and commutation relations	12
1.2	Quantum state representation	14
1.2.1	Discrete variable representation: the Fock basis	14
1.2.2	Continuous variables and Phase-Space representations	14
1.2.3	Statistical mixtures and the density operator	16
1.3	Importance of modes	16
1.3.1	Mode basis change	17
1.3.2	Intrinsically single-mode and multimode states	17
1.4	A zoo of quantum states	18
1.4.1	Fock states	18
1.4.2	Coherent states	18
1.4.3	Squeezed vacuum states	20
1.4.4	EPR states	23

1.1 Quantising the Electromagnetic (EM) field

In this section we briefly introduce the theoretical tools and notations used for a quantum description of the electromagnetic (EM) field. Following the description given in [79], we define the notion of modes and show that the EM field consists in a set of independent quantum harmonic oscillators, one for each mode.

1.1.1 The classical free EM field

Classically, the EM field is described by two real vector fields¹ ($\mathbf{E}(\mathbf{r}, t)$, $\mathbf{B}(\mathbf{r}, t)$). Their behaviours are governed by Maxwell's equations [80, 81] (see also [82, 83] for a modern course on classical electrodynamics). In vacuum, these equations lead to the following propagation equation for the electric and magnetic fields:

$$\nabla^2 \mathbf{E}(\mathbf{r}, t) - \frac{1}{c^2} \frac{\partial^2 \mathbf{E}(\mathbf{r}, t)}{\partial t^2} = 0 \quad (1.1)$$

¹Throughout this thesis we adopt the bold notation for vectors.

This equation has infinitely many solutions which are as many ways for the EM field to propagate (spherical waves, plane waves, pulses of light etc.). It is often useful to introduce a basis of such solutions, so that, thanks to the linearity of this equation, any field can be described as a linear superposition of those solutions. A mode of the EM field is just an element of such a basis. There are multiple bases of modes and the one we choose to use depends on the constraints and symmetries of a given situation.

It is convenient to consider a finite cubic volume of space¹ $V = L^3$ with periodic boundary conditions so that solutions to Eq. (1.1) can be expanded over a basis of linearly polarised, plane waves labelled by index l ²:

$$\mathbf{E}(\mathbf{r}, t) = \mathbf{E}^{(+)}(\mathbf{r}, t) + \mathbf{E}^{(-)}(\mathbf{r}, t) \quad (1.2)$$

$$\mathbf{E}^{(+)}(\mathbf{r}, t) = \sum_l \mathcal{E}_l \alpha_l(t) \mathbf{u}_l(\mathbf{r}) \quad \text{with} \quad \mathbf{u}_l(\mathbf{r}) = e^{i\mathbf{k}_l \cdot \mathbf{r}} \boldsymbol{\epsilon}_l \quad (1.3)$$

$$\mathbf{E}^{(-)}(\mathbf{r}, t) = \left(\mathbf{E}^{(+)}(\mathbf{r}, t) \right)^* \quad (1.4)$$

Because of the boundary conditions, components of the wave vector \mathbf{k} must satisfy:

$$k_x = \frac{2\pi n_x}{L} \quad \text{where} \quad n_x \in \mathbb{Z} \quad (1.5)$$

$$k_y = \frac{2\pi n_y}{L} \quad \text{where} \quad n_y \in \mathbb{Z} \quad (1.6)$$

$$k_z = \frac{2\pi n_z}{L} \quad \text{where} \quad n_z \in \mathbb{Z} \quad (1.7)$$

Index $l = (n_x, n_y, n_z, p)$ labels both the wave vector components and the polarisation $p = 1, 2$. We also use the convention $-l = (-n_x, -n_y, -n_z, p)$.

Several points are worth noticing in this expansion:

- The electric field is a real quantity which means its positive and negative frequency parts must be complex conjugate of each other. There is some redundancy in considering both of them and it is therefore convenient to introduce the analytical field³ $\mathbf{E}^{(+)}$. It also greatly simplifies the calculus and is useful for the quantisation of the EM field.
- The real quantity \mathcal{E}_l is introduced so that $\alpha_l(t)$ is unit-less, its physical meaning will become clear later.
- From the propagation Eq. (1.1) the form of $\alpha_l(t)$ is easily found to be:

$$\alpha_l(t) = \alpha_l(0) e^{-i\omega_l t} \quad \text{with} \quad \omega_l = ck_l \quad k_l \equiv |\mathbf{k}_l| \quad (1.8)$$

$\alpha_l(0)$ is just a constant that determines the initial condition of the field.

- Finally because of the boundary conditions (1.5) we have:

$$\int_V \mathbf{u}_l(\mathbf{r}) \cdot \mathbf{u}_{l'}(\mathbf{r}) dV = \boldsymbol{\epsilon}_l \cdot \boldsymbol{\epsilon}_{l'} \int_V e^{\pm i(\mathbf{k}_l - \mathbf{k}_{l'}) \cdot \mathbf{r}} dV = V \delta_{ll'} \quad (1.9)$$

Where $\delta_{ll'}$ is the Kronecker delta symbol. This relation guarantees the orthogonality of the modes.

¹This volume is introduced just as a tool for calculation and will then be taken to be infinite.

²The fact that the temporal and spatial parts of a mode can be factorised is not obvious and is a consequence of Eq. (1.1)

³Sometimes also referred to as complex amplitude or positive frequency part of the field.

Similarly we have for the magnetic field:

$$\mathbf{B}(\mathbf{r}, t) = \sum_l \epsilon'_l \frac{\mathcal{E}_l}{c} \alpha_l(t) e^{i\mathbf{k}_l \cdot \mathbf{r}} + \text{c.c.} \quad (1.10)$$

with $\epsilon'_l = \frac{\mathbf{k}_l}{k_l} \times \epsilon_l$ and c.c. is the complex conjugate.

1.1.2 The photon: a harmonic oscillator excitation

In this section we recall the canonical quantisation of the electromagnetic field detailed in [79]¹. In (non-relativistic) quantum mechanics, the state of a (pure) system is given by a vector $|\psi(t)\rangle$ of a Hilbert space \mathcal{H} [84]. Any physical observable correspond to a hermitian operator² acting on \mathcal{H} . The dynamic of a quantum system is given by a hermitian operator, the Hamiltonian, which represent the total energy.

The total energy of the electromagnetic field contained in a cubic volume $V = L^3$ is:

$$U = \int_V \frac{1}{2} \epsilon_0 (\|\mathbf{E}(\mathbf{r}, t)\|^2 + c^2 \|\mathbf{B}(\mathbf{r}, t)\|^2) dV \quad (1.11)$$

Using the expansions from Eq. (1.3), Eq. (1.10) and the boundary relations Eq. (1.9) one can show that:

$$U = \epsilon_0 V \sum_l \mathcal{E}_l^2 (\alpha_l(t) \alpha_l^*(t) + \alpha_l^*(t) \alpha_l(t)) \quad (1.12)$$

$$= \epsilon_0 V \sum_l \mathcal{E}_l^2 (\alpha_l(0) \alpha_l^*(0) + \alpha_l^*(0) \alpha_l(0)) \quad (1.13)$$

So the total energy of the EM field is just the sum of the energy contained in each mode and the energy of each mode is conserved. A quantum description of the field is obtained by promoting the complex constants $\alpha_l(0)$ to operators \hat{a}_l , called the field operators. The Hamiltonian of the free field is then a sum of Hamiltonians over each independent normal mode:

$$\hat{H} = \sum_l \hat{H}_l \quad \text{with} \quad \hat{H}_l = \epsilon_0 V \mathcal{E}_l^2 (\hat{a}_l \hat{a}_l^\dagger + \hat{a}_l^\dagger \hat{a}_l) \quad (1.14)$$

Each of those is the Hamiltonian of a harmonic oscillator (see Fig. 1.1). Excitations of these oscillators are photons, the fundamental particles of light. \mathcal{E}_l is the amplitude of the electric field in this mode for a single excitation (one photon). For the corresponding energy to be an energy quantum $\hbar\omega_l$ we need:

$$\mathcal{E}_l = \sqrt{\frac{\hbar\omega_l}{2\epsilon_0 V}} \quad (1.15)$$

For the quantum description to be complete, the field operators need to follow the commutation relations:

$$[\hat{a}_l, \hat{a}_{l'}^\dagger] = \delta_{ll'} \quad (1.16)$$

$$[\hat{a}_l, \hat{a}_{l'}] = 0 \quad (1.17)$$

¹Note however that the field here is described in the Heisenberg picture unlike in [79].

²More generally, measurements can be described by positive operator-valued measure (POVM).

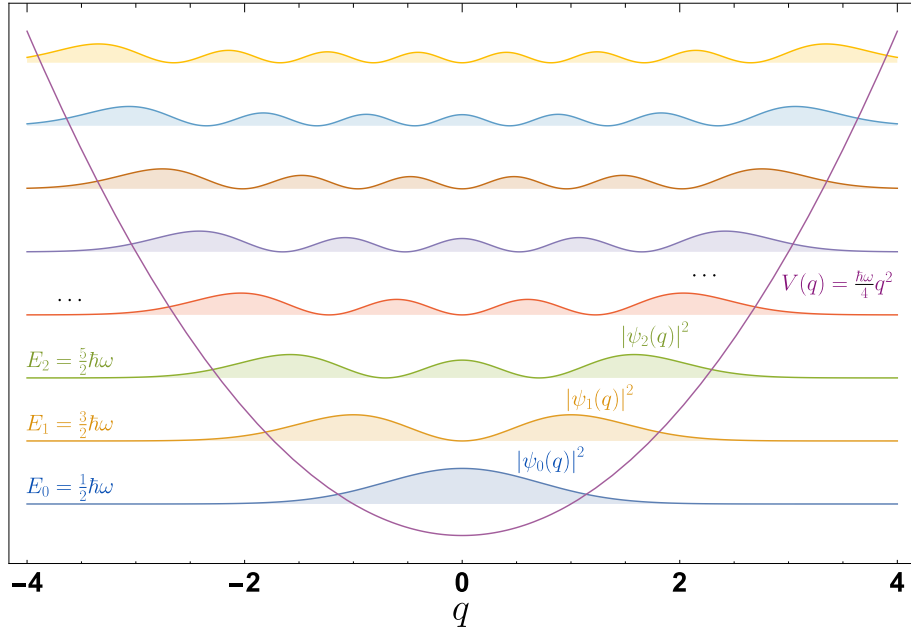


Fig. 1.1 Representation of the quantum harmonic oscillator eigenmodes. The $\psi_k(q)$ represent the eigenmodes wavefunction and their offset is their energy (eigenvalue). $V(q)$ is a harmonic potential.

So the Hamiltonian of mode l is finally:

$$\hat{H}_l = \frac{\hbar\omega_l}{2}(\hat{a}_l\hat{a}_l^\dagger + \hat{a}_l^\dagger\hat{a}_l) \quad (1.18)$$

$$= \hbar\omega_l\left(\hat{a}_l^\dagger\hat{a}_l + \frac{1}{2}\right) \quad (1.19)$$

$$(1.20)$$

And the quantum operator for the electric field reads:

$$\hat{\mathbf{E}}^{(+)}(\mathbf{r}, t) = \sum_l \mathcal{E}_l \hat{a}_l \mathbf{u}_l(\mathbf{r}, t) \quad (1.21)$$

where $\mathbf{u}_l(\mathbf{r}, t) = e^{i(\mathbf{k}_l \cdot \mathbf{r} - \omega_l t)} \boldsymbol{\epsilon}_l$.

1.1.3 Quadrature operators and commutation relations

The field operators we defined in the previous section are not hermitian operators and do not correspond to physical observables. From the field operators, we can define hermitian operators, analogous to momentum and position of a harmonic oscillator. They are called the quadrature operators and are given by¹:

$$\hat{q}_l = \hat{a}_l^\dagger + \hat{a}_l \quad (1.22)$$

$$\hat{p}_l = i(\hat{a}_l^\dagger - \hat{a}_l) \quad (1.23)$$

¹Other conventions exists for defining the quadratures, this one corresponds to a vacuum shotnoise equal to 1

And the converse:

$$\hat{a}_l = \frac{1}{2} (\hat{q}_l + i\hat{p}_l) \quad (1.24)$$

$$\hat{a}_l^\dagger = \frac{1}{2} (\hat{q}_l - i\hat{p}_l) \quad (1.25)$$

These hermitian operators correspond to the observables we will access in the experiment. Note that they do not correspond to external degrees of freedom like position and momentum, but are just mathematically similar. Instead they represent internal degrees of freedom of the field. Their meaning is clearer if we express the electric field in terms of those operator:

$$\hat{\mathbf{E}}(\mathbf{r}, t) = \sum_l \epsilon_l \sqrt{\frac{\hbar\omega_l}{2\epsilon_0 V}} (\hat{a}_l e^{-i(\omega_l t - \mathbf{k}_l \cdot \mathbf{r})} + \hat{a}_l^\dagger e^{i(\omega_l t - \mathbf{k}_l \cdot \mathbf{r})}) \quad (1.26)$$

$$= \sum_l \epsilon_l \sqrt{\frac{\hbar\omega_l}{2\epsilon_0 V}} (\hat{q}_l \cos(\omega_l t - \mathbf{k}_l \cdot \mathbf{r}) + \hat{p}_l \sin(\omega_l t - \mathbf{k}_l \cdot \mathbf{r})) \quad (1.27)$$

With this expression we see that the quadrature operators, sometimes referred to as, amplitude and phase, are just the amplitude of the cosine and sine channels of the electric field modes. From Eq. (1.16) and (1.24), we get the commutation relations for the quadrature operators:

$$[\hat{q}_l, \hat{p}_{l'}] = 2i\delta_{ll'} \quad (1.28)$$

$$[\hat{q}_l, \hat{q}_{l'}] = 0 \quad (1.29)$$

$$[\hat{p}_l, \hat{p}_{l'}] = 0 \quad (1.30)$$

Quadratures can also be defined at arbitrary phase θ with:

$$\hat{x}_l^\theta = \cos \theta \hat{q}_l + \sin \theta \hat{p}_l \quad (1.31)$$

$$= e^{i\theta} \hat{a}_l^\dagger + e^{-i\theta} \hat{a}_l \quad (1.32)$$

The commutation relation (1.28) leads to a Heisenberg inequality for the amplitude and phase quadratures of a given mode. For a pair of arbitrary operators \hat{O}_1 and \hat{O}_2 this inequality is determined by the commutation relation between those operator (see for example [85]):

$$\langle \Delta \hat{O}_1^2 \rangle \langle \Delta \hat{O}_2^2 \rangle \geq \left(\frac{1}{2i} \langle [\hat{O}_1, \hat{O}_2] \rangle \right)^2 \quad (1.33)$$

Where the variance of the operator in state ψ is defined by:

$$\langle \Delta \hat{O}^2 \rangle = \langle \psi | \hat{O}^2 | \psi \rangle - \langle \psi | \hat{O} | \psi \rangle^2 \quad (1.34)$$

This gives for the amplitude and phase quadratures:

$$\langle \Delta \hat{q}_l^2 \rangle \langle \Delta \hat{p}_l^2 \rangle \geq \delta_{ll} \quad (1.35)$$

This inequality indicates that there is a fundamental limit to the precision with which one can simultaneously measure both quadratures for a given mode of the EM field. This property is at the foundation of quantum communication protocols and is closely linked to the no-cloning theorem [86].

1.2 Quantum state representation

In this section we introduce representations of the quantum state of the EM field. There are many different representations and some may be more relevant to certain types of states.

1.2.1 Discrete variable representation: the Fock basis

The most natural way to describe an arbitrary quantum state is to expand it on a known basis of states. Eigenvectors of the single mode Hamiltonian \hat{H}_l of Eq. (1.18) form an orthonormal basis¹. They are called Fock states, they are eigenstates of the number operator $\hat{n}_l = \hat{a}_l^\dagger \hat{a}_l$, and are labelled according to their eigenvalues: $\hat{n}_l |k\rangle = k |k\rangle$. Any single mode state can be decomposed in that basis with:

$$|\psi\rangle = \sum_n c_n |n\rangle \quad (1.36)$$

This is called a discrete variable representation as the state is described by a discrete set of complex numbers $\{c_n\}$.

There is a Fock basis associated with each of the modes but since the total Hamiltonian is a sum over each mode $\hat{H} = \sum_l \hbar\omega_l \left(\hat{n}_l + \frac{1}{2}\right)$ and the \hat{n}_l commute (see Eq. (1.16)), the eigenvectors of \hat{H} are just tensor products of the single mode Fock states:

$$|n_1, n_2, \dots, n_l, \dots\rangle := |n_1\rangle \otimes |n_2\rangle \otimes \dots \otimes |n_l\rangle \otimes \dots \quad (1.37)$$

So any multimode state can be decomposed in that basis:

$$|\psi\rangle = \sum_{n_1, n_2, \dots, n_l, \dots} C_{n_1, n_2, \dots, n_l, \dots} |n_1, n_2, \dots, n_l, \dots\rangle \quad (1.38)$$

This representation is useful when one manipulates single or few photon states and does photon counting measurements. However, for continuous measurements which will be the main concern of this thesis, other representations are better suited.

1.2.2 Continuous variables and Phase-Space representations

In the laboratory, we often use a measurement technique called homodyne detection (detailed in section 2.3.3). It allows us to directly access the quadratures \hat{q}_l, \hat{p}_l of a given mode. It is therefore useful to represent a state using a basis of eigenvectors of the quadrature operators²(here we drop the mode index for simplicity):

$$|\psi\rangle = \int \psi(q) |q\rangle dq \quad (1.39)$$

$$= \int \tilde{\psi}(p) |p\rangle dp \quad (1.40)$$

¹This follows from the spectral theorem

²Here unlike in Eq. (1.36), the decomposition is continuous. This is because, even though \hat{q} is hermitian, it is not compact on \mathcal{H} so the spectral theorem does not apply. The pseudo-eigenvectors $|q\rangle$ do not belong to \mathcal{H} . Certain restrictions exist on $\psi(q)$ in order for $|\psi\rangle$ to belong to \mathcal{H} . As “good” experimental physicists we will swipe all those mathematical difficulties under the carpet.

where the eigenvectors $|q\rangle$ form an orthonormal and complete basis (similar expression for $|p\rangle$) :

$$\hat{q}|q\rangle = q|q\rangle \quad (1.41)$$

$$\langle q|q'\rangle = \delta(q - q') \quad (1.42)$$

$$\int |q\rangle\langle q| dq = \mathbf{1} \quad (1.43)$$

$\psi(q)$ and $\tilde{\psi}(p)$ both fully describe the quantum state, they are Fourier transform of each other. The q and p quadrature are referred to as conjugate variables. $\psi(q)$ (resp. $\tilde{\psi}(p)$) represents the amplitude probability distribution for measuring the quadrature value q (resp. p).

Since \hat{q} and \hat{p} do not commute and cannot be measured simultaneously, there exists no proper joint probability distribution in phase space to describe $|\psi\rangle$. Nevertheless one can still define a function on the full phase space that give a useful representation of $|\psi\rangle$. It's called the Wigner function [87–89] and is defined as:

$$W_{|\psi\rangle}(q, p) := \frac{1}{2\pi} \int_{\mathbb{R}} \psi\left(q + \frac{y}{2}\right)^* \psi\left(q - \frac{y}{2}\right) e^{-ipy} dy \quad (1.44)$$

It's marginals are $\int_{\mathbb{R}} W_{|\psi\rangle}(q, p) dp = |\psi(q)|^2$ and $\int_{\mathbb{R}} W_{|\psi\rangle}(q, p) dq = |\tilde{\psi}(p)|^2$ but it is not a probability density function and it can take negative values. It is sometimes called a quasi-probability distribution.

A Wigner distributions can also be associated to any operator with:

$$W_{\hat{O}}(q, p) := \frac{1}{2\pi} \int_{\mathbb{R}} \left\langle q + \frac{y}{2} \left| \hat{O} \left| q - \frac{y}{2} \right. \right\rangle e^{-ipy} dy \quad (1.45)$$

The Main properties and relations associated with the Wigner representation are given in Table. 1.1.

This phase space representation is extended to multimode states in a straightforward way. The multimode quadrature eigenvectors form an orthonormal and complete basis (similar expression for $|\mathbf{p}\rangle$) :

$$|\mathbf{q}\rangle := |q_1\rangle \otimes |q_2\rangle \otimes \cdots \otimes |q_l\rangle \otimes \cdots \quad (1.54)$$

$$\langle \mathbf{q}|\mathbf{q}'\rangle = \delta(\mathbf{q} - \mathbf{q}') \quad (1.55)$$

$$\int |\mathbf{q}\rangle\langle \mathbf{q}| d\mathbf{q} = \mathbf{1} \quad (1.56)$$

And the multimode quantum state is decomposed as:

$$|\psi\rangle = \int \psi(\mathbf{q}) |\mathbf{q}\rangle d\mathbf{q} \quad (1.57)$$

$$= \int \tilde{\psi}(\mathbf{p}) |\mathbf{p}\rangle d\mathbf{p} \quad (1.58)$$

The multimode Wigner function is defined as:

$$W_{|\psi\rangle}(\mathbf{q}, \mathbf{p}) := \left(\frac{1}{2\pi}\right)^n \int_{\mathbb{R}^n} \psi\left(\mathbf{q} + \frac{\mathbf{y}}{2}\right)^* \psi\left(\mathbf{q} - \frac{\mathbf{y}}{2}\right) e^{-i\mathbf{p}\cdot\mathbf{y}} d^n y \quad (1.59)$$

Other phase-space representation exist [90, 91] but their description lies outside the scope of this thesis.

$W_{\hat{\rho}}(q, p) := \left(\frac{1}{2\pi}\right) \int_{\mathbb{R}} \left\langle q + \frac{y}{2} \left \hat{\rho} \right q - \frac{y}{2} \right\rangle e^{-ipy} dy$	(1.46)
$W(q, p) \in \mathbb{R}$	(1.47)
$\int_{\mathbb{R}} W_{\hat{\rho}}(q, p) dp = \langle q \hat{\rho} q \rangle_{\text{pure state}} = \psi(q) ^2$	(1.48)
$\int_{\mathbb{R}} W_{\hat{\rho}}(q, p) dq = \langle p \hat{\rho} p \rangle_{\text{pure state}} = \tilde{\psi}(p) ^2$	(1.49)
$\int_{\mathbb{R}^2} W_{\hat{\rho}}(q, p) dq dp = \text{Tr}(\hat{\rho})_{\text{pure state}} = 1$	(1.50)
$ \langle \psi \phi \rangle ^2 = 4\pi \int_{\mathbb{R}^2} W_{\psi}(q, p) W_{\phi}(q, p) dq dp$	(1.51)
$\text{Tr}(\hat{\rho} \hat{O}) = \int_{\mathbb{R}^2} W_{\hat{\rho}}(q, p) W_{\hat{O}}(q, p) dq dp$	(1.52)
$-1 \leq W_{\hat{\rho}}(q, p) \leq 1$	(1.53)

Table 1.1 – Main properties of the Wigner function

1.2.3 Statistical mixtures and the density operator

Until now we have only described so called *pure* systems. When the quantum state is subject to classical noise or is not isolated, this description is not sufficient. It is necessary to describe statistical superposition of states $|\psi\rangle_1, |\psi\rangle_2, \dots$. Such *mixed* states are described by the density operator, first introduced by John Von Neumann [92]:

$$\hat{\rho} = \sum_i p_i |\psi_i\rangle\langle\psi_i| \quad \text{with} \quad \sum_i p_i = 1 \quad (1.60)$$

where the p_i represent the statistical weights of the pure states $|\psi_i\rangle$.

Just like pure states, mixed states can be decomposed on the Fock basis with:

$$\hat{\rho} = \sum_{mn} c_{mn} |m\rangle\langle n| \quad (1.61)$$

In this Fock representation the states are fully characterised by the matrix with coefficients $c_{mn} = \langle m | \hat{\rho} | n \rangle$. The diagonal terms $\{c_{nn}\}$ correspond to the probabilities of detecting the particular Fock state $|n\rangle$, they are called populations. The off diagonal terms $\{c_{mn}\}_{m \neq n}$ represent fixed phase relationships between the Fock states $|m\rangle$ and $|n\rangle$, they are called coherences. Example of Fock basis expansion will be given for several quantum states of interest. Incidentally, any other operator \hat{O} can also be described with its Fock basis matrix elements $\langle m | \hat{O} | n \rangle$.

Wigner distributions can also describe mixed states and are obtained from the density operator with:

$$W_{\hat{\rho}}(q, p) = \left(\frac{1}{2\pi}\right) \int_{\mathbb{R}} \left\langle q + \frac{y}{2} \left| \hat{\rho} \right| q - \frac{y}{2} \right\rangle e^{-ipy} dy \quad (1.62)$$

1.3 Importance of modes

The quantum state representations we introduced rely on Fock states $\{|n\rangle_l\}$ and quadrature eigenstates $\{|q\rangle_l\}$ which are associated to the monochromatic travelling plane wave

modes $\{\mathbf{u}_l\}$. This basis choice is somewhat arbitrary, and the EM field can be expanded on other bases. A given quantum state may therefore have very different representations for different mode bases. For this reason, there is a very intricate link between the modes structure and the quantum states structure. This motivates the search for properties of quantum states that are intrinsic i.e independent of the mode basis.

1.3.1 Mode basis change

Any basis of functions that solve Eq. (1.1) define a set of modes. A given set of mode functions $\{\mathbf{g}_l\}$ can be expanded on another set of modes $\{\mathbf{f}_l\}$ with:

$$\mathbf{g}_l(\mathbf{r}, t) = \sum_m U_{lm} \mathbf{f}_m(\mathbf{r}, t) \quad (1.63)$$

and the converse:

$$\mathbf{f}_l(\mathbf{r}, t) = \sum_m U_{ml}^* \mathbf{g}_m(\mathbf{r}, t) \quad (1.64)$$

where $\{U_l^m\}$ are complex coefficients given by:

$$U_{lm} = \frac{1}{V} \int_V \mathbf{f}_m(\mathbf{r}, t)^* \mathbf{g}_l(\mathbf{r}, t) dV \quad (1.65)$$

The new basis \mathbf{g}_l is associated with a new set of creation/annihilation operators $\{\hat{b}_l\}$. These are also related to the creation/annihilation operators $\{\hat{a}_l\}$ associated with $\{\mathbf{f}_l\}$. To find the right formulae for the field operator transformations, we require that the total electric field expressed in both bases is identical. This gives the formulae:

$$\hat{b}_l = \sum_m U_{lm}^* \hat{a}_m \quad (1.66)$$

$$\hat{b}_l^\dagger = \sum_m U_{lm} \hat{a}_m^\dagger \quad (1.67)$$

and the converse:

$$\hat{a}_l = \sum_m U_{ml} \hat{b}_m \quad (1.68)$$

$$\hat{a}_l^\dagger = \sum_m U_{ml}^* \hat{b}_m^\dagger \quad (1.69)$$

1.3.2 Intrinsically single-mode and multimode states

The notion of multimode states of light is particularly important to this thesis. Here we will briefly sketch the difference between a state of light that is essentially single-mode and one that is intrinsically multimode, more details can be found in [93].

As we already mentioned, there is an intricate link between the mode basis and the state representation. In particular the notion of separability¹ depends on the mode basis. Given two bases $\{\mathbf{u}_l\}$, $\{\mathbf{v}_l\}$ we may have for example:

$$|\Psi\rangle = \frac{1}{\sqrt{2}}(|10\rangle_{\mathbf{u}_1, \mathbf{u}_2} + |01\rangle_{\mathbf{u}_1, \mathbf{u}_2}) \otimes |0, 0, \dots\rangle_{\mathbf{u}_3, \dots} \quad (1.70)$$

$$= |1\rangle_{\mathbf{v}_1} \otimes |0, 0, \dots\rangle_{\mathbf{v}_2, \dots} \quad (1.71)$$

¹A given state is separable if it is written as a tensor product of single mode states.

In the representation corresponding to \mathbf{u}_l , the state is not separable and modes $\mathbf{u}_1, \mathbf{u}_2$ are entangled but it is not the case in the \mathbf{v}_l representation.

A state is said to be intrinsically single mode if there exists a basis of modes in which the state is written:

$$|\Psi\rangle = |\psi_1\rangle \otimes |0, 0, \dots\rangle \quad (1.72)$$

Conversely, if there is no such basis, the state is intrinsically multimode. Note that the full vacuum state (vacuum $|0\rangle$ for all modes) has the same representation in all mode bases.

We can examine further the multimode aspect of a state and define its minimal number of occupied mode or degree [94]. That is to say, for all possible mode bases, the minimal n such that the state can be written:

$$|\Psi\rangle = |\psi\rangle_{\mathbf{u}_1, \dots, \mathbf{u}_n} \otimes |0, 0, \dots\rangle_{\mathbf{u}_{n+1}, \dots} \quad (1.73)$$

The n first modes are then called the principal/minimal modes.

1.4 A zoo of quantum states

In this section we introduce the states most encountered in quantum optics. Unless specified otherwise, we will only consider a single mode of the EM field and won't write the index labelling the mode explicitly.

1.4.1 Fock states

Fock states (or Number states) $\{|n\rangle\}_{n \in \mathbb{N}}$ are eigenstates of the Hamiltonian, they define photons. They form a complete orthonormal basis so that any state can be written as a superposition of Fock states. Fock states are defined as eigenstates of the number operator $\hat{n} = \hat{a}^\dagger \hat{a}$.

The state $|0\rangle$ is called the vacuum state, it is the ground state of the EM field and corresponds to an empty field. Note however, that many physical observable can take non zero values in this state. In particular, the EM field fluctuations are non zero in vacuum $\langle 0 | \hat{E}^2 | 0 \rangle \neq 0$. The main properties of Fock states are summarised in Table. 1.2.

Fig. 1.2 shows typical quadrature measurements from the vacuum state. The electric field is non zero and shows some fluctuations, these fluctuations are at the origin of shot noise, it is the intrinsic quantum noise of the electric field. The field has no coherence, no defined phase, as is the case for any Fock state. The q and p distributions follow a normal distribution.

Fig.1.3 shows typical quadrature measurements for a two photon Fock state. The field does not have any defined phase, it's fluctuation are bigger than in the vacuum state. The q and p distributions follow a Hermite-Gauss distribution.

Fig. 1.4 shows the Wigner functions of the vacuum state and two photon state. Note the Wigner function of the two photon state goes negative, which reveals the quantum nature of that state.

1.4.2 Coherent states

Coherent states were first introduced by Erwin Schroedinger [95] and were later thoroughly studied by Glauber, Klauder and Sudarshan [96–98]. The coherent state is the state that most resembles the classical EM field state with defined amplitude and phase

$\hat{n} k\rangle = k k\rangle$	(1.74)
$ k\rangle = \frac{(\hat{a}^\dagger)^k}{\sqrt{k!}} 0\rangle$	(1.75)
$\hat{a} k\rangle = \sqrt{k} k-1\rangle$	(1.76)
$\hat{a}^\dagger k\rangle = \sqrt{k+1} k+1\rangle$	(1.77)
$\langle \hat{n} \rangle = k$	(1.78)
$\langle \Delta \hat{n}^2 \rangle = 0$	(1.79)
$\langle \hat{q} \rangle = \langle \hat{p} \rangle = 0$	(1.80)
$\langle \Delta \hat{q}^2 \rangle = \langle \Delta \hat{p}^2 \rangle = 2k + 1$	(1.81)
$\langle q n\rangle = \left(\frac{1}{2\pi}\right)^{\frac{1}{4}} \frac{1}{\sqrt{2^n n!}} H_n\left(\frac{q}{\sqrt{2}}\right) \exp\left(-\frac{q^2}{4}\right)$	(1.82)
$W_{ n\rangle}(q, p) = \frac{1}{2\pi} (-1)^n L_n(q^2 + p^2) \exp\left(-\frac{q^2 + p^2}{2}\right)$	(1.83)

Table 1.2 – Main properties of Fock states

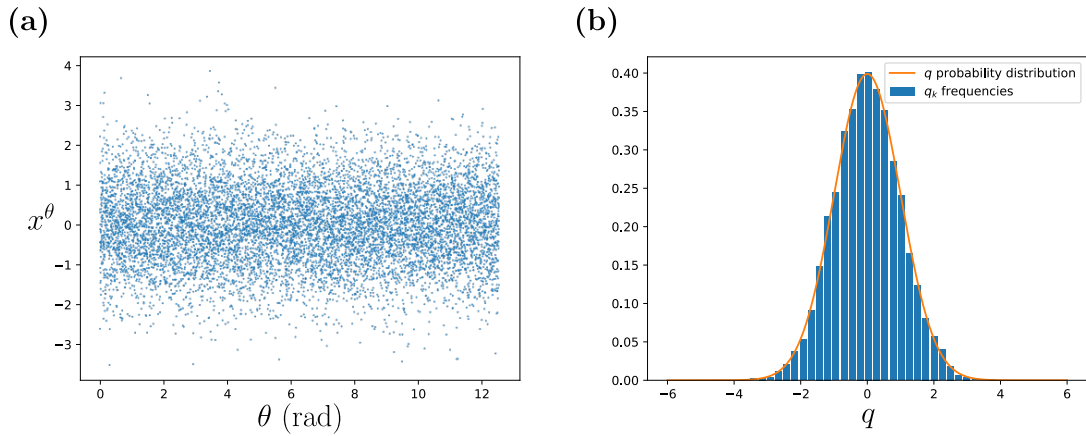


Fig. 1.2 (a) Typical quadrature sampling from the vacuum state $|0\rangle$ at different phases (x^θ is defined by Eq. (1.31)). (b) Probability distribution and sampling frequencies of \hat{q} in the vacuum state $|0\rangle$.

(see Fig. 1.6). The set of coherent states (for a given EM mode) $\{|\alpha\rangle\}_{\alpha \in \mathbb{C}}$ are parametrised by their coherent amplitude α . α is a complex number, its real/imaginary part represent the mean amplitude/phase of the EM field. Coherent states can be defined as eigenstates of the annihilation operator \hat{a} . The variances of the amplitude and phase quadratures of coherent states are equal to 1, thus, a coherent state is a minimum uncertainty state. A source of coherent states can be well approximated in the laboratory by a heavily attenuated source of laser light. The attenuation serves to reduce extraneous noise sources due

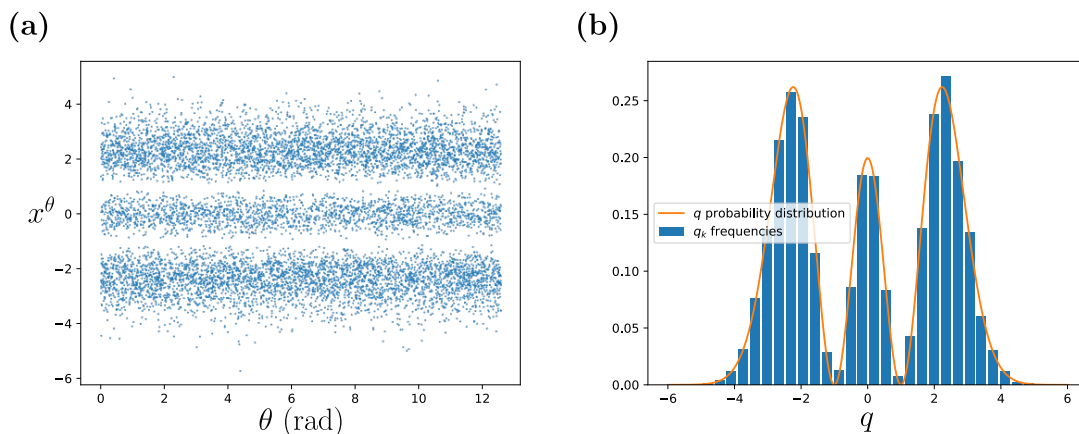


Fig. 1.3 (a) Typical quadrature sampling from the two photon state $|2\rangle$ at different phases (x^θ is defined by Eq. (1.31)). (b) Probability distribution and sampling frequencies of \hat{q} in the two photon state $|2\rangle$.

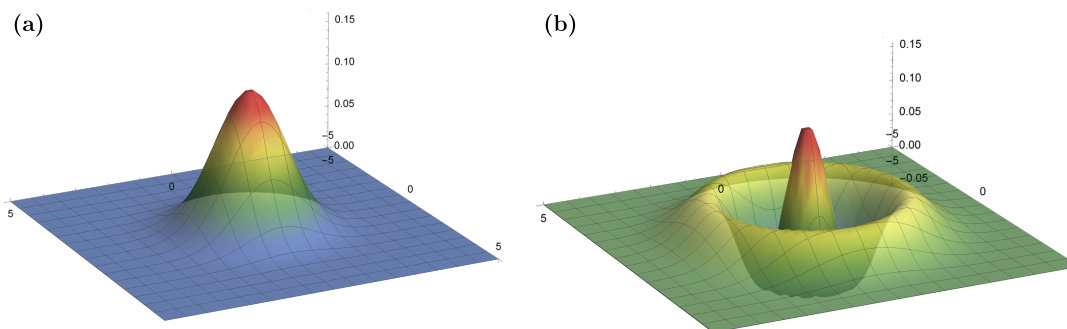


Fig. 1.4 (a) Wigner distribution of the vacuum state $|0\rangle$. Wigner distribution of the two photon state $|2\rangle$.

to the lasing mechanism, and thereby prepare a nearly pure, coherent state. Note that the coherent state with $\alpha = 0$ coincides with the vacuum state defined in section 1.4.1. Because the coherent states are labelled by a continuous index they form an over-complete basis of \mathcal{H} . The main properties of coherent states are summarised in table 1.3. The Fock decomposition of coherent states follows a Poissonian distribution (see Fig. 1.5). In Wigner representation the coherent state is represented by a bivariate normal distribution with variance 1 and mean given by $2\text{Re}(\alpha)$ and $2\text{Im}(\alpha)$ (see Fig. 1.6).

1.4.3 Squeezed vacuum states

Unlike coherent states, squeezed vacuum states have a quadrature variance below 1. They are also minimum uncertainty states, and the conjugate quadrature variance must exceed 1 to preserve the minimum uncertainty product. In phase space, these states therefore look like a vacuum state squeezed along a certain axis and stretched (anti-squeezed) along the orthogonal axis, hence their name.

Squeezed states can be obtained by the action of the squeezing operator on vacuum: $\hat{S}(\zeta) = e^{\frac{1}{2}(\zeta\hat{a}^{\dagger 2} - \zeta^*\hat{a}^2)}$ where $\zeta = re^{i\theta}$ is a complex parameter. The reduced quadrature

$\hat{a} \alpha\rangle = \alpha \alpha\rangle$	(1.84)
$ \alpha\rangle = \hat{D}(\alpha) 0\rangle$	(1.85)
$\hat{D}(\alpha) = e^{\alpha\hat{a}^\dagger - \alpha^*\hat{a}} = e^{-\frac{1}{2} \alpha ^2} e^{\alpha\hat{a}^\dagger} e^{-\alpha^*\hat{a}} = e^{\frac{1}{2} \alpha ^2} e^{-\alpha^*\hat{a}} e^{\alpha\hat{a}^\dagger}$	(1.86)
$ \alpha\rangle = e^{-\frac{1}{2} \alpha ^2} \frac{\alpha^n}{\sqrt{n!}} n\rangle$	(1.87)
$\langle \hat{n} \rangle = \langle \Delta \hat{n}^2 \rangle = \alpha ^2$	(1.88)
$\langle \hat{q} \rangle = 2 \text{Re}(\alpha)$	(1.89)
$\langle \hat{p} \rangle = 2 \text{Im}(\alpha)$	(1.90)
$\langle \Delta \hat{q}^2 \rangle = \langle \Delta \hat{p}^2 \rangle = 1$	(1.91)
$\langle q \alpha\rangle = \left(\frac{1}{2\pi}\right)^{\frac{1}{4}} \exp\left(-\frac{(q - \text{Re}(\alpha))^2 + i \text{Im}(\alpha)q}{4}\right)$	(1.92)
$W_{ \alpha\rangle}(q, p) = \frac{1}{\pi} \exp\left(-\frac{(q - \text{Re}(\alpha))^2 + (p - \text{Im}(\alpha))^2}{2}\right)$	(1.93)

Table 1.3 – Main properties of coherent states

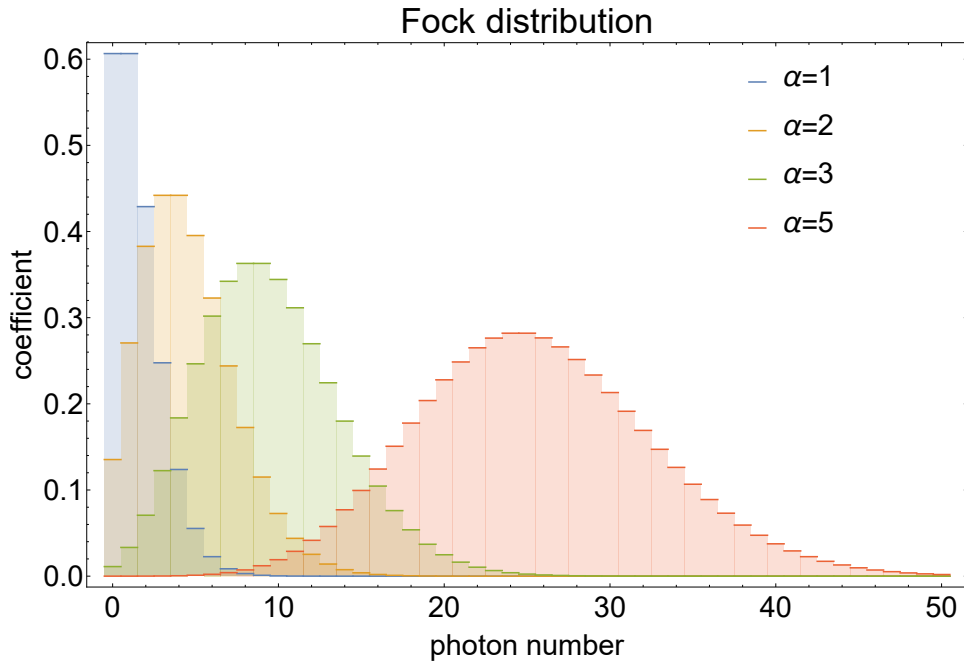


Fig. 1.5 Fock distribution of the coherent state

variance is a very useful characteristic of those state, it is used for example in metrology when a measurement is polluted by quadrature noise. Fig. 1.7 shows the photon number distribution of squeezed vacuum states with various squeezing parameters. Fig. 1.8 shows

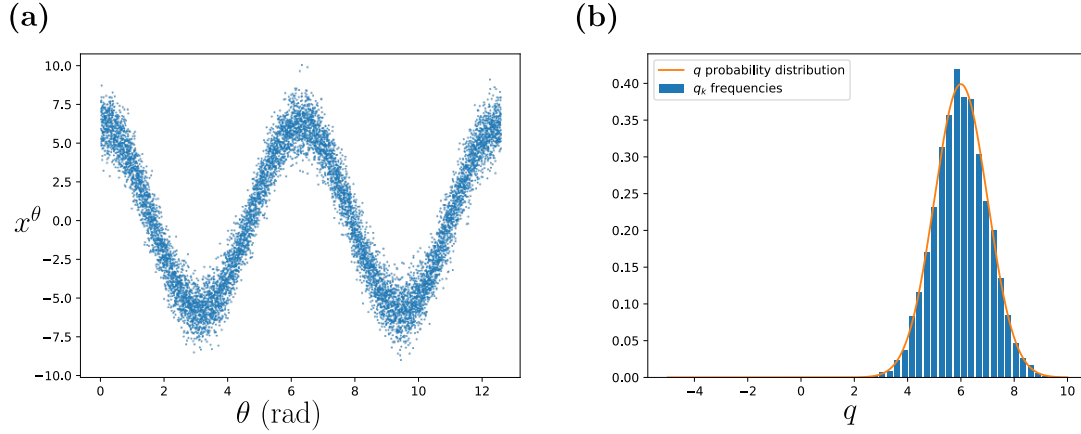


Fig. 1.6 (a) Typical quadrature sampling from the coherent state $|\alpha = 3\rangle$ at different phases (x^θ is defined by Eq. (1.31)). (b) Probability distribution and sampling frequencies of \hat{q} in the coherent state $|\alpha = 3\rangle$.

$ \zeta = re^{i\phi}\rangle = \hat{S}(\zeta) 0\rangle$	(1.94)
$\hat{S}(\zeta) = e^{\frac{1}{2}(\zeta\hat{a}^\dagger{}^2 - \zeta^*\hat{a}^2)}$	(1.95)
$ \zeta\rangle = \frac{1}{\sqrt{\cosh(r)}} \sum_{n=0}^{\infty} \frac{\sqrt{(2n)!}}{2^n n!} (e^{i\phi} \tanh(r))^n 2n\rangle$	(1.96)
$\langle \hat{n} \rangle = \sinh(r)^2$	(1.97)
$\langle \Delta \hat{n}^2 \rangle = 2 \sinh(r)^2 \cosh(r)^2 = \frac{\sinh(2r)^2}{2}$	(1.98)
$\langle \hat{q} \rangle = \langle \hat{p} \rangle = 0$	(1.99)
$\langle \Delta \hat{q}^2 \rangle = e^{2r} \cos^2\left(\frac{\phi}{2}\right) + e^{-2r} \sin^2\left(\frac{\phi}{2}\right)$	(1.100)
$\langle \Delta \hat{p}^2 \rangle = e^{-2r} \cos^2\left(\frac{\phi}{2}\right) + e^{2r} \sin^2\left(\frac{\phi}{2}\right)$	(1.101)
$\langle q \zeta \rangle = \left(\frac{1}{2\pi}\right)^{\frac{1}{4}} \exp\left(-\frac{q^2}{4\langle \Delta \hat{q}^2 \rangle}\right)$	(1.102)
$W_{ \zeta\rangle}(q, p) = \frac{1}{\pi} \exp\left(-\frac{q^2}{2\langle \Delta \hat{q}^2 \rangle} - \frac{p^2}{2\langle \Delta \hat{p}^2 \rangle}\right)$	(1.103)

Table 1.4 – Main properties of vacuum squeezed states

the typical quadrature measurements from a squeezed vacuum state and typical quadrature distributions.

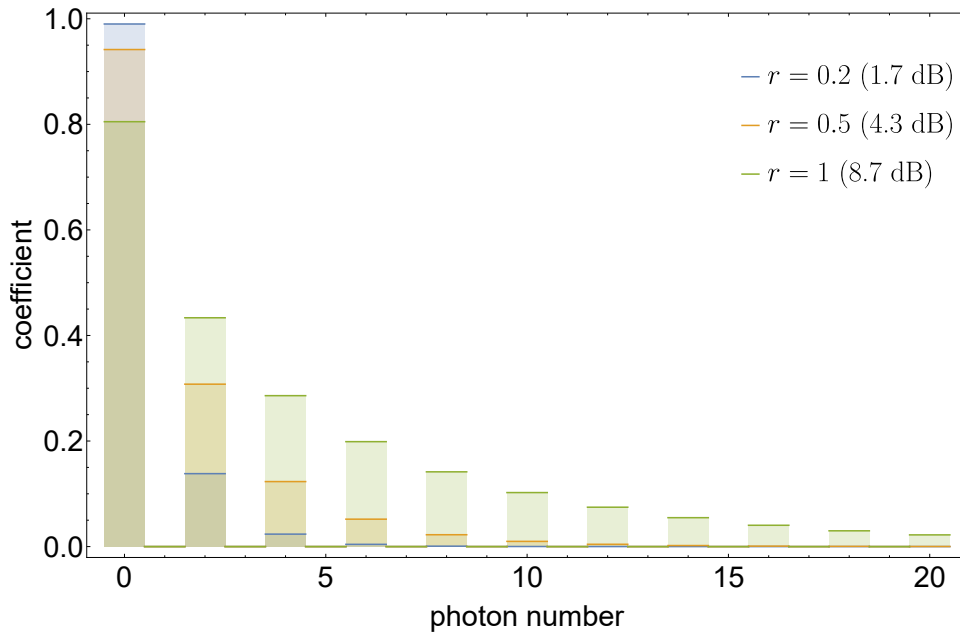


Fig. 1.7 Fock distribution of the squeezed vacuum state

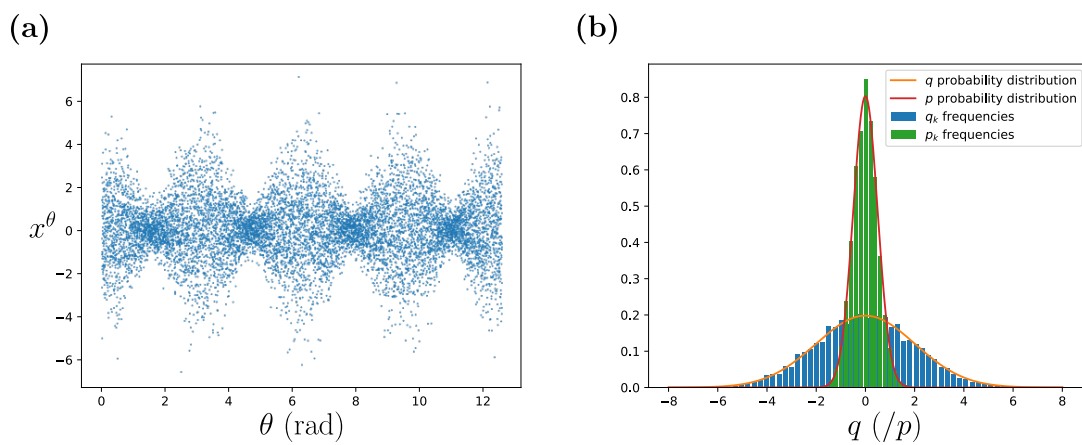


Fig. 1.8 (a) Typical quadrature sampling from the squeezed vacuum state $|\zeta = 0.7\rangle$ (6.1 dB) at different phases (x^θ is defined by Eq. (1.31)). (b) Probability distribution and sampling frequencies of \hat{q} and \hat{p} in the squeezed vacuum state $|\zeta = 0.7\rangle$.

1.4.4 EPR states

Another important state in CV quantum optics is the EPR state or two-mode squeezed vacuum state. Unlike all the states we presented until now, the EPR state is multimode.

EPR states can be obtained by the action of the two mode squeezing operator on vacuum:

$$|\zeta\rangle_{\text{EPR}} = \hat{S}_2(\zeta) |0, 0\rangle \quad (1.104)$$

$$= e^{\frac{1}{2}(\zeta \hat{a}_1^\dagger \hat{a}_2^\dagger - \zeta^* \hat{a}_1 \hat{a}_2)} |0, 0\rangle \quad (1.105)$$

$$= \frac{1}{\cosh(r)} \sum_{n=0}^{\infty} \left(e^{i\phi} \tanh(r) \right)^n |n, n\rangle \quad (1.106)$$

where $\zeta = r e^{i\theta}$ is a complex parameter. This form shows that the EPR state is made up of pairs of equal numbers of photons in two modes. This state exhibits correlation between the quadratures of the two modes:

$$\langle (q_1 - q_2)^2 \rangle = \langle (p_1 + p_2)^2 \rangle = e^{-2r} \leq 1 \quad (1.107)$$

These correlation cannot be accounted for classically, they are evidence of the entanglement between the two modes and exemplify the famous EPR paradox raised by Einstein, Podolsky and Rosen [5].

Chapter 2

Gaussian states and operations

Contents

2.1	Gaussian states, gaussian unitaries	26
2.1.1	Phase-space representation and covariance matrix	26
2.1.2	Example of Gaussian states	27
2.1.3	General Gaussian unitaries, Bogoliubov/Symplectic transformations	29
2.1.4	General mode basis change	30
2.2	Decompositions of Gaussian states and operations	30
2.2.1	Bloch-Messiah reduction	31
2.2.2	Williamson decomposition	32
2.2.3	One decomposition to rule them all	33
2.3	Gaussian measurements	33
2.3.1	Continuum of modes, two-mode formalism and envelope operators	33
2.3.2	Intensity measure	37
2.3.3	Homodyne detection	39
2.3.4	Squeezing and sideband noise correlations	41

Out of the large variety of quantum states and operations, the Gaussian ones are of particular interest for this thesis. There are several reasons that make the Gaussian framework useful:

- Gaussian states play a central role in quantum communication and information processing, in particular they are of great practical relevance for continuous variables (CV) quantum optics. Most standard light sources are well described by Gaussian states and Gaussian entanglement can be generated deterministically.
- Many practical transformations preserve the Gaussianity of quantum states.
- On the theoretical side, powerful analytic tools exist that make Gaussian analysis easier and insightful.

That being said, non-Gaussianity is also an interesting feature of quantum states. In quantum computing, in particular, non-Gaussianity is required in order to implement truly quantum algorithms. This non-Gaussianity feature can be added to a carefully prepared Gaussian state by photon subtraction. In our lab, this has been studied theoretically [99–104] and realized experimentally [105, 106] for multimode states. But the present work deals exclusively with the first step of preparing an optimised Gaussian state.

In this chapter we introduce the theoretical tools of Gaussian quantum information. Details on Gaussian quantum information can be found in [107] and reference therein. For an overview of the background mathematical formalism of real symplectic groups see [108]. For details on the multimode aspects of Gaussian states see [93].

2.1 Gaussian states, gaussian unitaries

Simply put, Gaussian states are just quantum states that have a Gaussian Wigner function. The vacuum squeezed state and coherent state introduced in section 1.4.3 are Gaussian states. Gaussian operations are processes that preserve the Gaussianity of the state.

2.1.1 Phase-space representation and covariance matrix

Any Gaussian function is fully determined by its first and second order moments, and the Wigner function fully describes the quantum state. Therefore, a reduced number of parameters is sufficient to describe Gaussian states. This makes their analysis simpler.

Here we introduce the tools to describe Gaussian states. For simplicity we will consider a finite number of modes n . In the following we will often arrange the quadrature field operators in vectors¹:

$$\hat{\mathbf{x}} := (\hat{\mathbf{q}}, \hat{\mathbf{p}})^T := (\hat{q}_1, \dots, \hat{q}_n, \hat{p}_1, \dots, \hat{p}_n)^T \quad (2.1)$$

We can also arrange the creation and annihilation operators in vectors:

$$\hat{\mathbf{a}} := (\hat{a}_1, \dots, \hat{a}_n)^T \quad (2.2)$$

$$\hat{\mathbf{a}}^\dagger := (\hat{a}_1^\dagger, \dots, \hat{a}_n^\dagger)^T \quad (2.3)$$

Note that with this notation $\hat{\mathbf{a}}^\dagger \neq \hat{\mathbf{a}}^{T*}$. One then goes from the quadratures to the field operators with²:

$$\begin{pmatrix} \hat{\mathbf{q}} \\ \hat{\mathbf{p}} \end{pmatrix} = \mathbf{W} \begin{pmatrix} \hat{\mathbf{a}} \\ \hat{\mathbf{a}}^\dagger \end{pmatrix} \quad (2.4)$$

$$\begin{pmatrix} \hat{\mathbf{a}} \\ \hat{\mathbf{a}}^\dagger \end{pmatrix} = \mathbf{W}^{-1} \begin{pmatrix} \hat{\mathbf{q}} \\ \hat{\mathbf{p}} \end{pmatrix} \quad (2.5)$$

with³ $\mathbf{W} = \begin{pmatrix} \mathbb{1} & \mathbb{1} \\ -i\mathbb{1} & i\mathbb{1} \end{pmatrix}$ and $\mathbf{W}^{-1} = \frac{1}{2} \begin{pmatrix} \mathbb{1} & i\mathbb{1} \\ \mathbb{1} & -i\mathbb{1} \end{pmatrix}$.

Gaussian states are states that are represented by a Gaussian Wigner function $W(\mathbf{x})$ of \mathbb{R}^{2n} in phase space. Any such function is fully characterised by its first and second moments. The first moment is called the displacement or mean vector:

$$\bar{\mathbf{x}} := \langle \hat{\mathbf{x}} \rangle = \text{Tr}(\hat{\mathbf{x}}\hat{\rho}) \quad (2.6)$$

¹In this thesis we'll use the "QQPP" convention where the quadratures are grouped by type, in the literature another convention exist ("QPQP") where the quadratures are arranged by mode: $\hat{\mathbf{x}} := (\hat{q}_1, \hat{p}_1, \dots, \hat{q}_n, \hat{p}_n)^T$.

²We adopt a bold notation for matrices in the following.

³These conventions correspond to shotnoise equal to 1.

The second moment is called the covariance matrix \mathbf{V} and is defined as:

$$V_{ij} := \frac{1}{2} \langle \{ \delta \hat{x}_i, \delta \hat{x}_j \} \rangle \quad (2.7)$$

Where $\delta \hat{x}_i := \hat{x}_i - \langle \hat{x}_i \rangle$ and $\{, \}$ is the anti-commutator¹.

It is a $2n \times 2n$ symmetric, real, positive semi-definite matrix which must satisfy the uncertainty relation²:

$$\mathbf{V} + i\mathbf{\Omega} \geq 0 \quad (2.8)$$

Where $\mathbf{\Omega}$ is the symplectic form:

$$\mathbf{\Omega} := \begin{pmatrix} 0 & \mathbf{1} \\ -\mathbf{1} & 0 \end{pmatrix} \quad (2.9)$$

The Wigner function can be expressed explicitly from the first and second moments with [109]:

$$W(\mathbf{x}) = \frac{1}{(2\pi)^n \sqrt{\det(\mathbf{V})}} \exp\left(-\frac{1}{2}(\mathbf{x} - \bar{\mathbf{x}})^T \mathbf{V}^{-1}(\mathbf{x} - \bar{\mathbf{x}})\right) \quad (2.10)$$

The purity of a Gaussian state is calculated from the covariance matrix with:

$$\mu = \frac{1}{\sqrt{\det(\mathbf{V})}} \quad (2.11)$$

2.1.2 Example of Gaussian states

In section 1.4 all the quantum states we introduced were Gaussian except for the Fock states. Table 2.1 summarise the moments of those states.

Gaussian states	$\bar{\mathbf{x}}$	\mathbf{V}
Vacuum state $ 0\rangle$	$\begin{pmatrix} 0 \\ 0 \end{pmatrix}$	$\begin{pmatrix} 1 & 0 \\ 0 & 1 \end{pmatrix}$
Coherent state $ \alpha\rangle$	$\begin{pmatrix} 2\text{Re}(\alpha) \\ 2\text{Im}(\alpha) \end{pmatrix}$	$\begin{pmatrix} 1 & 0 \\ 0 & 1 \end{pmatrix}$
Vacuum squeezed state $ \zeta = r\rangle$	$\begin{pmatrix} 0 \\ 0 \end{pmatrix}$	$\begin{pmatrix} e^{2r} & 0 \\ 0 & e^{-2r} \end{pmatrix}$
EPR state $ \zeta = r\rangle$	$\begin{pmatrix} 0 \\ 0 \\ 0 \\ 0 \end{pmatrix}$	$\mathbf{V}_{\text{EPR}} = \begin{pmatrix} \cosh 2r & \sinh 2r & 0 & 0 \\ \sinh 2r & \cosh 2r & 0 & 0 \\ 0 & 0 & \cosh 2r & -\sinh 2r \\ 0 & 0 & -\sinh 2r & \cosh 2r \end{pmatrix}$

Table 2.1 – First and second moments of common Gaussian states.

Given that Gaussian states are fully characterised by their first and second order quadrature moments, it is worth representing the quadratures of Gaussian states with a ball on a stick picture (see Fig. 2.1). In this phasor diagram representation, the stick

¹Note the definition of covariance matrix here differs from the classical definition because we use the anti-commutator. This is necessary to obtain a symmetric \mathbf{V} because of the non commutativity of \hat{q}_i and \hat{p}_i but this definition reduces to the standard one in the classical case.

²Here the ≥ 0 has to be understood as positive semi-definiteness.

represents the mean and the ball represent the covariance of the quadratures. This diagram can be seen as an extension of the classical phasor diagram defined for classical EM fields, where the field would exhibit some intrinsic noise.

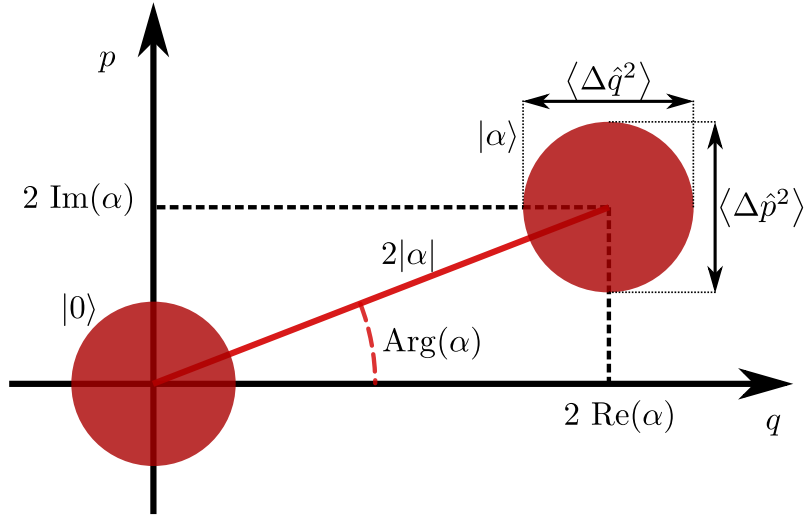


Fig. 2.1 Example of phasor diagram representation for $|0\rangle$ and $|\alpha\rangle$.

Fig. 2.2 illustrates the quadrature correlations of an EPR state. Taken individually, each mode is just a thermal state, but the quadrature of the two modes are correlated so that $\hat{q}_2 - \hat{q}_1$ and $\hat{p}_1 + \hat{p}_2$ are squeezed below the shot noise limit.

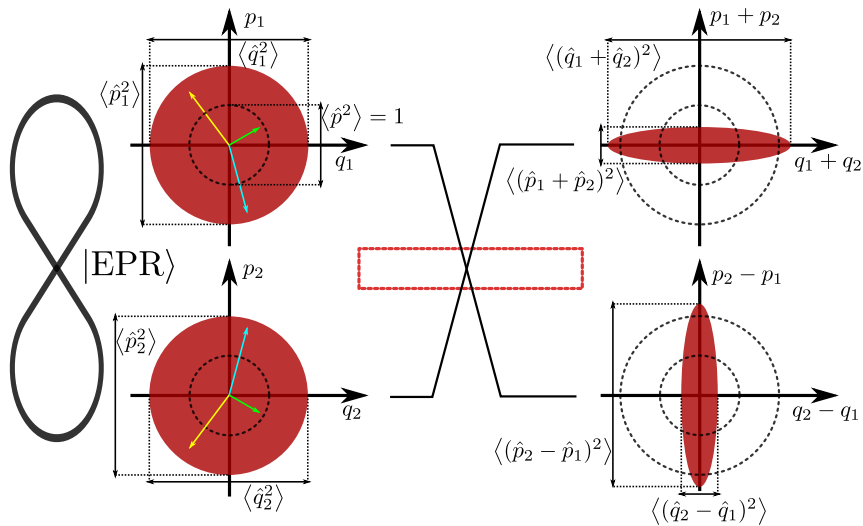


Fig. 2.2 Phasor diagram representation a two mode squeezed vacuum state. \hat{q}_1 and \hat{q}_2 are correlated while \hat{p}_1 and \hat{p}_2 are anti-correlated. Mixing a q squeezed vacuum state and a p squeezed vacuum state on a balanced beam splitter creates an EPR state.

2.1.3 General Gaussian unitaries, Bogoliubov/Symplectic transformations

Unitary transformations that map Gaussian states to Gaussian states are called Gaussian unitaries. They are generated from Hamiltonians that are at most second-order polynomials in the field operators [107]:

$$\hat{U} = \exp\left(-i\frac{\hat{H}t}{\hbar}\right) \quad \text{with} \quad \frac{\hat{H}t}{\hbar} = i\left(\hat{\mathbf{a}}^{\dagger T}\boldsymbol{\alpha} + \hat{\mathbf{a}}^{\dagger T}\mathbf{B}\hat{\mathbf{a}} + \hat{\mathbf{a}}^{\dagger T}\mathbf{C}\hat{\mathbf{a}}^{\dagger}\right) + \text{h.c.} \quad (2.12)$$

where $\boldsymbol{\alpha} \in \mathbb{C}^n$, \mathbf{B} and \mathbf{C} are $n \times n$ complex matrices, and h.c. designates the hermitian conjugate of the first term.

Using the Baker-Campbell-Hausdorff formula, one can show that, in the Heisenberg pictures, this corresponds to an affine transformation of the field operators:

$$\hat{\mathbf{b}} = \hat{U}^{\dagger}\hat{\mathbf{a}}\hat{U} = \mathbf{E}\hat{\mathbf{a}} + \mathbf{F}\hat{\mathbf{a}}^{\dagger} + \boldsymbol{\alpha} \quad (2.13)$$

where \mathbf{E} and \mathbf{F} are complex matrices¹. In order for the commutation relations to be conserved we have:

$$\mathbf{E}\mathbf{F}^T - \mathbf{F}\mathbf{E}^T = 0 \quad (2.14)$$

$$\mathbf{E}\mathbf{E}^T - \mathbf{F}\mathbf{F}^T = \mathbf{1} \quad (2.15)$$

We can rewrite the mode transformation in the compact form:

$$\begin{pmatrix} \hat{\mathbf{b}} \\ \hat{\mathbf{b}}^{\dagger} \end{pmatrix} = \begin{pmatrix} \mathbf{E} & \mathbf{F} \\ \mathbf{F}^* & \mathbf{E}^* \end{pmatrix} \begin{pmatrix} \hat{\mathbf{a}} \\ \hat{\mathbf{a}}^{\dagger} \end{pmatrix} + \begin{pmatrix} \boldsymbol{\alpha} \\ \boldsymbol{\alpha}^* \end{pmatrix} \quad (2.16)$$

This is the so-called Bogoliubov–Valatin transformation and the Hamiltonian in Eq. (2.12) is sometimes called a Bogoliubov Hamiltonian². For more details on Bogoliubov Hamiltonians see for example [111, 112].

In terms of the quadratures, such transformations correspond to an affine map:

$$\hat{\mathbf{x}}_b = \mathbf{S}\hat{\mathbf{x}}_a + \mathbf{d} \quad (2.17)$$

where $\mathbf{d} = \mathbf{W}\begin{pmatrix} \boldsymbol{\alpha} \\ \boldsymbol{\alpha}^* \end{pmatrix} \in \mathbb{R}^{2n}$ and $\mathbf{S} = \mathbf{W}\begin{pmatrix} \mathbf{E} & \mathbf{F} \\ \mathbf{F}^* & \mathbf{E}^* \end{pmatrix}\mathbf{W}^{-1}$. Because of Eqs. (2.14) and (2.15), the matrix \mathbf{S} is symplectic, i.e. $\mathbf{S}^T\boldsymbol{\Omega}\mathbf{S} = \boldsymbol{\Omega}$. Eq. (2.17) is referred to as a symplectic transformation.

Under such transformation, the displacement and covariance matrix are changed as:

$$\bar{\mathbf{x}} \rightarrow \mathbf{S}\bar{\mathbf{x}} + \mathbf{d} \quad (2.18)$$

$$\mathbf{V} \rightarrow \mathbf{S}\mathbf{V}\mathbf{S}^T \quad (2.19)$$

If the transformation does not change the mean photon number we have $\boldsymbol{\alpha} = \mathbf{0}$ and $\mathbf{d} = \mathbf{0}$.

The operators $\hat{D}(\alpha)$, $\hat{S}(\zeta)$, and $\hat{S}_2(\zeta)$ that we introduced in section 1.4 are all Gaussian unitaries. A table that summarises the main Gaussian unitaries and their properties is given in appendix A.2, to be used as an aide-memoire.

¹In general \mathbf{E} and \mathbf{F} both depend on $\boldsymbol{\alpha}$, \mathbf{B} and \mathbf{C} in a non trivial way.

²Bogoliubov introduced such quadratic Hamiltonian to describe a weakly interacting Bose gas [110]

2.1.4 General mode basis change

A particular type of Gaussian unitary is the one corresponding to a simple basis change (as described in section 1.3.1). Indeed according to Eq. (1.66) the mode and field operators were changed according to:

$$\mathbf{v} = \mathbf{U}\mathbf{u} \quad (2.20)$$

$$\hat{\mathbf{b}} = \mathbf{U}^*\hat{\mathbf{a}} \quad (2.21)$$

$$\hat{\mathbf{b}}^\dagger = \mathbf{U}\hat{\mathbf{a}}^\dagger \quad (2.22)$$

and

$$\mathbf{u} = \mathbf{U}^\dagger\mathbf{v} \quad (2.23)$$

$$\hat{\mathbf{a}} = \mathbf{U}^T\hat{\mathbf{b}} \quad (2.24)$$

$$\hat{\mathbf{a}}^\dagger = \mathbf{U}^\dagger\hat{\mathbf{b}}^\dagger \quad (2.25)$$

This corresponds to a particular case of Eq. (2.16) with $\mathbf{E} = \mathbf{U}^*$ and $\mathbf{F} = \mathbf{0}$ and Eq. (2.15) then expresses the unitarity of \mathbf{U}^1 . This mode basis change is generated by the second term in the Hamiltonian of Eq. (2.12).

In terms of the quadratures it is easy to show that the transformation is given by the matrix:

$$\hat{\mathbf{x}}_b = \begin{pmatrix} \mathbf{X} & \mathbf{Y} \\ -\mathbf{Y} & \mathbf{X} \end{pmatrix} \hat{\mathbf{x}}_a \quad (2.26)$$

Where $\mathbf{X} = \text{Re}(\mathbf{U})$, $\mathbf{Y} = \text{Im}(\mathbf{U})$ and we have by unitarity of \mathbf{U} :

$$\mathbf{X}\mathbf{X}^T + \mathbf{Y}\mathbf{Y}^T = \mathbf{1} \quad (2.27)$$

$$\mathbf{X}\mathbf{Y}^T - \mathbf{Y}\mathbf{X}^T = 0 \quad (2.28)$$

Which implies that $\mathbf{O} := \begin{pmatrix} \mathbf{X} & \mathbf{Y} \\ -\mathbf{Y} & \mathbf{X} \end{pmatrix}$ is orthogonal and symplectic².

The state moments are changed according to:

$$\bar{\mathbf{x}} \rightarrow \mathbf{O}\bar{\mathbf{x}} \quad (2.29)$$

$$\mathbf{V} \rightarrow \mathbf{O}\mathbf{V}\mathbf{O}^T \quad (2.30)$$

2.2 Decompositions of Gaussian states and operations

A convenient feature of Gaussian transformation is that they can be decomposed into a set of subtransformations [113] (also Gaussian), which are easier to interpret physically, and construct experimentally. For a unitary (lossless) transformation this decomposition is the Bloch-Messiah (BM) reduction³. A lossy transformation is non-unitary so the BM decomposition doesn't apply to it. Losses will result in classical noise in the quantum state. But, using the Williamson decomposition, any Gaussian state can be modelled

¹The unitary matrix \mathbf{U} must not be confused with the time evolution unitary operator \hat{U} .

²Every orthogonal symplectic matrix can be written in this form.

³Sometimes called Euler decomposition.

as an initial state with independent modes containing all the classical noise that evolved under a unitary Gaussian transformation. Combining these two decompositions gives a general way to describe a lossy Gaussian operations.

In our experiment we use a synchronously pumped optical parametric oscillator (SPOPO). It acts as a complex Gaussian transformation that mixes and entangles its input modes (see section 6.4). Using these decompositions we will be able to recover the eigenmodes of this transformation.

2.2.1 Bloch-Messiah reduction

The Bloch Messiah theorem [114,115] states that in transformations such as (2.16), \mathbf{E} and \mathbf{F} can be decomposed into a pair of unitary matrices \mathbf{U} and \mathbf{V} and a pair of non-negative diagonal matrices Λ_E and Λ_F satisfying $\Lambda_E^2 - \Lambda_F^2 = \mathbb{1}$ by¹:

$$\mathbf{E} = \mathbf{U}\Lambda_E\mathbf{V}^\dagger \quad (2.31)$$

$$\mathbf{F} = \mathbf{U}\Lambda_F\mathbf{V}^T \quad (2.32)$$

The physical meaning behind this decomposition, in the context of a multimode optical circuit, is that any complex combination of multi-port linear interferometers, squeezers and down-converters is equivalent to a circuit with a multi-port interferometer, a set of single-mode squeezers and a second interferometer (see Fig.2.3).

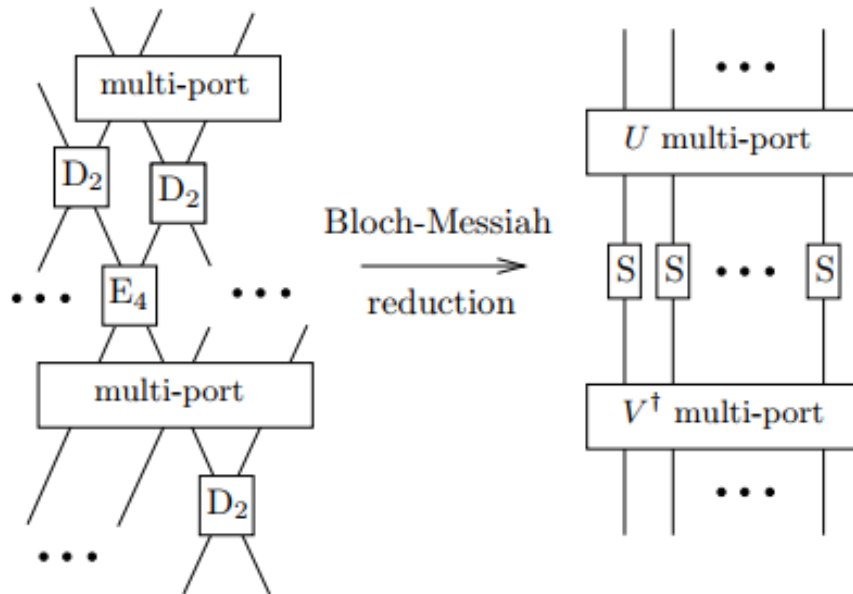


Fig. 2.3 A schematic view of the Bloch-Messiah theorem (Figure from [115]). D_2 (resp. E_4) represents a 2 (resp. 4) mode down converter, S represents a single mode squeezer.

The Bloch-Messiah decomposition is sometimes formulated in terms of the quadrature transformation. In that case, it states that any symplectic matrix \mathbf{S} can be decomposed

¹Bloch-Messiah decomposition is a particular case of singular value decomposition (SVD) of \mathbf{E} and \mathbf{F} . It is unique up to a permutation of the modes.

into:

$$\mathbf{S} = \mathbf{O}_1 \begin{pmatrix} \mathbf{K} & 0 \\ 0 & \mathbf{K}^{-1} \end{pmatrix} \mathbf{O}_2 \quad (2.33)$$

Where \mathbf{K} is a positive diagonal matrix and $\mathbf{O}_1, \mathbf{O}_2$ are orthogonal and symplectic.

Given that $\mathbf{S} = \mathbf{W} \begin{pmatrix} \mathbf{E} & \mathbf{F} \\ \mathbf{F}^* & \mathbf{E}^* \end{pmatrix} \mathbf{W}^{-1}$, it is easy to show¹ that these two formulations are related by²:

$$\mathbf{O}_1 = \begin{pmatrix} \text{Re}(\mathbf{U}) & -\text{Im}(\mathbf{U}) \\ \text{Im}(\mathbf{U}) & \text{Re}(\mathbf{U}) \end{pmatrix} \quad \mathbf{O}_2 = \begin{pmatrix} \text{Re}(\mathbf{V}) & -\text{Im}(\mathbf{V}) \\ \text{Im}(\mathbf{V}) & \text{Re}(\mathbf{V}) \end{pmatrix}^T \quad (2.34)$$

$$\mathbf{K} = \mathbf{\Lambda}_E + \mathbf{\Lambda}_F \quad \mathbf{K}^{-1} = \mathbf{\Lambda}_E - \mathbf{\Lambda}_F \quad (2.35)$$

This theorem is very useful to find the eigenmodes of the SPOPO (supermodes). Indeed as we will see in section 6.4, the SPOPO transformation creates complex correlations between the different frequency components of the signal beam. This transformation is formally identical to the circuit picture in Fig. 2.3 where each input is a different frequency mode. Assuming we start with a vacuum state input $\mathbf{V}_0 = \mathbf{1}$, the output covariance matrix can be written:

$$\mathbf{V} = \mathbf{S}\mathbf{V}_0\mathbf{S}^T = \mathbf{O}_1\mathbf{K}\mathbf{O}_2\mathbf{V}_0\mathbf{O}_2^T\mathbf{K}\mathbf{O}_1^T = \mathbf{O}_1\mathbf{K}^2\mathbf{O}_1^T \quad (2.36)$$

Where \mathbf{S} represents the symplectic transformation of the SPOPO, \mathbf{O}_1 describes a mode basis change, from the basis in which \mathbf{V} is defined to the basis of the SPOPO eigenmodes, and \mathbf{K}^2 describes the squeezing level of the individual eigenmodes.

2.2.2 Williamson decomposition

Williamson's theorem [116, 117] states that any real positive definite matrix can be decomposed as:

$$\mathbf{V} = \mathbf{S}\mathbf{V}_W\mathbf{S}^T \quad (2.37)$$

where \mathbf{S} is symplectic and $\mathbf{V}_W = \text{diag}(\kappa_1, \dots, \kappa_n, \kappa_1, \dots, \kappa_n)$ is called the Williamson normal form of \mathbf{V} . $0 \leq \kappa_1 \leq \dots \leq \kappa_n$ are the Williamson/symplectic eigenvalues. If we require \mathbf{V} to be a bona fide covariance matrix (i.e. that verifies Eq. (2.8)) then the Williamson eigenvalues must be ≥ 1 . This theorem shows that any Gaussian state can be reduced into a collection of independent symmetric thermal states under symplectic transformations. This is called the thermal decomposition and the κ_n represent the thermal states' quadrature variance.

We can therefore model any measured noisy covariance matrix as an initial matrix \mathbf{V}_W that contains all the classical noise, which is then transformed in a symplectic way by the unitary operation of the SPOPO.

¹The proof of this relation is given in Appendix A.2.

²Note that here the sign of $\text{Im}(\mathbf{U})$ is reversed compared to formula (2.26). This is because in (2.31) \mathbf{U} is acting on the annihilation operators, whereas, in the mode basis definition of Eq. (2.20), \mathbf{U}^* is acting on the annihilation operators.

2.2.3 One decomposition to rule them all

Since \mathbf{S} from Eq. (2.37) is symplectic we can apply the BM decomposition to it. Combining the decompositions of Eqs. (2.37) and (2.33) one gets:

$$\mathbf{V} = \mathbf{O}_1 \underbrace{\mathbf{K} \mathbf{O}_2 \mathbf{V}_W \mathbf{O}_2^T \mathbf{K}}_{\tilde{\mathbf{V}}} \mathbf{O}_1^T \quad (2.38)$$

So that the quantum state measured at the SPOPO output can be modelled as the result of an input state with independent modes containing classical noise, on which the SPOPO acts with a symplectic transformation. First mixing the original independent modes with a basis change \mathbf{O}_2 , then squeezing each of the resulting modes independently with \mathbf{K} , then mixing them again with the basis change \mathbf{O}_1 .

\mathbf{O}_1 gives the transformation from the measurement basis to the supermode basis and $\tilde{\mathbf{V}}$ describes the covariance matrix of the quantum state in the supermode basis. The diagonal of $\tilde{\mathbf{V}}$ contains the supermodes' predicted squeezing levels taking into account losses. $\tilde{\mathbf{V}}$ is not diagonal in general because classical noise induces correlation between the supermodes but it is close to diagonal as long as the classical noise isn't too large. Finally we get the eigenmodes of the SPOPO as the columns of \mathbf{U} defined from \mathbf{O}_1 as:

$$\mathbf{O}_1 = \begin{pmatrix} \text{Re}(\mathbf{U}) & \text{Im}(\mathbf{U}) \\ -\text{Im}(\mathbf{U}) & \text{Re}(\mathbf{U}) \end{pmatrix} \quad (2.39)$$

2.3 Gaussian measurements

In this section we introduce the tools needed to describe the main measurement technique used throughout this thesis: homodyne detection. It is an example of Gaussian measurement i.e. a measurement scheme that produces a Gaussian probability distribution of outcomes for any Gaussian state. We also show how a squeezing operation affects the quantities we measure in the experiment.

In order to fully understand the spectral features of the homodyne detection signal in the MHz range, we first change the discrete mode description to a continuum and introduce the sideband/two-mode formalism [118, 119]. Under this formalism, the amplitude and phase modulation of the electric field appear as excitations in the side-band modes around the carrier optical frequency ω_0 . This allows us to define modulation quadratures as combination of the side-band quadratures. Homodyne detection gives direct access to those modulation quadratures. A degenerate down conversion process squeezes the modulation quadratures.

2.3.1 Continuum of modes, two-mode formalism and envelope operators

Until now we have described the quantum EM field by a discrete set of modes and associated operators. This discrete set emerged because we considered a finite volume of space $V = L^3 = LA$ with periodic boundary conditions. In some cases, this volume might be physically relevant, when the field is confined into a cavity or if conditions are really periodic, like on a lattice for example. However, in free space, there is often no particular meaningful volume to consider. In particular we want to take the limit when the longitudinal distance tends to infinity.

In the following we show that under some approximations, taking this limit allows to define continuous field operators and quadratures that represent the sine and cosine amplitude and phase modulation channels around the carrier optical frequency ω_0 [120]. In the time domain, they represent time-dependent envelope operators for the electric field.

We will only consider a single polarisation for simplicity. Let us assume that the only populated modes are those corresponding to plane wavefront propagating in the $+z$ direction, the electric field then reads:

$$\hat{\mathbf{E}}^{(+)}(z, t) = \sum_{l \geq 0} \sqrt{\frac{\hbar \omega_l}{2 \epsilon_0 V}} \hat{a}_l e^{-i \omega_l (t - \frac{z}{c})} \quad (2.40)$$

$$= \sum_{l \geq 0} \Delta \omega \sqrt{\frac{\hbar \omega_l}{4 \pi \epsilon_0 c A}} \frac{\hat{a}_l}{\sqrt{\Delta \omega}} e^{-i \omega_l (t - \frac{z}{c})} \quad (2.41)$$

Because of boundary condition (1.5), the (positive) frequencies ω_l are separated by $\Delta \omega = \frac{2\pi c}{L}$. As we increase L , the mode spacing will shrink to zero and this sum will become an integral $\sum_l \Delta \omega \rightarrow \int d\omega$. The field modes operators will be labelled by a continuous frequency parameter:

$$\frac{\hat{a}_l}{\sqrt{\Delta \omega}} \rightarrow \hat{a}(\omega) \quad (2.42)$$

The discrete Kronecker delta symbol of the periodic boundary condition will become a Dirac delta function:

$$\frac{\delta_{l,l'}}{\Delta \omega} \rightarrow \delta(\omega - \omega') \quad (2.43)$$

So the continuous mode commutation relation becomes:

$$[\hat{a}(\omega), \hat{a}^\dagger(\omega')] = \delta(\omega - \omega') \quad (2.44)$$

Finally the analytic field reads:

$$\hat{\mathbf{E}}^{(+)}(z, t) = \int_0^\infty d\omega \sqrt{\frac{\hbar \omega}{4 \pi \epsilon_0 c A}} \hat{a}(\omega) e^{-i \omega (t - \frac{z}{c})} \quad (2.45)$$

Note that $\hat{a}(\omega)$ now has $\text{Hz}^{-1/2}$ units, so that $\hat{n}(\omega) = \hat{a}^\dagger(\omega) \hat{a}(\omega)$ can be interpreted as the spectral density of photons.

In practice we are only interested in modes in a small bandwidth $\Delta \omega$ around a central optical frequency $\omega_0 \gg \Delta \omega$, and all the other modes will be left in the vacuum state. So it is useful to count modes starting from the central frequency ω_0 and expand the analytical field over a new set of modes that combine the upper and lower sidebands of ω_0 . With a change a variable $\Omega = \omega - \omega_0$, and leaving the longitudinal space dependence out for simplicity we can rewrite Eq. (2.45) as:

$$\hat{\mathbf{E}}^{(+)}(t) = \mathcal{E}_0 e^{-i \omega_0 t} \left(\int_0^{\omega_0} d\Omega \sqrt{\frac{\omega_0 - \Omega}{\omega_0}} \hat{a}(\omega_0 - \Omega) e^{i \Omega t} + \int_0^\infty d\Omega \sqrt{\frac{\omega_0 + \Omega}{\omega_0}} \hat{a}(\omega_0 + \Omega) e^{-i \Omega t} \right) \quad (2.46)$$

with $\mathcal{E}_0 = \sqrt{\frac{\hbar \omega_0}{4 \pi \epsilon_0 c A}}$. All the side-band frequencies we will consider are small compared to the optical frequency so we can extend the integration range of the first term to infinity

without significant errors and approximate $\sqrt{\frac{\omega_0 - \Omega}{\omega_0}} \approx \sqrt{\frac{\omega_0 + \Omega}{\omega_0}} \approx 1$. The real electric field operator can now be re-written:

$$\hat{\mathbf{E}}(t) = \hat{\mathbf{E}}^{(+)}(t) + \hat{\mathbf{E}}^{(-)}(t) \quad (2.47)$$

$$\begin{aligned} &= \mathcal{E}_0 \left(\cos(\omega_0 t) \int_0^\infty d\Omega \left(\hat{a}(\omega_0 - \Omega) + \hat{a}^\dagger(\omega_0 + \Omega) \right) e^{i\Omega t} + \left(\hat{a}(\omega_0 + \Omega) + \hat{a}^\dagger(\omega_0 - \Omega) \right) e^{-i\Omega t} \right. \\ &\quad \left. + \sin(\omega_0 t) \int_0^\infty d\Omega \left(-i\hat{a}(\omega_0 - \Omega) + i\hat{a}^\dagger(\omega_0 + \Omega) \right) e^{i\Omega t} + \left(-i\hat{a}(\omega_0 + \Omega) + i\hat{a}^\dagger(\omega_0 - \Omega) \right) e^{-i\Omega t} \right) \end{aligned} \quad (2.48)$$

$$\begin{aligned} &= \mathcal{E}_0 \left(\cos(\omega_0 t) \int_0^\infty d\Omega \hat{q}_c(\Omega) \cos(\Omega t) + \hat{q}_s(\Omega) \sin(\Omega t) \right. \\ &\quad \left. + \sin(\omega_0 t) \int_0^\infty d\Omega \hat{p}_c(\Omega) \cos(\Omega t) + \hat{p}_s(\Omega) \sin(\Omega t) \right) \end{aligned} \quad (2.49)$$

Where we have introduced the new quadratures:

$$\hat{q}_c(\Omega) = \hat{q}(\omega_0 - \Omega) + \hat{q}(\omega_0 + \Omega) \quad (2.50)$$

$$\hat{p}_c(\Omega) = \hat{p}(\omega_0 - \Omega) + \hat{p}(\omega_0 + \Omega) \quad (2.51)$$

$$\hat{q}_s(\Omega) = -\hat{p}(\omega_0 - \Omega) + \hat{p}(\omega_0 + \Omega) \quad (2.52)$$

$$\hat{p}_s(\Omega) = \hat{q}(\omega_0 - \Omega) - \hat{q}(\omega_0 + \Omega) \quad (2.53)$$

And $\hat{q}(\omega_0 \pm \Omega)$, $\hat{p}(\omega_0 \pm \Omega)$ are the standard quadratures associated with mode $(\omega_0 \pm \Omega)$.

$\hat{q}_{c/s}$ and $\hat{p}_{c/s}$ correspond to the cosine/sine modulation channels. $\hat{q}_{c/s}$ represent amplitude modulation while $\hat{p}_{c/s}$ represent phase modulation as described in Fig. 2.4. The modulation quadratures follow the commutation relations:

$$\left[\hat{q}_{c/s}(\Omega), \hat{q}_{c/s}(\Omega') \right] = \left[\hat{p}_{c/s}(\Omega), \hat{p}_{c/s}(\Omega') \right] = 0 \quad (2.54)$$

$$\left[\hat{q}_{c/s}(\Omega), \hat{p}_{c/s}(\Omega') \right] = 4i\delta(\Omega - \Omega') \quad (2.55)$$

$$\left[\hat{q}_{c/s}(\Omega), \hat{p}_{s/c}(\Omega') \right] = 0 \quad (2.56)$$

To finish we will introduce a last set of operators, which will be useful to define the notion of envelope operators:

$$\hat{\mathbf{q}}(\Omega) = \hat{a}^\dagger(\omega_0 - \Omega) + \hat{a}(\omega_0 + \Omega) = \frac{\hat{q}_c(\Omega) + i\hat{q}_s(\Omega)}{2} \quad (2.57)$$

$$\hat{\mathbf{p}}(\Omega) = i \left(\hat{a}^\dagger(\omega_0 - \Omega) - \hat{a}(\omega_0 + \Omega) \right) = \frac{\hat{p}_c(\Omega) + i\hat{p}_s(\Omega)}{2} \quad (2.58)$$

This formula may appear strange at first, in particular, notice how these operators mix creation and annihilation operators at different frequencies. They are not proper quadrature operators as they are not hermitian, but they follow quadrature-like commutation relations:

$$\left[\hat{\mathbf{q}}(\Omega), \hat{\mathbf{q}}^\dagger(\Omega') \right] = \left[\hat{\mathbf{p}}(\Omega), \hat{\mathbf{p}}^\dagger(\Omega') \right] = 0 \quad (2.59)$$

$$\left[\hat{\mathbf{q}}(\Omega), \hat{\mathbf{p}}^\dagger(\Omega') \right] = 2i\delta(\Omega - \Omega') \quad (2.60)$$

$$\left[\hat{\mathbf{q}}(\Omega), \hat{\mathbf{p}}(\Omega') \right] = 0 \quad (2.61)$$

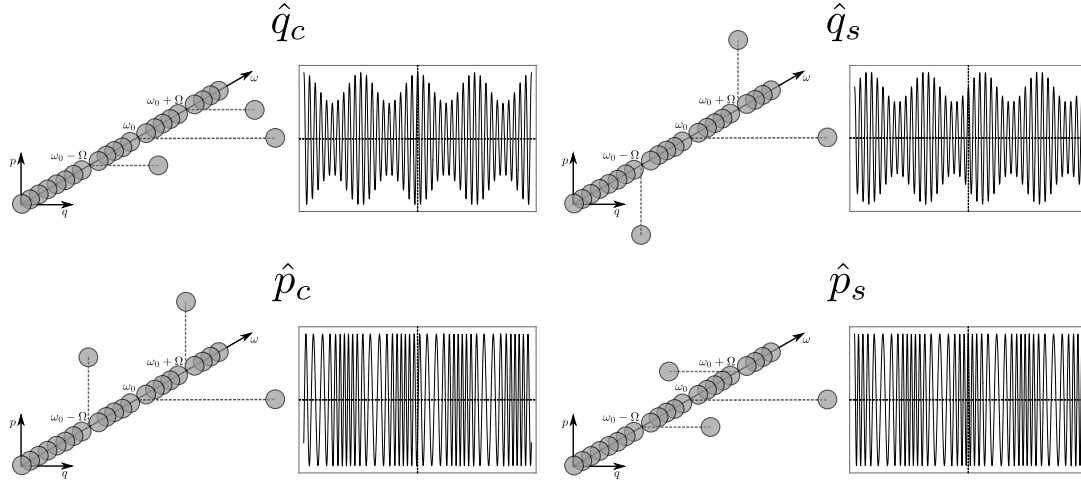


Fig. 2.4 Phasor diagram representation of the cosine/sine amplitude and phase modulation channels.

Upper left: even coherent excitations of the sidebands in phase with the carrier produces cosine amplitude modulation of the envelope.

Upper right: odd coherent excitations of the sidebands in quadrature with the carrier produces sine amplitude modulation of the envelope.

Lower left: even coherent excitations of the sidebands in quadrature with the carrier produces cosine phase modulation of the envelope.

Lower right: odd coherent excitations of the sidebands in phase with the carrier produces sine phase modulation of the envelope.

Their definition can be naturally extended to negative frequencies with:

$$\hat{q}(-\Omega) = \hat{q}^\dagger(\Omega) \quad (2.62)$$

$$\hat{p}(-\Omega) = \hat{p}^\dagger(\Omega) \quad (2.63)$$

So that the electric field can be re-written:

$$\hat{E}(t) = \mathcal{E}_0 \left(\cos(\omega_0 t) \int_0^\infty d\Omega \left(\hat{q}^\dagger(\Omega) e^{i\Omega t} + \hat{q}(\Omega) e^{-i\Omega t} \right) \right) \quad (2.64)$$

$$+ \sin(\omega_0 t) \int_0^\infty d\Omega \left(\hat{p}^\dagger(\Omega) e^{i\Omega t} + \hat{p}(\Omega) e^{-i\Omega t} \right) \quad (2.65)$$

$$= \mathcal{E}_0 \left(\cos(\omega_0 t) \int_{\mathbb{R}} d\Omega \hat{q}(\Omega) e^{-i\Omega t} + \sin(\omega_0 t) \int_{\mathbb{R}} \hat{p}(\Omega) e^{-i\Omega t} \right) \quad (2.66)$$

We can now define the time domain envelope quadrature operators as the Fourier transform of \hat{q} and \hat{p} :

$$\hat{q}(t) := \int_{\mathbb{R}} \frac{d\Omega}{\sqrt{2\pi}} \hat{q}(\Omega) e^{-i\Omega t} \quad (2.67)$$

$$\hat{p}(t) := \int_{\mathbb{R}} \frac{d\Omega}{\sqrt{2\pi}} \hat{p}(\Omega) e^{-i\Omega t} \quad (2.68)$$

$$(2.69)$$

This gives the following simple form to the real electric fields:

$$\hat{E}(t) = \mathcal{E}_0 \left(\hat{q}(t) \cos(\omega_0 t) + \hat{p}(t) \sin(\omega_0 t) \right) \quad (2.70)$$

We can also define a time domain envelope annihilation operator:

$$\hat{a}(t) = \frac{\hat{q}(t) + i\hat{p}(t)}{2} \quad (2.71)$$

$$= \int_{\mathbb{R}} \frac{d\Omega}{\sqrt{2\pi}} \hat{a}(\omega_0 + \Omega) e^{-i\Omega t} \quad (2.72)$$

So that the complex field is simply (reintroducing the longitudinal spatial dependency of Eq. (2.45)):

$$\hat{\mathbf{E}}^{(+)}(z, t) = \mathcal{E}_0 \hat{a}(t - \frac{z}{c}) e^{-i\omega_0(t - \frac{z}{c})} \quad (2.73)$$

The name envelope operator becomes clear with the last expression: the field is the product of a carrier travelling plane wave with an envelope given by $\hat{a}(t - \frac{z}{c})$. Finally, the envelope field operator can be defined in the spectral domain as well, as the Fourier transform of $\hat{a}(t)$:

$$\hat{A}(\Omega) := \mathcal{F}[\hat{a}(t)](\Omega) = \hat{a}(\omega_0 + \Omega) \quad (2.74)$$

Likewise, in the spectral domain, the analytical field just reads:

$$\hat{\mathbf{E}}^{(+)}(z, \omega) := \mathcal{F}[\hat{\mathbf{E}}^{(+)}(z, t)](\Omega) = \mathcal{E}_0 \hat{A}(\omega - \omega_0) e^{ik(\omega)z} \quad (2.75)$$

$$= \mathcal{E}_0 \hat{a}(\omega) e^{ik(\omega)z} \quad (2.76)$$

All this two-mode formalism may seem a bit convoluted given that we end up with a simple and intuitive definition for $\hat{a}(t)$ and $\hat{A}(\Omega)$ but it's crucial to a complete understanding of squeezing and how it is linked with sideband modes correlations as we will see in section 2.3.4. Some points are worth noticing:

- The envelope operator $\hat{a}(t)$ is only properly defined as the Fourier transform of $\hat{A}(\Omega)$ as long as its temporal and spatial variation are slow compared with the carrier variations which is exactly equivalent to the narrow bandwidth excitation condition.
- Although the envelope quadrature $\hat{q}(t)$ is a well defined observable, the Fourier component Ω of $\hat{q}(t)$ is not. It is not given by $\hat{q}(\omega_0 + \Omega)$. Rather, it is a combination of the sideband quadratures $\hat{q}(\omega_0 - \Omega)$, $\hat{q}(\omega_0 + \Omega)$, $\hat{p}(\omega_0 - \Omega)$ and $\hat{p}(\omega_0 + \Omega)$ (same for $\hat{p}(t)$). In the spectral domain the relevant observables that we access with measurements are the modulation channel quadratures \hat{q}_c , \hat{p}_c , \hat{q}_s , and \hat{p}_s . More details will be given in the following sections where we look at intensity and homodyne measurements.

2.3.2 Intensity measure

To measure light we use photodiodes. They are made of P-N doped semi-conductors and, when used with a reverse bias voltage, they emit an electrical current proportional to the intensity of the incident light. In this configuration, photodiodes are able to detect large amounts of light with high efficiency and low noise. Their quantum efficiency (photon to electron conversion ratio) typically reaches 90 % to 95 %.

In the following we will consider that the photocurrent generated by a photodiode is proportional to the field intensity operator integrated over the surface of the detector and over its temporal response. The intensity operator¹ is defined as [120]:

$$\hat{I}(\mathbf{r}, t) = 2\epsilon_0 c \hat{\mathbf{E}}^{(-)}(\mathbf{r}, t) \hat{\mathbf{E}}^{(+)}(\mathbf{r}, t) \quad (2.77)$$

¹This expression is valid under the electric-dipole and rotating wave approximations for a parallel polarised beam

So the photocurrent reads:

$$\hat{i}(t) = R \int_{S_d} d^2\rho \int_{\mathbb{R}} d\tau r(\tau) \hat{I}(\mathbf{r}, t - \tau) \quad (2.78)$$

Where S_d is the detector area, R is the photodetector responsivity in A W^{-1} and $r(t)$ is the (real) normalised temporal response of the detector¹. The typical width of $r(t)$ is the inverse of the detector Bandwidth: $\tau_{\text{BW}} = \frac{1}{\text{BW}}$. If we only consider a single transverse spatial mode entirely contained in the detector surface, using Eq. (2.73) we see the photocurrent is just proportional to the integrated photon number rate:

$$\hat{i}(t) = R \hbar\omega_0 \int_{\mathbb{R}} d\tau r(\tau) \hat{a}^\dagger(t - \tau) \hat{a}(t - \tau) \quad (2.79)$$

We can now specifically look at the photocurrent when a bright excitation $\alpha_0 \in \mathbb{R}$, $\alpha_0 \gg \sqrt{BW}$ is present in the field at the carrier frequency ω_0 :

$$\langle \hat{\mathbf{E}}^{(+)}(t) \rangle = \mathcal{E}_0 \alpha_0 e^{-i\omega_0 t} \quad (2.80)$$

Note that in this expression α_0 has $\text{s}^{-1/2}$ units, α_0^2 can be interpreted as the mean photon rate. To take into account this bright excitation we can displace the field operators with $\hat{D}_{\omega_0}(\alpha_0)$:

$$\hat{D}_{\omega_0}^\dagger(\alpha_0) \hat{a}(\omega) \hat{D}_{\omega_0}(\alpha_0) = \hat{a}(\omega) + \alpha_0 \delta(\omega - \omega_0) \quad (2.81)$$

$$\Rightarrow \hat{D}_{\omega_0}^\dagger(\alpha_0) \hat{a}(t) \hat{D}_{\omega_0}(\alpha_0) = \alpha_0 + \hat{a}(t) \quad (2.82)$$

If we assume α_0 is large compared to the field excitations at any other frequency we can keep only terms in α_0 , we get:

$$\hat{i}(t) = R \hbar\omega_0 \left(\alpha_0^2 + \alpha_0 \int_{\mathbb{R}} d\tau r(\tau) \hat{q}(t - \tau) \right) \quad (2.83)$$

We see two contributions in the photocurrent. The first term is constant, it corresponds to the DC contribution and is proportional to the mean photon rate $\bar{n} = \alpha_0^2$. The second term corresponds to the AC contribution, it contains the time dependence and is proportional to $\sqrt{\bar{n}}$. Its time fluctuations are given by the photodetector response and the envelope amplitude quadrature $\hat{q}(t)$, which corresponds to amplitude modulations in the field. As expected, with intensity measurements, we are sensitive to the amplitude modulation in the beam but not the phase modulation.

In the case where all modes but ω_0 are in the vacuum we find that $\langle 0 | \hat{i}(t) | 0 \rangle = R \hbar\omega_0 \alpha_0^2$ and² $\langle 0 | \Delta \hat{i}(t) \Delta \hat{i}(t + \tau) | 0 \rangle = (R \hbar\omega_0)^2 \alpha_0^2$. We get back the standard result that the signal to noise ratio is proportional to $\sqrt{\bar{n}}$ (Poissonian noise).

We can go one step further and expand $\hat{q}(t - \tau)$ in the frequency domain using Eq. (2.67) to get:

$$\hat{i}(t) = R \hbar\omega_0 \left(\alpha_0^2 + \alpha_0 \int_{\mathbb{R}} d\Omega \hat{q}_1(\Omega) e^{-i\Omega t} \underbrace{\int_{\mathbb{R}} \frac{d\tau}{\sqrt{2\pi}} r(\tau) e^{i\Omega \tau}}_{\tilde{r}(\Omega)} \right) \quad (2.84)$$

¹ $\int_{\mathbb{R}} dt r(t) = 1$ and for causality reasons we have $r(t > 0) = 0$

² This is immediate once we show $\langle 0 | \hat{q}(t - \tau) \hat{q}(t) | 0 \rangle = \delta(\tau)$

Finally using the fact that $\hat{q}(\Omega) + \hat{q}(-\Omega) = q_c(\Omega)$ and $i(\hat{q}(-\Omega) - \hat{q}(\Omega)) = q_s(\Omega)$ we have:

$$\hat{i}(t) = R \hbar \omega_0 \left(\alpha_0^2 + \alpha_0 \int_0^\infty d\Omega \tilde{r}(\Omega) (\cos(\Omega t) \hat{q}_c(\Omega) + \sin(\Omega t) \hat{q}_s(\Omega)) \right) \quad (2.85)$$

Again we see the photocurrent signal is sensitive to amplitude modulations of the field, since \hat{q}_c and \hat{q}_s represent the amplitude modulation channels¹ as we illustrated in Fig. 2.4.

In a realistic intensity measurement the photocurrent will be polluted by some electronic noise². In general this noise is orders of magnitude larger than the noise induced by the terms \hat{q}_c and \hat{q}_s . But direct intensity measurements can still resolve the poissonian noise coming from these terms because of the scaling by α_0 .

When the field does not contain a bright coherent excitation, however, the contribution from the electronic noise dominates the signal. Another measurement technique is needed in order to detect the vacuum field fluctuations. This technique called homodyne detection is described in the next section. Incidentally, this technique allows us to recover the phase modulations channel (\hat{p}_c and \hat{p}_s) as well.

2.3.3 Homodyne detection

The homodyne detection (HD) technique consists in interfering the field to be measured (the signal) with a strong coherent reference field (the local oscillator). This way the fluctuations of the signal are amplified by the local oscillator above the electronic noise level of the detector. One also needs to make sure the noise contributions from the local oscillator does not pollute the measurement.

To achieve this the first homodyne detection schemes [121] (one port HD) used the configuration depicted in Fig. 2.5 (a). The local oscillator (LO) and signal were interfered on a very unbalanced beam splitter with high transmission and low reflection $t \gg r$. This way the signal is almost fully transmitted and amplified by a factor $r|\alpha_{LO}|$ by interference. The LO noise that leaks in is scaled by $r^2|\alpha_{LO}|$ so it is negligible if r is sufficiently small.

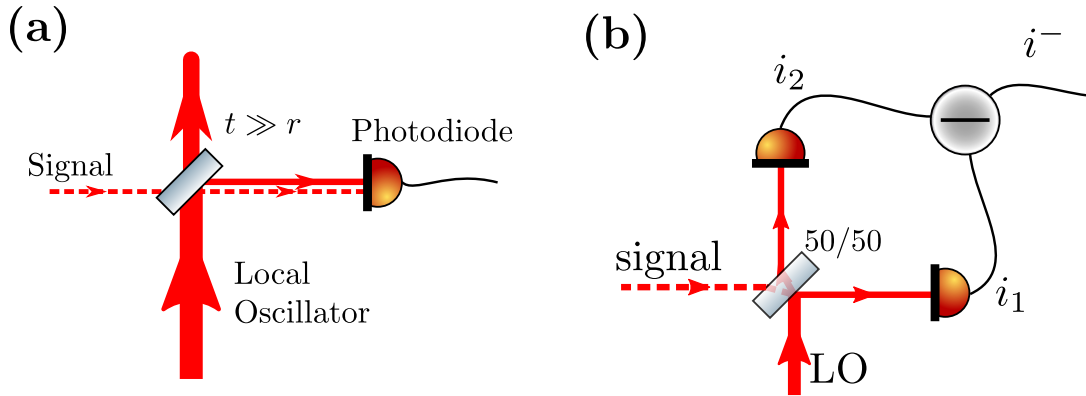


Fig. 2.5 (a) Single port and (b) dual port homodyne detection schemes.

¹Note that what defines amplitude or phase modulation depends on the carrier phase. Here we found the AC photocurrent depends only on \hat{q}_c and \hat{q}_s because we set $\alpha_0 \in \mathbb{R}$. More generally, AM correspond to even (resp. odd) excitations in phase (resp. in quadrature) with the carrier and PM correspond to even (resp. odd) excitations in quadrature (resp. in phase) with the carrier.

²This noise comes from the photodiode and the electronic circuit used after the photodiode to amplify the signal

Nowadays we use a more practical technique introduced by Yuen and Chan [122, 123] that allows to better suppress the noise contribution of the LO while using it's amplitude fully. For that, the signal and LO are interfered on a balanced beam splitter, the two output photocurrents are measured and subtracted (see Fig. 2.5 (b)). The signal is still amplified by the LO amplitude. Most of the LO noise contributions are perfectly correlated on the two detectors and therefore cancel on the subtracted signal.

To see this let's calculate the subtracted photocurrent:

$$\hat{i}^-(t) = \hat{i}_2(t) - \hat{i}_1(t) \quad (2.86)$$

$$\begin{aligned} \propto \int_{\mathbb{R}} d\tau r(\tau) & \left(\left(\hat{\mathbf{E}}_{\text{LO}}^{(-)}(t-\tau) + \hat{\mathbf{E}}^{(-)}(t-\tau) \right) \left(\hat{\mathbf{E}}_{\text{LO}}^{(+)}(t-\tau) + \hat{\mathbf{E}}^{(+)}(t-\tau) \right) \right. \\ & \left. - \left(\hat{\mathbf{E}}_{\text{LO}}^{(-)}(t-\tau) - \hat{\mathbf{E}}^{(-)}(t-\tau) \right) \left(\hat{\mathbf{E}}_{\text{LO}}^{(+)}(t-\tau) - \hat{\mathbf{E}}^{(+)}(t-\tau) \right) \right) \end{aligned} \quad (2.87)$$

$$= 2 \int_{\mathbb{R}} d\tau r(\tau) \hat{\mathbf{E}}^{(-)}(t-\tau) \hat{\mathbf{E}}_{\text{LO}}^{(+)}(t-\tau) + \text{h.c.} \quad (2.88)$$

$$\propto \int_{\mathbb{R}} d\tau r(\tau) \hat{a}(t-\tau) \hat{a}_{\text{LO}}^\dagger(t-\tau) + \text{h.c.} \quad (2.89)$$

If the LO is a strong, coherent monochromatic beam at frequency ω_0 , we can write $\hat{a}_{\text{LO}}(t) = \alpha_{\text{LO}} + \delta\hat{a}_{\text{LO}}(t)$. Keeping only terms in $\alpha_{\text{LO}} = |\alpha_{\text{LO}}|e^{i\phi_{\text{LO}}}$ we simply get:

$$\hat{i}^-(t) \propto |\alpha_{\text{LO}}| \int_{\mathbb{R}} d\tau r(\tau) \hat{x}^{\phi_{\text{LO}}}(t-\tau) \quad (2.90)$$

$$\text{with } \hat{x}^{\phi_{\text{LO}}}(t) = e^{i\phi_{\text{LO}}} \hat{a}^\dagger(t) + e^{-i\phi_{\text{LO}}} \hat{a}(t) = \cos \phi_{\text{LO}} \hat{q}(t) + \sin \phi_{\text{LO}} \hat{p}(t) \quad (2.91)$$

The homodyne detection therefore measures the quadrature of the signal in phase with the LO. We can again look at $\hat{i}^-(t)$ in the frequency domain and see that it measures the AM and PM channels:

$$\hat{i}^-(t) \propto |\alpha_{\text{LO}}| \int d\Omega \tilde{r}(\Omega) \hat{a}(\omega_0 + \Omega) e^{-i\phi_{\text{LO}}} e^{-i\Omega t} \quad (2.92)$$

$$= |\alpha_{\text{LO}}| \left(\cos \phi_{\text{LO}} \int_0^\infty d\Omega \tilde{r}(\Omega) (\cos(\Omega t) \hat{q}_c(\Omega) + \sin(\Omega t) \hat{q}_s(\Omega)) \right) \quad (2.93)$$

$$+ \sin \phi_{\text{LO}} \int_0^\infty d\Omega \tilde{r}(\Omega) (\cos(\Omega t) \hat{p}_c(\Omega) + \sin(\Omega t) \hat{p}_s(\Omega)) \quad (2.94)$$

In our analysis, to extract useful information from the homodyne photocurrent signals we will demodulate them and only extract a small bandwidth. There are two main reasons for that. First, the interesting quantum correlations that we want to access are only present up to a few MHz as they are limited by the OPO cavity linewidth (see chapter 4). The second reason is that classical noise sources dominate the signal at low frequencies. To get the best ratio of quantum signal over classical noise we will therefore restrict our measurement to a band of tens of kHz at 1 MHz.

Mixing down $\hat{i}(t)$ with an electronic local oscillator (eLO) signal $e(t) \propto \cos(\omega_m t + \phi_m)$ and a low pass filter of bandwidth $\Delta\Omega = \frac{2\pi}{T} \ll \omega_m$ allows to sample the quantity:

$$\hat{s} = \cos \phi_{\text{LO}} \left(\cos \phi_m \int_{\omega_m - \Delta\Omega}^{\omega_m + \Delta\Omega} d\Omega \hat{q}_c(\Omega) + \sin \phi_m \int_{\omega_m - \Delta\Omega}^{\omega_m + \Delta\Omega} d\Omega \hat{q}_s(\Omega) \right) \quad (2.95)$$

$$+ \sin \phi_{\text{LO}} \left(\cos \phi_m \int_{\omega_m - \Delta\Omega}^{\omega_m + \Delta\Omega} d\Omega \hat{p}_c(\Omega) + \sin \phi_m \int_{\omega_m - \Delta\Omega}^{\omega_m + \Delta\Omega} d\Omega \hat{p}_s(\Omega) \right) \quad (2.96)$$

Here we removed the term $\tilde{r}(\Omega)$ which is justified if the detected bandwidth ($\omega_m - \Delta\Omega, \omega_m + \Delta\Omega$) is well within the detector bandwidth. The relevant quantities we access in the experiment are the $\hat{q}_{c/s}$ and $\hat{p}_{c/s}$ integrated over the demodulation bandwidth ($\omega_m - \Delta\Omega, \omega_m + \Delta\Omega$). We can change which one we access by tuning the LO phase (to select q or p) and the electronic demodulation signal phase (to select c or s). See [124] for more details on the spectral analysis of homodyne measurements.

Another important feature of the homodyne detection is that it is a projective measurement. By this we mean that homodyne detection measures the part of the signal that is in the LO spatial and temporal mode. In this analysis where the LO is monochromatic at frequency ω_0 we measure modes in the signal at frequencies in the vicinity of ω_0 . Anything in the signal at frequencies far¹ from ω_0 , would not be measured. But the LO mode need not be a monochromatic one and in general we will measure the sidebands of whatever spectral mode the LO is in. These sidebands may include a broad range of frequencies, but they will always describe phase/amplitude modulation of the LO temporal mode. We will give more details on homodyne measurement in the case of a non monochromatic LO in section 3.3.

2.3.4 Squeezing and sideband noise correlations

Now that we have precisely defined the quantities we measure with homodyne detection, we will show that a second order linearity acts as a two mode squeezing operator on the sideband modes $\hat{a}(\omega_0 \pm \Omega)$. This creates correlations in the $\hat{q}(\omega_0 \pm \Omega)$ and $\hat{p}(\omega_0 \pm \Omega)$ which amounts to squeezing/anti-squeezing of the modulation channel quadratures $\hat{q}_c(\Omega)$, $\hat{p}_c(\Omega)$, $\hat{q}_s(\Omega)$ and $\hat{p}_s(\Omega)$.

More details on second order linearities will be given in chapter 6, but the important feature here is that under certain conditions it is possible to convert photons from a pump at frequency ω_p into pairs of signal and idler photons at frequencies ω_i and ω_s , a process called parametric down conversion (PDC). For reasons of energy conservation we have $\omega_i + \omega_s = \omega_p$. Writing $\omega_p = 2\omega_0$, we can label the signal and idler frequencies from the pump half frequency: $\omega_s = \omega_0 + \Omega$. So that the idler photon frequency has to be $\omega_i = \omega_0 - \Omega$. In other words the pump photons are converted to side-band photons around half the pump frequency. This can be modelled by a Hamiltonian of the form²:

$$\hat{H} = i\zeta(\hat{a}^\dagger(\omega_0 - \Omega)\hat{a}^\dagger(\omega_0 + \Omega)) + \text{h.c.} \quad (2.97)$$

The corresponding unitary evolution is:

$$\hat{U} = e^{\zeta\hat{a}^\dagger(\omega_0 - \Omega)\hat{a}^\dagger(\omega_0 + \Omega) - \zeta^*\hat{a}(\omega_0 - \Omega)\hat{a}(\omega_0 + \Omega)} \quad (2.98)$$

This is just the two mode squeezing operator we introduced in section 1.4.4. Through this unitary evolution the quadrature of the signal and idler modes are transformed according to³:

$$\begin{pmatrix} \hat{q}(\omega_0 - \Omega) \\ \hat{q}(\omega_0 + \Omega) \end{pmatrix} \rightarrow \begin{pmatrix} \cosh r \hat{q}(\omega_0 - \Omega) + \sinh r \hat{q}(\omega_0 + \Omega) \\ \sinh r \hat{q}(\omega_0 - \Omega) + \cosh r \hat{q}(\omega_0 + \Omega) \end{pmatrix} \quad (2.99)$$

¹further than the bandwidth of the detector

²This process happens for all side-band frequencies within the phase-matching bandwidth.

³We take $\zeta = r \in \mathbb{R}^+$ for simplicity

and:

$$\begin{pmatrix} \hat{p}(\omega_0 - \Omega) \\ \hat{p}(\omega_0 + \Omega) \end{pmatrix} \rightarrow \begin{pmatrix} \cosh r \hat{p}(\omega_0 - \Omega) - \sinh r \hat{p}(\omega_0 + \Omega) \\ -\sinh r \hat{p}(\omega_0 - \Omega) + \cosh r \hat{p}(\omega_0 + \Omega) \end{pmatrix} \quad (2.100)$$

This introduces coupling between the quadrature at $\omega_0 - \Omega$ and $\omega_0 + \Omega$. Going to the AM and PM channels, this transformation acts independently on each mode and takes the simple form:

$$\begin{pmatrix} \hat{q}_c(\Omega) \\ \hat{q}_s(\Omega) \\ \hat{p}_c(\Omega) \\ \hat{p}_s(\Omega) \end{pmatrix} \rightarrow \begin{pmatrix} e^r \hat{q}_c(\Omega) \\ e^{-r} \hat{q}_s(\Omega) \\ e^{-r} \hat{p}_c(\Omega) \\ e^r \hat{p}_s(\Omega) \end{pmatrix} \quad (2.101)$$

In other words, a PDC process can create EPR correlations between the modes $\omega_0 - \Omega$ and $\omega_0 + \Omega$. These correlations result in squeezing of the modulation channel quadratures. In general PDC is a two mode process, the only frequency for which the PDC acts as a single mode squeezing operation is the carrier frequency ω_0 .

Part II

Experimental tools

Chapter 3

Ultrafast light

Contents

3.1 Optical frequency combs	45
3.1.1 The Mira laser	46
3.1.2 Single pulse of light	46
3.1.3 Spectral representation	47
3.1.4 Temporal representation	49
3.2 Dispersion effects	50
3.2.1 Spectral phase	50
3.2.2 Constant phase	51
3.2.3 Linear phase	51
3.2.4 Quadratic phase: chirp	52
3.3 Homodyne measurement with a frequency comb reference . .	53

3.1 Optical frequency combs

The term optical frequency comb (OFC) refers to a particular class of pulsed laser where a large number of the laser cavity longitudinal modes are excited coherently using a technique called mode-locking. This broadband excitation along with a high degree of coherence allows to produce ultra-short pulses down to the femtosecond and even attosecond regime¹. OFC were first developed as tools to measure the cycles of atomic optical clocks. The high phase stability between the “teeth” of the comb allows to reach unprecedented precisions in time and frequency measurement. Since then, they have been used for a wide range of applications as well as fundamental research in metrology, spectroscopy, on optical, atomic, molecular, and solid-state systems [65, 73, 125, 126]. In 2005, John Hall and Theodor Hänsch won the Nobel prize [127, 128] for their life long contributions to the field of precision optical frequency metrology as well as for their technical vision and expertise that resulted in the realisation of the OFC.

In the following sections we detail the characteristics of the femtosecond laser used in our experiment and give some precision on the temporal and spectral representation of the laser output field.

¹An attosecond (10^{-18} s) is inconceivably short: there are more attoseconds in one second than there are seconds in the age of the universe !

3.1.1 The Mira laser

In our experiment, we use a titanium-sapphire (Ti:Al₂O₃) MIRA-900 [129] laser pumped by a continuous-wave beam at 532 nm produced by a VERDI G-15 [130] laser. The MIRA laser has a ~ 4 m long cavity that contains a pulse compressor [131] and a Lyot filter [132]. The Ti:Sapph crystal has a broadband gain curve which allows many longitudinal modes of the cavity to be above threshold and oscillate (see Fig. 3.1). The pulse compressor is used to compensate intra-cavity dispersion and obtain regular longitudinal resonances over a broad spectral range. The Lyott filter allows to tune the gain central frequency. Coherent oscillation of all the longitudinal modes above threshold (mode locking) is achieved passively using a slit thanks to the Kerr lensing effect in the crystal (see [133–135]).

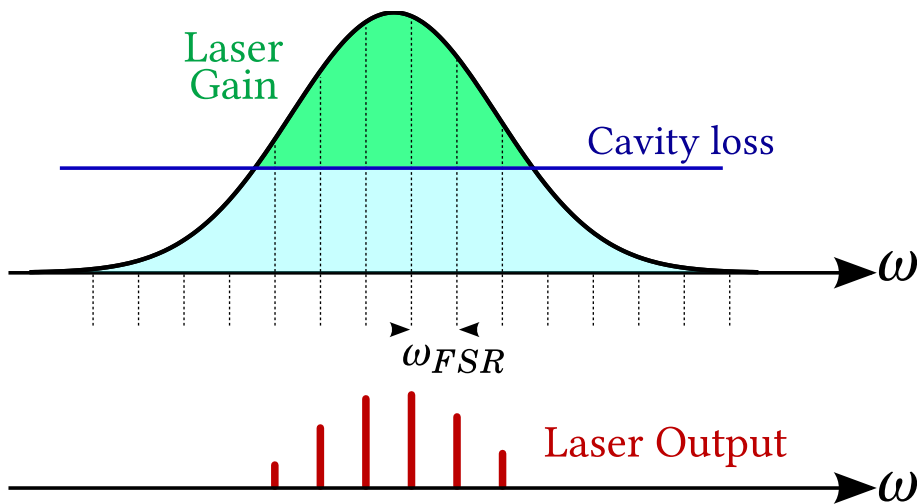


Fig. 3.1 Principle of mode-locked oscillation of ultra-fast lasers. The crystal gain curve is broad enough to cover many of the available longitudinal modes of the cavity (dotted line). As a result many longitudinal mode can lase (oscillate). If they do so conjointly and coherently (in phase), the laser emits a train of ultra-short pulses: this is the mode-locked operation. (Figure from [136])

As a result the laser outputs a ~ 76 MHz repetition rate frequency comb centred at 795 nm, with a ~ 10 nm full width half maximum (intensity) envelope well approximated by a Gaussian function. The available average power is around 1.8 W (\sim MW peak power). For a more detailed description of the laser source and beam preparation in our set-up see [137, 138] (thorough but in french) or [139] (in english but less complete).

3.1.2 Single pulse of light

In this section we will look at a single pulse of light and its description in the time and frequency domains. Let's consider a pulse with a carrier frequency ω_0 , and pulse envelope $a(t)$, its analytical field reads:

$$\mathbf{E}^{(+)}(t) = \mathcal{E}_0 a(t) e^{-i\omega_0 t} \quad (3.1)$$

Which is simply the following in the spectral domain:

$$E^{(+)}(\omega) = \mathcal{E}_0 \mathcal{F}[a(t)e^{-i\omega_0 t}](\omega) \quad (3.2)$$

$$= \mathcal{E}_0 a(\omega - \omega_0) := \mathcal{E}_0 a(\Omega) \quad (3.3)$$

In the spectral domain, the field is given by the Fourier transform of the envelope centred at the carrier frequency. This shows that to have short pulses, one needs a broad spectral envelope.

3.1.3 Spectral representation

An OFC (like the one depicted in Fig. 3.1) can be modelled by a set of evenly spaced Dirac distributions¹ with an envelope. The Dirac comb structure comes from the laser cavity longitudinal modes whereas the envelope depends on the response of the laser gain medium². The laser cavity longitudinal modes correspond to frequencies for which the round-trip phase is a multiple of 2π :

$$\phi(\omega_k) = 2\pi k \quad \text{for } k \in \mathbb{Z} \quad (3.4)$$

If we neglect (non-linear) intra-cavity dispersion³ the round-trip phase can be developed to first order around the gain envelope central frequency ω_0 :

$$\phi(\omega) \approx \phi^{(0)} + (\omega - \omega_0)\phi^{(1)} \quad (3.5)$$

Where the 0th and 1st order coefficients are given by:

$$\phi^{(0)} := \phi(\omega_0) = \frac{L}{c}\omega_0 n_0 \quad (3.6)$$

$$= \frac{L\omega_0}{v_\varphi} \quad (3.7)$$

$$\phi^{(1)} := \left(\frac{\partial \phi}{\partial \omega} \right)_{\omega=\omega_0} = \frac{L}{c} \left(n_0 + \omega_0 \left(\frac{\partial n}{\partial \omega} \right)_{\omega_0} \right) \quad (3.8)$$

$$= \frac{L}{v_g} \quad (3.9)$$

L being the cavity length and $n(\omega)$ the cavity medium refractive index⁴. We also defined the phase and group velocity:

$$v_\varphi = \frac{c}{n_0} \quad (3.10)$$

$$v_g = \frac{1}{\frac{1}{v_\varphi} + \frac{\omega_0}{c} \left(\frac{\partial n}{\partial \omega} \right)_{\omega_0}} \quad (3.11)$$

¹More realistically the teeth of the comb can be described by Lorentzian functions with widths equal to the laser cavity linewidth

²It is also affected by the intra-cavity dispersion

³In practice femtosecond lasers are so broadband that dispersion needs to be compensated.

⁴If the cavity contains media of different index (air and cavity crystal), $n(\omega)$ should be understood as the effective index (mean index weighted by medium length).

The phase velocity corresponds to the speed of a monochromatic light component ω_0 whereas the group velocity corresponds to the speed of a narrow pulse of light with carrier frequency ω_0 . Eq. (3.5) can now be re-written:

$$\phi(\omega) = \underbrace{\omega_0 L \left(\frac{1}{v_\varphi} - \frac{1}{v_g} \right)}_{\Delta\phi_{\text{CE}}} + \frac{\omega L}{v_g} \quad (3.12)$$

We will see in the next section that the first term can be interpreted as the round trip dephasing between the pulse envelope and its carrier. It is straightforward to show that the resonance condition (3.4) implies the resonant frequencies are given by:

$$\forall k \in \mathbb{Z}, \omega_k = \omega_{\text{CE}} + k\omega_r \quad (3.13)$$

with:

$$\omega_r = \frac{2\pi}{\phi_1} = \frac{2\pi v_g}{L} \quad (3.14)$$

$$\omega_{\text{CE}} = -\frac{v_g}{L} \Delta\phi_{\text{CE}} = \omega_0 \left(1 - \frac{v_g}{v_\varphi} \right) = \frac{L\omega_0\omega_r}{2\pi} \left(\frac{1}{v_g} - \frac{1}{v_\varphi} \right) \quad (3.15)$$

So that finally the electric field emitted by this laser can be described in the spectral domain by:

$$E^{(+)}(\omega) = a(\omega - \omega_0) \text{III}_{\omega_r}(\omega - \omega_{\text{CE}}) \quad (3.16)$$

Where $a(\omega)$ describes the envelope and $\text{III}_{\omega_r}(\omega) := \sum_{k \in \mathbb{Z}} \delta(\omega - k\omega_r)$ describes the comb structure. Such a spectrum is represented in Fig. 3.2. ω_r is the repetition frequency of the laser and ω_{CE} is the carrier to envelope offset (CEO) frequency. Note that in general the envelope is not centred on one of the longitudinal mode frequency, so the frequency ω_0 is not part of the frequency comb.

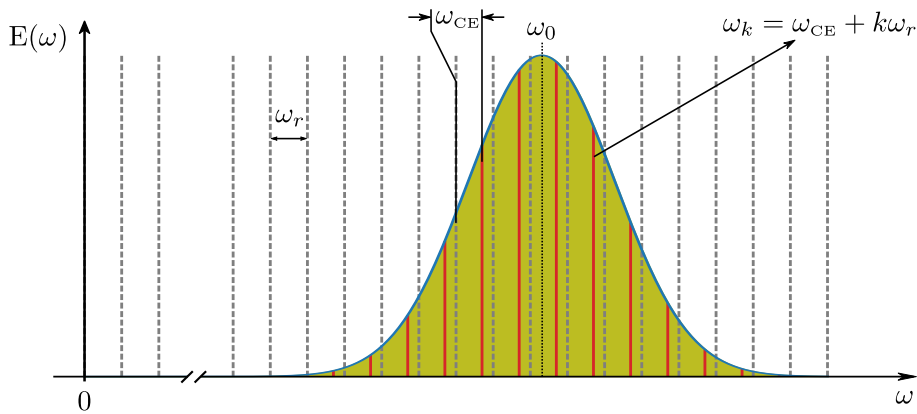


Fig. 3.2 Spectral field of a frequency comb. It consists of many narrow and evenly spaced frequencies, the “teeth”, with a broadband envelope. This is just a schematic representation, for the laser used in our experiment, the envelope contains hundreds of thousands of “teeth”.

3.1.4 Temporal representation

Now that we gave a spectral description of an OFC let us look at it in the time domain. The electric field in the time domain is given by the Fourier transform of Eq. (3.16), using the standard properties of the Fourier transform (see Appendix A.3) we get:

$$\mathbf{E}^{(+)}(t) = \mathcal{F}^{-}[a(\omega - \omega_0) \text{III}_{\omega_r}(\omega - \omega_{\text{CE}})](t) \quad (3.17)$$

$$= \frac{1}{\sqrt{2\pi}} \left(a(t) e^{-i\omega_0 t} \right) \otimes \left(\mathcal{F}^{-1}[\text{III}_{\omega_r}(\omega)](t) e^{-i\omega_{\text{CE}} t} \right) \quad (3.18)$$

$$= \frac{T_r}{2\pi} \sum_{k \in \mathbb{Z}} a(t - kT_r) e^{-i\omega_0(t - kT_r)} e^{-ik\Delta\phi_{\text{CE}}} \quad (3.19)$$

with $T_r = \frac{2\pi}{\omega_r}$, $\Delta\phi_{\text{CE}} = \omega_{\text{CE}} \frac{2\pi}{\omega_r}$. Therefore we see that this laser emits a train of pulses separated by T_r , which is consistent with ω_r being the repetition rate. The pulses envelope is given by $a(t)$ which is the Fourier transform of $a(\omega - \omega_0)$. Note that the carrier frequency of the pulses is ω_0 . However, ω_0 is not necessarily a resonant frequency of the cavity. The successive pulses carrier are dephased by $\Delta\phi_{\text{CE}}$. This is called the carrier to envelope phase (CEP), it can be given an intuitive meaning if we look at its definition in terms of the phase and group velocities:

$$\Delta\phi_{\text{CE}} = L\omega_0 \left(\frac{1}{v_g} - \frac{1}{v_\varphi} \right) \quad (3.20)$$

The carrier frequency speed is v_φ therefore on each cavity round-trip it accumulates a phase $\frac{L\omega_0}{v_\varphi}$. Due to intra-cavity linear dispersion, the envelope speed is $v_g \neq v_\varphi$ so its cavity round-trip phase is $\frac{L\omega_0}{v_g}$. Therefore there is an increasing dephasing between the carrier and the envelope from pulse to pulse (see Fig. 3.3).

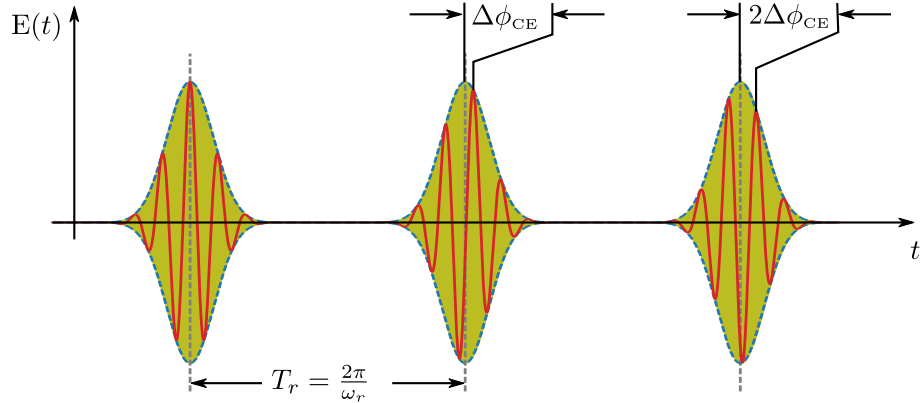


Fig. 3.3 Temporal field of a femtosecond laser: the train of pulses. The laser emits a train of femtosecond pulses with carrier frequency ω_0 . The pulses are spaced by the repetition period T_r . At each successive pulse the carrier accumulates a phase delay $\Delta\phi_{\text{CE}}$ relative the envelope. The temporal envelope of the pulse is the Fourier transform of the frequency comb spectral envelope.

It is often convenient to consider only the spectral envelope $a(\Omega)$ of the frequency comb and forget about the “teeth” structure. Given the Fourier relation between the spectral envelope and the single pulse temporal envelope, this corresponds to looking at a single

pulse of the train. For many cases this is sufficient as all the pulses will experience the same effects. However, there are exceptions. For example, when using an oscillator like a cavity which makes successive pulses interact.

3.2 Dispersion effects

As we saw in the previous sections, short pulses of light have a broad spectral content. They are therefore sensitive to dispersion effects in media with a refractive index that varies with frequency. These effects are important to consider when working with ultra-fast lasers. In particular second-order phase dispersion (also called group delay dispersion (GDD), group velocity dispersion (GVD) or simply chirp) can have detrimental effect as it will lead to a broadening of the pulses as they propagate. One needs to avoid or compensate chirp in order to preserve short pulses and their high peak powers. But chirp can also be harnessed as a resource. For example, it is used in the chirp pulse amplification (CPA) technique [140, 141] that allows to amplify femtosecond pulses up to PW peak powers. In 2018, Donna Strickland and Gérard Mourou shared half a Nobel price for their ground-breaking work on this technique.

Part of the work of this thesis consisted in analysing the effect of the dispersion in the SPOPO cavity. As we will see in section 6.4.2, dispersion is the main effect that limits the squeezing in higher order supermode. In this section we will discuss the effects of dispersion on pulses by looking at spectral phase on the frequency combs. Propagation through any lossless medium can be described by a spectral phase.

3.2.1 Spectral phase

Let's write the analytical field in the time/frequency domain as:

$$\mathbf{E}^{(+)}(t) = \mathcal{E}_0 a(t) e^{-i\omega_0 t} \quad (3.21)$$

$$\mathbf{E}^{(+)}(\Omega) = \mathcal{E}_0 a(\Omega) \quad \text{with} \quad \Omega = \omega - \omega_0 \quad (3.22)$$

We will define the temporal and spectral phases as the phases of the envelopes, namely:

$$a(t) = |a(t)| e^{i\varphi(t)} \quad (3.23)$$

$$a(\Omega) = |a(\Omega)| e^{i\phi(\Omega)} \quad (3.24)$$

We now look at the effect of propagation in a dispersive medium on temporal and spectral phases. In particular we will look at 0th, 1st and 2nd order effects as most situations we encountered experimentally correspond to these. We will therefore Taylor expand the spectral phase to 2nd order around the carrier frequency ω_0 :

$$\phi(\Omega) \sim \phi^{(0)} + \Omega \phi^{(1)} + \frac{\Omega^2}{2} \phi^{(2)} \quad (3.25)$$

where:

$$\phi^{(0)} := \phi(\omega_0) \quad (3.26)$$

$$\phi^{(1)} := \left(\frac{\partial \phi}{\partial \omega} \right)_{\omega_0} \quad (3.27)$$

$$\phi^{(2)} := \left(\frac{\partial^2 \phi}{\partial \omega^2} \right)_{\omega_0} \quad (3.28)$$

3.2.2 Constant phase

A constant phase $\phi(\Omega) = \phi^{(0)}$ corresponds to a dephasing of the carrier (see Fig. 3.4):

$$\mathbf{E}^{(+)}(t) = \mathcal{E}_0 |a(t)| e^{-i(\omega_0 t - \phi^{(0)})} \quad (3.29)$$

A constant phase is identical in the spectral and temporal domain.

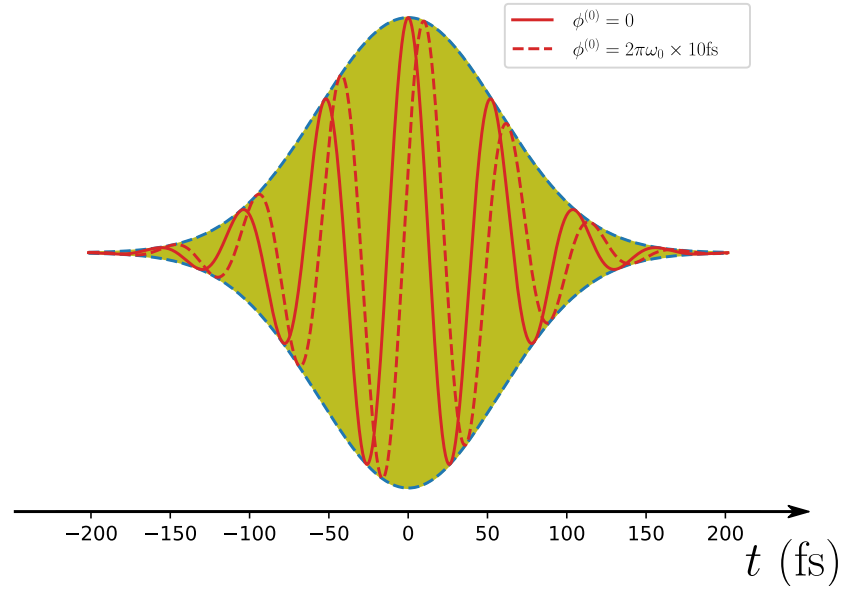


Fig. 3.4 *Effect of constant spectral phase in the time domain: the carrier is delayed.*

3.2.3 Linear phase

For a linear spectral phase $\phi(\Omega) = \Omega\phi^{(1)}$, the field in the time domain becomes:

$$\mathbf{E}^{(+)}(t) = \mathcal{E}_0 |a(t - \phi^{(1)})| e^{-i\omega_0 t} \quad (3.30)$$

This results in a delayed pulse envelope as shown in Fig. 3.5. The carrier is not delayed with respect to the original pulse which results in a carrier to envelope offset in the delayed pulse. $\phi^{(1)} = \frac{L}{v_g}$ is called the group delay.

Propagation through a non dispersive medium ($n = \text{cst}$) just correspond to delaying the pulse envelope and carrier by the same amount. Indeed, if the refractive index is constant, the accumulated phase over a distance l is just:

$$\phi(\Omega) = \underbrace{\frac{\omega_0 n l}{c}}_{\phi^{(0)}} + \Omega \underbrace{\frac{n l}{c}}_{\phi^{(1)}} \quad (3.31)$$

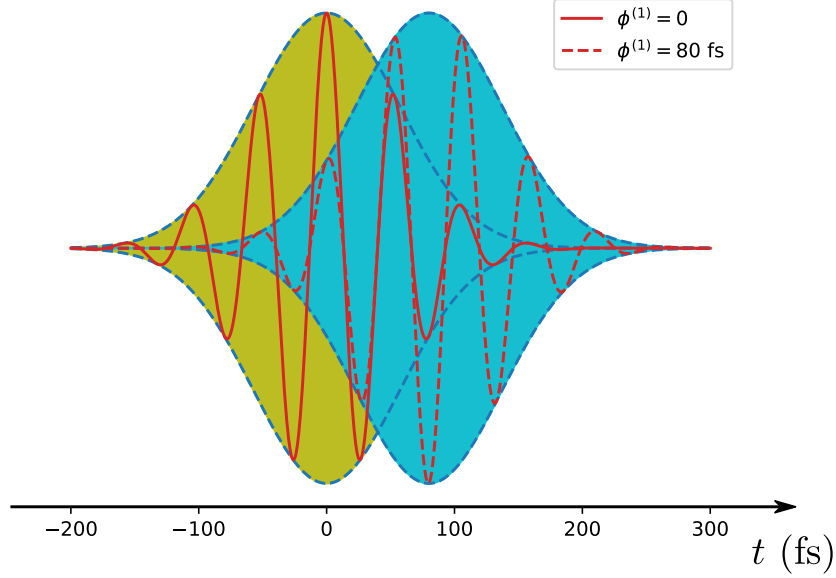


Fig. 3.5 *Effect of linear spectral phase in the time domain: the envelope is delayed.*

3.2.4 Quadratic phase: chirp

For a quadratic spectral phase $\phi(\Omega) = \frac{\Omega^2}{2}\phi^{(2)}$ both the carrier and envelope are affected in the time domain. The exact effect will depend on the type of spectral envelope. Let us take a Gaussian envelope for example:

$$|a(\Omega)| = \frac{1}{(2\pi)^{1/4}\Delta\Omega^{1/2}} e^{-\frac{\Omega^2}{4\Delta\Omega^2}} \quad (3.32)$$

Without chirp the pulse temporal envelope is simply:

$$a(t) = \frac{1}{(2\pi)^{1/4}\Delta t^{1/2}} e^{-\frac{t^2}{4\Delta t^2}} \quad (3.33)$$

with $\Delta t = \frac{1}{2\Delta\Omega}$. With the quadratic linear phase the temporal pulse envelope becomes:

$$a(t) = \frac{1}{(2\pi)^{1/4}\gamma^{1/2}} e^{-\frac{t^2}{4\gamma^2}} \quad \text{with} \quad \gamma = \Delta t \sqrt{1 - i\frac{\phi^{(2)}}{2\Delta t^2}} \in \mathbb{C} \quad (3.34)$$

$$= \frac{1}{(2\pi)^{1/4}\Delta t^{1/2}} e^{-\frac{t^2}{4\Delta t'^2}} e^{i\frac{t^2\phi^{(2)}}{8\Delta t'^4}} e^{i\psi_2} \quad (3.35)$$

Where:

$$\Delta t' = \Delta t \sqrt{1 + \left(\frac{\phi^{(2)}}{2\Delta t^2}\right)^2} \quad (3.36)$$

$$\psi_2 = \text{Arg} \gamma^{-1/2} \quad (3.37)$$

So after the propagation in a second order dispersive medium, a Gaussian pulse stays Gaussian, but it broadens (regardless of the dispersion sign). The carrier is also changed, the envelope temporal phase becomes:

$$\varphi(t) = \psi_2 + \frac{t^2 \phi^{(2)}}{8\Delta t'^4} \quad (3.38)$$

The first term is just a constant dephasing of the carrier. The second represent a linear change in the frequency of the carrier from the beginning to the end of the pulse¹ (see Fig. 3.6). This is why this phenomena is called chirp. In the acoustic wave domain such pulses produce a chirping sound because of the ramping of the carrier frequency.

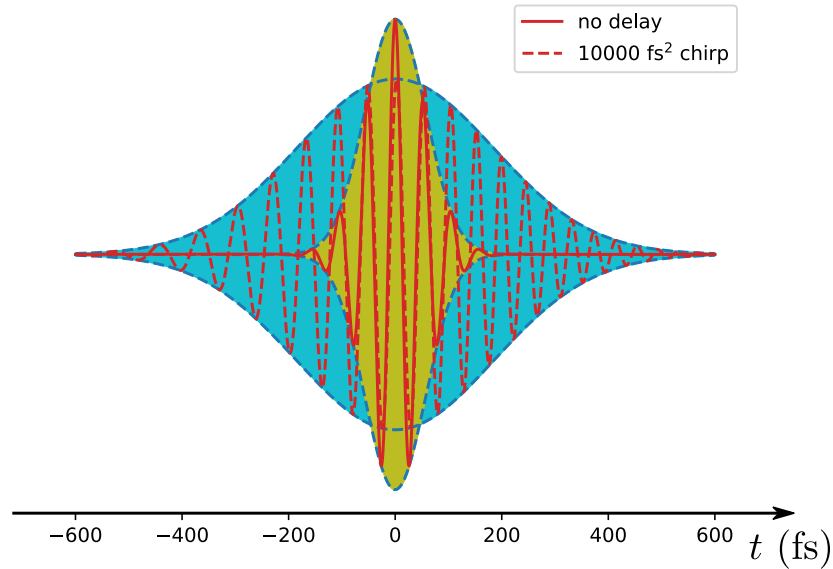


Fig. 3.6 *Effect of quadratic spectral phase in the time domain: the pulse is broadened, the carrier is delayed and the carrier instantaneous frequency ramps up ($\phi^{(2)} > 0$) or down ($\phi^{(2)} < 0$) from the beginning to the end of the pulse.*

Group velocity dispersion (GVD) and group delay dispersion (GDD) are other common names for chirp. They represent other quantities than the quadratic phase coefficient $\phi^{(2)}$ but they describe the same effect.

3.3 Homodyne measurement with a frequency comb reference

Now that we described what an OFC looks like in the temporal and spectral domain. Let us take a step back, and consider what a homodyne detection measures when the LO beam is an OFC. Let $\psi_n(t)$ be a complete and orthonormal basis of functions for the envelope

¹The instantaneous frequency can be defined as the time derivative of the phase

of the pulses. We consider that the support of those functions is $[-\frac{T_r}{2}, \frac{T_r}{2}]$. Since the basis is orthonormal and complete, we have:

$$\int_{-\frac{T_r}{2}}^{\frac{T_r}{2}} \psi_n(t)\psi_{n'}(t)dt = \delta_{nn'} \quad (3.39)$$

$$\sum_n \psi_n(t)\psi_{n'}(t') = \delta(t - t') \quad (3.40)$$

The envelope for the full train of pulses can then be written:

$$f_n(\Omega, t) = \sum_{k \in \mathbb{Z}} \psi_n(t - kT_r) e^{ik2\pi(\frac{\omega_0}{\omega_r} + \frac{\Omega}{\omega_r})} \quad \text{with } \Omega \in [-\omega_r/2, \omega_r/2] \quad (3.41)$$

This equation is identical to Eq. (3.19), we have just taken out the carrier term $e^{-i\omega_0 t}$ (here we look at the envelope), and Ω is just the carrier to envelope frequency (noted ω_{CE} in Eq. (3.19)). Note that f_n is a function of time and describes the pulse train in the time domain. Ω can be thought of as a labelling parameter for f_n . Each value of $\Omega \in [-\omega_r/2, \omega_r/2]$ corresponds to a frequency comb with different CEO.

The envelope quantum field operator of Eq. (2.73) can now be expanded over such trains of pulse (see [138] for details):

$$\hat{a}(t) = \sum_n \int_{-\frac{\omega_r}{2}}^{\frac{\omega_r}{2}} d\Omega \hat{s}_n(\Omega) f_n(\Omega, t) \quad (3.42)$$

Note how this expansion spans over two parameters:

- A discrete parameter n that labels the pulse envelope function $\psi_n(t)$.
- A continuous parameter Ω that labels the carrier to envelope frequency of the pulse train.

Operator $\hat{s}_n(\Omega)$ is the annihilation operator for a pulse train in mode $f_n(\Omega, t)$:

$$\hat{s}_n(\Omega) = \int_{\mathbb{R}} dt f_n^*(\Omega, t) \hat{a}(t) \quad (3.43)$$

These new operators follow the commutation relations:

$$[\hat{s}_n(\Omega), \hat{s}_{n'}(\Omega')] = 0 \quad \text{and} \quad [\hat{s}_n(\Omega), \hat{s}_{n'}^\dagger(\Omega')] = \delta_{nn'} \delta(\Omega - \Omega') \quad (3.44)$$

Let's say the LO is a bright coherent beam with amplitude α_0 in mode $f_0(\Omega_0, t)$. Provided that the detector bandwidth is small compared with the repetition rate of the pulse train f_0 , one can show that the photocurrent takes the same form as Eq. (2.92), except this time the $\hat{q}_{c/s}(\Omega)/\hat{p}_{c/s}(\Omega)$ represent the *frequency comb* amplitude and phase modulation channels defined as:

$$\hat{q}_c(\Omega) = \hat{q}_{f_0}(\Omega_0 - \Omega) + \hat{q}_{f_0}(\Omega_0 + \Omega) \quad (3.45)$$

$$\hat{p}_c(\Omega) = \hat{p}_{f_0}(\Omega_0 - \Omega) + \hat{p}_{f_0}(\Omega_0 + \Omega) \quad (3.46)$$

$$\hat{q}_s(\Omega) = -\hat{p}_{f_0}(\Omega_0 - \Omega) + \hat{p}_{f_0}(\Omega_0 + \Omega) \quad (3.47)$$

$$\hat{p}_s(\Omega) = \hat{q}_{f_0}(\Omega_0 - \Omega) - \hat{q}_{f_0}(\Omega_0 + \Omega) \quad (3.48)$$

Where $\hat{q}_{f_0}(\Omega)$ and $\hat{p}_{f_0}(\Omega)$ are the quadrature operators corresponding to the pulse train mode $f_0(\Omega, t)$:

$$\hat{q}_{f_0}(\Omega) = \hat{s}_0^\dagger(\Omega) + \hat{s}_0(\Omega) \quad (3.49)$$

$$\hat{p}_{f_0}(\Omega) = i \left(\hat{s}_0^\dagger(\Omega) - \hat{s}_0(\Omega) \right) \quad (3.50)$$

Fig. 3.7 gives a pictorial representation of $\hat{q}_c(\Omega)$ when $\psi_0(t)$ is a Gaussian function. A detailed explanation is given in the figure caption.

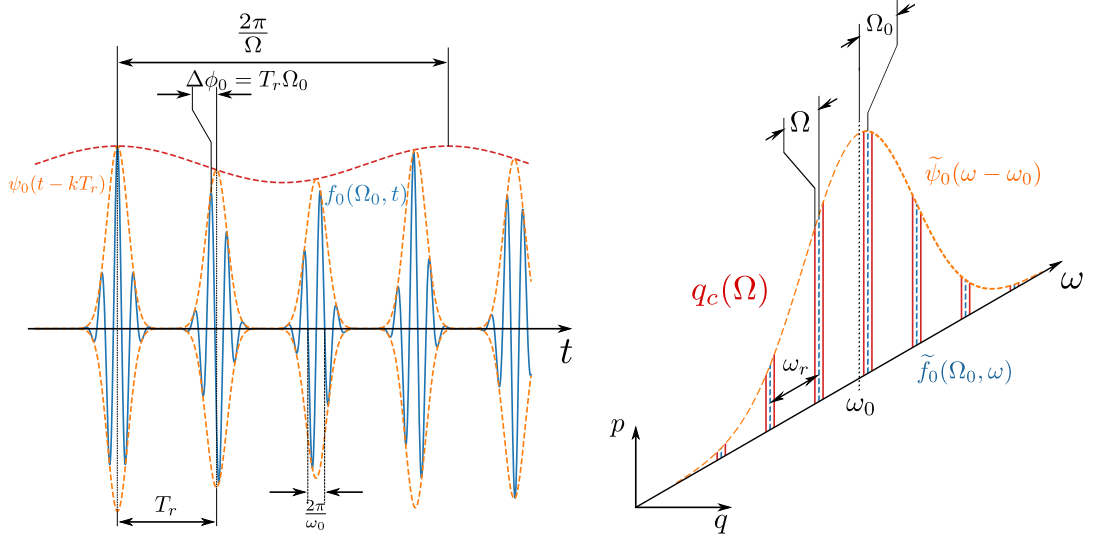


Fig. 3.7 Representation of the cosine amplitude modulation channel quadrature for a frequency comb with a Gaussian envelope.

Left part: time domain representation of a train of Gaussian pulses with amplitude modulation. $\Delta\phi_0$ is the carrier to envelope phase of the pulse train. Ω is the amplitude modulation frequency.

Right part: spectral domain representation of the modulated pulse train. The dotted blue line corresponds to the frequency comb without amplitude modulation $\tilde{f}_0(\Omega_0, \omega)$. ω_0 is the central frequency of the comb envelope (it is also the carrier frequency). Ω_0 is the carrier offset frequency of the comb \tilde{f}_0 , it corresponds to the difference between the carrier frequency ω_0 and the frequency of the central tooth of the comb. When amplitude modulation is applied to the train pulse, sidebands appear around each of the comb teeth.

$\hat{q}_c(\Omega)$ represents the amplitude modulation channel of a frequency comb mode.

One last point is worth noting here. In section 2.3.1 when we introduced the sideband modes and modulation channels, we insisted that this description is only valid if the sideband frequencies considered are small compared to the carrier frequency: $\Omega \ll \omega_0$. In a similar manner, the description given in the present section is only valid because the different frequencies involved have very different scales. In particular we require that $\Omega \ll \omega_r \ll \omega_0$. Otherwise, the commutation relations of Eq. (3.44) are no longer valid.

Chapter 4

Synchronous optical cavities

Contents

4.1	Ring cavity input-output relations	57
4.2	Synchronous cavities	60
4.2.1	Transmission of a frequency comb without CEO and partial resonances	60
4.2.2	CEO effects	63
4.2.3	Intra-cavity dispersion effects	65

In this thesis, we generate multimode entangled states by optically pumping a non-linear crystal. In order to enhance this effect, the non-linear component is placed within an optical cavity to form an optical parametric oscillator (OPO). As light circulates in the cavity, it experiences the non-linearity at every round-trip. The laser source used in our experiment is an optical frequency comb (see chapter 3), it contains a very large number of modes (the teeth of the comb). In order for this comb structure to be preserved in the output quantum state of the OPO we need to ensure the pump repetition rate is matched with the OPO cavity free spectral range. This happens for a particular length of the cavity, when it is matched to the distance between two pulses of the pump. We refer to this condition as synchronous pumping, hence the name SPOPO. In this chapter, we describe optical cavities and the particular effects that arises when sending an OFC through a cavity.

4.1 Ring cavity input-output relations

The SPOPO cavity is a ≈ 4 m long ring cavity¹. The overall cavity geometry is rather complex but it can be modelled with a simpler ideal cavity as in Fig. 4.1. Here is a list of the cavity components (as labelled in Fig. 4.1) and their functions:

- The crystal (labelled as BIBO) is a 2 mm BIBO crystal, it is the non linear component that is used to generate entanglement (see chap. 6)
- M2 and M13 are concave mirrors ($R = 250$ mm) used to focus the intra-cavity beam into the crystal with a waist of ≈ 38 μ m.

¹A ring cavity is a particular type of cavity geometry where the light circulate one-way as opposed to the Fabry-Perot geometry where the light goes back and forth

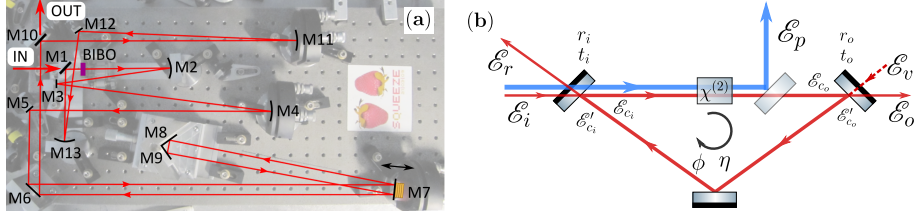


Fig. 4.1 (a) Real SPOPO cavity used in the experiment. (b) Schematic representation of the SPOPO cavity. The pump beam \mathcal{E}_p is non resonant and is tapped off with a dichroic mirror. The cavity is modelled with an input coupler, an output coupler, a roundtrip phase ϕ and roundtrip losses η .

- M4 and M11 are also concave mirrors ($R = 6$ m) that allow to further control the beam waist and ensure the cavity stability.
- M1 is the input coupler mirror, its reflectivity is $R_i = r_i^2 = 99.85\%$ (at 795 nm).
- M10 is the output coupler mirror, its reflectivity is $R_o = r_o^2 = 80\%$.
- M3 and M7 are chirped mirror, they each compensate for 50 fs^2 of dispersion.
- The cavity contains a delay line (mirrors M8 and M9) to fine tune its length, and a piezo-electric transducer (on mirror M7) to lock it.
- All other mirrors are highly reflective folding mirrors.

We now give the input output relations for such a cavity. We call \mathcal{E}_i , \mathcal{E}_r , \mathcal{E}_o , \mathcal{E}_v , the input, reflected input, transmitted output and incoming output fields respectively. And \mathcal{E}_{c_i} , \mathcal{E}'_{c_i} , \mathcal{E}_{c_o} and \mathcal{E}'_{c_o} will refer to the intra-cavity fields as apparent in Fig. 4.1. Finally, let us call $t_{i/o}$ and $r_{i/o}$ the input/output coupler amplitude transmission and reflection coefficients, and, η_{io} and η_{oi} , the intra-cavity losses from input to output and output to input respectively.

The various fields are related according to the following equations:

$$\mathcal{E}_{c_i} = t_i \mathcal{E}_i - r_i \mathcal{E}'_{c_i} \quad (4.1)$$

$$\mathcal{E}_r = t_i \mathcal{E}'_{c_i} + r_i \mathcal{E}_i \quad (4.2)$$

$$\mathcal{E}_o = t_o \mathcal{E}_{c_o} + r_o \mathcal{E}_v \quad (4.3)$$

$$\mathcal{E}'_{c_o} = t_o \mathcal{E}_v - r_o \mathcal{E}_{c_o} \quad (4.4)$$

$$\mathcal{E}_{c_o} = t_{\eta_{io}} e^{i\phi_{io}} \mathcal{E}_{c_i} \quad (4.5)$$

$$\mathcal{E}'_{c_i} = t_{\eta_{oi}} e^{i\phi_{oi}} \mathcal{E}'_{c_o} \quad (4.6)$$

Where $t_{\eta_{io/oi}} = \sqrt{1 - \eta_{io/oi}}$ and $\phi_{io/oi}$ represent the phase accumulated from the input/output coupler to the output/input coupler.

Note we keep the term \mathcal{E}_v that corresponds to light sent into the cavity from the output coupler because this term will be relevant for the quantum treatment. Indeed, in the quantum description of light, vacuum has some associated non zero field. \mathcal{E}_v corresponds to this vacuum field and it will couple in and out of the cavity and affect the output quantum state. In fact when we use the SPOPO to produce squeezing, the only bright

coherent light we send into the cavity is the pump field \mathcal{E}_p which is non resonant. So all the contributions in Eq. (4.1) correspond to vacuum fields. Since $r_i \approx 1$, the major input contribution to the intra-cavity field will be \mathcal{E}_v .

Technically, to keep a unitary description, we should also include a vacuum field contribution from the intra-cavity losses because they are modelled with a reflective interface.

After a few calculation these Eqs. (4.1) are reduced to a linear input/output system:

$$\mathcal{E}_o = t\mathcal{E}_i + r_v\mathcal{E}_v \quad (4.7)$$

$$\mathcal{E}_r = t_v\mathcal{E}_v - r\mathcal{E}_i \quad (4.8)$$

With:

$$t = \frac{t_i t_o t_{\eta_{io}} e^{i\phi_{io}}}{1 - r_i r_o t_{\eta} e^{i\phi}} \quad r = -\frac{r_i - r_o t_{\eta} e^{i\phi}}{1 - r_i r_o t_{\eta} e^{i\phi}} \quad (4.9)$$

$$t_v = \frac{t_i t_o t_{\eta_{oi}} e^{i\phi_{oi}}}{1 - r_i r_o t_{\eta} e^{i\phi}} \quad r_v = \frac{r_o - r_i t_{\eta} e^{i\phi}}{1 - r_i r_o t_{\eta} e^{i\phi}} \quad (4.10)$$

When there are no losses inside the cavity we have $|t|^2 = |t_v|^2$, $|r|^2 = |r_v|^2$ and $|t|^2 + |r|^2 = 1$. The cavity is then symmetric in terms of input and output, but in the more general case the input and output are not symmetric.

The intensity transmission can be put in the form:

$$T = |t|^2 = \frac{T_{max}}{1 + m \sin^2(\frac{\phi}{2})} \quad (4.11)$$

with $T_{max} = \frac{(1-R_i)(1-R_o)(1-\eta_{io})}{(1-\sqrt{R_i R_o(1-\eta)})^2}$ and $m = \frac{4\sqrt{R_i R_o(1-\eta)}}{(1-\sqrt{R_i R_o(1-\eta)})^2}$.

We see that the cavity will be resonant for frequencies with a round-trip phase that is a multiple of 2π . The round-trip phase at frequency ω is:

$$\phi(\omega) = k(\omega)L = \frac{\omega n(\omega)L}{c} \quad (4.12)$$

$$\approx \frac{\omega L}{c} \quad (4.13)$$

where L is the cavity round-trip length and we considered the optical index of air constant $n(\omega) \approx 1$. Therefore, the round-trip phase varies linearly with frequency and the resonant frequencies are just given by:

$$\omega_p = 2\pi p \frac{c}{L} \quad (4.14)$$

The spectral response of the cavity is then given by evenly spaced resonances, the spacing between two resonant frequency is called the free spectral range (FSR): $\omega_r^{cav} = 2\pi \frac{c}{L}$.

If the cavity input and output coupler reflectivity is high and the intra-cavity losses small we have $m \gg 1$. The sine function can then be linearised around resonances and the cavity spectral response is well approximated by a Lorentzian:

$$T(\omega) = \frac{T_{max}}{1 + (2\frac{\omega - \omega_l}{\Delta\omega})^2} \quad \text{with} \quad \Delta\omega = \frac{4c}{L\sqrt{m}} \quad (4.15)$$

Figure 4.2 show the typical spectral response around a resonance frequency.

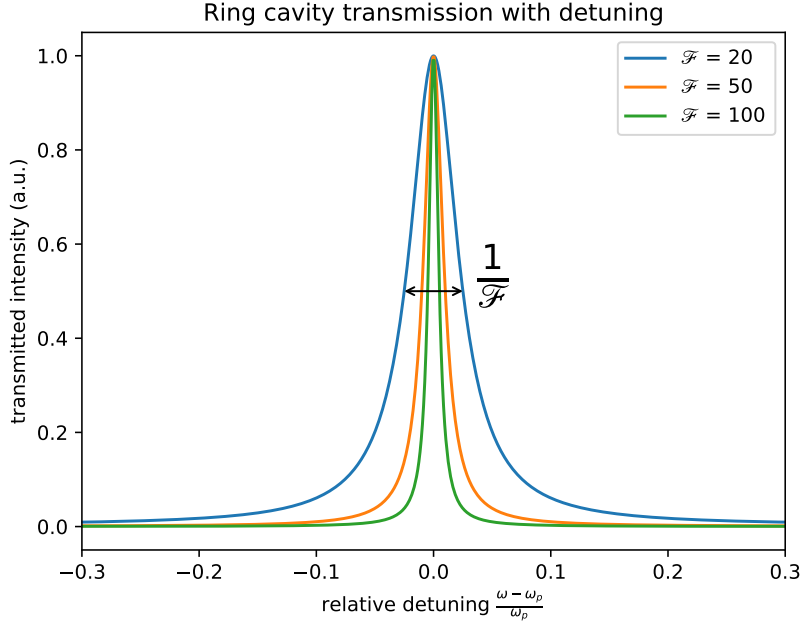


Fig. 4.2 Spectral response of an optical cavity near resonance.

The cavity finesse is defined as the ratio between the free spectral range and the resonances FWHM. It quantifies the quality of the cavity as a resonator. It can be thought of as the photons typical number of cavity round-trip. If m is large enough its given by:

$$\mathcal{F} = \pi \frac{\sqrt{m}}{2} \quad (4.16)$$

If the cavity is injected onto a single spatial mode with a monochromatic laser of wavelength λ_0 , we observe evenly spaced resonances as we scan the cavity length. Those resonances are separated by integer multiples of λ_0 . The width of those peaks is also determined by the finesse¹, their FWHM is given by $\Delta l = \frac{\lambda_0}{\mathcal{F}}$ (see Fig. 4.3).

4.2 Synchronous cavities

We now look at what happens when the cavity is injected with an OFC.

4.2.1 Transmission of a frequency comb without CEO and partial resonances

If we neglect the CEO, the frequencies of an optical comb are: $\omega_k = k\omega_r$ with $k \in \mathbb{N}$, ω_r being its repetition frequency. We can also label them starting from the central tooth ω_0 : $\omega_p = \omega_0 + p\omega_r$ with $p \in \mathbb{Z}$. The central tooth is a large multiple of ω_r : $\omega_0 = N\omega_r$, $N \gg 1$.

Given that the cavity is resonant for all frequencies verifying Eq. (4.14) (without dispersion), it is possible to tune the cavity length in order for all the frequencies of a frequency

¹Provided the linewidth of the laser is small compared with the cavity linewidth

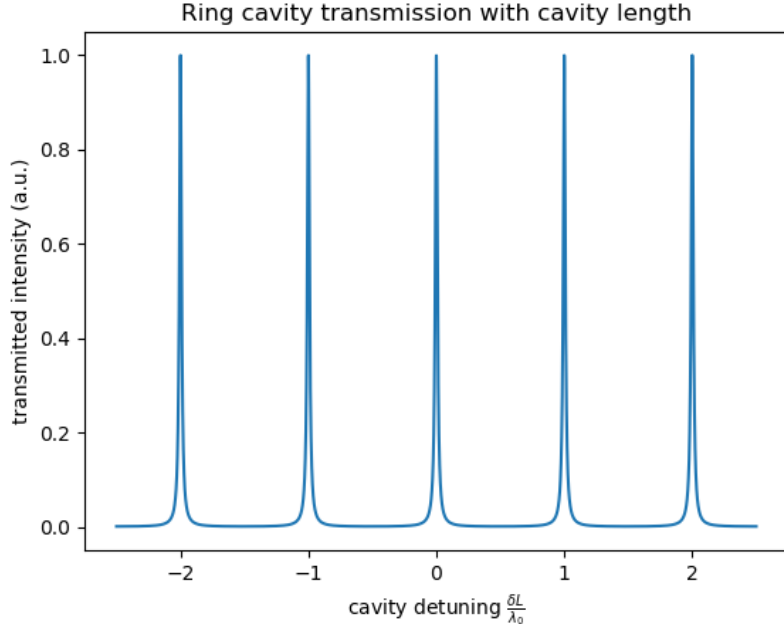


Fig. 4.3 Response of an optical cavity pumped by a monochromatic laser when scanning the cavity length.

comb to be simultaneously resonant. For a synchronous cavity we have:

$$\forall p \quad \phi(\omega_p) = 0 \pmod{2\pi} \quad (4.17)$$

This corresponds to matching the cavity free spectral range with the comb repetition rate $\omega_r^{cav} = \omega_r$, the corresponding cavity length is:

$$L_r = 2\pi \frac{c}{\omega_r} \quad (4.18)$$

The frequency comb is then fully transmitted through the cavity (see Fig. 4.4):

$$\forall p \in \mathbb{Z} \quad I^{\text{out}}(\omega_p) = T_{\text{max}} I_{\text{in}}(\omega_p) \quad (4.19)$$

In the time domain, this means the cavity round-trip time is equal to the delay between successive pulses. This is the so-called synchronous cavity.

L_r is the only cavity length for which all the comb teeth are simultaneously resonant. However, there are some other cavity lengths for which a sufficient portion of the teeth are resonant so that the output intensity is significant. These are called partial resonances. Partial resonances occur for:

$$L = L_r + \delta L = L_r + p\lambda_0 \quad \text{with } p \in \mathbb{Z} \quad (4.20)$$

$p = \pm 1$ correspond to the closest cavity length for which ω_0 becomes resonant again. Fig. 4.4 represents the spectral response for different values of δL . The red and black arrows represent the transmitted teeth at main and partial resonance respectively. At the first partial resonance, ω_0 is perfectly resonant. But the other teeth are not, they are

slightly detuned from the cavity resonances. This detuning increase as we move further away from ω_0 . As a result the transmitted spectrum will be altered. Note this detuning is exaggerated here to underline this effect. In practice for our laser $\frac{\omega_0}{\omega_r} \approx 10^6$ so this detuning effect will only be visible for high order partial resonance and/or for teeth far from ω_0 .

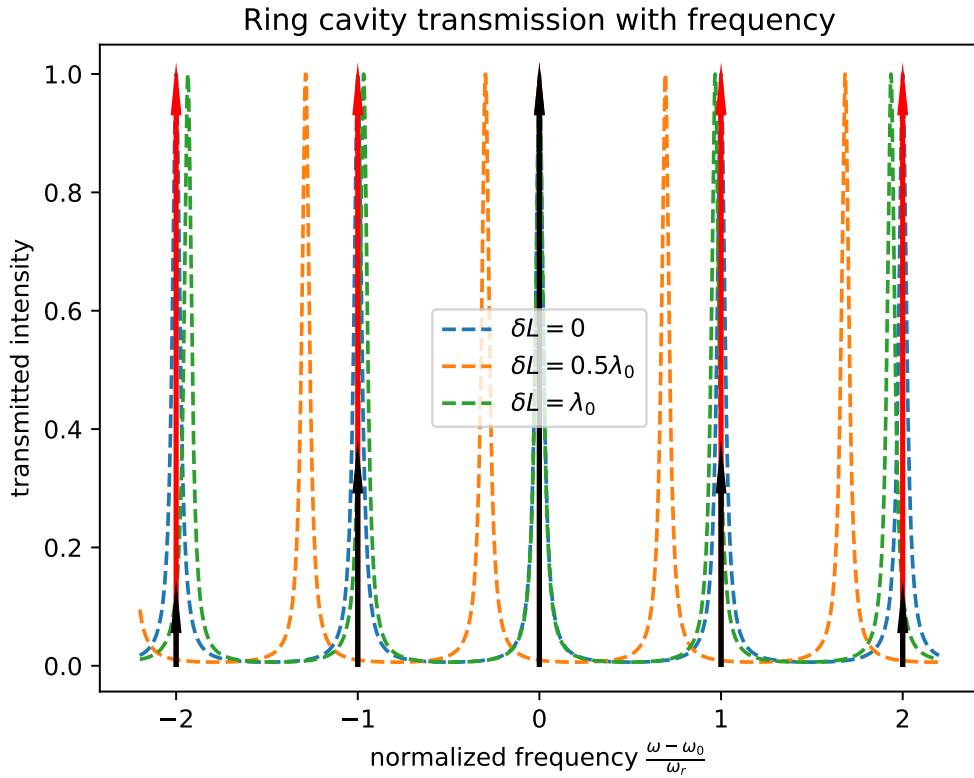


Fig. 4.4 Spectral response of an optical cavity pumped by a frequency comb at main and partial resonance. The red arrows represent the frequency teeth of the transmitted OFC at main resonance (full transmission). The black arrows represent the frequency teeth of the transmitted OFC at first secondary resonance $\delta L = \lambda_0$. The comb is not fully transmitted, the teeth transmission weakens as we move away from the comb central frequency ω_0 . Here the effect is exaggerated for clarity. In our experimental condition, the decrease in teeth transmission is only visible far from ω_0 .

Fig. 4.5 shows the typical profile of the transmitted intensity when scanning the cavity length around the main resonance $\delta L = L - L_r$. We clearly distinguish the secondary resonance, they have a smaller finesse and a smaller peak intensity. Unlike when pumped by a continuous laser, the successive resonance are no longer equivalent, there is a unique preferred resonance corresponding to the synchronous pumping.

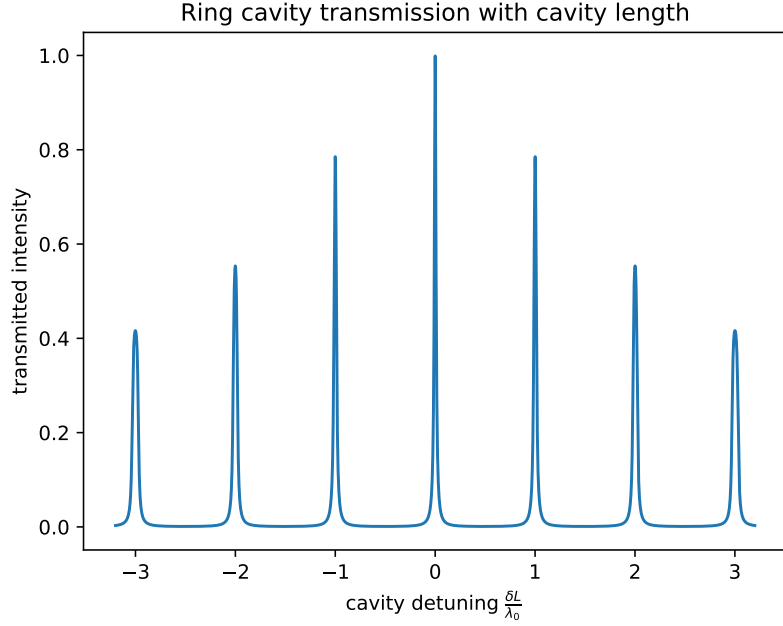


Fig. 4.5 Transmitted intensity through a cavity injected by an OFC when scanning the cavity length.

4.2.2 CEO effects

Until now we considered that the teeth of the frequency comb corresponded to multiples of ω_r . But as we saw in section 3.1.3 the tooth of the frequency comb are actually shifted relative to the $\omega = 0$ frequency by the carrier to envelope frequency ω_{CE} :

$$\omega_p = \omega_{\text{CE}} + p\omega_r \quad (4.21)$$

This shift came from the fact that inside the laser cavity the phase and group velocity are different, so the carrier accumulates a phase relative to the pulse envelope.

This is true for other cavities as well. This means that equation (4.13) is not strictly correct. For a more accurate description, we need to take into account the dispersion effects and consider the frequency dependence of the refractive index in the cavity. This dispersion comes from the intra-cavity mirrors as well as the cavity medium. If we linearise the round-trip phase around ω_0 we get, as in Eq. (3.12):

$$\phi(\omega) = \omega_0 L \left(\frac{1}{v_\varphi^{\text{cav}}} - \frac{1}{v_g^{\text{cav}}} \right) + \frac{\omega L}{v_g^{\text{cav}}} \quad (4.22)$$

$$= 2\pi \frac{\omega - \omega_{\text{CE}}^{\text{cav}}}{\omega_r^{\text{cav}}} \quad (4.23)$$

Where v_φ^{cav} and v_g^{cav} are the intra-cavity phase and group velocities, defined as in Eq. (3.10). As in section 3.1.3, we have used $\omega_{\text{CE}}^{\text{cav}} = \omega_0 \left(1 - \frac{v_g^{\text{cav}}}{v_\varphi^{\text{cav}}}\right)$. The free spectral range is now changed to $\omega_r^{\text{cav}} = 2\pi \frac{v_g^{\text{cav}}}{L}$. The cavity resonances are shifted from the 0 frequency by $\omega_{\text{CE}}^{\text{cav}}$ just like

the frequencies of the optical comb¹. The p^{th} teeth of the comb then has a round-trip phase in the cavity:

$$\phi(\omega_p) = 2\pi \left(\frac{\omega_{\text{CE}} - \omega_{\text{CE}}^{\text{cav}} + p\omega_r}{\omega_r^{\text{cav}}} \right) \quad (4.24)$$

Because of the CEO term $\delta\omega_{\text{CE}} = \omega_{\text{CE}} - \omega_{\text{CE}}^{\text{cav}}$ here, even if we match the FSR to the comb repetition rate, the teeth will be shifted off resonance. So the synchronous cavity condition is no longer given by matching the repetition rate and the FSR. We show in Fig. 4.6, for different values of $\delta\omega_{\text{CE}}$, what the typical transmitted intensity looks like when scanning the cavity length. For non zero $\delta\omega_{\text{CE}}$ the main resonance length shifts by:

$$\delta L = -\lambda_0 \frac{\delta\omega_{\text{CE}}}{\omega_r} \quad \text{mod} \quad \lambda_0 \frac{\delta\omega_{\text{CE}}}{2\omega_r} \quad (4.25)$$

The partial resonances are still present at integer values of λ_0 from the main resonance. When scanning the cavity length, because of this CEO offset effect, it is sometimes difficult

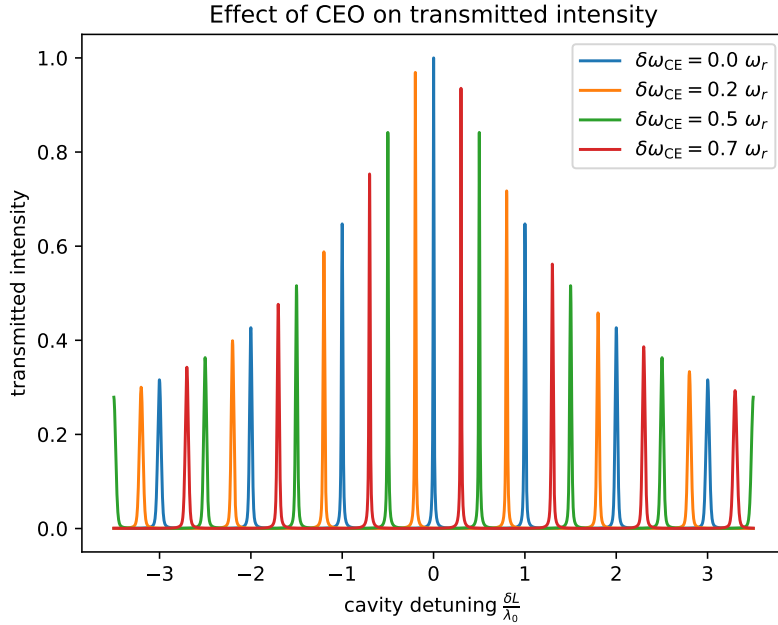


Fig. 4.6 *Effect of CEO on the scanning response of an optical cavity pumped by a frequency comb*

to distinguish between the main resonance and the second one². This can be a problem, when locking the cavity length to a resonance. If the main and secondary resonance look similar in terms of transmitted intensity, it means the transmitted spectrum is roughly identical. However, in the experiment, we need to make sure we always lock the cavity length to the same length. Indeed, we use the cavity transmission as a reference beam for the alignment of other components. For example, we use it to optimise the homodyne detection contrast. If we change the cavity lock point, and switch to the nearest secondary

¹Note in general $\omega_{\text{CE}}^{\text{cav}}$ and ω_{CE} are not equal as the group and phase velocities of the laser cavity and SPOPO cavity are not necessarily equal

²They become identical when $\frac{\delta\omega_{\text{CE}}}{\omega_r} = \frac{1}{2}$

resonance, the CEO of the transmitted OFC changes. This can drastically affect the homodyne contrast.

In the experiment, we ensure to be consistently locked to the same resonance and we use the neighbouring peaks to identify our locking peak. For example if two peaks appear to have the same resonance intensity, it is not relevant which one we choose as the transmitted spectrum will be similar, but we have to stay consistent, so we just choose the “left” one and make sure we always lock to the “left” peak.

4.2.3 Intra-cavity dispersion effects

The last effect to consider for synchronous cavities is the intra-cavity chirp (quadratic dispersion). It is particularly relevant when working with a broadband laser or when the cavity contains a highly dispersive medium. As we explained in section 3.2.4, chirp is just the quadratic term in the Taylor expansion of the phase. Because of this term, the resonant frequencies of the cavities will no longer be evenly spaced. As we move away from the central frequency ω_0 , the cavity FSR will decrease. The resonance are therefore desynchronised relative to the OFC teeth. This detuning increase as we move further away from ω_0 . This limits the number of teeth that can be resonant simultaneously. Fig 4.7 shows the spectral intensity transmission of the cavity in our experimental conditions for increasing values of intra-cavity chirp. We consider an input OFC, with central wavelength $\lambda_0 = 795$ nm and a 10 nm FWHM Gaussian envelope. Note we do not consider CEO effects here and the cavity length is set to the main resonance. Since the OFC contains a very large number of teeth (> 100000), we only represent the envelope of the frequency comb. We see that chirp imposes limits to the spectral width of the comb envelop that the cavity can transmit. This effect is non negligible, for $\phi^{(2)} = 500$ fs² the FWHM is reduced by almost half. In our experiment the SPOPO cavity chirp is $\phi^{(2)} \approx 250$ fs². This dispersion is mostly caused by the non-linear crystal in the cavity.

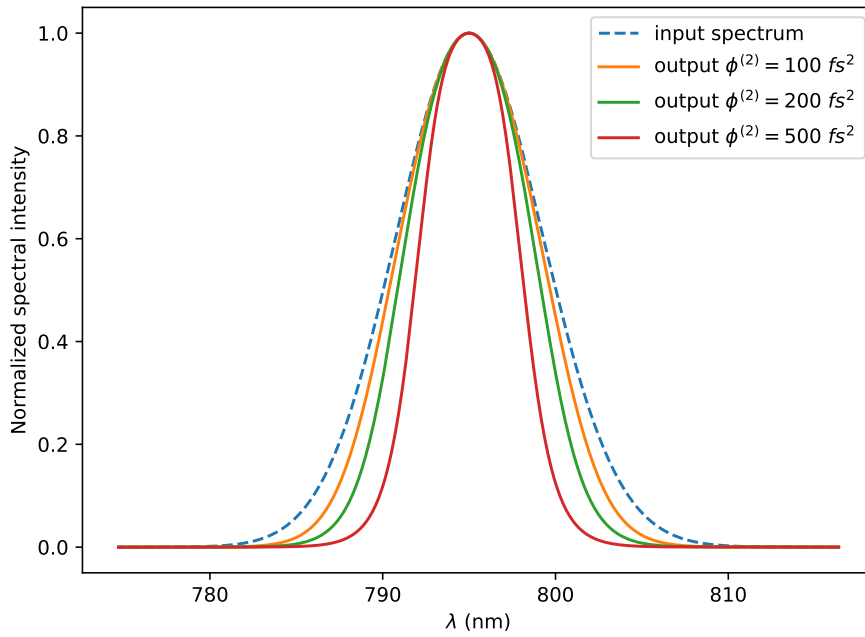


Fig. 4.7 Effect of intra-cavity chirp on the transmitted spectral intensity $|a(\omega)|^2$ ($a(\omega)$ is defined from Eq. (3.16)). Because of the quadratic phase term, the cavity resonances are not evenly spaced. But the frequency comb teeth are, so they are detuned. This detuning increase for teeth far from the central frequency ω_0 , to the point that the teeth are no longer transmitted through the cavity. The net effect is a narrowing of the OFC spectral envelope.

Chapter 5

The pulse shaper

Contents

5.1	General principle	67
5.1.1	Diffraction grating	68
5.1.2	SLM	69
5.2	Input output transformation	70
5.2.1	Simplified model: plane waves - pixel complexity	70
5.2.2	Effect of finite beam size - optical complexity	72
5.3	Effects of various misalignments	74
5.3.1	Input waist position	75
5.3.2	Grating rotation	75
5.3.3	Grating-cylindrical mirror distance	75
5.3.4	SLM-cylindrical mirror distance	77

A pulse shaper, as its name suggests, is a device that can manipulate the temporal variation of the amplitude and phase of a pulse of light. This thesis deals extensively with the notion of temporal/spectral modes of light and how they can be shaped to produce and measure multimode entangled states. So the pulse shaper is a central tool in our experiment. Pulse shaping techniques were originally proposed for pico-second pulses [142] and applied later to femto-second pulses [143].

In this chapter we first explain the basic working principles of pulse shapers and give details about the design of the pulse shaper we used in the experiment to tune the pump beam spectrum. We then describe the effect of various misalignments on the pulse shaper response. For more details about the different pulse shaper designs and its applications see [144, 145].

5.1 General principle

The pulse shaping technique we use in this work is often referred to as Fourier Optical Processing [146], and the general idea is quite simple. Femtosecond pulses are incredibly short, so it is hopeless to try to directly manipulate the temporal properties of individual pulses with acousto-optic or electro-optic devices. But as we saw in section 3.1.2 the temporal and spectral properties of light are related. So we can instead manipulate the pulse in the spectral domain. This is what a pulse shaper does.

Fig. 5.1 shows the general principle of a pulse shaper. Using a diffraction element (a

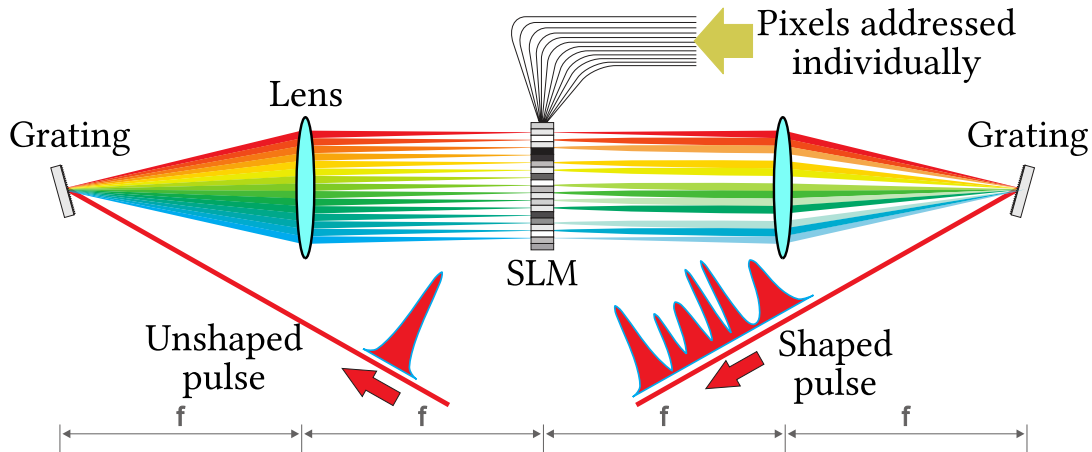


Fig. 5.1 Scheme of a pulse shaper. The spectral component of the incoming pulse are spatially separated with a grating and imaged onto an SLM which imprint a tunable phase shift on each of them. The spectral components are then recombined in a symmetric way.

grating in our case), the various frequency components of light may be spatially separated, allowing one to access and manipulate each of them independently. After that, these components are recombined into a single beam with the same diffracting element. Given Eq. (3.2), if one can shape the spectral amplitude of a pulse, the temporal envelope of the pulse will be changed accordingly.

Each spectral component is usually manipulated using a phase plate or a spatial light modulator (SLM), which can be thought of as an array of tunable phase-shifters. After being separated by the grating the spectral components of the beam are imaged onto the SLM with a cylindrical lens or mirror. The SLM then adds a given phase to each frequency component. In other words we tune the spectral phase $\phi(\Omega)$ of the beam. Additionally using a “trick” detailed in section 5.1.2 one can also tune the spectral amplitude $|a(\Omega)|$. The different frequency components of the beam are then recombined.

As a result the temporal pulse envelope $a(t)$ is fully tunable. Of course there are some resolution limits to the pulse shaping abilities. Those will be discussed in section 5.2.

5.1.1 Diffraction grating

The diffraction grating is an optical element with a fine periodic structure. When the typical size of this structure is of the same order of magnitude or smaller than the wavelength of the incident light, diffraction will occur: due to an interference effect, the various spectral components of light get spatially separated (see Fig. 5.2). The diffraction formula relates the output propagation angle of each spectral component θ_d of wavelength λ with its input incidence angle on the grating θ_i and the grating pitch d ¹:

$$\sin \theta_i + \sin \theta_d = m \frac{\lambda}{d} \quad \text{for } m \in \mathbb{Z} \quad (5.1)$$

¹This formula is written for a reflective grating (θ_d counted from the incidence normal) with oriented values for angles.

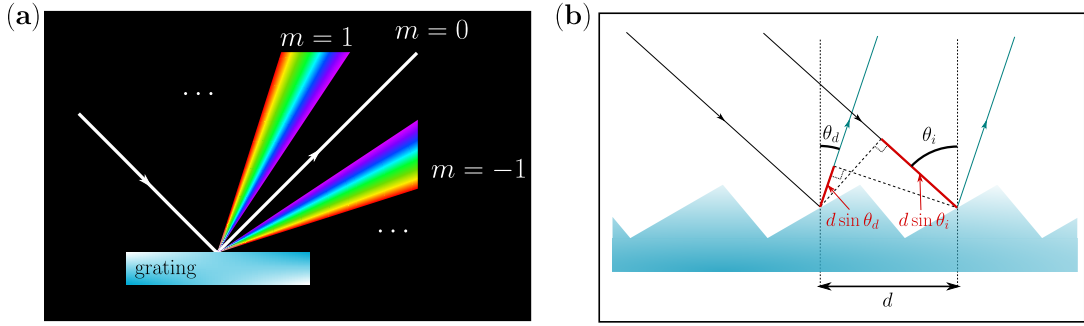


Fig. 5.2 Scheme of a reflection grating. (a) Polychromatic light is diffracted by a grating. The various frequency components have different diffraction angles except for diffraction order $m = 0$. (b) The diffraction angles correspond to constructive interference of light paths scattered from adjacent rulings of the grating.

This formula is easily understood if we require that the phase difference between light rays hitting different parts of the grating be a multiple of λ (condition for constructive interference, see Fig. 5.2). Diffraction grating can be reflective or transmissive.

Each wavelength can constructively interfere at a different output angle for each value of m . These are referred to as diffraction orders. Order 0 corresponds to the condition $\sin \theta_d = -\sin \theta_i$ which is simply the standard reflection law for mirrors $\theta_i = \theta_d$ in the case of reflection gratings (or parallel transmission for transmission gratings). In the standard convention, negative (resp. positive) diffraction orders $m < 0$ (resp. $m > 0$) correspond to θ_d being more obtuse (resp. acute) than the standard ($m = 0$) reflection angle.

The particular shape of the grating pattern will determine the repartition of light between the various diffraction orders. Gratings are sometimes optimised to diffract maximally in a single diffraction order, these are called blazed gratings. Additionally they are often designed to be more efficient when the diffraction angle coincides with the incidence angle, this is called the Littrow configuration. In our experiment we use a 2400 gr/mm holographic grating model 05HG2400-400-1 from Richardson [147]. The grating is optimised to diffract in order -1 so the diffraction angle is found with:

$$\theta_d(\theta_i, \lambda) = \arcsin\left(-\frac{\lambda}{d} - \sin \theta_i\right) \quad (5.2)$$

5.1.2 SLM

A spatial light modulator is a device that can imprint some spatial phase modulation on a light beam. In our case we use a liquid crystal SLM (LCOS-SLM model X10468-05 from Hamamatsu [148]), which is a 2D array of liquid crystals that can be individually addressed with an electrical signal. The liquid crystals act as tunable wave-plates that change the phase of light reflected by the SLM surface without any intensity change. The SLM has 792×600 square pixels of size $\delta x_{\text{px}} = 20 \mu\text{m}$.

When used in a straight forward way SLM can only affect the phase of the incoming beam, not its amplitude. However, we can use a special trick to tune the spectral amplitude as well. In our geometry the beam is diffracted horizontally by the grating and the different spectral components of the beam are imaged horizontally on the SLM with a cylindrical mirror. The vertical degree of freedom of the beam remains unchanged. We can use it

to imprint a vertical blazed grating pattern on the SLM (see Fig. 5.3). The output beam

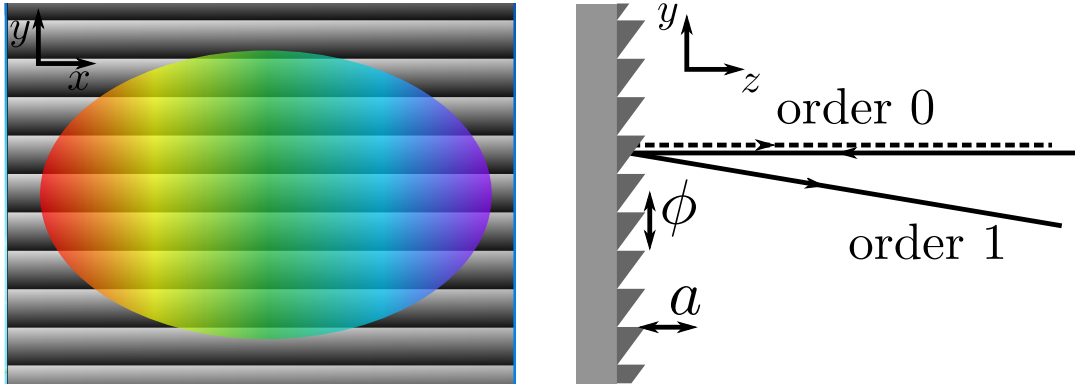


Fig. 5.3 Even though the liquid crystal of the SLM only affect the phase of the input beam, one can imprint a vertical grating structure on the SLM therefore tuning the amplitude of light diffracted in order 1. We use the depth of the grating pattern to control the amplitude of light a diffracted in order 1. We use the vertical position of the grating pattern to control the phase ϕ .

will then be vertically diffracted. Using a sawtooth structure, the light is only diffracted in orders 0 and 1. If we fix the grating pitch and make sure we filter the first order on the output with a pinhole, we can then tune the amplitude of each spectral component by modulating the magnitude of the vertical grating pattern. Additionally, the relative phase between horizontally adjacent components can be tuned by shifting vertically the grating pattern instead of adding a global phase offset (see [149, 150] for more details).

5.2 Input output transformation

In this section we establish the input-output relationships for a pulse shaper. First with an idealised plane-wave model that allows us to point out one of the pulse shaper resolution limits. Then we improve this model and take the input beam size into account, this leads to a second resolution limit. When designing a pulse shaper both these resolutions must be considered, the worst of the two will be the limiting factor of the pulse shaper.

5.2.1 Simplified model: plane waves - pixel complexity

Let us assume that the input beam can be modelled by a polychromatic plane wave with spectral width $\Delta\lambda$, centred at λ_0 . Assuming this spectral width is not too big we can linearise Eq. (5.2) in λ , we get the diffraction angle:

$$\theta_d(\lambda) \approx \theta_d^{(0)} + \theta_d^{(1)}(\lambda - \lambda_0) \quad \text{with} \quad \theta_d^{(0)} := \theta_d(\lambda_0) = \theta_L \quad (5.3)$$

$$\theta_d^{(1)} := \frac{\partial \theta_d}{\partial \lambda} = \frac{-1}{d \cos \theta_d^{(0)}} \quad (5.4)$$

After the grating the diffracted light is then imaged onto the SLM with a cylindrical mirror of focal length f . For the grating plane and SLM plane to be imaged on one another the set-up must respect a $4f$ configuration (as in Fig. 5.1). In this case the grating and SLM

planes are Fourier image planes and an angle out of the grating will be matched to a position on the SLM. So the typical total spread of the light on the SLM will be:

$$\Delta L = \alpha \Delta \lambda \quad \text{with} \quad \alpha = \left| \theta_d^{(1)} \right| f = \frac{f}{d \cos \theta_d^{(0)}} \quad (5.5)$$

α is the spatial dispersion of the pulse shaper often expressed in mm/nm. The wavelength resolution on the SLM is fixed by the difference in wavelength of light hitting two neighbouring pixels:

$$\delta \lambda_{\text{px}} = \frac{\delta x_{\text{px}}}{\alpha} \quad (5.6)$$

Where δx_{px} is the SLM pixel pitch. The quality of a pulse shaper is often expressed in terms of its complexity, that is the maximum number of features one can imprint on a given spectrum. Given that the input light has spectral width $\Delta \lambda$ and that the resolution is $\delta \lambda_{\text{px}}$, the complexity is then simply:

$$\eta_{\text{px}} = \frac{\Delta \lambda}{\delta \lambda_{\text{px}}} = \frac{f \Delta \lambda}{d \delta x_{\text{px}} \cos \theta_d^{(0)}} \quad (5.7)$$

Note that this expression assumes the SLM surface is wide enough to encapsulate the whole $\Delta \lambda$. For that the SLM width must be large enough compared to ΔL .

We see that, for a given input spectrum, the complexity can be improved in several ways:

- increase the focal distance f : with a longer focal distance the diffracted light is collimated into a larger beam. Two wavelength components will be spread further apart on the SLM hence the improvement in complexity.
- increase the groove density $a = \frac{1}{d}$: a higher groove density will mean the grating spreads light with a broader angle, leading to a larger spread on the SLM hence the higher complexity.
- decrease the pixel pitch δx_{px} : a smaller pixel size means two neighbouring pixel will shape closer wavelength hence the higher resolution.

It is important to note that the complexity cannot be improved indefinitely by changing a and f because at some point the beam size will exceed the available SLM size. a and f should be tuned to spread the beam optimally on the SLM. So ultimately the complexity is limited by the only incompressible parameter, that is the number of pixel on the SLM. This is why we call $\delta \lambda_{\text{px}}$ and η_{px} the *pixel* resolution and *pixel* complexity.

In our experiment, $a = 2400 \text{ mm}^{-1}$, $f = 250 \text{ mm}$, $\Delta \lambda \approx 1.3 \text{ nm}$, $\delta x_{\text{px}} = 20 \text{ }\mu\text{m}$ and $\theta_d^{(0)} = 28.5^\circ$ so the pixel resolution is $\delta \lambda_{\text{px}} \approx 0.0293 \text{ nm}$ and the pixel complexity is $\eta_{\text{px}} \approx 44.4$.

There is another limit to resolution and complexity in a pulse shaper that comes from entirely optical considerations. It is called the optical complexity. This limit appears when the input beam size is taken into account. We detail it in the next section.

5.2.2 Effect of finite beam size - optical complexity

When we looked at the effect of the grating we considered the incoming beam as a plane wave. A plane wave would be focused into an infinitely small point (or vertical line) in the SLM plane, but that won't be true for any realistic input beam with finite size. For a realistic beam, a single spectral component coming out of the grating will have some finite spatial extension which will result in a spot on the SLM plane. Only when this spot size is significantly smaller than the SLM pitch can the plane wave approximation be valid.

Consider for example, an input Gaussian beam with waist $w_i \approx 1$ mm at $\lambda_0 = 795$ nm, and a focal length $f = 250$ mm, the focused waist size is given by the standard relation:

$$w_o = \frac{\lambda_0 f}{\pi w} \approx 0.05 \text{ mm} \quad (5.8)$$

This is bigger than the pixel pitch of 0.02 mm that we used. So in our case, the input beam size needs to be taken into account. A single frequency component will actually spread on several pixels on the SLM and smear our shaping. This can severely limit the resolution of the pulse shaper, regardless how good its *pixel* complexity is.

We refer to the resolution limit coming from this effect as the *optical* resolution. Note that the bigger the input beam, the smaller the spot on the SLM. This is consistent with the previous treatment of section 5.2.1, in the limit of an input beam with infinite spatial extension we recover the plane wave approximation.

An additional complication appears when we consider the input beam's width. Even for a single spectral component, the beam size right after the grating is different to the input beam size. To understand this, consider the spatial Fourier decomposition of the input beam. The beam can be described as a collection of plane waves with direction spanning a small angle around the main propagation direction of the beam. Each of these plane waves will therefore have a slightly different incidence angle on the grating. According to Eq. (5.2) the diffraction angle depends not only on the wavelength but also on the incidence angle on the grating. So each plane wave in the Fourier spatial decomposition of the input beam will be diffracted at a slightly different angle. The net effect will be a change in the output beam size, whenever the incidence angle on the grating is different from the Littrow angle.

Consider a Gaussian input beam with waist w_i onto the grating. We will also consider that the input beam has a Gaussian spectrum with width $\Delta\lambda$ (standard deviation in intensity). The field envelope on the grating reads:

$$E(x, \lambda) = \mathcal{E}_0 e^{-\frac{x^2}{w_i^2}} e^{-\frac{\lambda^2}{4\Delta\lambda^2}} \quad (5.9)$$

where x correspond to the transverse direction relative to the beam's direction of propagation. In the spatial-Fourier domain this gives:

$$E(k_x, \lambda) = \tilde{\mathcal{E}}_0 e^{-\frac{k_x^2}{4\Delta k_i^2}} e^{-\frac{\lambda^2}{4\Delta\lambda^2}} \quad \text{with} \quad \Delta k_i = \frac{1}{w_i} \quad (5.10)$$

k_x is the transverse wave-vector that parametrises the plane wave components. We can also parametrise it with the angle β relative to the $k_x = 0$ component: $k_x = k_0 \sin(\beta)$. Using basic geometry we see the component with angle β has an incidence angle on the grating given by:

$$\theta_i = \beta + \theta_i^{(0)} \quad (5.11)$$

So the relative incidence angle $\delta\theta_i = \theta_i - \theta_i^{(0)}$ is just given by β . If the incident beam is large enough ($\frac{\Delta k_i}{k_0} \ll 1$), β is small and we can linearise the sine function:

$$k_x = k_0 \sin \beta \quad (5.12)$$

$$\approx k_0 \beta \quad (5.13)$$

$$\approx k_0 \delta\theta_i \quad (5.14)$$

Similarly, we can write the beam coming out of the grating in the Fourier domain and we have:

$$k_x \approx k_0 \delta\theta_d \quad \text{with} \quad \delta\theta_d = \theta_d - \theta_d^0 \quad (5.15)$$

If we differentiate the diffraction law of Eq. (5.2) we obtain:

$$d\theta_d = \alpha d\lambda - \frac{\cos \theta_i d\theta_i}{\sqrt{1 - (-a\lambda - \sin \theta_i)^2}} \quad (5.16)$$

$$= \alpha d\lambda - \frac{\cos \theta_i}{\cos \theta_d} d\theta_i \quad (5.17)$$

So that in the small angle approximation we have:

$$\Delta k_{\text{out}} \approx k_0 \Delta\theta_d = k_0 \frac{\cos \theta_i^{(0)}}{\cos \theta_d^{(0)}} \Delta\theta_i \quad (5.18)$$

Where Δk_{out} is the width of the Fourier distribution of the diffracted beam. So that finally the waist right after the grating is:

$$w' = \frac{\cos \theta_d^{(0)}}{\cos \theta_i^{(0)}} w_i \quad (5.19)$$

Note that here we considered that each frequency component had the same spatial shape and we fully separated the spatial and frequency dependencies in the expression of $E(x, \lambda)$. This approximation is valid in most cases when the light spectrum is narrow enough.

Given the waist of the beam after the grating it will be focused onto the SLM to a typical size:

$$\delta x_{\text{opt}} = 2w_o = 2 \frac{\lambda_0 f}{\pi w'} = 2 \frac{\cos \theta_i^{(0)}}{\cos \theta_d^{(0)}} \frac{\lambda_0 f}{\pi w_i} \quad (5.20)$$

This corresponds to a wavelength resolution:

$$\delta \lambda_{\text{opt}} = \frac{\delta x_{\text{opt}}}{\alpha} = 2 \frac{\cos \theta_i^{(0)} \lambda_0}{\pi w_i a} \quad (5.21)$$

and the corresponding complexity is:

$$\eta_{\text{opt}} = \frac{\Delta \lambda}{\delta \lambda_{\text{opt}}} = \frac{\pi w_i a \Delta \lambda}{2 \cos \theta_i^{(0)} \lambda_0} \quad (5.22)$$

We see that, for a given input spectrum, the optical complexity can be improved in two ways:

- increase the groove density a : a grating with higher groove density will spread light with a broader diffraction angle, leading to a larger spread on the SLM hence the higher complexity. Just as before with the pixel complexity, one cannot increase a indefinitely because the SLM has a finite size.
- increase the input waist w_i : for a single frequency component, a bigger input waist leads to a smaller waist on the SLM, which reduces the smearing of different frequencies. The input beam cannot be made arbitrary big for obvious reasons. At some point it will start clipping on the optical components of the pulse shaper. The limiting one is usually the grating or SLM (vertical size).

Note that, unlike in the case of pixel complexity, increasing the focal length does not improve the optical complexity. This is because even if it would broaden the spread of the diffracted beam, it would also increase the waist size of individual frequencies on the SLM by the same amount, therefore cancelling the improvement.

In our experiment, $w_i \approx 3 \text{ mm}$, $a = 2400 \text{ mm}^{-1}$, $\Delta\lambda \approx 1.3 \text{ nm}$, $\lambda_0 = 397.5 \text{ nm}$ and $\theta_d(0) = 28.5^\circ$ so the optical resolution is $\delta\lambda_{\text{opt}} = 0.031 \text{ nm}$ and the optical complexity is $\eta_{\text{opt}} \approx 42.1$.

The pulse shaper was designed to maximise and have similar values for both the optical and pixel complexities. Ultimately the resolution of the pulse shaper is limited by the smaller complexity, so there is no point in increasing one, if the other stays small. Both complexities being around 40 we should be able to imprint up to 40 “features” in the pump spectrum. The real complexity of the pulse shaper in the experiment may be smaller because of effects we did not consider here (misalignment for example). Nevertheless, this design analysis gives us a rough idea of the resolutions to expect. In section 7.2 when we optimise the pump profile, we consider that the pump is divided into 8 frequency bands. So the complexity of our design should be enough to implement the optimal pump shape we find.

5.3 Effects of various misalignments

Until now we considered an ideal pulse shaper configuration, with an input beam waist on the grating, and a perfect $4-f$ configuration. In practice the pulse shaper needs to be aligned and the different distances tuned in order to approach these conditions. It is therefore useful to know the detrimental effects that appear when one deviates from these conditions. This will allow the experimentalist to isolate the parameter that needs to be corrected for a given observed error.

In this section we present the effects of various misalignments on the pulse shaper output. We won’t look at the effects of horizontal angles, details on that can be found in [151]. There are four separate distances to tune to reach the $4-f$ configuration, however in our case we use a folded pulse shaper configuration with a reflective SLM, only one grating and one cylindrical mirror. The light back-propagates to the mirror and grating after reaching the SLM. So there are only two independent distances to tune: the grating to cylindrical mirror distance and the SLM to cylindrical mirror distance. We also look at effects of input waist position and grating rotation.

5.3.1 Input waist position

The first parameter that might be off is the input waist position. In section 5.2.2 we assumed the waist of the input beam was positioned on the grating. If the input waist position is displaced longitudinally, the waist of the beam in the SLM plane would change as Eq. (5.8) is only valid when the input waist is in the object plane of the focusing element. But this effect is actually negligible as long as the waist position offset is small compared with the Rayleigh range of the input beam. This is the case in our design as the input waist is typically several millimetres so the Rayleigh range is several meters.

5.3.2 Grating rotation

The diffraction grating needs to be aligned so that the rulings of the grating lie in a plane normal to the optical table. This ensures that the beam is diffracted horizontally. If this is not the case, the diffraction plane is tilted and resolution will decrease because single frequency components will spread on several pixel columns on the SLM. Moreover when coming back to the grating, the different spectral components will recombine at different heights which will result in vertical spatial chirp on the output beam. By spatial chirp we designate any kind of spatio-temporal coupling in the beam. When a beam is spatially chirped, different transverse point of the beam have different spectral contents. And equivalently, different frequency components of the beam have different spatial profiles. To correct the vertical chirp, we need to rotate the grating around the axis perpendicular to its plane and correct alignment with vertical angle. This procedure must be repeated until the vertical chirp is minimised.

5.3.3 Grating-cylindrical mirror distance

The distance between the cylindrical mirror and the grating is the most critical. If it is not equal to f the output beam will be both temporally and spatially (horizontally) chirped.

Temporal chirp or group velocity dispersion refers to the quadratic spectral phase we described in section 3.2.4. It appears because the different spectral components of the beam have different paths and therefore different optical path lengths in the pulse shaper (see Fig. 5.4). In the following we will show that this path difference amounts to a quadratic phase. We consider the different frequency components on a plane orthogonal to the direction of propagation of the central frequency of the beam. For a given frequency component, the accumulated phase from the grating is just $\phi(\omega) = \frac{\omega}{c}l(\omega)$, where $l(\omega)$ is the optical path length. For frequencies close to the central frequency ω_0 , writing the Taylor expansion of $\phi(\omega)$ up to 2nd order, we have:

$$\delta\phi(\Omega) := \phi(\omega) - \phi(\omega_0) \quad (5.23)$$

$$\approx \Omega\phi^{(1)} + \frac{\Omega^2}{2}\phi^{(2)} \quad (5.24)$$

$$\text{with } \Omega := \omega - \omega_0 \quad (5.25)$$

$$\text{and } \phi^{(1)} := \left(\frac{\partial\phi}{\partial\omega}\right)_{\omega_0} = \frac{l_0}{c} + \frac{\omega_0}{c} \left(\frac{\partial l}{\partial\omega}\right)_{\omega_0} \quad (5.26)$$

$$\phi^{(2)} := \left(\frac{\partial^2\phi}{\partial\omega^2}\right)_{\omega_0} = \frac{2}{c} \left(\frac{\partial l}{\partial\omega}\right)_{\omega_0} + \frac{\omega_0}{c} \left(\frac{\partial^2 l}{\partial\omega^2}\right)_{\omega_0} \quad (5.27)$$

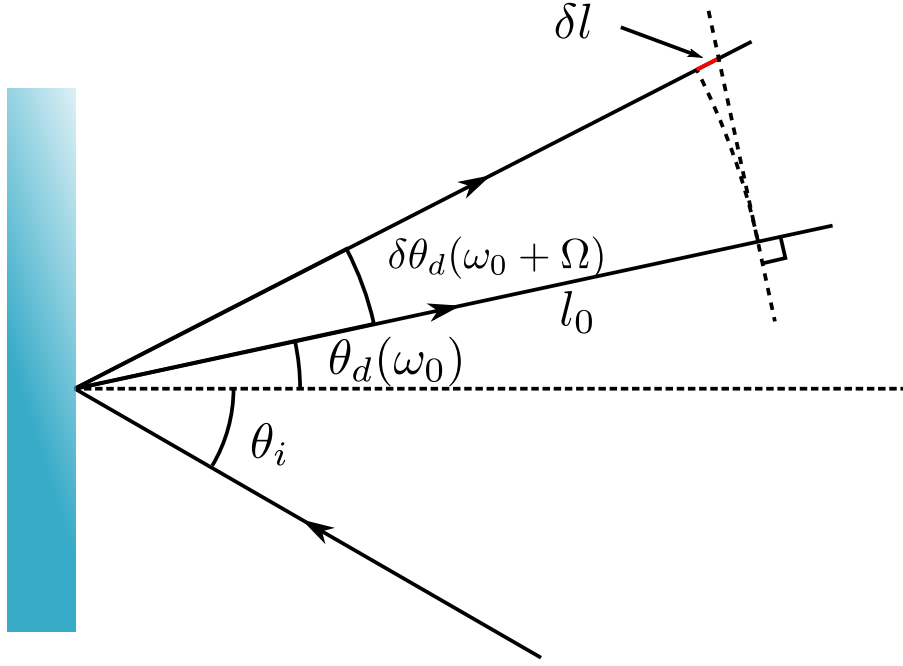


Fig. 5.4 Schematic representation of the diffraction path of two different frequencies ω_0 and $\omega_0 + \Omega$, and the resulting path difference δl . For small deviations around the central diffraction angle $\theta_d(\omega_0)$, the phase difference scales quadratically with the frequency offset Ω .

$l(\omega)$ is linked to the diffraction angle difference $\delta\theta_d(\omega) := \theta_d(\omega) - \theta_d(\omega_0)$ by (see Fig. 5.4):

$$l(\omega) = \frac{l_0}{\cos(\delta\theta_d(\omega))} \quad (5.28)$$

Using this expression, it is easy to show that:

$$\left(\frac{\partial l}{\partial \omega}\right)_{\omega_0} = 0 \quad (5.29)$$

$$\left(\frac{\partial^2 l}{\partial \omega^2}\right)_{\omega_0} = l_0 \left(\frac{\partial \theta_d}{\partial \omega}\right)_{\omega_0}^2 \quad (5.30)$$

So that finally the phase difference between different frequency components can be written:

$$\delta\phi(\Omega) = \frac{l_0}{c}\Omega + \frac{\omega_0 l_0}{c} \left(\frac{\partial \theta_d}{\partial \omega}\right)_{\omega_0}^2 \frac{\Omega^2}{2} \quad (5.31)$$

The first term just corresponds to the standard linear phase that different frequencies accumulate when propagating conjointly. The second is responsible for the temporal chirp, using Eq. 5.3 it can be written:

$$\phi^{(2)} = \frac{l_0 \lambda_0^3 a^2}{2\pi c^2 \cos^2(\theta_d^{(0)})} \quad (5.32)$$

When the grating to cylindrical mirror distance is equal to f this optical path difference is exactly compensated by the cylindrical mirror so that there is no resulting chirp after the

mirror. When the cylindrical mirror is at distance $f + \delta$ from the grating, however, the temporal chirp is not entirely compensated. After the mirror there remains the temporal chirp:

$$\phi^{(2)} = \frac{\delta \lambda_0^3 a^2}{2\pi c^2 \cos^2 \theta_d^0} \quad (5.33)$$

As a typical example, for $\lambda_0 = 397.5 \text{ nm}$, $\delta = 1 \text{ mm}$, $a = 2400 \text{ mm}^{-1}$ and $\theta_d^{(0)} = \theta_L = 28.5^\circ$ we obtain $\phi_2 \approx 830 \text{ fs}^2$, which is non negligible. Note that it is possible to compensate this chirp with the SLM profile.

The second detrimental effect of a wrong grating-mirror distance is horizontal chirp. It comes from the fact that if the diffracted beam is not properly collimated with the cylindrical mirror, each frequency component will return on the grating with a different incidence angle than when it left. As a result the various frequency components will not properly recombine into a single beam, hence the horizontal chirp.

5.3.4 SLM-cylindrical mirror distance

We now look at what happens when the SLM-cylindrical mirror distance is off. If the cylindrical mirror is placed at f relative to the grating then, regardless of the SLM position, the individual spectral component are all parallel after the mirror. After reflection on the SLM they will back-propagate to the grating with the same angle. So the output beam should be well recombined and won't show any sign of spatial chirp. The SLM position will not change the temporal chirp either for the same reason (remember temporal chirp is caused by the angular dispersion as we saw in the previous section).

The position of the SLM is therefore not critical in terms of spatial or temporal chirp. The main effect will be a loss of resolution when the SLM is not in the focal plane of the cylindrical mirror. We can estimate how sensitive this will be. The waist of a single frequency component in the focal plane of the cylindrical mirror is $w_o = \frac{\cos \theta_i^{(0)}}{\cos \theta_d^{(0)}} \frac{\lambda_0 f}{\pi w_i}$. We can estimate how critical the SLM position is by looking at the Rayleigh range corresponding to this waist size:

$$z_R = \frac{\pi w_o^2}{\lambda_0} = \frac{\lambda_0 f^2}{\pi w_i^2} \quad (5.34)$$

where we have assumed for simplicity $\theta_i^{(0)} = \theta_d^{(0)} = \theta_L$. This gives about 0.9 mm for a 25 cm focal length and 3 mm input waist. So the SLM position is quite critical, if it's off by only a few millimetre, the optical resolution of the pulse shaper will be considerably reduced.

To tune the position of the SLM, one can look at the output beam and try to collimate it. Note however that the distance between the grating and cylindrical mirror will also affect the output beam collimation. So ideally one must first optimise the grating-mirror distance, and then optimise the SLM position. We can also optimise the SLM position by looking at the pulse shaper resolution. To measure the resolution, we can for example, put the vertical diffraction pattern on a single column of the SLM and look at the spectral width of the pulse shaper output with a spectrometer.

When studying the effects of pulse shaper misalignment, I ran into a common misconception that I would like to highlight here. In many textbooks and articles on pulse shaping where the pulse shaper has an unfolded configuration as in Fig. 5.1 (with 2 gratings), the distance between gratings is often cited as the cause of temporal chirp (as in [152] for

example). The equation for chirp is then often given in terms of $L - 4f$, where L is the actual grating-grating distance:

$$\phi^{(2)} = \frac{\lambda_0^3 a^2}{2\pi c^2 \cos^2 \theta_d^{(0)}} (L - 4f) \quad (5.35)$$

This is a bit misleading because, even if the full line is not $4f$ long, there won't be any chirp as long the grating-lens distances are both equal to f . So really it is the grating-lens distance that matters. Of course if the lens-SLM distances are both f , then any departure from the $4f$ configuration comes from error in the grating-lens distances and in that case formula (5.35) is correct.

I believe this misleading way of presenting chirp in pulse shapers comes from pulse compressors, which were studied before pulse shapers were invented. In pulse compressors [153–157], there is no lens or SLM, just two grating. The chirp depends on the grating-grating distance, and is given by Eq. (5.35) where $L - 4f$ is replaced by the grating-grating distance.

In the folded geometry, if the SLM position is off, the full line won't be $4f$ long. If one uses formula (5.35), this may lead to think that the position of the SLM has an effect on temporal chirp, but that is not true.

Chapter 6

Non linear optics

Contents

6.1	Introduction	79
6.2	Second harmonic generation	81
6.3	Parametric down conversion	85
6.3.1	Classical treatment for real signal envelopes	86
6.3.2	Complex signal envelope and quantum treatment	88
6.3.3	Pump spectral phase effects	89
6.4	SPOPO	91
6.4.1	SPOPO without dispersion, input-output relations.	91
6.4.2	Simulation of intra-cavity dispersion	93
6.4.2.1	Naive approach	94
6.4.2.2	Full treatment	94

6.1 Introduction

In this thesis we aimed at producing particular types of entangled states. This entanglement is produced using a second order linearity inside a dielectric material. In this section we introduce such non-linearities and explain how second order non-linearities can be used to generate entangled states.

A dielectric medium is an insulating material that can be polarised in the presence of an external electric field. It contains no free charges but its constituents (atoms or molecules) do contain bound charges that will move under the influence of an external field. The charge distribution “stretches” locally and produces an effective electric dipole. All these dipoles add up and contribute to an effective bulk polarisation density. This polarisation then acts as a source term for the electromagnetic field.

In the simplest case the polarisation density at a given point is just proportional to the applied external field: $P(t) = \epsilon_0 \chi^{(1)} E(t)$. The total field within the material is then usually described by the electric displacement field $D(t) = \epsilon_0 E(t) + P(t)$. $\chi^{(1)}$ is the linear susceptibility, it is used to describe effects like refraction at the interface between materials and is linked to the refractive index with $n^2 = 1 + \chi^{(1)}$.

In more general cases, if the external field is sufficiently intense, we observe a non-linear response:

$$P(t) = \epsilon_0 (\chi^{(1)} E(t) + \chi^{(2)} E(t)^2 + \chi^{(3)} E(t)^3 + \dots) \quad (6.1)$$

This expansion of the polarization density as a Taylor series is a perturbative description, it is valid as long as the external field is not too large. Here we omitted the time dependency of the susceptibilities for simplicity. If the susceptibilities $\chi^{(n)}$ do not depend on time, the response is called instantaneous. $\chi^{(2)}$ describes the second order non-linearity. It is responsible for effects like sum frequency generation or parametric down conversion. The most relevant aspect of second order non-linearity for the generation of entanglement is its ability to mix field components at different frequencies.

To see this, consider an input field with two monochromatic components: $E(t) = \mathcal{E}_1 e^{-i\omega_1 t} + \mathcal{E}_2 e^{-i\omega_2 t} + \text{c.c.}$, the second order part of the polarisation will then be:

$$P^{(2)}(t) = \epsilon_0 \chi^{(2)} \left(|\mathcal{E}_1|^2 + |\mathcal{E}_2|^2 \right) \quad (6.2)$$

$$+ \mathcal{E}_1^2 e^{-2i\omega_1 t} + \mathcal{E}_2^2 e^{-2i\omega_2 t} \quad (6.3)$$

$$+ 2\mathcal{E}_1 \mathcal{E}_2 e^{-i(\omega_1 + \omega_2)t} \quad (6.4)$$

$$+ 2\mathcal{E}_1 \mathcal{E}_2^* e^{-i(\omega_1 - \omega_2)t} \Big) + \text{c.c.} \quad (6.5)$$

So the second order response of the medium creates new field components at frequencies 0, $2\omega_1$, $2\omega_2$, $\omega_1 - \omega_2$ and $\omega_1 + \omega_2$. Each new component is a result of the interaction of 2 components in the input field:

- The 0 frequency term corresponds to the interaction of the ω_1 (resp. ω_2) component with itself. This effect is called *optical rectification*
- The $2\omega_1$ (resp. $2\omega_2$) frequency term also corresponds to the interaction of the ω_1 (resp. ω_2) component with itself. This effect is called *second harmonic generation*
- The $\omega_1 + \omega_2$ frequency term corresponds to the interaction of the ω_1 and ω_2 components. This effect is called *sum frequency generation*
- The $\omega_1 - \omega_2$ frequency term also corresponds to the interaction of the ω_1 and ω_2 components. This effect is called *difference frequency generation*

In general all these effects do not happen simultaneously. Indeed, we still haven't considered the spatial degree of freedom of the fields. Each of the new excited fields will propagate in the medium. To generate a non zero contribution on average, the excited fields produced in each point of the medium need to interfere constructively. If we consider sum frequency generation for example, with plane input waves: $E_{1/2}(t) = \mathcal{E}_{1/2} e^{-i(\omega_{1/2} t - \mathbf{k}_{1/2} \cdot \mathbf{r})}$, the sum field created at $\omega_3 = \omega_1 + \omega_2$ will propagate with wave-vector \mathbf{k}_3 with $|\mathbf{k}_3| = \frac{n(\omega_3)\omega_3}{c}$. The different source contributions will then constructively interfere only if:

$$\mathbf{k}_3 = \mathbf{k}_1 + \mathbf{k}_2 \quad (6.6)$$

This is the so called phase matching condition.

In equation (6.1) we did not consider the vectorial nature of the electric field, if we do the non linear susceptibility becomes a tensor and the i^{th} component of the polarisation now reads ¹:

$$P_i = \epsilon_0 (\chi_i^{j(1)} E_j + \chi_i^{jk(2)} E_j E_k + \chi_i^{jkl(3)} E_j E_k E_l + \dots) \quad (6.7)$$

¹Here we used Einstein's notation for summation

Now the linear response of the medium is described by a matrix $\chi^{(1)}$. It accounts for birefringence effects in the medium. Higher order terms are tensors of increasing order that describe the non-linear response. Now, different polarisation may interact to produce the new frequencies.

In particular for second order effects, it is possible to satisfy the phase matching conditions (Eq.(6.6)) even for co-propagating fields. Indeed, if the medium is birefringent, different polarisation components experience different optical index. If the medium is a *uniaxial* crystal, there is one preferred polarisation that experiences an extraordinary index n_e while the others have the ordinary index n_o . With a carefully designed dielectric crystal and input field polarisation we may have for example:

$$n_e(\omega_1 + \omega_2) = \frac{n_o(\omega_1)\omega_1 + n_o(\omega_2)\omega_2}{\omega_1 + \omega_2} \quad (6.8)$$

This would then ensure the phase matching condition of Eq. (6.6) is met for co-propagating beams. This way of ensuring phase matching is very commonly used. It is the technique we used in this experiment.

The second order non-linear effects are often called three wave mixing. This is because when a field is created at say $\omega_3 = \omega_1 + \omega_2$, this new frequency component can then interact with the ω_1 (resp. ω_2) component to produce a source term for the ω_2 (resp. ω_1) component through down-conversion. This effect is the converse of the first one and has the same phase matching condition. Therefore, any newly excited frequency can convert back into the field that it originated from. The three field component will effectively be coupled by a set of differential equations.

6.2 Second harmonic generation

In the experiment we use second harmonic generation to produce a field that is later used as a pump for a down-conversion process. This is a common technique. Down-conversion involves input fields that have different frequencies. Instead of using two separate lasers, which would not be coherent with each other (unless stabilised to a common reference), we first generate the pump with second harmonic generation (which only requires a single input field).

Technically speaking, we should call it sum frequency generation because, as we saw, our laser is a frequency comb and contain many frequency components. Any component ω_k will interact with any other ω_l to produce the sum frequency $\omega_k + \omega_l$. The frequencies of the input comb are given by Eq. (3.13) and the resulting frequency comb will have the same repetition rate:

$$\omega_k = 2\omega_{\text{CE}} + k\omega_r \quad (6.9)$$

Phase matching will only be satisfied over a finite bandwidth so the envelope of the newly generated comb will depend both on the input envelope and on the phase matching.

Throughout this section we refer to the input field as the pump and the generated sum frequency field as the signal. Let us now derive the equations for the produced signal field. The propagation equation for the electric field in the non-linear crystal is deduced from Maxwell's equations (see appendix A.4):

$$\nabla^2 \mathbf{E}(\mathbf{r}, t) - \frac{1}{c^2} \frac{\partial^2 \mathbf{E}(\mathbf{r}, t)}{\partial t^2} = \frac{1}{\epsilon_0 c^2} \frac{\partial^2 \mathbf{P}(\mathbf{r}, t)}{\partial t^2} \quad (6.10)$$

where $\mathbf{P} \equiv \mathbf{P}_L + \mathbf{P}_{NL}$ is the electric polarisation of the medium:

$$P_{L,i} = \varepsilon_0 \sum_j \chi_{ij}^{(1)} E_j \quad (6.11)$$

$$P_{NL,i} = \varepsilon_0 \sum_{jk} \chi_{ijk}^{(2)} E_j E_k \quad (6.12)$$

Here we only consider up to second order non linearity. We can rewrite this equation for analytical fields, in the spectral domain. Looking only at the relevant polarisation for the signal field we get:

$$\nabla^2 \mathbf{E}_s^{(+)}(\mathbf{r}, \omega) + \frac{\omega^2}{c^2} (1 + \chi^{(1)}(\omega)) \mathbf{E}_s^{(+)}(\mathbf{r}, \omega) = -\frac{\omega^2}{\varepsilon_0 c^2} \mathbf{P}_{NL}^{(+)}(\mathbf{r}, \omega) \quad (6.13)$$

where index s refers to the polarisation of the signal field. Under the paraxial approximation, the field can be described with transverse envelope whose longitudinal variation are slow compared to the carrier phase $\left| \frac{\partial^2 a}{\partial z^2} \right| \ll \left| k \frac{\partial a}{\partial z} \right|$:

$$\mathbf{E}_s^{(+)}(\mathbf{r}, \omega) = a_s(\mathbf{r}, \omega) e^{ik(\omega)z} \quad (6.14)$$

and assuming that the spatial profile remains unaffected, the propagation equation for the signal field envelope constrained to the z axis is given by:

$$\frac{\partial a_s(z, \omega)}{\partial z} = \frac{i\omega}{2\varepsilon_0 c n(\omega)} \mathbf{P}_{NL}^{(+)}(z, \omega) e^{-ik(\omega)z} \quad (6.15)$$

where we used the dispersion relation $k^2(\omega) = n(\omega)^2 \omega^2 / c^2$ and $n(\omega)^2 = 1 + \chi^{(1)}(\omega)$.

For SFG, the second order non-linear polarisation is given by:

$$\mathbf{P}_{NL}^{(+)}(z, \omega) = \varepsilon_0 \chi^{(2)} \int_{\mathbb{R}} \frac{d\omega'}{\sqrt{2\pi}} \mathbf{E}_p^{(+)}(z, \omega') \mathbf{E}_p^{(+)}(z, \omega - \omega') \quad (6.16)$$

where the input pump¹ field is $\mathbf{E}_p^{(+)}$. We will also describe the pump field under the paraxial approximation with its envelope²:

$$\mathbf{E}_p^{(+)}(z, \omega) = \mathcal{E}_p u_p(z, \omega) e^{ik_p(\omega)z} \quad (6.17)$$

Injecting equations (6.14) and (6.16) into (6.15) yields the propagation equation for the envelope of the signal:

$$\frac{\partial a_s(z, \omega)}{\partial z} = \frac{i\omega \chi^{(2)}}{2n_s(\omega)c} \mathcal{E}_p^2 \int_{\mathbb{R}} \frac{d\omega'}{\sqrt{2\pi}} u_p(z, \omega') u_p(z, \omega - \omega') e^{i\Delta k(\omega, \omega')z} \quad (6.18)$$

where we introduced the wave vector mismatch along the propagation axis:

$$\Delta k(\omega, \omega') = k_p(\omega') + k_p(\omega - \omega') - k_s(\omega) \quad (6.19)$$

¹Note in this section we refer to the input beam at 800 nm as the pump and the generated SHG beam at 400 nm as the signal. Next when we will look at PDC the roles will be inverted

²Note here, unlike in Eq. (6.14), we introduced the constant \mathcal{E}_p so that $u_p(z, \omega)$ is unitless.

If we assume the pump is undepleted¹ we may neglect the longitudinal variations of u_p and integrate Eq. (6.18) over the length of the crystal l_c to get the output signal envelope:

$$a_s(\omega) = \frac{i\omega\chi^{(2)}l_c}{2n_s c} \mathcal{E}_p^2 \int_{\mathbb{R}} \frac{d\omega'}{\sqrt{2\pi}} u_p(\omega') u_p(\omega - \omega') \Phi(\omega, \omega') \quad (6.20)$$

Where $\Phi(\omega, \omega') = \text{sinc}(\frac{\Delta k(\omega, \omega')l_c}{2})$ is the phase matching function. In the following the frequency dependence of the pre-factor will be neglected and it will be evaluated at the signal central frequency $2\omega_0$. We will write: $\chi = \frac{2\omega_0 d_{\text{eff}} l_c}{n_s c} = \frac{4\pi d_{\text{eff}} l_c}{n_s \lambda_0}$, where $d_{\text{eff}} = \frac{\chi^{(2)}}{2}$ is the effective non-linear coefficient.

Eq. (6.20) can be simplified even further if we neglect second order dispersion in the crystal, in which case:

$$\Delta k(\Omega) \approx (2k_p^{(0)} - k_s^{(0)}) + \Omega(k_p^{(1)} - k_s^{(1)}) \quad \text{with} \quad \Omega = \omega - 2\omega_0 \quad (6.21)$$

With $k_p^{(0)} := k_p(\omega_0)$, $k_s^{(0)} := k_s(2\omega_0)$, $k_p^{(1)} := \left(\frac{\partial k_p}{\partial \omega}\right)_{\omega=\omega_0}$ and $k_s^{(1)} := \left(\frac{\partial k_s}{\partial \omega}\right)_{\omega=2\omega_0}$. We assume that phase matching is verified for the central pump and signal frequencies ω_0 and $2\omega_0$ so that the 0th order term is null. Δk does not depend on $\Omega' = \omega' - \omega_0$ and may be taken out of the integral, so the signal becomes:

$$a_s(\Omega) = i \frac{\chi \mathcal{E}_p^2}{\sqrt{2\pi}} \Phi(\Omega) (u_p \otimes u_p)(\Omega) \quad (6.22)$$

The signal is simply the auto-convolution of the pump field multiplied by Φ which will act as a filter function. For short crystal, the phase matching function is broader and the signal bandwidth will be limited by the pump bandwidth while for long crystal Φ will be the limiting factor.

The first order approximation is not sufficient to properly model the SHG when the input spectrum is broad enough and/or the crystal is long enough. We can go one step further and Taylor expand the phase mismatch to second order:

$$\Delta k(\Omega, \Omega') = \Omega(k_p^{(1)} - k_s^{(1)}) + \frac{\Omega^2}{2}(k_p^{(2)} - k_s^{(2)}) + \Omega'^2 k_p^{(2)} - \Omega\Omega' k_p^{(2)} \quad (6.23)$$

Fig. 6.1 illustrates how the first term of the integral (Eq. (6.20)) limits the bandwidth of the signal. Fig. 6.2 shows the exact and first order approximation phase matching function.

In our experiment the input spectrum has a 9.8 nm FWHM (in intensity) and we use a 300 μm BiBO crystal, it is a good compromise to get good signal power and bandwidth. In these conditions the first order approximation is sufficient to calculate the output signal field (see Fig. 6.3). The numerical calculation give a 2.44 nm FWHM output, the measured experimental width is around 2.8 nm. This discrepancy could be due to walk-off effects in the crystal: walk-off reduces the effective length over which the signal and pump overlap which can result in a broader spectrum (shorter effective crystal length).

¹This approximation will be valid for sufficiently thin crystals.

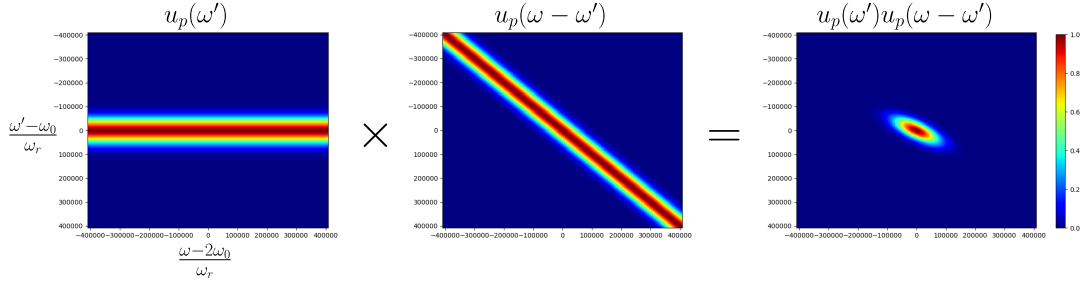


Fig. 6.1 Illustration of how the term $u_p(\omega')u_p(\omega - \omega')$ in Eq. (6.20) limits the bandwidth of the SHG beam.

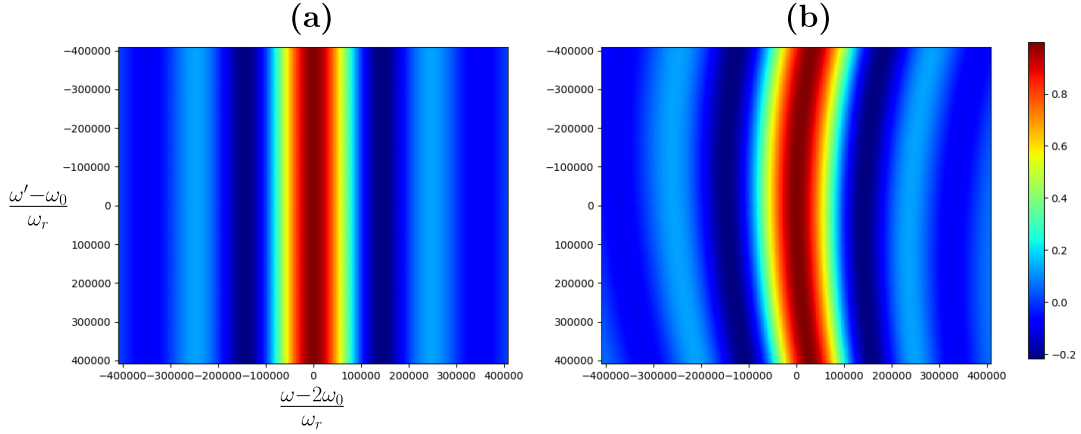


Fig. 6.2 First order approximation (a) and exact form (b) of the phase matching function $\Phi(\omega, \omega')$.

The SHG power at the crystal output is given by (see appendix A.5):

$$\mathcal{P}_{\text{SHG}} = 2n_s c \varepsilon_0 f_r \int_{\mathbb{R}} dt \int_{\mathbb{R}^2} d^2 \rho \left| \mathbf{E}_s^{(+)}(\rho, t) \right|^2 \quad (6.24)$$

$$= 2n_s c \varepsilon_0 f_r S_s \int_{\mathbb{R}} d\omega |a_s(\omega)|^2 \quad (6.25)$$

$$= \underbrace{2n_s c \varepsilon_0 f_r \chi^2 \mathcal{E}_p^4}_{g} \frac{1}{2\pi} \int_{\mathbb{R}} d\omega \left| \int_{\mathbb{R}} d\omega' u_p(\omega') u_p(\omega - \omega') \Phi(\omega, \omega') \right|^2_{\mathcal{I}} \quad (6.26)$$

Where S_s is the effective transverse area of the signal beam and we used Parseval's identity to replace the time integral by a frequency one. The integral term \mathcal{I} can be calculated numerically and the pre-factor can be expanded in terms of the input beam's power \mathcal{P}_p , effective area S_p , and repetition rate f_r using $\mathcal{E}_p = \sqrt{\frac{\mathcal{P}_p}{2n_p c \varepsilon_0 f_r S_p}}$:

$$g = \frac{n_s c \varepsilon_0 S_s f_r}{\pi} \chi^2 \mathcal{E}_p^4 \quad (6.27)$$

$$= 4\pi \frac{S_s}{S_p} \frac{\mathcal{P}_p^2 d_{\text{eff}}^2 l_c^2}{n_s n_p^2 c \varepsilon_0 \lambda_0^2 f_r S_p} \quad (6.28)$$

For Gaussian beams of waist w the effective area is $S = \frac{\pi w^2}{2}$. The waist of the signal beam will just be $w_s = \frac{w_p}{\sqrt{2}}$, so that $\frac{S_s}{S_p} = 1/2$. Note this is consistent with the signal field being

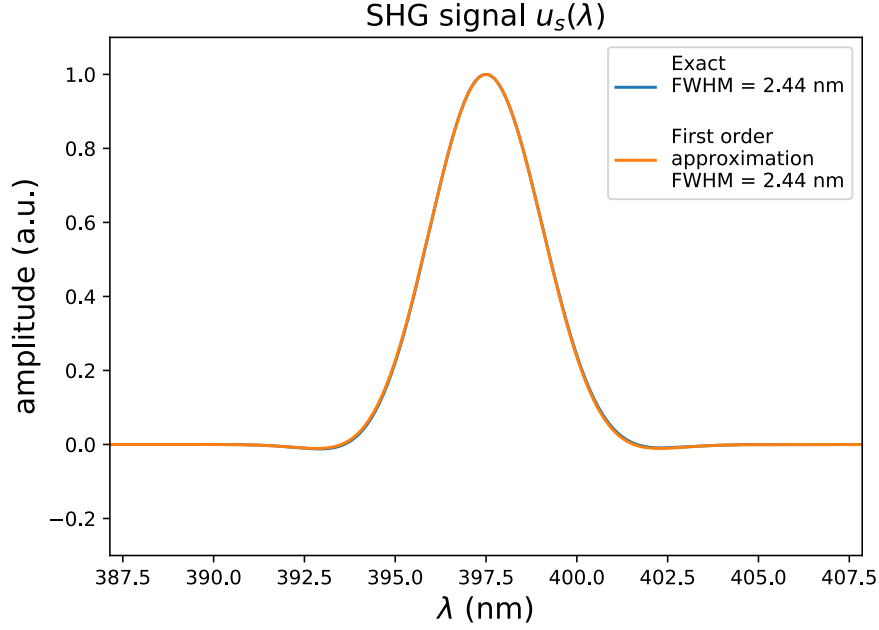


Fig. 6.3 Signal generated by second-harmonic generation for a $300\ \mu\text{m}$ BiBO crystal and a pump centred at $795\ \text{nm}$ with a $9.8\ \text{nm}$ FWHM. The first order approximation gives the same result as the exact treatment. The FWHM are given in intensity and correspond to the width of a Gaussian fit.

quadratic in the pump field, it also corresponds to matching the pump and signal beam Rayleigh ranges. Since there is perfect phase matching for the central frequencies we have $n_s = n_p = n$, so the SHG efficiency reads¹:

$$\eta_{\text{SHG}} := \frac{\mathcal{P}_{\text{SHG}}}{\mathcal{P}_p} = 2\pi \frac{\mathcal{P}_p d_{\text{eff}}^2 l_c^2}{n^3 c \varepsilon_0 \lambda_0^2 f_r S_p} \mathcal{I} \quad (6.29)$$

In Fig. 6.4 we show the SHG power and efficiency calculated for different pump values.

6.3 Parametric down conversion

We now describe parametric down conversion (PDC). It is the non-linear effect we use to produce multimode entangled states. The pump we use for this process is produced using SHG as described in the previous section. PDC can be seen as the converse of SHG, instead of two input field interacting to produce an output field at higher frequencies, we now have one input field that is converted into two output fields at lower frequencies. For PDC, the second order non-linear polarisation is given by

$$\mathbf{P}_{\text{NL}}^{(+)}(z, \omega) = \varepsilon_0 \chi^{(2)} \int_{-\infty}^{+\infty} \mathbf{E}_p^{(+)}(z, \omega + \omega') \mathbf{E}_s^{(-)}(z, \omega') \frac{d\omega'}{\sqrt{2\pi}} \quad (6.30)$$

¹Even though the pump bandwidth/pulse duration does not appear explicitly in this expression, it does affect the value of \mathcal{I}

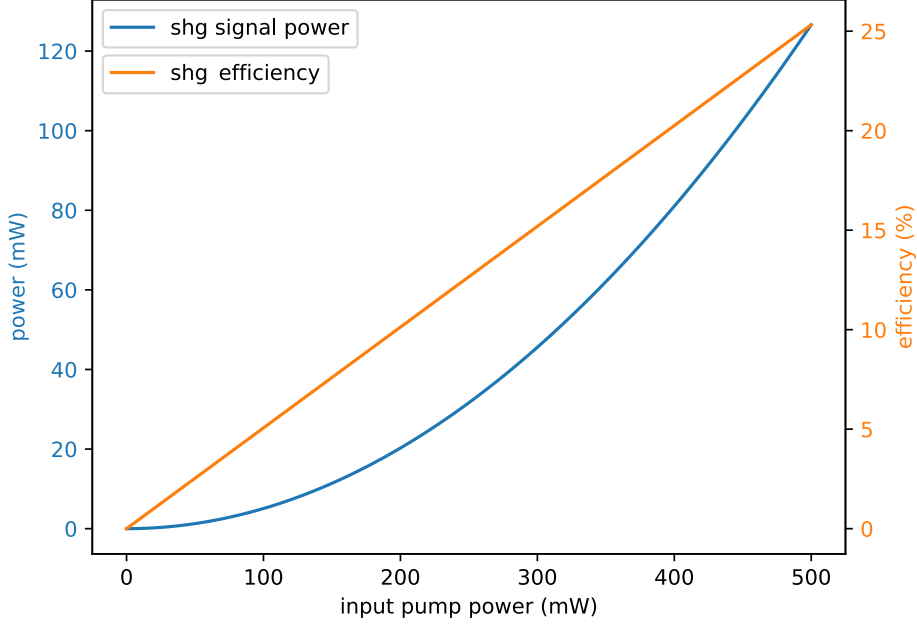


Fig. 6.4 SHG conversion efficiency for a 300 μm BiBO crystal and a 20 μm waist input pump field with a $f_r = 76$ MHz repetition rate, $\lambda_0 = 795$ nm central wavelength and 9.8 nm FWHM.

where $E_p^{(+)}$ is the pump¹ field and $E_s^{(+)}$ is the generated signal field.

Injecting equations (6.14) and (6.30) into (6.15) yields the propagation equation for the envelope of the signal:

$$\frac{\partial a_s(z, \omega)}{\partial z} = i \frac{\omega \chi^{(2)}}{2n_s c} \mathcal{E}_p \int_{\mathbb{R}} \frac{d\omega'}{\sqrt{2\pi}} u_p(z, \omega + \omega') a_s^*(z, \omega') e^{i\Delta k(\omega, \omega')z} \quad (6.31)$$

where we used Eq. (6.17) to define the pump envelope u_p and we have introduced the wave vector mismatch along the propagation axis

$$\Delta k(\omega, \omega') = k_p(\omega + \omega') - k_s(\omega') - k_s(\omega) \quad (6.32)$$

6.3.1 Classical treatment for real signal envelopes

Let us first consider a real signal envelope, we can rewrite Eq. (6.31) as

$$\frac{\partial a_s(z, \omega)}{\partial z} = \mathcal{K}(z) a_s(z, \omega) \quad (6.33)$$

Where $\mathcal{K}(z)$ is an integral transform with kernel $K(z, \omega, \omega')$ acting on envelopes $a(z, \omega)$ as:

$$\mathcal{K}(z) a(z, \omega) := \int_{\mathbb{R}} d\omega' K(z, \omega, \omega') a(z, \omega') \quad (6.34)$$

$$\text{with } K(z, \omega, \omega') = i \frac{\omega \chi^{(2)}}{2\sqrt{2\pi} n_s c} \mathcal{E}_p u_p(z, \omega + \omega') e^{i\Delta k(\omega, \omega')z} \quad (6.35)$$

¹Note that by “pump” we now refer to the 400 nm light.

Using a Magnus expansion [158] Eq.(6.34) may be formally integrated into:

$$a_s^{\text{out}}(\omega) = \exp\left(\sum_{k=0}^{\infty} \mathcal{S}_k\right) a_s^{\text{in}}(\omega) \quad (6.36)$$

$$\text{where } \mathcal{S}_0 = \int_{z_{\text{in}}}^{z_{\text{out}}} dz \mathcal{K}(z) \quad (6.37)$$

$$\mathcal{S}_1 = \frac{1}{2} \int_{z_{\text{in}}}^{z_{\text{out}}} dz \int_{z_{\text{in}}}^z dz' [\mathcal{K}(z), \mathcal{K}(z')] \quad (6.38)$$

$$\mathcal{S}_2 = \frac{1}{6} \int_{z_{\text{in}}}^{z_{\text{out}}} dz \int_{z_{\text{in}}}^z dz' \int_{z_{\text{in}}}^{z'} dz'' \left([\mathcal{K}(z), [\mathcal{K}(z'), \mathcal{K}(z'')]] \right. \quad (6.39)$$

$$\left. + [\mathcal{K}(z''), [\mathcal{K}(z'), \mathcal{K}(z)]] \right) \quad (6.40)$$

$$\dots \quad (6.41)$$

In the weak pumping limit we may just keep the first term of the expansion so that:

$$a_s^{\text{out}}(\omega) = \underbrace{e^{\mathcal{S}_0}}_{\mathcal{G}} a_s^{\text{in}}(\omega) \quad (6.42)$$

If we neglect the pump depletion and assume it's homogeneous along the crystal we may evaluate the z integral over the phase factor (as we did with Eq. (6.20)). We will also evaluate the pre-factor at the central frequency ω_0 so the kernel of \mathcal{S}_0 becomes:

$$S_0(\omega, \omega') = ig \underbrace{u_p(\omega + \omega') \Phi(\omega, \omega')}_{L(\omega, \omega')} \quad \text{with} \quad g = \frac{\omega_0 \chi^{(2)} l_c}{2n_s c} \frac{\mathcal{E}_p}{\sqrt{2\pi}} \quad (6.43)$$

where as in section 6.2 the phase matching function is given by:

$$\Phi(\omega, \omega') = \text{sinc}\left(\frac{\Delta k(\omega, \omega') l_c}{2}\right) \quad (6.44)$$

In order for the envelope $a_s(\omega)$ to stay real (as we required) we need the pump to be purely imaginary: $E_p^{(+)}(\omega) = i\mathcal{E}_p u_p(\omega)$. In other words the pump needs to be in quadrature with the signal. In that case $L(\omega, \omega')$ is real and it is also symmetric by definition (see Eq. (6.32) and (6.43)), so it can be diagonalised¹ in an orthogonal basis of real eigenvectors:

$$L(\omega, \omega') = \sum_k \Lambda_k s^{(k)}(\omega) s^{(k)}(\omega') \quad (6.45)$$

We can write this relation without explicitly writing the kernel of \mathcal{L} with the notation: $\mathcal{L} = \sum_k \Lambda_k |s^{(k)}\rangle \langle s^{(k)}|$. It follows immediately that the $|s^{(k)}\rangle$ are also eigenvectors of \mathcal{G} :

$$\mathcal{G} |s^{(k)}\rangle = e^{r_k} |s^{(k)}\rangle \quad \text{with} \quad r_k = g\Lambda_k \quad (6.46)$$

The envelope functions $s^{(k)}(\omega)$ are called the supermodes, they correspond to spectral shape that remain the same when propagating in the crystal. They are amplified or de-amplified by a factor $e^{\pm r_k}$ depending on the pump phase.

¹Other hypotheses are necessary since the space is infinite dimensional but we will assume it's valid.

Given a phase matching function and a pump spectral shape, we can diagonalise $L(\omega, \omega')$ numerically to find the supermodes. To do so we discretise the frequency range, replace the integral operator \mathcal{L} with a matrix and the envelope functions $a(\omega)$ with vectors. The eigen-decomposition of Eq. 6.45 can be written:

$$\mathbf{L} = \mathbf{V}\mathbf{\Lambda}\mathbf{V}^T \quad (6.47)$$

Where $\mathbf{\Lambda}$ is a diagonal matrix containing the eigen-values¹ and \mathbf{V} is orthogonal and contains the eigen-vectors as columns.

6.3.2 Complex signal envelope and quantum treatment

In the general case where we keep a complex signal envelope, Eq. (6.31) couples $a_s(z, \omega)$ and its conjugate $a_s^*(z, \omega)$, we may write them as a 2 component vector:

$$\mathbf{a}_s(z, \omega) = \begin{pmatrix} a_s(z, \omega) \\ a_s^*(z, \omega) \end{pmatrix} \quad (6.48)$$

which allows to rewrite equation (6.33) as a matrix linear differential equation:

$$\frac{\partial \mathbf{a}_s(z, \omega)}{\partial z} = \mathcal{K}(z)\mathbf{a}_s(z, \omega) \quad \text{with} \quad \mathcal{K}(z) = \begin{pmatrix} 0 & \mathcal{K}(z) \\ \mathcal{K}(z)^* & 0 \end{pmatrix} \quad (6.49)$$

The Magnus expansion from Eq. (6.36) is still valid if we replace $\mathcal{K}(z)$ by it's matrix operator version $\mathcal{K}(z)$ and we again keep the first term only:

$$\mathbf{a}_s^{\text{out}}(\omega) = \mathcal{G}\mathbf{a}_s^{\text{in}}(\omega) \quad (6.50)$$

where:

$$\mathcal{G} = \exp \begin{pmatrix} 0 & \mathcal{S}_0 \\ \mathcal{S}_0^* & 0 \end{pmatrix} \quad (6.51)$$

The quantum description is simply obtained by replacing the envelope functions by the quantum field operators $\hat{a}(\omega)$.

Again we will discretise the frequency and work with a discrete set of operators:

$$\hat{\mathbf{a}} := (\dots, \hat{a}_k, \dots)^T \quad \text{with} \quad \hat{a}_k := \hat{a}(\omega_k) \quad (6.52)$$

As in Eq. (6.47) the linear integral operators \mathcal{G} and \mathcal{S}_0 become (infinite) matrices that we write with bold straight notation: \mathbf{G} , \mathbf{S}_0 . In the case where the pump has a flat spectral phase: $E_p^{(+)}(\omega) = \underbrace{\mathcal{E}_p e^{i\phi_p}}_{\in \mathbb{R}} u_p(\omega)$, we can take out the phase term out of \mathbf{S}_0 and write:

$$\mathbf{G} = \exp \begin{pmatrix} 0 & e^{i(\phi_p + \pi/2)} \mathbf{S}_0 \\ e^{-i(\phi_p + \pi/2)} \mathbf{S}_0 & 0 \end{pmatrix} \quad (6.53)$$

$$= \begin{pmatrix} \cosh(\mathbf{S}_0) & e^{i(\phi_p + \pi/2)} \sinh(\mathbf{S}_0) \\ e^{-i(\phi_p + \pi/2)} \sinh(\mathbf{S}_0) & \cosh(\mathbf{S}_0) \end{pmatrix} \quad (6.54)$$

¹Note that when we discretise the frequency, we need to scale the eigen-values by the discretisation step for consistency: $\Lambda^{\text{cont}} \rightarrow \Lambda^{\text{discr}} \delta\omega$

So that given the spectral decomposition of \mathbf{L} (6.47), \mathbf{G} can be decomposed as:

$$\mathbf{G} = \mathbf{G}_1 \oplus \mathbf{G}_2 \oplus \dots \quad (6.55)$$

Where each \mathbf{G}_n acts on the subspace generated by $\begin{pmatrix} \hat{s}_n \\ \hat{s}_n^\dagger \end{pmatrix}$ with:

$$\mathbf{G}_n = \begin{pmatrix} \cosh(r_n) & \sinh(r_n) \\ \sinh(r_n) & \cosh(r_n) \end{pmatrix} \quad (6.56)$$

$$\text{and } \hat{\mathbf{s}} = \mathbf{U}_\phi \mathbf{V} \hat{\mathbf{a}} \quad \text{with} \quad \mathbf{U}_\phi = \begin{pmatrix} e^{i(\phi_p + \pi/2)/2} & 0 \\ 0 & e^{-i(\phi_p + \pi/2)/2} \end{pmatrix} \quad (6.57)$$

\mathbf{G}_n is the mode transformation of the single mode squeezing operator (see table A.1). So when expressed in the supermode basis (basis of the eigenvectors of \mathbf{L}), the transformation acts independently on each mode and corresponds to a simple squeezing operation. The supermodes quadrature are squeezed along \hat{p} (resp. \hat{q}) for positive (resp. negative) eigenvalues Λ_n :

$$\mathbf{W} \mathbf{G}_n \mathbf{W}^{-1} = \begin{pmatrix} e^{r_n} & 0 \\ 0 & e^{-r_n} \end{pmatrix} \quad (6.58)$$

The term \mathbf{U}_ϕ represents a global phase factor identical for all the supermodes, it shows that the squeezed supermodes are in quadrature with the pump.

The squeezing factor r_n is obtained with:

$$r_n = g\delta\omega\Lambda_k = \frac{2\pi d_{\text{eff}} l_c}{n\lambda_0} \sqrt{\frac{\mathcal{P}_0 f_r \tau}{nc\epsilon_0 A}} \gamma \Lambda_n \quad (6.59)$$

Where $\gamma = \frac{\delta\omega}{\omega_r}$ is the discretisation rate.

Thanks to the eigen-decomposition of \mathbf{L} we just did a Bloch-Messiah decomposition of \mathbf{G} .

Figure 6.5 shows the supermode calculated numerically for a Gaussian pump of 2.8 nm FWHM (intensity) centred at $\lambda_p = 397.5$ nm, with a 2 mm BIBO crystal. The supermode obtained do not depend on the sampling rate and frequency range as long as they are sufficient to sample the variation of $L(\omega, \omega')$ and cover its range. Fig 6.6(a) shows the squeezing value calculated for a 20 mW pump with a waist in the crystal of 38 μm .

6.3.3 Pump spectral phase effects

When the pump phase is not flat, \mathbf{L} is not real so it no longer has an eigenvalue decomposition. But we can use the Autonne-Takagi decomposition [159]:

$$\mathbf{L} = \mathbf{V} \mathbf{\Lambda} \mathbf{V}^T \quad (6.60)$$

where $\mathbf{\Lambda}$ is a real non negative diagonal matrix containing the singular values of \mathbf{L}^1 and \mathbf{V} is unitary. With this decomposition it follows that:

$$\mathbf{S}_0 \mathbf{S}_0^* = \mathbf{V} \mathbf{K}^2 \mathbf{V}^\dagger \quad \text{with} \quad \mathbf{K} = g\delta\omega \mathbf{\Lambda} \quad (6.61)$$

¹We will often refer to these as eigenvalues although strictly speaking this term should be reserved for diagonalisation.

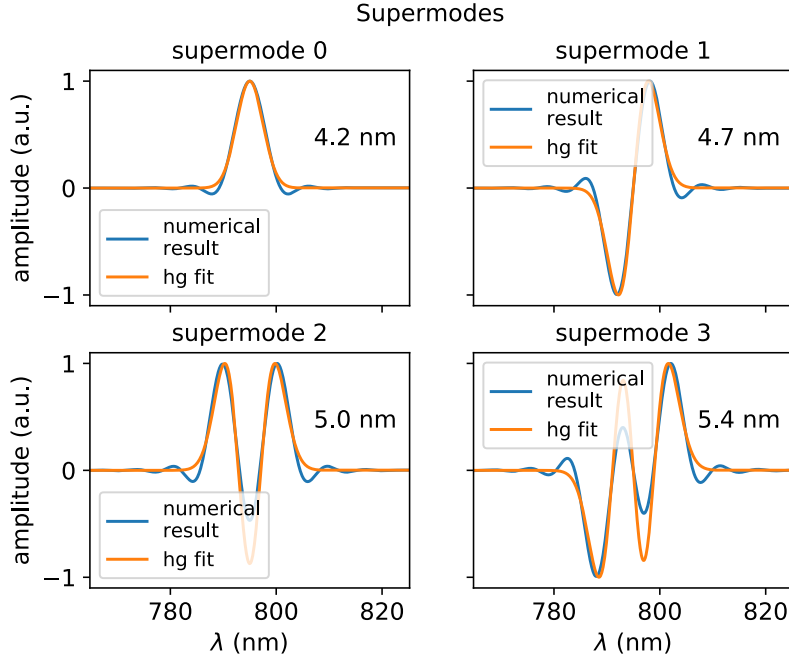


Fig. 6.5 Supermodes of the down conversion process for a Gaussian pump of 2.8 nm FWHM (intensity) centred at $\lambda_p = 397.5$ nm, with a 2 mm BIBO crystal. The FWHM of the Hermite-Gauss fits are indicated on each graph.

Evaluating the exponential in \mathbf{G} explicitly and using Eq. (6.61) we have:

$$\mathbf{G} = \begin{pmatrix} \mathbf{E} & \mathbf{F} \\ \mathbf{F}^* & \mathbf{E}^* \end{pmatrix} \quad (6.62)$$

$$\mathbf{E} = \mathbf{1} + \mathbf{S}_0 \mathbf{S}_0^* + \mathbf{S}_0 \mathbf{S}_0^* \mathbf{S}_0 \mathbf{S}_0^* + \dots \quad (6.63)$$

$$= \mathbf{V} \cosh(\mathbf{K}) \mathbf{V}^\dagger \quad (6.64)$$

$$\mathbf{F} = \mathbf{S}_0 + \mathbf{S}_0 \mathbf{S}_0^* \mathbf{S}_0 + \dots \quad (6.65)$$

$$= \mathbf{V} \sinh(\mathbf{K}) \mathbf{V}^T \quad (6.66)$$

So that again \mathbf{G} acts independently on the supermode as:

$$\mathbf{G}_n = \begin{pmatrix} \cosh(r_n) & \sinh(r_n) \\ \sinh(r_n) & \cosh(r_n) \end{pmatrix} \quad (6.67)$$

$$\hat{\mathbf{s}} = \mathbf{V} \hat{\mathbf{a}} \quad (6.68)$$

Again we just did a Bloch-Messiah decomposition of \mathbf{G} using the Takagi factorisation of \mathbf{L} . Now the squeezing parameters r_n are all positive and all the supermodes are \hat{p} squeezed. This results looks identical to the one of Eq. (6.56) but there is a significant difference. In Eq. (6.56), the matrix \mathbf{V} that defines the supermode basis is a real orthogonal matrix, and all the supermodes are real up to a common global phase factor. In Eq. (6.67) however, \mathbf{V} is now a unitary complex matrix, so a priori, each of the supermodes can have arbitrary phases relative to the pump. In other words, if we look at q and p quadratures defined with a fixed phase relative to the pump, in the first case the supermode were all either

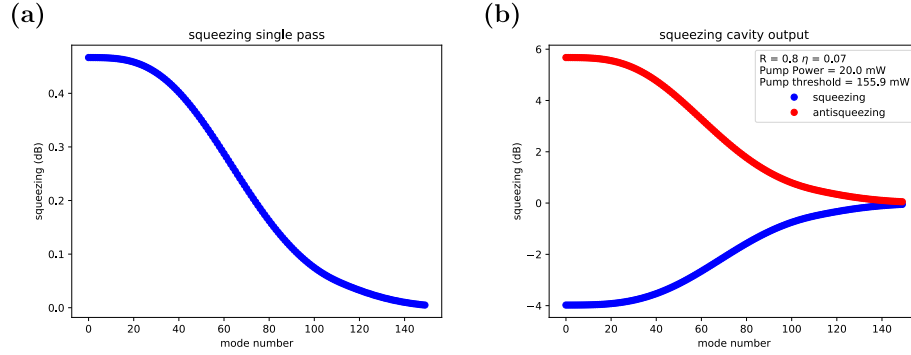


Fig. 6.6 (a) Single pass squeezing values. (b) SPOPO squeezing/antisqueezing values.

q or p squeezed while in the second each supermode can be squeezed along an arbitrary axis.

This method will allow us to calculate the supermodes and their squeezing parameters for general complex spectral shapes of the pump. As an example, Fig. 6.7 shows the result of this factorisation method for a pump with a quadratic phase (chirp) of 750 fs^2 . This changes significantly the shapes of the supermode but the squeezing level are not changed.

The Autonne-Takagi decomposition will be useful to calculate the SPOPO output when we shape the spectrum of the pump (see section 7.2).

6.4 SPOPO

In our experimental set-up, the non linear crystal we use for PDC is placed inside a cavity. This allows to amplify the non-linear effect and reach higher squeezing levels. In this section, we will first recall a few results obtained in [138, 160] that allow to describe the supermodes of the SPOPO when intra-cavity dispersion is neglected. We then try to extend the description to take into account the intra-cavity dispersion.

6.4.1 SPOPO without dispersion, input-output relations.

A thorough model for the SPOPO supermodes has already been developed. We won't reproduce this analysis here but give the main results. The SPOPO cavity is modelled with a single coupling mirror of reflectivity r for simplicity. This is justified as we will be interested in the output field when no seed field is coupled into the cavity and the input coupler reflectivity is high compared to the output coupler one. So it is sufficient to only consider the input vacuum field coupling into the output coupler (see chapter 4 for the details of our cavity). It can be shown [138] that the SPOPO acts as a symplectic transformation on the input field:

$$\begin{pmatrix} \hat{\mathbf{a}}^{\text{out}} \\ \hat{\mathbf{a}}^{\text{out}\dagger} \end{pmatrix} = \mathbf{R} \begin{pmatrix} \hat{\mathbf{a}}^{\text{in}} \\ \hat{\mathbf{a}}^{\text{in}\dagger} \end{pmatrix} \quad (6.69)$$

$$\mathbf{R} = \begin{pmatrix} \mathbf{E} & \mathbf{F} \\ \mathbf{F}^* & \mathbf{E}^* \end{pmatrix} \quad (6.70)$$

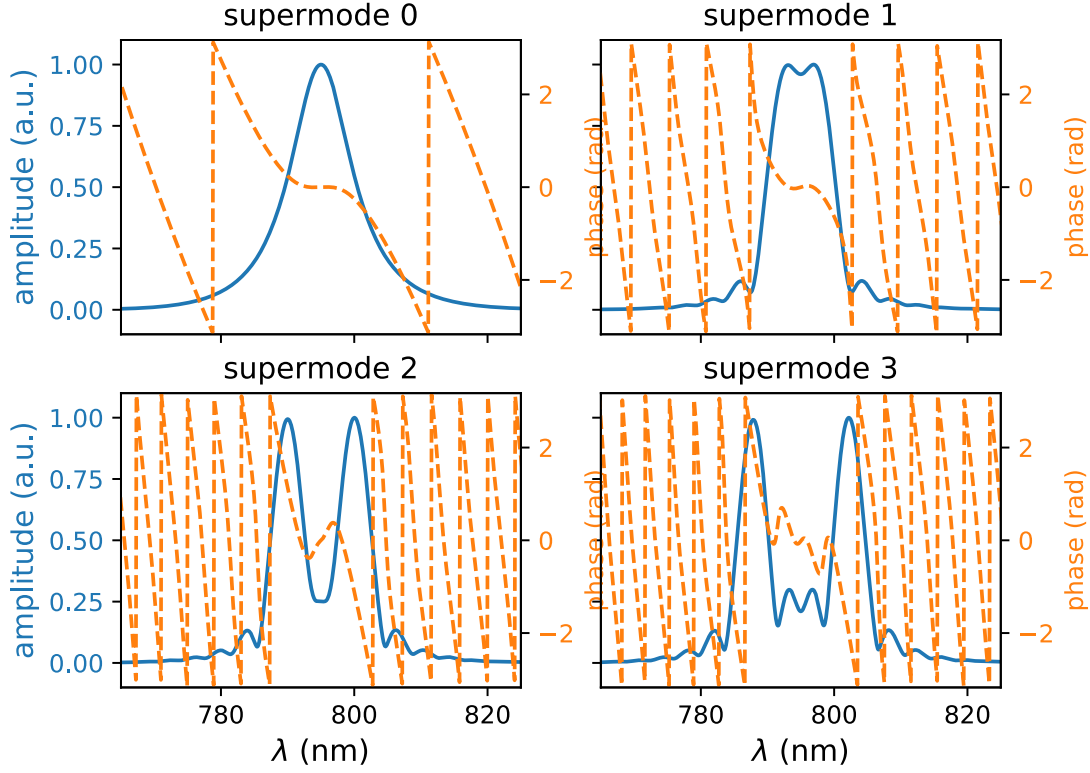


Fig. 6.7 First supermodes of the PDC process for a complex pump with a quadratic phase corresponding to a chirp of 750 fs^2 . All other parameters are identical to the simulation of section 6.3.2.

And \mathbf{R} is related to the cavity round-trip transformation \mathbf{T} by:

$$\mathbf{R} = (\mathbf{T} - r\mathbf{1})(\mathbf{1} - r\mathbf{T})^{-1} \quad (6.71)$$

The round trip transformation is also symplectic and can be decomposed into $\mathbf{T} = \mathbf{G}\mathbf{U}$. Where \mathbf{G} is defined as in section 6.3.2 and \mathbf{U} is the round-trip transformation without pump, it acts independently on each frequency component and can be described with a spectral phase Φ :

$$\mathbf{U} = \begin{pmatrix} e^{i\Phi} & 0 \\ 0 & e^{-i\Phi} \end{pmatrix} \quad (6.72)$$

Φ is diagonal and represents the phase accumulated per round-trip by each frequency component.

When the intra-cavity dispersion is neglected, Φ contains a constant and a linear component. In this case, when pumping synchronously with an optical frequency comb, \mathbf{U} and \mathbf{G} share a family of eigen-modes. Those modes are frequency-combs whose envelopes are given by the supermodes obtained for the single pass PDC in section 6.3.2. In the

supermode basis, the SPOPO transformation is then reduced to:

$$\mathbf{R} = \mathbf{R}_1 \oplus \mathbf{R}_2 \oplus \dots \quad (6.73)$$

$$\text{with } \mathbf{R}_n = \begin{pmatrix} C_n & S_n \\ S_n & C_n \end{pmatrix} \quad (6.74)$$

$$(6.75)$$

Where¹:

$$C_n = \frac{2r - (r^2 + 1) \cosh r_n}{-(1 + r^2) + 2r \cosh r_n} \quad (6.76)$$

$$S_n = \frac{(r^2 - 1) \sinh r_n}{-(1 + r^2) + 2r \cosh r_n} \quad (6.77)$$

$$(6.78)$$

This allows to estimate the squeezing levels of the supermodes from the single-pass gains r_n obtained in section 6.3.2. If we include the effect of intra-cavity round-trip losses η the squeezing/anti-squeezing level of supermode n are given by [150]:

$$\langle \hat{p}_n^2 \rangle = \frac{\eta(1 - r^2)e^{-2r_n} + (\sqrt{1 - \eta}e^{-r_n} - r)^2}{(1 - r\sqrt{1 - \eta}e^{-r_n})^2} \quad (6.79)$$

$$\langle \hat{q}_n^2 \rangle = \frac{\eta(1 - r^2)e^{2r_n} + (\sqrt{1 - \eta}e^{r_n} - r)^2}{(1 - r\sqrt{1 - \eta}e^{r_n})^2} \quad (6.80)$$

We show in Fig. 6.6(b) the calculated squeezing levels for a cavity with coupler reflectivity $r = 0.8$, and intra-cavity losses $\eta = 0.074$.

6.4.2 Simulation of intra-cavity dispersion

We now consider the problem of modelling intra-cavity dispersion effects on the supermodes of the SPOPO. Calculations based on the Edlén model [161] shows that dispersion due to air amounts to about 80 fs^2 per cavity round trip. The amount of dispersion from the crystal is about 330 fs^2 (for $l_c = 2 \text{ mm}$) and 150 fs^2 is compensated with chirped mirrors. So in our set-up the total intracavity round-trip dispersion is around 250 fs^2 . Although this may not seem like a lot, it is already enough to start to limit the bandwidth of the transmitted seed field as we saw in section 4.2.3. We are at the limits of tolerable dispersion. If we wanted more broadband supermode we would have to compensate more dispersion inside the cavity².

More importantly, high order supermodes have a large bandwidth and will be drastically filtered by dispersion. This means the squeezing curve in Fig 6.6 is not realistic, squeezing will drop much faster as higher order modes get increasingly filtered by the cavity.

¹Here we neglect the CEO effects for simplicity, see [138] for the full expressions.

²It is not straight forward to compensate dispersion inside the SPOPO cavity. Having a pulse compressor inside the cavity would introduce too much intra-cavity losses. Similarly dispersion compensation mirrors tend to be more lossy for larger compensation.

6.4.2.1 Naive approach

A somewhat naive approach to model the effects of intra-cavity dispersion is to follow the same approach we used in section 4.2.3 when analysing an input field transmission. In other words we first find the supermodes for a single pass process (no cavity), then we simulate the transmission of these modes through a filtering dispersive cavity. This approach is not strictly correct for reasons that we will detail in the next section, however it gives the right results for our dispersion regime.

6.4.2.2 Full treatment

The model of the previous section is not strictly correct because, the dispersion and non-linear gain effect inside the cavity happen conjointly and at every round-trip. In general, the phase effect described by \mathbf{U} and the gain effect described by \mathbf{G} do not commute. In which case the Bloch-Messiah decomposition of \mathbf{R} and \mathbf{T} do not correspond to the same supermodes. But we may still calculate \mathbf{R} numerically and perform a Bloch-Messiah decomposition. This is done in symplectic space, by first noting that:

$$\mathbf{WRW}^{-1} = (\mathbf{WTW}^{-1} - r\mathbf{1})(\mathbf{1} - r\mathbf{WTW}^{-1})^{-1} \quad (6.81)$$

Then calculating the inverse of $\mathbf{1} - r\mathbf{WTW}^{-1}$ by block using the Schur complement. The Bloch-Messiah decomposition of \mathbf{R} is then calculated using an algorithm based on the polar decomposition¹ (see [163] for example).

Fig. 6.8 shows the simulations of the SPOPO supermodes and squeezing levels using this technique for various dispersion values. Dispersion reduces the spectral width of the supermodes. It decreases the squeezing of high order supermodes.

Although the full-treatment give similar results to the naive approach, it would be interesting to study it further. In particular to find out case when the dispersion not only filters the supermodes bandwidth but also changes significantly the supermode shape and structure.

¹We use the bloch messiah decomposition from the strawberry field package of Xanadu [162]

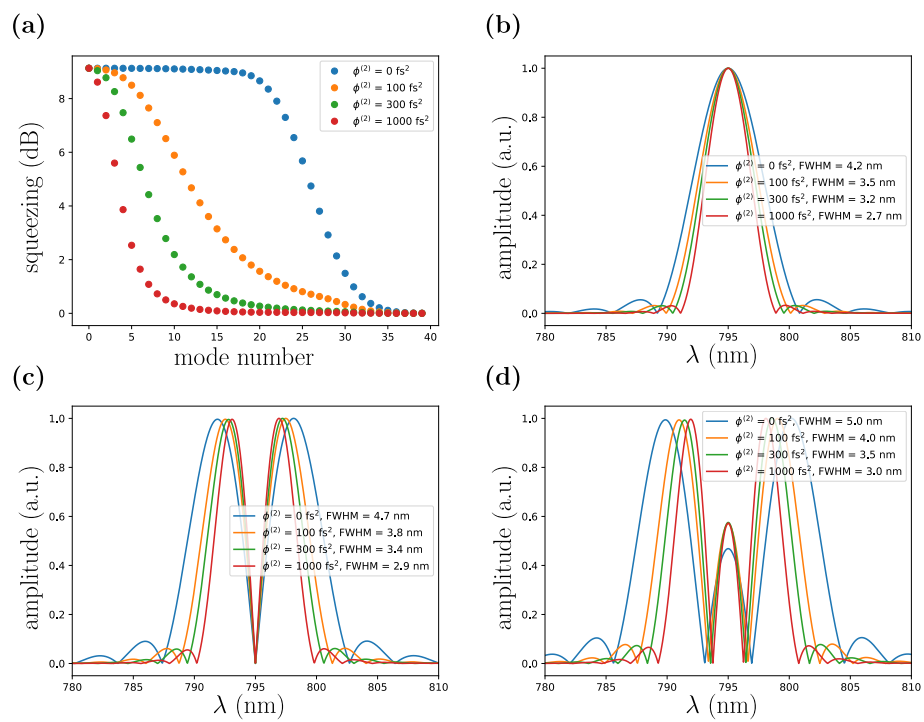


Fig. 6.8 SPOPO simulation with intra-cavity dispersion for $r = 0.8$. (a): squeezing levels. (b), (c) and (d): first supermodes (amplitude absolute value).

Part III

Pump-shape optimisation with machine-learning

Chapter 7

Numerical optimisation of the pump spectrum

Contents

7.1	Introduction to machine learning	100
7.1.1	Reinforcement learning with projective simulation	100
7.1.2	Supervised learning with neural networks	102
7.1.2.1	Generalities	102
7.1.2.2	Experiemental test: cavity auto-alignment	104
7.2	Pump spectral shape optimisation	105
7.2.1	Previous results	105
7.2.2	Simulation parameters and details	107
7.2.2.1	ANN parameters	109
7.2.2.2	PS parameters	109
7.3	Results	110
7.3.1	Maximising parametric gain	111
7.3.2	Maximising eigenvalue degeneracy	113

In this chapter we present the results of SPOPO pump optimisation using numerical simulations. We maximise certain desirable features of the SPOPO output state by tuning the spectral shape of the pump. The SPOPO output modes and squeezing levels are obtained by Autonne-Takagi decomposition of the joint spectral distribution as presented in section 6.3.3. Two different machine learning algorithms (MLA) are used for optimisation: an *artificial neural network* (ANN) algorithm and a *reinforcement learning* algorithm based on *projective simulation* (PS). This is a continuation of the work done by Francesco Arzani in [164], where the pump profile was optimised using an evolutionary algorithm.

Machine learning algorithms are not necessarily more effective than other standard optimisation algorithms for solving this particular problem. But they have already been proven efficient for the optimisation of experimental set-up [165]. They can automatically discover interesting features within the system to be optimised. This makes them promising for a future live optimisation of our set-up. Indeed, our experiment suffers from technical limitations that are hard to estimate and model, like the diffraction losses in the pulse shaper for example. A direct optimisation of the experimental set-up would then probably lead to different solutions than the ones obtained from simulation.

This chapter is divided in 3 sections: first we introduce the two algorithms we used and give an example of live optimisation of a simple experimental set-up with ANN. We then discuss the particular problem of pump shape optimisation. We recall previous results and give the details of our optimisation. Finally, we present the results for various cost functions and parameters.

7.1 Introduction to machine learning

In the 1950s and early 1960s, theoretical research on the concept of artificial intelligence and how to design it created the building blocks of machine learning as we know it today [166, 167]. Later, in the 90s, thanks to the improvement in processor hardware capabilities these algorithms could be implemented on practical tasks. Since then, they have known a huge success especially in tasks like image recognition [168], language processing [169] and game solving [170]. They now dominate the industry of internet and big data. The range of applications and different types of MLA is very large and a complete review of MLA is well outside the scope of this thesis. We will however, introduce the framework of the two algorithm we used. The first algorithm is a *reinforcement learning* algorithm based on *projective simulation* (PS), the second is a *deep learning* algorithm based on *artificial neural networks* (ANN). Both techniques have been shown to outperform humans on complex tasks [170, 171].

7.1.1 Reinforcement learning with projective simulation

In the reinforcement learning framework, the algorithm is described by an agent that learns through interaction with a dynamic rewarding (or punishing) environment (see Fig. 7.1). The agent's task is divided in steps, at each time-step the agent chooses randomly within a set of possible actions in order to maximise a cumulative reward. The action is chosen given the current (and possibly past) state of the environment and will influence the future state of the environment. Given the new state of the environment, a reward is produced that quantifies the quality and relevance of the previous action. The training is done by tuning the probabilities for the agent to choose a given action conditioned on a given state of the environment. The goal of the training is to reach an optimum between exploration of new actions that may lead to good rewards and exploitation of accumulated knowledge by repeating previously successful actions.

Reinforcement learning algorithms are generally described mathematically by a Markov decision process. There is a set of possible environment states or *percepts*, $s \in S$, a set of available *actions*, $a \in A$, and the decision making process of the agent at time step t is determined by a set of conditional probabilities $P^{(t)}(a|s)$. The reward $\lambda^{(t)}(s')$ is determined given the new state of the environment s' and is used to update the probabilities for the agent decision making.

Projective simulation [173, 174] (PS) is a type reinforcement learning algorithm that allows the agent to show some creative behaviour i.e. deal with unprecedented situation. It can relate a given situation to other conceivable ones and project itself into potential future situations. This is achieved with the introduction of an Episodic Compositional Memory (ECM). The ECM consists in a network of elementary patches called clips which represent remembered percepts and actions. The learning process consists in a stochastic walk in the ECM network. In the original algorithm the agent is allowed to reinvoke past

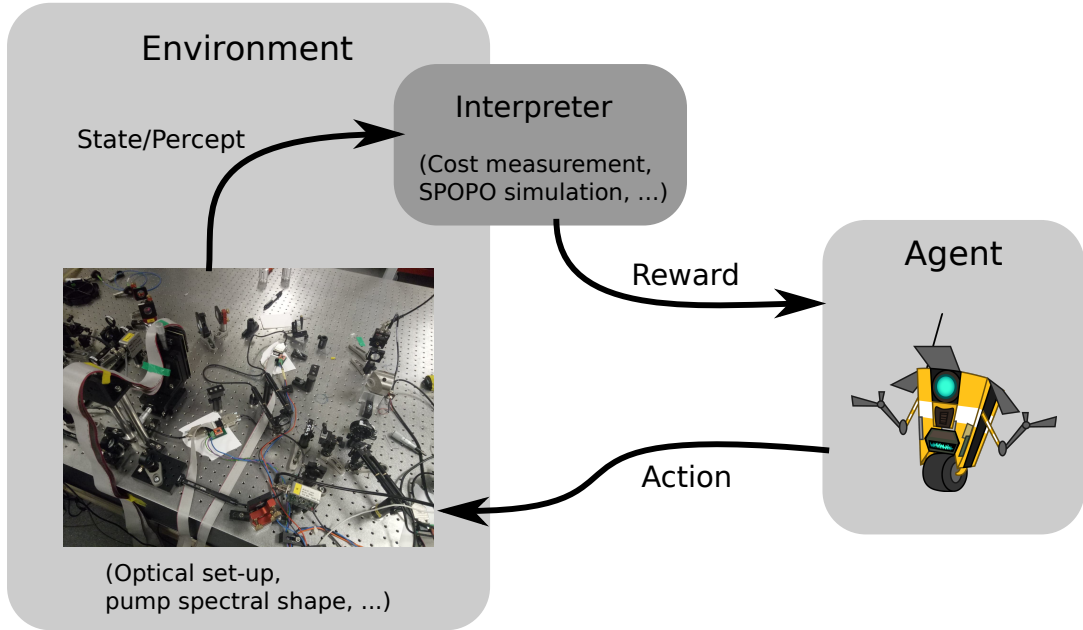


Fig. 7.1 Schematic view of a reinforcement learning algorithm. At each time step, the agent/actor performs an action, this action modifies the state of the environment, leading to a reward. (Image of the agent reproduced from [172])

experience before real action is taken but that feature will not be used in the present work.

We use an implementation of PS developed by Alexei Melnikov and Katja Ried [175] and later used for quantum optics experiments design [176]. Let N be the number of percepts (possible states of the environment) and M the number of actions, the probability $p_{ij}^{(t)}$ for taking action a_j ($j \in [1, M]$) given the current percept s_i ($i \in [1, N]$) is written as:

$$p_{ij}^{(t)} = \frac{h_{ij}^{(t)}}{\sum_{k=1}^M h_{ik}^{(t)}} \quad (7.1)$$

where \mathbf{h} is the weight matrix and is initialised to $\mathbf{h}^{(0)} = \mathbf{J}$. Where \mathbf{J} is the $N \times M$ matrix with every coefficient equal to 1. After each interaction with the environment the weight matrix is updated to:

$$\mathbf{h}^{(t+1)} = \mathbf{h}^{(t)} - \gamma(\mathbf{h}^{(t)} - \mathbf{J}) + \lambda^{(t)}\mathbf{g}^{(t+1)} \quad (7.2)$$

where γ is the damping parameter responsible for memory loss (decay towards uniform probability distribution), $\lambda^{(t)}$ is the reward set by the user depending on the new percept state and $\mathbf{g}^{(t)}$ is a matrix, called the *glow matrix*, that allows to reward recent successes more than old ones. \mathbf{g} is initialised to $\mathbf{0}$ and if edge (i, j) was traversed during the last decision making process, g_{ij} is set to one. \mathbf{g} decays to zero according to:

$$\mathbf{g}^{(t+1)} = (1 - \eta)\mathbf{g}^{(t)} \quad (7.3)$$

where η is the glow matrix damping parameter that control the dynamic of the decay. Note that \mathbf{g} allows for “long term” decision making as even if a single action does not lead

to an immediate reward ($\lambda^{(t_1)} = 0$), the corresponding edge $g_{ij}^{t_1}$ is still set to 1 so that if a reward is later awarded ($\lambda^{(t_2 > t_1)} > 0$), the corresponding edge (i, j) will still be modified in $\mathbf{h}^{(t_2)}$. This is necessary because in many optimisations, a given action may be useless in the short term, but necessary as a transition step in the long run .

The description of the algorithm we gave here is rather abstract and general. Indeed the code developed by Alexei Melnikov and Katja Ried is a general framework that can be applied to various optimisation problems. The details of our implementation will be discussed in section 7.2.2.

7.1.2 Supervised learning with neural networks

7.1.2.1 Generalities

The second ML algorithm we used is a deep learning algorithm, i.e. an algorithm based on artificial neural networks (ANN). These types of structures are inspired by biological neural networks in brains. A neuron has input connections to other neurons, the dendrites, from which it can receive stimuli in the form of an electro-chemical signal, and an output connection, the axon, from which it can stimulate another neuron¹. The neuron will “fire” if it’s stimulated above some threshold. The ANN mimics this architecture with a network of elementary blocks called *perceptrons* (or simply neurons) that are dispatched in layers and connected to one another (see Fig. 7.2). The first layer is connected to the inputs of the program, this input can take various forms, for example in the context of image recognition it could be the pixel RGB values. The last layer outputs the result of the computation, again this output can take various form, for example the estimated probability for an input image to contain a cat. The neural network is called deep when it contains multiple layers between the input and output layers. These are called the hidden layers.

The output is calculated sequentially, starting from the input layer, each neuron j outputs a number:

$$a_j = f \left(\sum_{i \in \text{inputs}} w_{ij} x_i + b_j \right) \quad (7.4)$$

Where the x_i are input signals (either the output of perceptrons in the previous layer, or direct input), w_{ij} are weights associated with each connections and b_j are biases (offsets) associated to each perceptron. The function f is a threshold-type function that introduces non-linearity in the system².

In supervised deep learning, one has access to a large number of inputs and corresponding objective outputs called the training set. The weights and biases are initialised to random values and are then modified until the output of the ANN is satisfactory for the training set, that is, it is sufficiently close to the objective output. This optimisation, called back-propagation, is done using another algorithm, usually some kind of gradient descent. The idea is that if the training set is sufficiently large, the ANN can be trained to approximate the mapping between the input and output space sufficiently closely, such that a yet unseen input, may also be mapped accurately. The art of training is subtle, one must be careful not to train the ANN too hard on the training set to prevent overfitting which would reduce the ANN performance outside the training set.

¹This is a major simplification of course, a real neural network is far more complex.

²This non-linearity is necessary for the network to achieve complex tasks

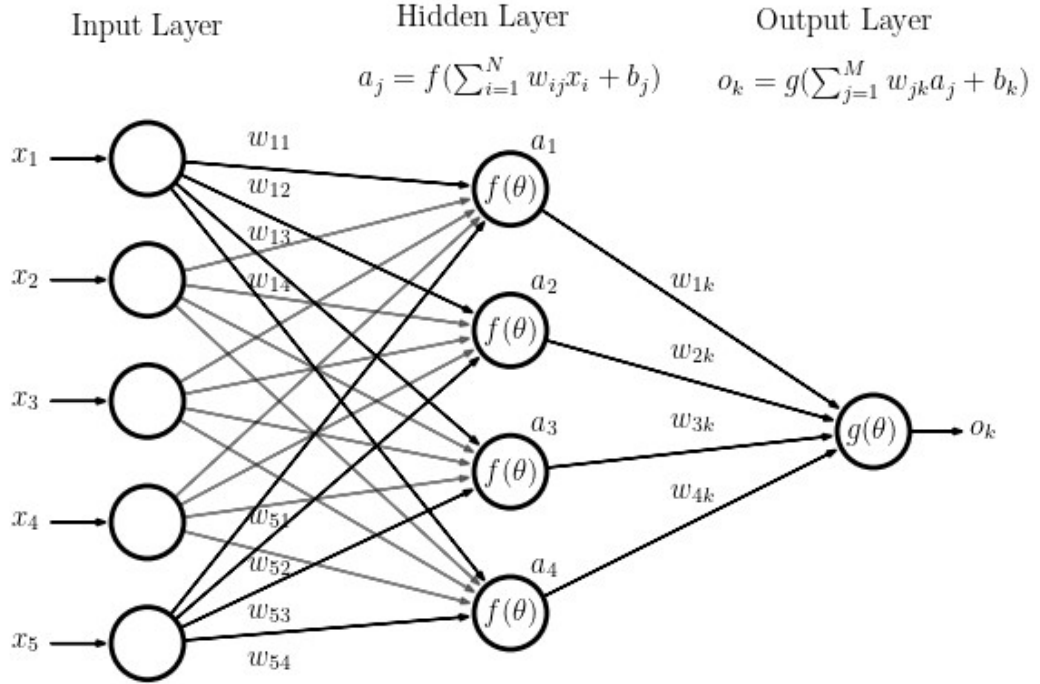


Fig. 7.2 Schematic overview of a deep artificial neural network

In our case, we are interested in the optimisation of some parameters of our experiment and are trying to optimise some cost function (level of squeezing of the first supermode for example). The goal of the ANN is to predict accurately the landscape of this cost function (dependence on the input parameter). Once the ANN is trained, it is very fast to evaluate an output. This allows us to find input parameters that minimise the cost by a minimisation algorithm.

The ANN algorithm we used was developed by Aaron D. Tranter and Harry J. Slatyer. It was used in [165] to successfully optimise the experimental parameters of a magneto-optical trap. We had no role in the development of this algorithm, our work was mainly to interface it with our problem and Aaron Tranter provided formidable help in doing so. The algorithm consists of a 5-hidden layer (densely connected) network with 64 neurons each. Gaussian error linear unit (GELU) is used as the activation function and back-propagation is done with the Adam optimisation algorithm [177] (extension of stochastic gradient descent).

A training set of parameters is generated randomly in a way that ensures the parameter space is uniformly sampled. Three separate ANNs are trained on this set. Each ANN is used to predict the input parameters that will minimise the cost function using the L-BFGS-B algorithm [178]. These new parameters are tested and added to the training set and the ANNs are trained again. This last step is repeated until the algorithm gets “stuck” in a local minima. When the algorithm sees no significant improvement in the cost and has been exploring the same region for a certain number of steps, it is randomly kicked into another region.

7.1.2.2 Experimental test: cavity auto-alignment

Before running it on the SPOPO pump optimisation, this algorithm was tested on a simple experimental set-up. It was a good occasion to get familiar with the interfacing of this machine learning code while working on a set-up with a reduced number of parameters.

The set-up (see Fig. 7.3) is made of a high finesse ring cavity to which a laser beam can be aligned with 6 parameters: the vertical and horizontal angle of two alignment mirrors (position/angle) and the longitudinal position of two lenses (mode matching). The laser is a Nd:YAG laser based on a Non-Planar Ring Oscillator (NPRO) cavity (model Prometheus [179]). It provides a low noise coherent light source (≈ 1 kHz linewidth) at 1064 nm. The mirror angle and lens position is tuned using DC servo motor actuators

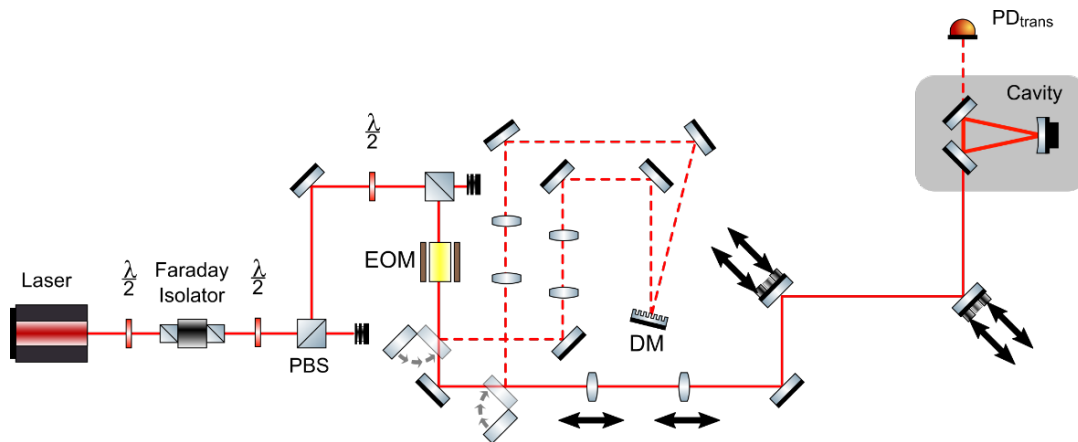


Fig. 7.3 Scheme of the cavity auto-alignment set-up. 4 actuators placed on the x and y axes of steering mirrors are used for beam alignment to the cavity. 2 actuators placed on translation stages allow to tune the longitudinal position of two lenses for cavity mode-matching. A deformable mirror (DM) can also be used to shape the beam's spatial phase.

(models Z812B and Z825B from thorlabs [180]). The motors contain a rotary encoder which allows us to determine the position of the actuator and control it with a feedback loop. We use a homebuilt motor driver circuit board using a TB6612FNG chip [181] and an FPGA (model NI-7813R from National Instrument [182]) to generate the driving signal and collect and analyse the encoder signals from the actuators.

The quality of the cavity alignment is determined from a cavity scan signal. A photodiode collects the transmitted beam from the cavity output as its length is scanned with a piezoelectric transducer. The cost function can be set to maximise the amplitude of a target peak using a peak detection code or more simply on the maximum of the whole trace.

The algorithm has to be started from a position where peaks are present in the cavity trace, so it cannot be used on a completely misaligned set-up. From there the algorithm will first sample the parameters randomly then converge towards an optimal alignment. Results of a typical optimisation are shown in Fig. 7.4. We empirically set the number of original training runs to 300. After those training runs, the algorithm starts testing parameters predicted from the ANNs, it gets to an optimal alignment after ~ 300 more runs. It then continues exploring the parameter space without noticeable improvement.

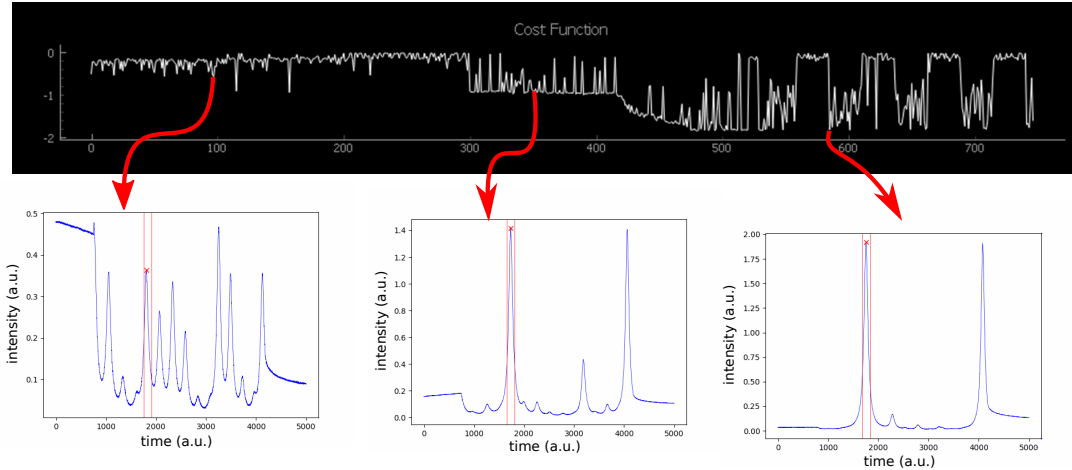


Fig. 7.4 *Result of optimisation of the actuator position. The graph in the first row shows the cost for each run and the second row shows the corresponding typical cavity scan traces. The cost function to minimise, is defined as minus the amplitude of a target cavity peak. The first 300 runs randomly sample the parameter space. The subsequent runs correspond to minima in the trained ANN landscape or exploration “kicks”.*

We then tried to optimise the transverse profile of the beam using a deformable mirror (DM) with the same algorithm. We used a Segmented Deformable Mirror model Multi-1.5-SLM from Boston Micromachine [183]. The SDM surface consists in 144 reflective pixels placed on MEMS (micro-electro-mechanical systems) covering a surface of $3.3 \times 3.3 \text{ cm}^2$. Each pixel can be individually addressed and displaced longitudinally, therefore changing the transverse phase of the reflected beam.

We tried a very naive way of implementing the optimisation by letting the algorithm directly control the 140 pixel positions (The 4 corner pixels are locked). Figure 7.5 shows the result of a typical run, with some configuration of the DM and the corresponding cavity scan traces. After the initial training phase the algorithm rapidly converged toward a position where almost all the pixels of the DM either at one or zero. This is a local minimum and is less preformant than a flat DM shape. But the corresponding trace is barely distinguishable from the one given by a flat DM. A more relevant approach would be to put larger shapes on the DM like superposition of Zernick polynomials and have the algorithm tune the coefficient of those polynomials.

7.2 Pump spectral shape optimisation

7.2.1 Previous results

Numerical optimisation of the pump spectral profile for various tasks has already been studied by Francesco Arzani in [184]. He used an evolutionary algorithm developed in [185]. In this section we recall his main results. The pump was optimised for two main tasks:

- Maximisation of the squeezing degeneracy among the first k supermodes¹. The

¹Ideal cluster states, which have applications in quantum computation and communication, can be

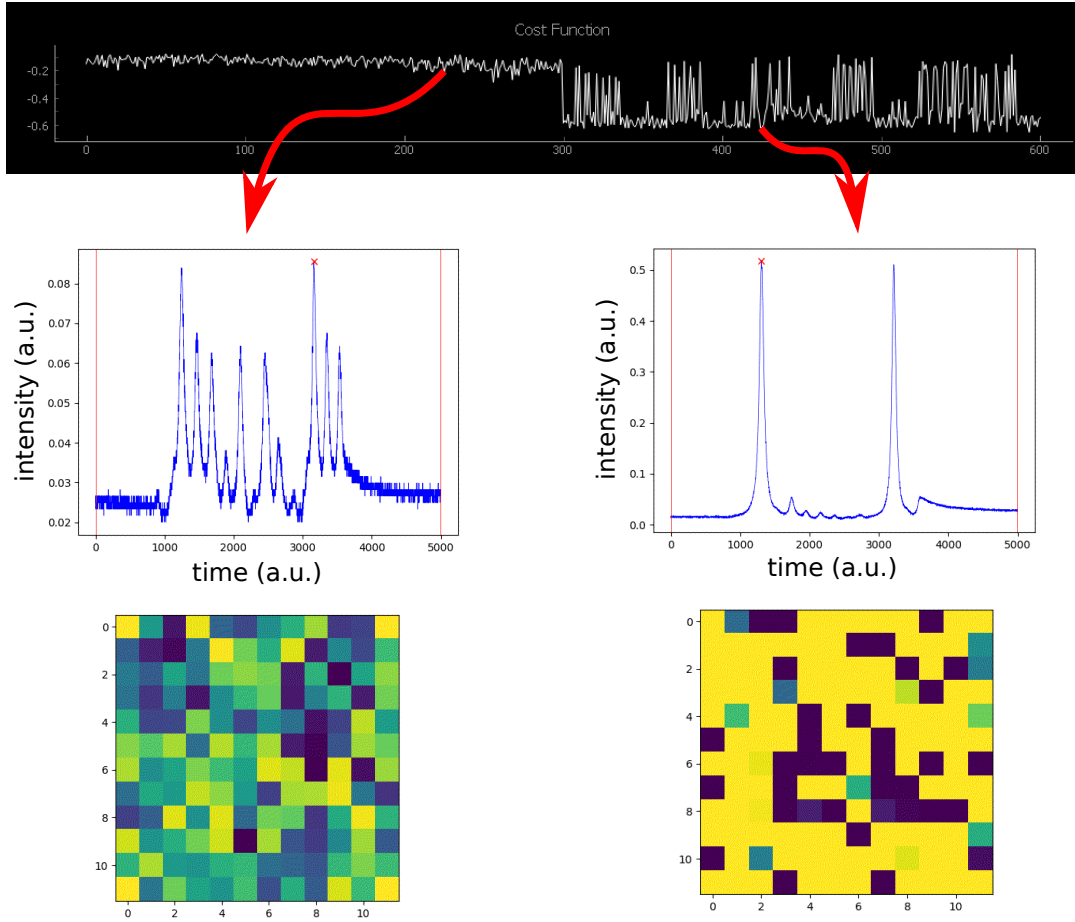


Fig. 7.5 Result of optimisation of the DM profile. The graph in the first row shows the cost for each run. The second and third rows show the corresponding typical cavity scan traces and DM profiles. The cost function to minimise, is defined as minus the maximum of the cavity scan trace. The first 300 runs randomly sample the parameter space. The subsequent runs correspond to minima in the trained ANN landscape or exploration “kicks”.

fitness function to maximise is:

$$f_1(\mathbf{u}) = \frac{1}{\Lambda_1(\mathbf{u})} \sum_{j=1}^{100} \Lambda_j \quad (7.5)$$

where \mathbf{u} represent the parameters of the pulse shaper and $\Lambda_j > 0$ are the singular values¹ of the joint spectral distribution (diagonal elements of $\mathbf{\Lambda}$ obtained by Eq. (6.60)). The supermode squeezing levels (in dB) are proportional to the $\Lambda_j > 0$. The fitness function is normalised by the singular values of the first supermode (the absolute value of squeezing can be adjusted in principle by changing the power of the pump).

well approximated experimentally if we have as many degenerate squeezed modes as possible

¹We also use the term eigenvalue although that is an abuse as the joint spectral distribution is not always diagonalisable.

- Maximisation of the squeezing of the first supermode relative to the others. The function to maximise is¹:

$$f_2(\mathbf{u}) = \frac{\Lambda_1(\mathbf{u})}{\Lambda_2(\mathbf{u})} \quad (7.6)$$

Note the values Λ_j are in decreasing order so maximising f_2 does amount to maximising squeezing of the first supermode relative to all the others.

Since the pulse shaper is a passive component, it can be difficult to implement experimentally pump shapes that differ significantly (in amplitude) from the initial Gaussian shape. Indeed, using solutions with little amplitude overlap with the original unshaped profile would mean throwing away a lot of the available power. That could be acceptable in theory if we're only interested in relative squeezing level. However in practice we want to be able to achieve an absolute experimental improvement of squeezing with pump shaping. For this reason, Francesco adapted the optimisation using constrained fitness functions:

$$\bar{f}_1 = f_1 - \frac{3}{(5w(\mathbf{u}))^6} \quad (7.7)$$

$$\bar{f}_2 = f_2 - \frac{1}{(5w(\mathbf{u}))^6} \quad (7.8)$$

Where $w(\mathbf{u})$ is the power ratio between the shaped and initial pump profile. Its multiplicative coefficient and exponent have been adjusted empirically.

Result of optimisation of \bar{f}_1 and \bar{f}_2 is shown in Fig. 7.6. The optimal pump profiles obtained this way ((c) and (d)) have complex variations and seem hard to implement experimentally. Indeed, the limited resolution of the pulse shaper, and the diffraction losses when implementing a shape with such small features would mean losing a lot of pump power. Ultimately the performance would be worse than with an unoptimised pump profile. Worse, the corresponding supermode spectral shapes in Fig. 7.6(b) are quite complex which makes them impossible to measure experimentally.

We therefore seek a simpler optimisation with a reduced number of pump parameters that constrain the pump to simpler shapes. There is also hope for simple desirable features to emerge in the pump. The idea behind the present work was to use an algorithm that could eventually be run directly on the experiment, therefore including all those detrimental effects in the optimisation without having to model them. Using a different optimisation algorithm is also a way to confirm the results obtained in [164] independently.

7.2.2 Simulation parameters and details

We now detail the parameters of our optimisation. For both algorithm, we consider a pump spectrum centred at 397.5 nm with a 3.54 nm FWHM (intensity), the simulation spans a frequency range of 9 nm corresponding to 6 standard deviation of the pump spectrum. This range is divided in $n = 4, 8, 16$ or 32 frequency bands. For each of these frequency bands (frexels) the pump is shaped by a factor $a_k e^{i\phi_k}$, $k \in [1, n]$. The phases ϕ_k and amplitudes a_k of the frexels are the parameter to be optimised. We ran 3 types of optimisation: using just amplitude shaping ($\phi_k = 0$), just phase shaping ($a_k = 1$), and both (full shaping).

¹Note the values Λ_j are in decreasing order

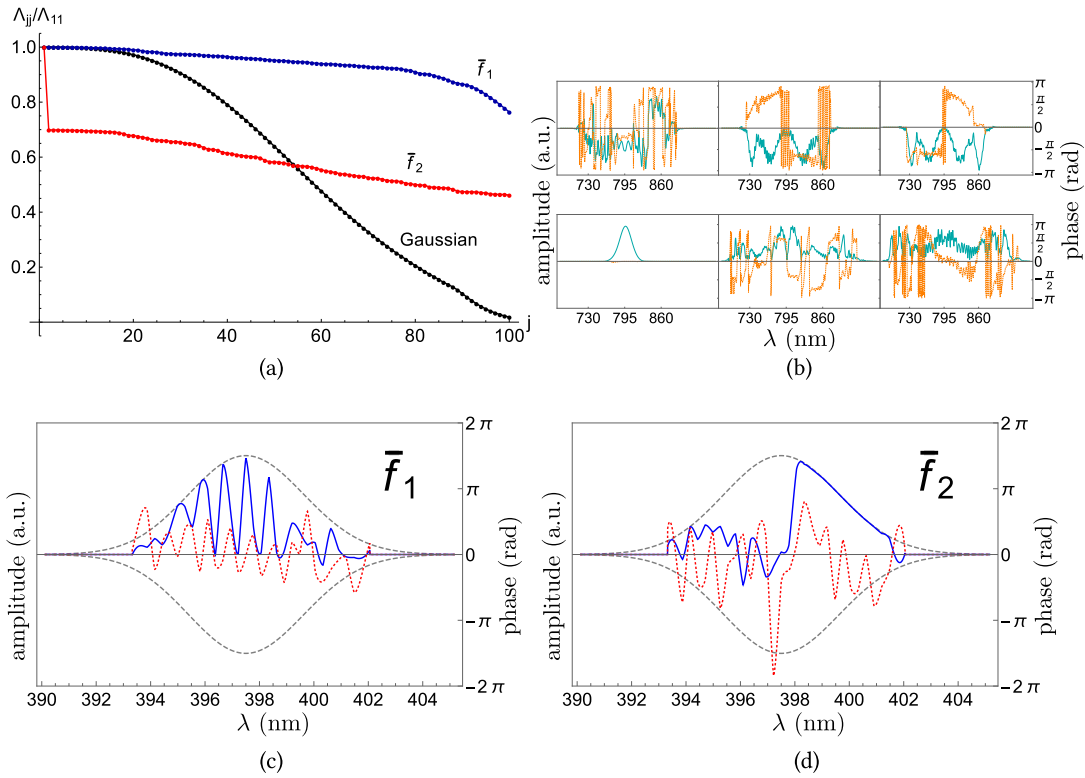


Fig. 7.6 Results of pump shaping optimisation from [164] for degenerate squeezing (\bar{f}_1) and maximum first to second mode squeezing ratio (\bar{f}_2). (a) Normalised gain distributions obtained for unshaped (Gaussian) profile and optimised profiles. (b) First supermodes resulting from the pump optimising \bar{f}_1 (top) and \bar{f}_2 (bottom). The solid blue line represents the amplitude, in arbitrary units, while the orange dashed line represents phase, in radians (scale on the right). (c) and (d) show the pump profiles maximising \bar{f}_1 and \bar{f}_2 , respectively. The gray dashed line shows the original Gaussian, the solid blue line shows the optimal amplitude profile, and the red dotted line shows the optimal phase.

For a given pump profile, we calculate the supermodes eigenvalues Λ_k using the Autonne-Takagi decomposition¹ as presented in section 6.3. From the eigenvalues we can evaluate the cost functions to be maximised. We ran the optimisation with two different fitness/cost functions:

- Optimising degenerate eigenvalues:

$$\bar{f}_1(\mathbf{u}) = \sum_{k=1}^{100} \frac{\Lambda_k}{\Lambda_1} - \frac{3}{(5w(\mathbf{u}))^6} \quad (7.9)$$

- Optimising the first eigenvalue:

$$\bar{f}_2(\mathbf{u}) = \Lambda_1 \quad (7.10)$$

¹For the optimisation we actually just use singular value decomposition (SVD) as it sufficient to get the eigenvalues and less computationally intensive. The Takagi decomposition is used when we want to recover the supermode spectral shapes.

This function differs from the one used by Francesco. We did not normalise it to Λ_2 so that the pump power penalty is already included in this cost.

7.2.2.1 ANN parameters

For the ANN algorithm, the amplitude and phase span a continuous range:

$$\forall k \in [1, n], \quad a_k \in (0, 1) \quad (7.11)$$

$$\phi_k \in (-\pi, \pi) \quad (7.12)$$

The ANN ensemble is trained to learn the landscape of the cost function $f(\mathbf{a}, \boldsymbol{\phi})$ exactly as in section 7.1.2.2:

- The cost is evaluated for a certain set of random parameters, the ANNs are trained to reproduce this landscape.
- A minimisation algorithm finds the optimal of the ANNs landscapes and these next parameters are tested experimentally.
- After appending these new parameters and cost to the training set, the ANNs are trained again.
- The last two steps are repeated a certain number of times until satisfactory solution is found or the algorithm is halted.

7.2.2.2 PS parameters

With the PS algorithm the amplitudes and phases span discrete values corresponding to a given dynamic range m :

$$\forall k \in [1, n], \quad a_k \in \left\{0, \frac{1}{m-1}, \dots, 1\right\} \quad (7.13)$$

$$\phi_k \in \left\{0, \frac{2\pi}{m-1}, \dots, 2\pi\right\} \quad (7.14)$$

The pump initial state corresponds to $a_k = 0.5$ and $\phi_k = 0$, $\forall k$, except when using only phase shaping, in which case $a_k = 1$ and $\phi_k = 0$, $\forall k$. Available actions for the agent are to raise the amplitude or phase value of a pump frexel by one increment. This increase is cyclic so that the amplitude or phase will be set to its minimum if it had reached its maximum value. The training consists in tuning the probabilities associated to the available actions of the agent. These actions correspond to transition between different possible states of the pump spectral shape (the environment) and can be represented as a network of clips as in Fig. 7.7.

The optimisation is divided into trials. Each trial consists of individual steps in which the agent chooses an action. If the action leads to a fitness function $\bar{f}_{1/2}$ that beats a certain threshold, the agent is rewarded (with $\lambda = 1$) and the trial ends. Otherwise ($\lambda = 0$) and the trial continues. There is a maximum number of steps for each trial, if it is reached, the trial ends regardless of the agent's success. At the beginning, the threshold is set to the first obtained value of the fitness function. When, the threshold has been beaten 5 times it is refreshed to the last obtained fitness function value. This is to ensure the agent doesn't get stuck repeating the same action forever. Note that even if the initial successes

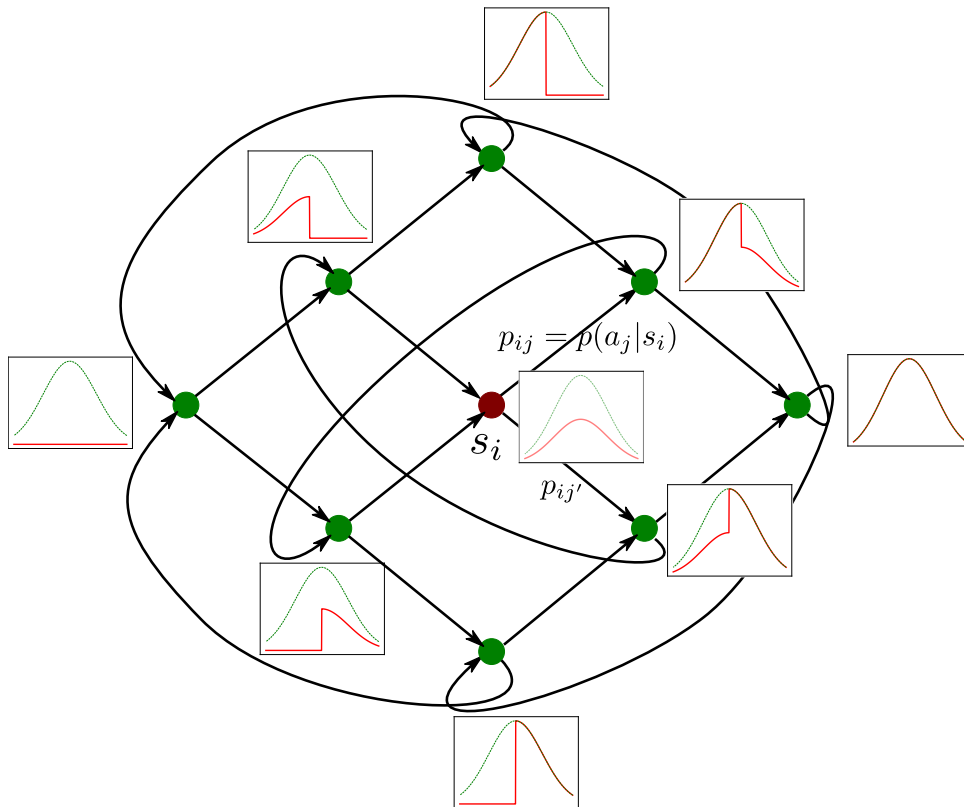


Fig. 7.7 Simple example of percept network for $n = 2$, $m = 3$, with amplitude shaping only. The agent starts at the red node. At each step it can go up (amplitude increase in the left frexel) or down (increase in the right frexel). The corresponding transition probabilities are initialised to $\frac{1}{2}$ and evolve according to Eqs. (7.2) and (7.3). The green curves show the unshaped pump profile.

of the agent are no longer rewarded after a while, the agent still keeps a “memory” of them thanks to the glow matrix \mathbf{g} (see section 7.1.1 for more details).

After each step the agent actions probabilities are updated with the \mathbf{h} matrix according to Eqs. (7.2) and (7.3). The damping factors are set to $\gamma = 0.01$ and $\eta = 0.4$. Further analysis would be required to find optimal values for these hyper-parameters. This is left for future work.

The total number of possible percepts is m^{2n} and the number of edges $2n \times m^{2n}$ (in the case of full shaping). The percept space gets huge even for a small number of frexels and dynamic range so it's out of the question to store and manipulate an \mathbf{h} matrix containing that many elements. Instead we just keep record of the already explored routes and new routes are added to \mathbf{h} when they are explored for the first time.

7.3 Results

We now present the results of the optimisation by the two algorithms. For the ANN algorithm we ran the optimisation with 4, 8, 16 and 32 pump frexels. For the PS algorithm, the dynamic range was set to $m = 5$. The bad scaling of percept space meant we could not

divide the pump any more than 16 frexels. This is sufficient for a first analysis because the spectral resolution of the pump shaper limits the number of frequency bands that can be shaped experimentally. In chapter 5, we found the pulse shaper complexity was around 40 so any simulation with 40 frexels or more is beyond what our pulse shaper can achieve. Moreover, in the experiment, detrimental effects, like power loss from diffraction, start appearing when we try to imprint more complex features in the pump. Finally, this small number of frexel was enough for interesting features to emerge from the optimisation. In some cases, we found the same optimal pump shape for $n = 8$ and $n = 16$. In the future, it would be interesting however to investigate optimisation keeping a small number of parameters but shaping the pump in a continuous way (polynomial functions for example). A first investigation in that direction was done with a cubic interpolation of the shaping profiles but it is not reported in this thesis.

To test out the algorithms we first run them with amplitude shaping only, then phase shaping only, then both. For both cost functions \bar{f}_1 and \bar{f}_2 , we find that phase shaping only is sufficient to achieve the optimum. Indeed, with full shaping, the algorithms converged towards no changes in the spectrum amplitude. This is understandable as any amplitude shaping will somehow “waste” some of the available input pump power.

7.3.1 Maximising parametric gain

In this section we show the results obtained for optimisation of fitness function \bar{f}_2 .

We first show the result corresponding to amplitude shaping only. Fig. 7.8 shows the optimal pump shapes found by the PS algorithm for various numbers of frexels. For $n = 4$ and $n = 8$, the number of percepts is reasonable (625 and 390625), so we were able to find and confirm the optimum by a brute force approach exploring all the possibilities (see Fig. 7.9). For $n = 4$ the algorithm converged to the best possible pump shape. For $n = 8$ it reached a shape that resembles the actual optimum found by brute force, but it would need more trials to converge. For $n = 16$, it is obvious the algorithm didn’t reach the optimum as the best cost obtained is less than for $n = 8$, but the obtained shape seems to share common features with the $n = 8$ optimum.

We confirmed these results with the second algorithm (ANN). Fig. 7.10 shows the obtained pump shapes for $n = 8, 16$ and 32 . The ANN algorithm was more efficient to deal with larger parameter spaces, it converged even for $n = 16$ and obtained the same shape as for $n = 8$. For $n = 32$ the algorithm didn’t converge but again it seems the optimal pump shape would share features with the $n = 16$ case or would even be identical.

Interestingly, the optimal pump shape for \bar{f}_2 with amplitude shaping are quite simple and symmetric, with amplitude values either at 1 or 0. For the PS algorithm, one could suspect this result is an artefact coming from a too small dynamic range ($m = 5$). This is not the case however because the ANN algorithm, which uses a continuous amplitude range, confirmed those shapes.

We then ran the same optimisation with phase shaping only. Fig. 7.11 shows the results for the PS algorithm with $n = 4$ and $n = 8$. In both cases the algorithm did converge to the optimum (as confirmed by the brute force approach of Fig. 7.9). This optimum is better than the one obtained with amplitude shaping only. Again, for $n = 8$, the optimal shapes obtained are quite simple with phases either at 0 or π (note there is a degeneracy here as $-\pi \equiv \pi$), so the optimal pump is real (with sign flips). For $n = 4$, it’s more complicated, and the optimal pump is complex.

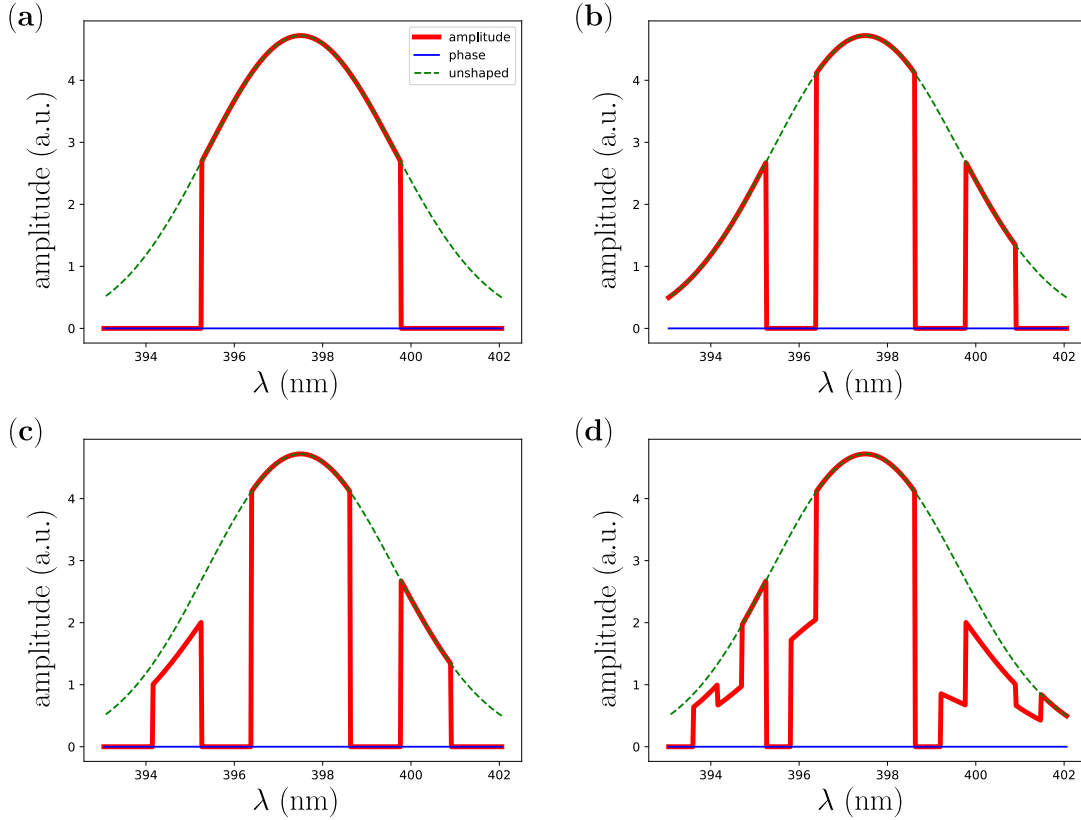


Fig. 7.8 Result of the pump amplitude shaping optimisation of \bar{f}_2 using the PS algorithm for various parameters.

(a) 4 frexels, 100 trials of 50 steps. 42 rewarded states, best is the 36th with $\bar{f}_2 = 35.39$.

(b) 8 frexels, 400 trials of 200 steps. 58 rewarded states, best is the 56th with $\bar{f}_2 = 39.89$.

(c) 8 frexels, 500 trials of 400 steps. 101 rewarded states, best is the 91st with $\bar{f}_2 = 39.88$.

(d) 16 frexels, 700 trials of 400 steps. 143 rewarded states, best is the 143rd with $\bar{f}_2 = 38.39$.

For full shaping the percept space is twice as large and the PS algorithm struggles to converge even for $n = 8$. However the ANN performs better (see Fig. 7.12). For $n = 8$, it converged to a pump profile with almost no amplitude shaping and a phase profile almost identical to the one obtained in Fig. 7.11. The value of \bar{f}_2 is also slightly smaller than what was obtained with phase shaping only. So it appears amplitude shaping is not necessary and the optimal value of \bar{f}_2 is achieved with phase shaping only (at least for $n = 8$).

All the results of this section on the optimisation of the first supermode eigenvalue (\bar{f}_2) are summarised in Table 7.1. In the following, we will refer to the optimal pump shape for maximising \bar{f}_2 using amplitude shaping only and $n = 8$ frexels as the $\bar{f}_2^{(a)}$ shape (Fig. 7.10 (a)). And we will refer to the optimal pump shape for maximising \bar{f}_2 using phase shaping and $n = 8$ frexels as the $\bar{f}_2^{(\phi)}$ shape (Fig. 7.11 (b)).

We now look, at the spectral shapes of the supermodes obtained with these pump

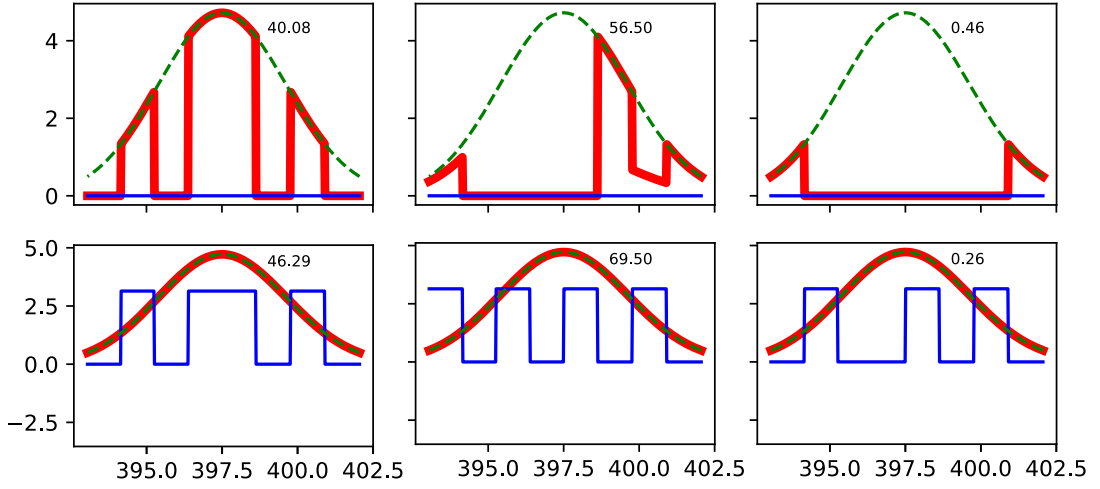


Fig. 7.9 Result of brute force pump shaping optimisation with amplitude (top row) and phase (bottom row) when maximising \bar{f}_2 (left column), \bar{f}_1 (middle column), and maximum squeezing measured in a frequency band basis (right column). The green dotted line is the unshaped pump profile, the red and blue lines are the shaped amplitude and phase respectively. The x-axis is wavelength in nm and the y-axis is arbitrary unit for amplitude and radian for phase.

Pump shaping type		Amplitude	Phase
\bar{f}_2 (see Eq. (7.10))	$n = 4$	35.39	39.97
	$n = 8$	40.08	46.29
	$n = 16$	40.08	N/A
Best pump profile	$n = 4$	$(0 \ 1 \ 1 \ 0)$	$(\pi \ -\pi/2 \ \pi \ -\pi/2)$
	$n = 8$	$(0 \ 1 \ 0 \ 1 \ 1 \ 0 \ 1 \ 0)$	$(0 \ \pi \ 0 \ \pi \ \pi \ 0 \ \pi \ 0)$
	$n = 16$	$(0 \ 0 \ 1 \ 1 \ 0 \ 0 \ 1 \ 1 \ 1 \ 1 \ 0 \ 0 \ 1 \ 1 \ 0 \ 0)$	N/A

Table 7.1 – Results of optimisation of \bar{f}_2 . For full shaping the best profiles match the phase shaping ones.

shapes. In Fig. 7.13 we show the supermodes corresponding to the $\bar{f}_2^{(\phi)}$ shape. The supermodes have similar shapes to the unshaped pump case but they are significantly broader. The relative simple spectral shapes of those supermodes compared to the one obtained in the previous results of Francesco (Fig. 7.6) is promising. Indeed, provided we have a local oscillator beam with a broad enough spectrum, we could measure those modes directly in our experiment. For the $\bar{f}_2^{(a)}$ shape, the supermodes are very similar (same shapes, similar widths) and we don't show them here.

7.3.2 Maximising eigenvalue degeneracy

We now look at the optimisation of fitness function \bar{f}_1 (defined in Eq. (7.9)). As in the previous section 7.3.1, the optimal pump shapes are achieved with phase shaping only. Fig. 7.14 shows the results of optimisation of \bar{f}_1 with the PS algorithm using phase shaping only (we also confirmed those results with the brute-force approach). Once again

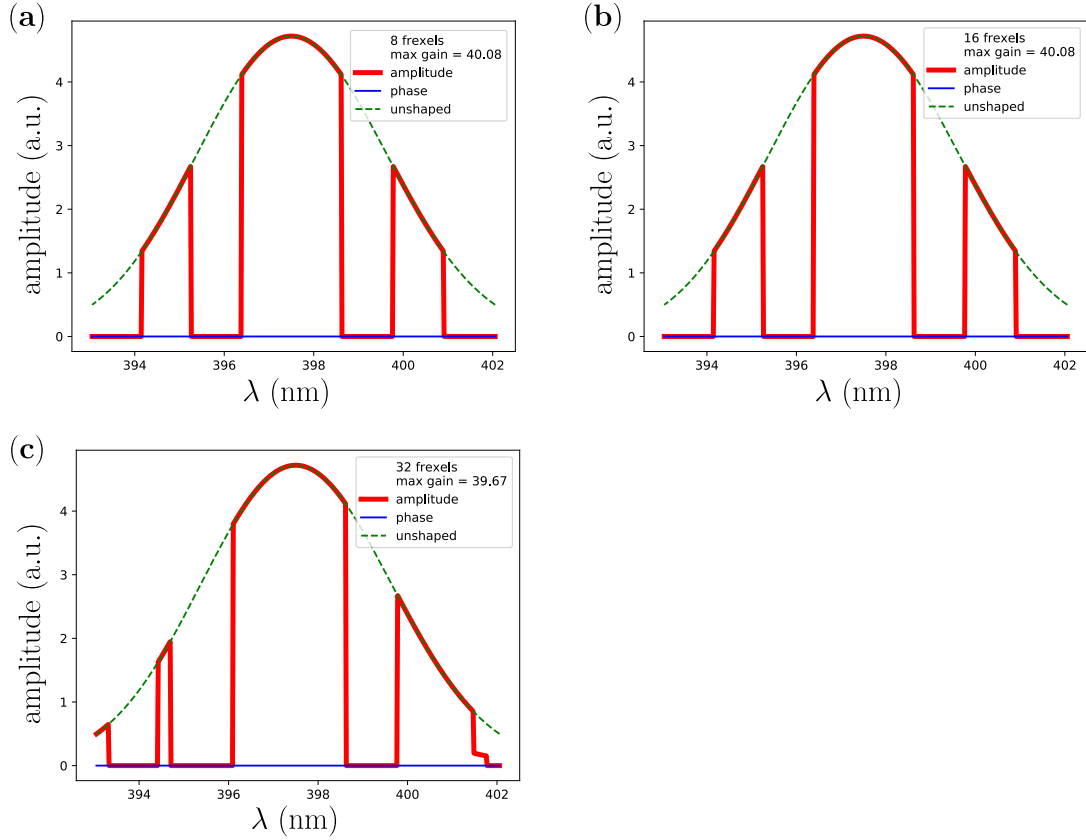


Fig. 7.10 Result of the pump amplitude shaping optimisation of \bar{f}_2 using the deep learning algorithm for various parameters.

(a) 8 frexels, 500 total runs, 300 training runs, best cost $\bar{f}_2 = 40.08$.

(b) 16 frexels, 600 total runs, 300 training runs, best cost $\bar{f}_2 = 40.08$.

(c) 32 frexels, 600 total runs, 300 training runs, best cost $\bar{f}_2 = 39.67$.

the optimal pump shapes have simple forms with frexel phase values of 0 or π . Results of the optimisation of \bar{f}_1 are summarised in Table 7.2. In the following, we will refer to the

Pump shaping type		Amplitude	Phase
\bar{f}_1 (see Eq. (7.9))	$n = 4$	49.38	48.20
	$n = 8$	56.50	69.50
Best pump profile	$n = 4$	$(1 \ 0.5 \ 0.25 \ 1)$	$(\pi \ -\pi/2 \ \pi \ -\pi/2)$
	$n = 8$	$(1 \ 0.25 \ 1 \ 0 \ 0 \ 0 \ 0 \ 0.75)$	$(0 \ \pi \ 0 \ \pi \ 0 \ \pi \ 0 \ \pi)$

Table 7.2 – Results of optimisation of \bar{f}_1 . For full shaping the best profiles match the phase shaping ones.

optimal pump shape for maximising \bar{f}_1 and $n = 8$ frexels as the $\bar{f}_1^{(\phi)}$ shape (Fig. 7.14 (a)).

The corresponding supermodes and gains are given in Fig. 7.15. There is important degeneracies in the eigenvalues which is not surprising since by optimising \bar{f}_1 , we are trying to get eigenvalues as degenerate as possible. The first 12 eigenvalues are degenerate

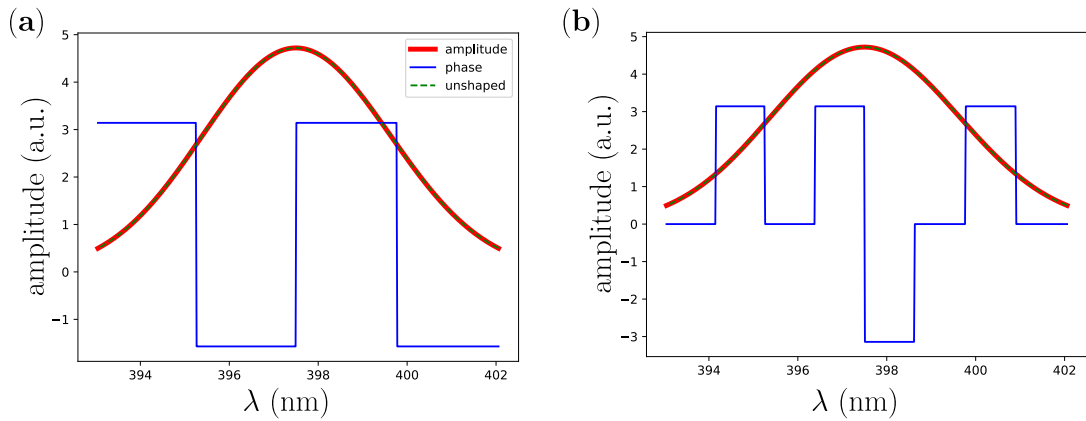


Fig. 7.11 Result of the pump phase shaping optimisation of \bar{f}_2 using the PS algorithm for various parameters.

(a) 4 frexels, 100 trials of 50 steps. 20 rewarded states, best is the 15th with $\bar{f}_2 = 39.97$.

(b) 8 frexels, 400 trials of 200 steps. 79 rewarded states, best is the 70th with $\bar{f}_2 = 46.29$

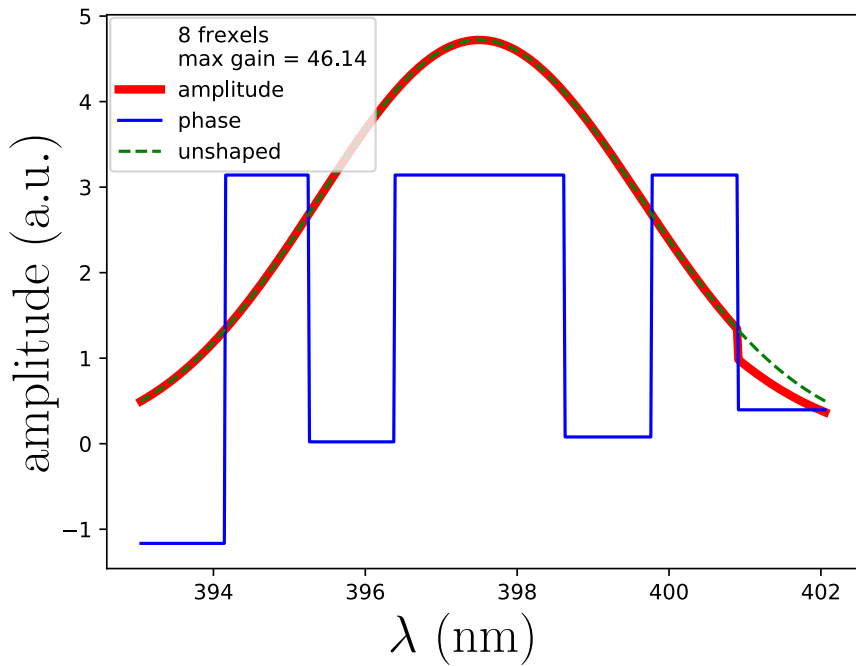


Fig. 7.12 Result of the full pump shaping optimisation of \bar{f}_2 using the ANN algorithm. 8 frexels, 700 total runs, 300 training runs, best cost $\bar{f}_2 = 46.14$.

by groups of 4. The supermodes have a very interesting structure with quite complex spectral shapes. They look very different from the one we obtained when optimising \bar{f}_2 . We can look at the first degenerate subspace in a different basis of mode to get a better understanding of the physical meaning of this SPOPO output. It is possible to find linear combination of the first 4 supermodes to find modes that have simpler spectral shape. These simpler modes are shown in Fig. 7.16. The corresponding basis change is given by

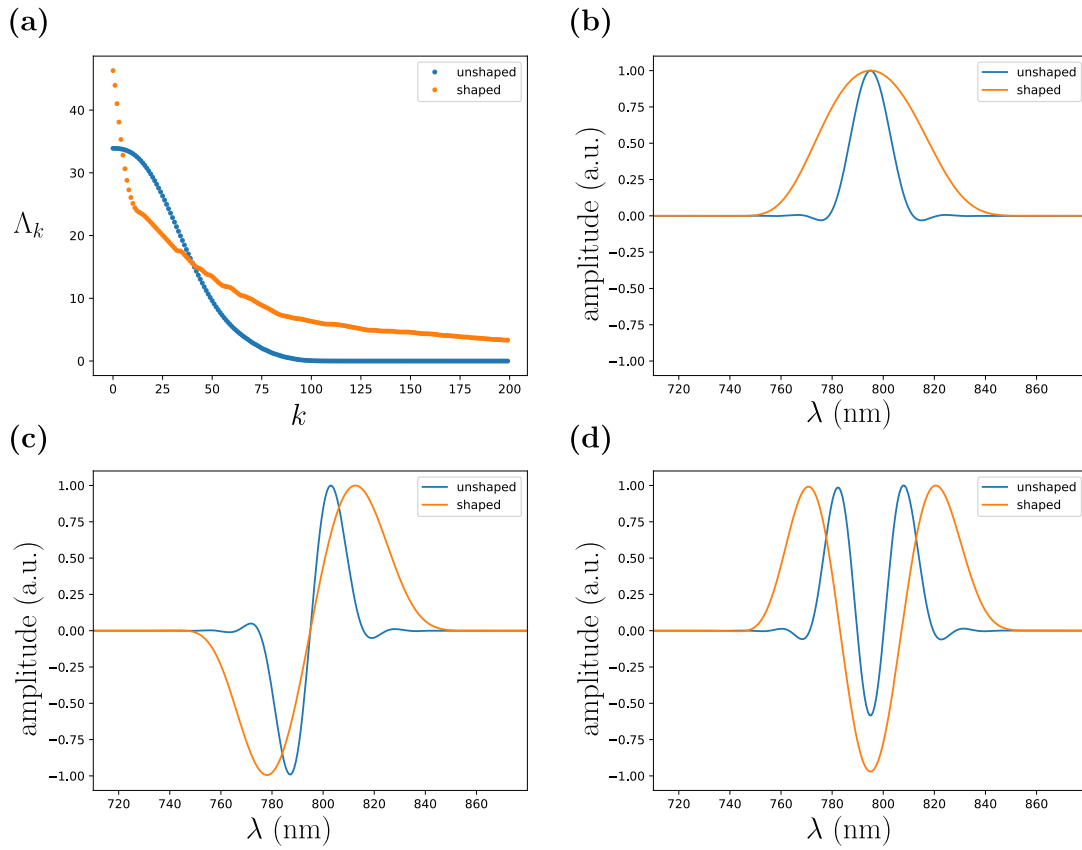


Fig. 7.13 (a) Gains of the Takagi decomposition for unshaped and optimal pump profile for maximising \bar{f}_2 . (b), (c) and (d) first 3 supermodes (they are real).

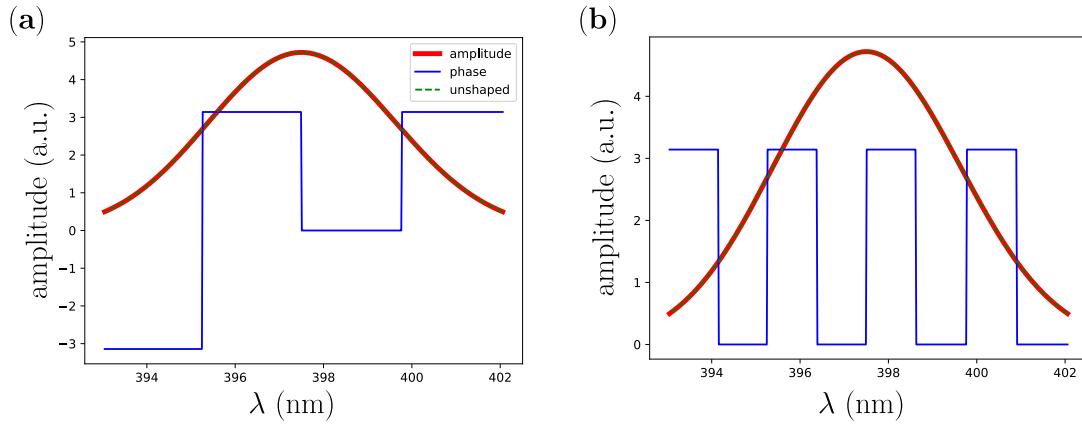


Fig. 7.14 Result of the pump phase shaping optimisation of \bar{f}_1 using the PS algorithm for various parameters.

(a) 4 frexels, 100 trials of 50 steps. 20 rewarded states, best is the 19th with $\bar{f}_1 = 48.20$.

(b) 8 frexels, 1000 trials of 200 steps. 81 rewarded states, best is the 77th with $\bar{f}_1 = 69.50$

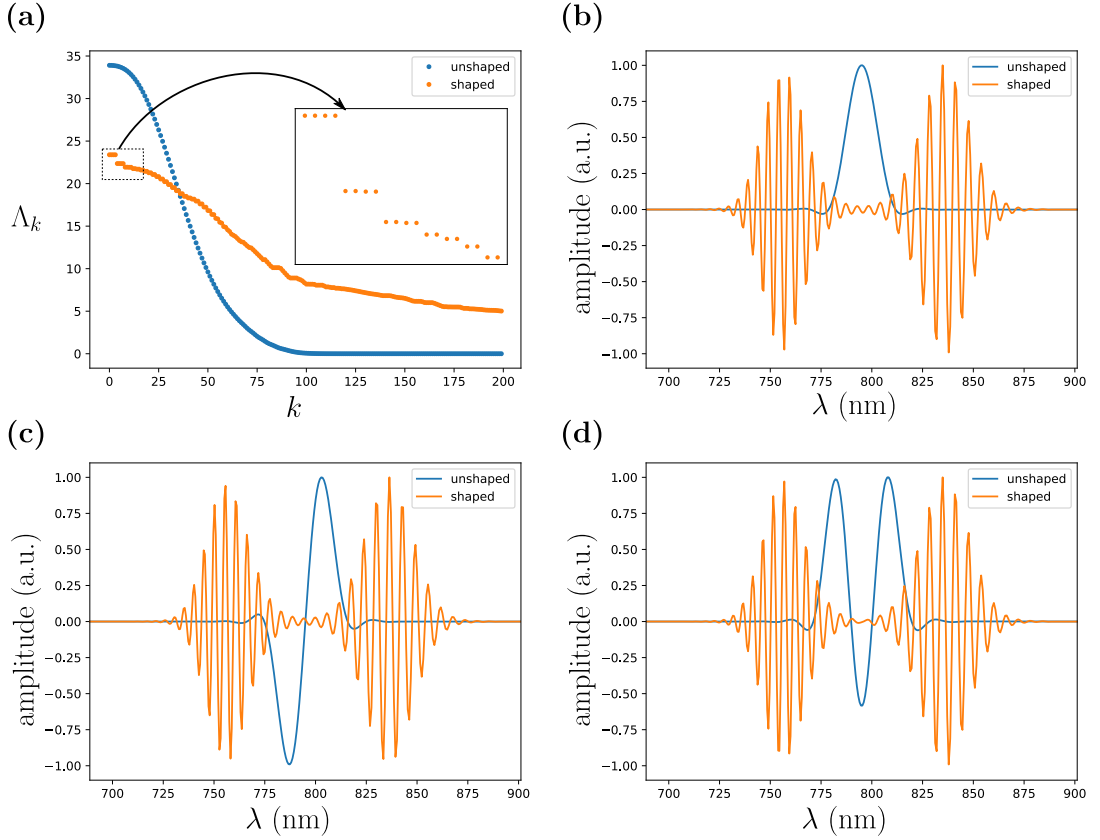


Fig. 7.15 (a) Gains of the Takagi decomposition for unshaped and optimal pump profile maximising \bar{f}_1 . (b), (c) and (d) First 3 supermodes.

the unitary matrix:

$$\mathbf{U} = \frac{1}{2} \begin{pmatrix} 1 & i & 1 & i \\ 1 & -i & 1 & -i \\ 1 & -i & -1 & i \\ 1 & i & -1 & -i \end{pmatrix} \quad (7.15)$$

The spectral shapes of the new modes are simple Gaussian functions with a central wavelength at $\approx 795 \pm 40$ nm, and a linear spectral phase corresponding to a delay of $\approx \pm 360$ fs. Given that the 4 first eigenvalues are equal: $\Lambda_1 = \Lambda_2 = \Lambda_3 = \Lambda_4$, in the supermode basis the covariance matrix of the first degenerate subspace can be simply written:

$$\mathbf{V} = \begin{pmatrix} \mathbf{V}_{qq} & \mathbf{0} \\ \mathbf{0} & \mathbf{V}_{pp} \end{pmatrix} \quad (7.16)$$

$$\text{with } \mathbf{V}_{qq} = \begin{pmatrix} e^{2r} & & & 0 \\ & e^{2r} & & \\ & & e^{2r} & \\ 0 & & & e^{2r} \end{pmatrix} = \mathbf{V}_{pp}^{-1} \quad \text{and} \quad r = g\Lambda_1 \quad (7.17)$$

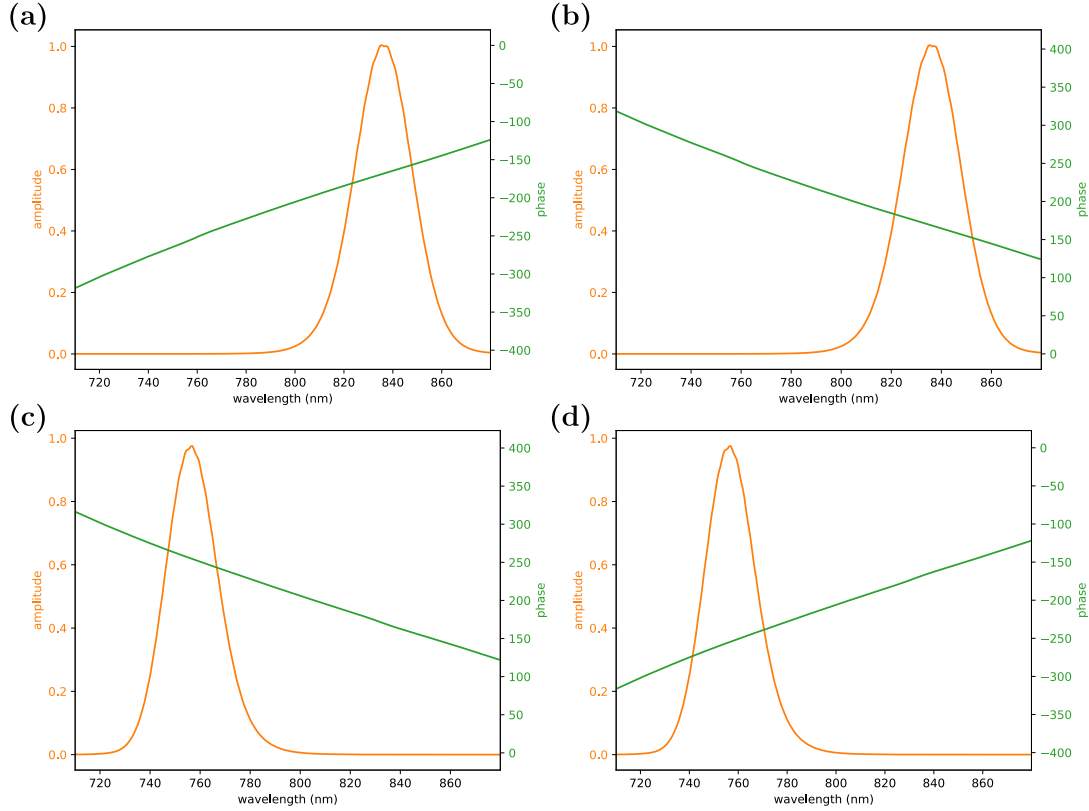


Fig. 7.16 Spectral shapes of the modes given by the linear combinations: (a) $\frac{s_1 + is_2 + s_3 + is_4}{2}$, (b) $\frac{s_1 - is_2 + s_3 - is_4}{2}$, (c) $\frac{s_1 - is_2 - s_3 + is_4}{2}$, (d) $\frac{s_1 + is_2 - s_3 - is_4}{2}$. Where s_{1-4} are the 4 first supermodes of Fig. 7.15.

In the new basis the covariance matrix reads (see section 2.1.4):

$$\mathbf{V}' = \mathbf{O}\mathbf{V}\mathbf{O}^T \quad (7.18)$$

$$= \begin{pmatrix} \mathbf{V}_{\text{EPR}}^+ & \mathbf{0} & \mathbf{0} & \mathbf{0} \\ \mathbf{0} & \mathbf{V}_{\text{EPR}}^+ & \mathbf{0} & \mathbf{0} \\ \mathbf{0} & \mathbf{0} & \mathbf{V}_{\text{EPR}}^- & \mathbf{0} \\ \mathbf{0} & \mathbf{0} & \mathbf{0} & \mathbf{V}_{\text{EPR}}^- \end{pmatrix} \quad \text{with} \quad \mathbf{V}_{\text{EPR}}^\pm = \begin{pmatrix} \cosh r & \pm \sinh r \\ \pm \sinh r & \cosh r \end{pmatrix} \quad (7.19)$$

where $\mathbf{O} = \begin{pmatrix} \text{Re}(\mathbf{U}) & \text{Im}(\mathbf{U}) \\ -\text{Im}(\mathbf{U}) & \text{Re}(\mathbf{U}) \end{pmatrix}$. \mathbf{V}' is just the concatenation of two EPR states covariance matrices (see Table 2.1). So for this subspace the SPOPO output consists in two independent EPR states. One where the two correlated modes are centred at $\approx 795 + 40$ nm and another with modes centred at $\approx 795 - 40$ nm. In both cases, the two correlated mode have an opposite time delay of $\approx \pm 360$ fs. A similar type of structure with a degeneracy of 2 was found in the context of non-degenerate phase matching [186].

This interesting mode structure is exactly identical for the second and third degenerate subspace, except the corresponding modes are given by first and second order Hermite-Gauss function (also with a central wavelength of $\approx 795 \pm 40$ nm, and a linear spectral phase corresponding to a delay of $\approx \pm 360$ fs).

This optimisation was carried out without taking into account the effects of intra-cavity

dispersion. As we discussed in section 6.4.2, one of the effect of dispersion is to limit the spectral width of the supermodes. The modes we just discussed are very broadband so this simulation is unlikely to be accurate in the case of a realistic set-up. In practice supermodes like the one of Fig. 7.15 would be completely filtered out by the cavity. This is also true to a lesser extent with the optimisation of \bar{f}_2 in section 7.3.1 as we found pump shaping was broadening the spectral shapes of the supermodes.

Nevertheless it would be interesting to investigate those modes without a cavity in a single pass parametric down conversion setting. In particular, one may think about using those modes as the building blocks to construct a large continuous variable cluster state in a similar way to what was done for the continuous wave regime in [63].

A more complete analysis of the pump optimisation is still to be carried out (with more frexels, different dynamic range and hyperparameters, etc.), and other cost functions could be implemented. The optimisation could also be adapted to include the effect of intra-cavity dispersion using technique described in section 6.4.2.2. This wasn't done here because the method of section 6.4.2.2 is quite computationally intensive. Its running time would have to be improved before it can be used efficiently in the pump shaping optimisation.

Nevertheless, the results we obtained in this section are enough to start implementing them in the experiment. Indeed the supermodes obtained when maximising the gain of the supermode are simple enough and the gain improvement seems significant enough to be measured experimentally.

Chapter 8

Covariance matrix reconstruction

Contents

8.1 Reconstruction from standard homodyne measurement	121
8.1.1 Principle	121
8.1.2 Fixel modes and supermodes reconstruction	124
8.1.3 Measurement details	124
8.2 Multipixel homodyne detection	126
8.2.1 Principle	126
8.2.2 Design	126
8.2.3 Measurement details	129
8.3 Reconstruction from multipixel homodyne	130
8.3.1 Principle	130
8.3.2 Phase reconstruction	134

Given the simple pump spectral shapes obtained with the MLA optimisation in chap. 7, we now want to implement them in the experiment and measure the effect on the SPOPO output state. The SPOPO output is a Gaussian state and is fully characterised by its covariance matrix. In this chapter we detail how the covariance matrix of the SPOPO output can be reconstructed with homodyne measurements.

We use two different techniques, a standard single mode homodyne detection with a tunable LO and a frequency resolved multimode homodyne detection: the *multipixel homodyne detection*. The first technique only allows a partial recovery of the covariance matrix but has reduced losses compared to the second. It can also be used to directly measure the squeezing level of individual supermodes. The second can recover the full covariance matrix, however it is more lossy. It is useful to recover the spectral shapes of the supermodes but does not give very good estimates for the squeezing levels. In this chapter we give the details of these two techniques.

8.1 Reconstruction from standard homodyne measurement

8.1.1 Principle

In this section we present how standard homodyne detection (SHD) can be used to reconstruct the covariance matrix of a Gaussian quantum state in a given real mode basis $\{\mathbf{u}_k(\mathbf{r}, t)\}$ (the measurement basis). This technique only allows partial recovery of the covariance matrix. Indeed, one has to assume that the qp correlation terms of the covariance

matrix are zero. This means the off-diagonal blocks of the covariance matrix are null:

$$\mathbf{V}_{qp} = \mathbf{V}_{pq} = \mathbf{0} \quad (8.1)$$

$$\text{with } \mathbf{V} = \begin{pmatrix} \mathbf{V}_{qq} & \mathbf{V}_{qp} \\ \mathbf{V}_{pq} & \mathbf{V}_{pp} \end{pmatrix} \quad (8.2)$$

Because of the assumption of Eq. (8.1), we cannot use this technique to reconstruct arbitrary Gaussian quantum states. For the SPOPO output state, assumption of Eq. (8.1) is valid as long as the pump is real (if we neglect intra-cavity dispersion). This follows from the results of section 6.3.2 where we showed that for a real pump¹, the supermodes are real and in the supermode basis the covariance matrix takes the simple form:

$$\mathbf{V}^{(s)} = \begin{pmatrix} \mathbf{V}_{qq}^{(s)} & 0 \\ 0 & \mathbf{V}_{pp}^{(s)} \end{pmatrix} \quad (8.3)$$

$$\text{with } \mathbf{V}_{qq}^{(s)} = \begin{pmatrix} e^{2r_1} & & 0 \\ & \ddots & \\ 0 & & e^{2r_n} \end{pmatrix} = \left(\mathbf{V}_{pp}^{(s)} \right)^{-1} \quad (8.4)$$

For any real mode basis change, given by the orthogonal matrix \mathbf{O} , from the supermode basis, to the measurement basis, the covariance matrix is given in the measurement basis by:

$$\mathbf{V} = \begin{pmatrix} \mathbf{O} & 0 \\ 0 & \mathbf{O} \end{pmatrix} \mathbf{V}^{(s)} \begin{pmatrix} \mathbf{O} & 0 \\ 0 & \mathbf{O} \end{pmatrix}^T \quad (8.5)$$

$$= \begin{pmatrix} \mathbf{O} \mathbf{V}_{qq}^{(s)} \mathbf{O}^T & 0 \\ 0 & \mathbf{O} \mathbf{V}_{pp}^{(s)} \mathbf{O}^T \end{pmatrix} \quad (8.6)$$

So the qp terms stay null for any real basis change. In our experiment we use a basis of real modes as the measurement modes (see section 8.1.2), so the assumption on qp terms is justified for real pump shapes.

We now detail how the qq and pp block of \mathbf{V} can be reconstructed from homodyne measurements. We already gave the general working principle of homodyne detection in section 2.3.3. For a coherent LO beam in mode $\mathbf{u}_k(\mathbf{r}, t)$ with amplitude $\alpha_0 = |\alpha_0|e^{i\theta}$, the signal of the subtracted photocurrent can be written:

$$s_k(\theta) = |\alpha_0| (\cos \theta q_k + \sin \theta p_k) + e \quad (8.7)$$

where q_k and p_k are samples from the signal quadratures in mode \mathbf{u}_k and e corresponds to electronic noise. If we scan the LO phase θ slowly compared to our acquisition speed, we can calculate the variance over a rolling window to get²:

$$V_k(\theta) := \text{Var}[s_k(\theta)] \quad (8.8)$$

$$= |\alpha_0|^2 \left(\cos^2 \theta \langle q_k^2 \rangle + \sin^2 \theta \langle p_k^2 \rangle + 2 \cos \theta \sin \theta \langle q_k p_k \rangle \right) + \langle e^2 \rangle \quad (8.9)$$

¹More precisely a pump with a flat phase, the absolute phase of the pump doesn't matter

²In our experiment we directly measured the variance with an electronic spectrum analyser.

For simplicity of notation and without loss of generality we assume $\langle q_k \rangle = \langle p_k \rangle = 0$. We can measure the electronic noise (dark noise) $\langle e^2 \rangle$ and shot noise variance $|\alpha_0|^2$ separately by blocking either all inputs or only the signal input to the homodyne detection:

$$V^{\text{dark}} = \langle e^2 \rangle \quad (8.10)$$

$$V_k^{\text{shot}} = |\alpha_0|^2 + \langle e^2 \rangle \quad (8.11)$$

and using these measures, calculate the corrected signal variance trace:

$$\tilde{V}_k(\theta) := \frac{V_k(\theta) - V^{\text{dark}}}{V_k^{\text{shot}} - V^{\text{dark}}} \quad (8.12)$$

$$= \cos^2 \theta \langle q_k^2 \rangle + \sin^2 \theta \langle p_k^2 \rangle + 2 \cos \theta \sin \theta \langle q_k p_k \rangle \quad (8.13)$$

$$= \underbrace{\frac{\langle q_k^2 \rangle + \langle p_k^2 \rangle}{2}}_{a_k} + \underbrace{\frac{\langle q_k^2 \rangle - \langle p_k^2 \rangle}{2}}_{b_k} \cos(2\theta) \quad (8.14)$$

where in the last equality we made the assumption $\langle q_k p_k \rangle = 0$. a_k can be obtained by taking the mean of this signal over a large number of periods of θ (or integer number of periods of θ). And b_k can be obtained from the amplitude of the trace oscillations (with a sine fit for example). From these coefficients we can immediately recover the diagonal terms of \mathbf{V}_{qq} and \mathbf{V}_{pp} .

To reconstruct the non diagonal terms, we collect homodyne traces where the LO mode is shaped into all the possible sums of pairs of modes from $\{\mathbf{u}_k\}$. If we shape the LO (using a pulse shaper) into the mode $\frac{\mathbf{u}_k + \mathbf{u}'_k}{\sqrt{2}}$, the corrected variance of the signal we get is:

$$\tilde{V}_{kk'}(\theta) = \frac{1}{2} \underbrace{\frac{\langle q_k^2 \rangle + \langle q_{k'}^2 \rangle + 2 \langle q_k q_{k'} \rangle + \langle p_k^2 \rangle + \langle p_{k'}^2 \rangle + 2 \langle p_k p_{k'} \rangle}{2}}_{a_{kk'}} \quad (8.15)$$

$$+ \frac{1}{2} \underbrace{\frac{\langle q_k^2 \rangle + \langle q_{k'}^2 \rangle + 2 \langle q_k q_{k'} \rangle - \langle p_k^2 \rangle - \langle p_{k'}^2 \rangle - 2 \langle p_k p_{k'} \rangle}{2}}_{b_{kk'}} \cos 2\theta \quad (8.16)$$

where we also assumed $\langle q_k p_{k'} \rangle = 0$. Again $a_{kk'}$ and $b_{kk'}$ are easily recovered from this trace with a fit. Combining terms from the mode $\frac{\mathbf{u}_k + \mathbf{u}'_k}{\sqrt{2}}$ and individual \mathbf{u}_k and $\mathbf{u}_{k'}$ measurements we get:

$$A_{kk'} := a_{kk'} - a_k - a_{k'} = \langle q_k q_{k'} \rangle + \langle p_k p_{k'} \rangle \quad (8.17)$$

$$B_{kk'} := b_{kk'} - b_k - b_{k'} = \langle q_k q_{k'} \rangle - \langle p_k p_{k'} \rangle \quad (8.18)$$

$$(8.19)$$

Finally the qq and pp blocks of the covariance matrix are given by:

$$\mathbf{V}_{qq} = \frac{\mathbf{A} + \mathbf{B}}{2} \quad (8.20)$$

$$\mathbf{V}_{pp} = \frac{\mathbf{A} - \mathbf{B}}{2} \quad (8.21)$$

As we will eventually shape the pump beam, we can't always assume the pump is real, so we need a more general way to reconstruct the covariance matrix. This alternative technique will be presented in section 8.2

8.1.2 Frexel modes and supermodes reconstruction

In theory the technique we described in the previous section works for any real mode basis $\{\mathbf{u}_k\}$. In practice, we use a frequency band basis, we call them the frexels modes. The frequency range of interest is divided into frequency bands of equal width: $\mathcal{I}_k = (\omega_k, \omega_{k+1})$. The frexel modes correspond to portions of the LO spectrum over these bands:

$$u_k(\omega) = \begin{cases} c_k u_{\text{LO}}(\omega) & \text{if } \omega \in \mathcal{I}_k \\ 0 & \text{otherwise.} \end{cases} \quad (8.22)$$

where u_{LO} is the full spectrum of the unshaped LO beam and c_k is a normalisation constant. These modes are particularly convenient to use. They are easy to produce with our pulse shaper and their orthogonality is guaranteed because they don't overlap. It is also the most natural basis to use. In this basis the various terms of the covariance matrix are interpreted as correlation between frequency bands.

In our experiments, the (unshaped) LO beam has a FWHM around 10 nm. We cannot properly measure a quantum state if its spectral content is large compared to this width because the frexel modes only have significant power within the range of the LO spectrum. In other words, for frexel modes well outside the typical LO range, the α_0 in Eq. (8.7) would be null and we would only measure electronic noise (no clearance). The simulations of section 6.3.2 (see Fig. 6.5) show that the first few supermodes are well within this frequency range. However, higher order supermodes are increasingly broadband so we need a broader LO spectrum to measure them.

To get a broader LO spectrum, we use a photonic crystal fibre (PCF). This nano-structured fibre was designed and fabricated specifically for our purposes in the Max Planck Institute by Nicolas Joly. It has a core of $\sim 1.3 \mu\text{m}$ with a honeycomb structure (see Fig. 8.1 upper right corner). The fibre produces Kerr type non-linearities that coherently broadens the spectrum of the injected light through phase auto-modulation effects. This broadening increases with the fibre length and input power. Fig. 8.1 shows the measured output spectra for a 40 mm long PCF and various input powers.

With the PCF we get new frexel modes with significant power over a broader frequency range. Fig. 8.2 shows the measured frexels modes (not normalized) obtained by shaping of the LO, with and without PCF. For all measurements within this thesis, we used the PCF frexel modes.

Once we have reconstructed the covariance matrix we can apply the decomposition presented in section 2.2.3. Because we assume the qp terms are zero, the basis change matrix \mathbf{O}_1 then takes the simple form:

$$\mathbf{O}_1 = \begin{pmatrix} \mathbf{U} & 0 \\ 0 & \mathbf{U} \end{pmatrix} \quad (8.23)$$

Where \mathbf{U} is a real orthogonal matrix. The supermodes are reconstructed as linear combination of the frexels modes given by the columns of \mathbf{U} .

8.1.3 Measurement details

We use a homodyne detector with a photodiode pair (model S3590 from hamamatsu [187]), the photodiode are mounted back to back so that their output photocurrent is directly subtracted. The quantum efficiency of the photodiodes is around 95 %. A home-made

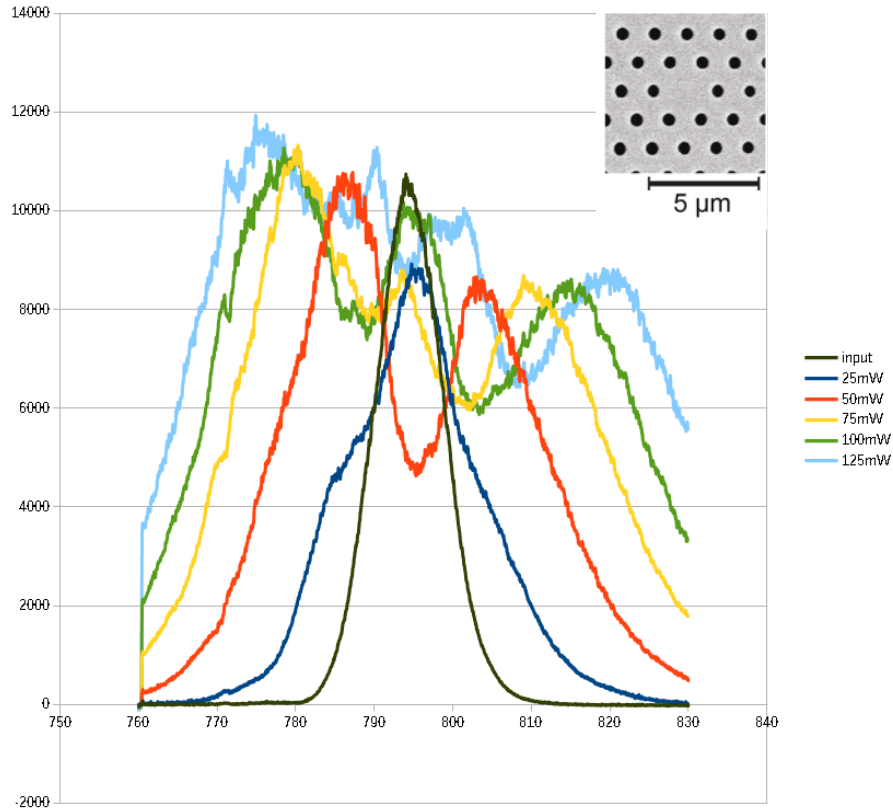


Fig. 8.1 Effect of a 40 mm photonic crystal fiber (PCF) on the LO spectrum for various input powers.

transimpedance amplifier circuit¹ then amplifies this subtracted photocurrent and converts it to a voltage. The signal is then further amplified and filtered with:

- a 5 MHz cut-off frequency low pass filter (LPF) model *BLP-5+* from minicircuit [188].
- a low noise amplifiers model *ZFL-500LN-BNC+* from minicircuit [189].

This signal is analysed with an electronic spectrum analyser (ESA) model *MXA N2090A* from Agilent Technologies. It gives access to the power spectral density of the photocurrent, which is proportional to the quadrature variance as given by Eq. (8.8) (see [124, 190] for details). The variance traces are acquired at 1 MHz with a 100 kHz resolution bandwidth (RBW) and a 1 kHz video bandwidth (VBW). The LO phase is scanned at 5 Hz with a PZT. The typical visibility of the homodyne detection, measured as the contrast between the LO beam and the SPOPO transmitted seed beam, was 91 %. The spatial and temporal/spectral mismatches of the LO and seed beam both contribute in reducing the visibility.

The shot noise variance was measured for different LO powers (see Fig. 8.3) to determine the saturation point of the homodyne detection. The LO power is adjusted to about 1 mW to ensure the highest clearance (~ 10 dB) between shot noise and dark noise while staying in the linearity region.

¹circuit designed by Young-Sik Ra

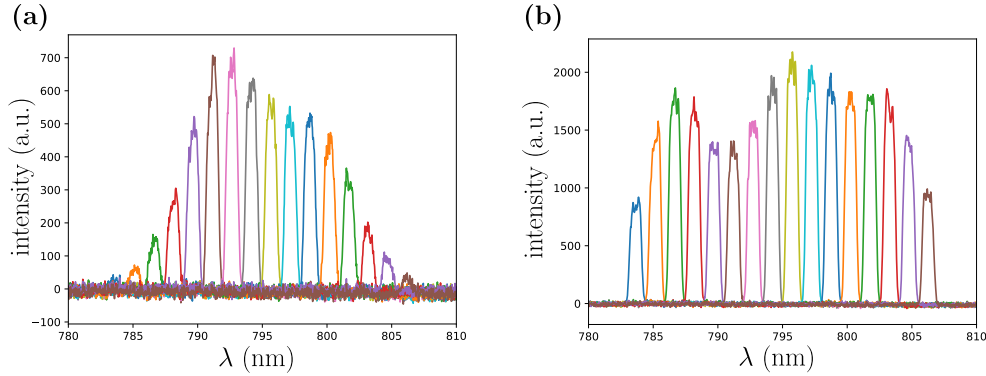


Fig. 8.2 Measured frexel modes intensity spectrum, (a) without PCF, (b) with PCF. The modes are not normalised to highlight the advantage of using PCF.

8.2 Multipixel homodyne detection

8.2.1 Principle

The multipixel homodyne detection (MHD) is a measurement technique designed to reconstruct the full covariance matrix of a quantum state. In particular, it allows to recover the qp terms of the covariance matrix that remained inaccessible to the standard homodyne detection (SHD). In the SHD technique, the reason we can not extract the qp terms is that we do not have phase information on the homodyne traces. Because each trace $V_{kk'}(\theta)$ is measured sequentially there is no reliable way to determine the phase relationship between two successive traces. In other words the LO phase θ is initialised at a random value for each new trace. The MHD technique, solves this issue by acquiring all traces simultaneously, so there is a fixed phase between them. The MHD is nothing but a frequency resolved homodyne detection.

Fig 8.4 shows a multipixel homodyne detection scheme. After interfering the LO and the signal beams on a balanced beam-splitter, the different frequency components of both outputs are spatially separated using a diffracting element (a grating in our case). Each frequency band is measured separately with a photodiode, and the photocurrents are subtracted two by two for matching frequency bands. With this technique, traces of the form of Eq. 8.7 are acquired simultaneously for all frexels. Calculating the covariance between those traces and using simple phase shaping on the LO beam (see section 8.3), we can then recover all the terms of the covariance matrix.

8.2.2 Design

The elements of the multipixel homodyne detection have to be chosen according to the bandwidth of the LO beam and the supermodes to be measured. Ideally, we want each frexel to encapsulate a part of the signal spectrum that is big enough so that the whole signal modes fall into our detection. But small enough to be able to resolve the spectral variation of those modes. Ultimately we are limited by the number of frequency pixel, i.e. photodiodes, available. In the following section we will derive the relevant parameters to optimise for the design and show the characteristics of the chosen design.

We consider an input LO field with a Gaussian spectral intensity width (standard

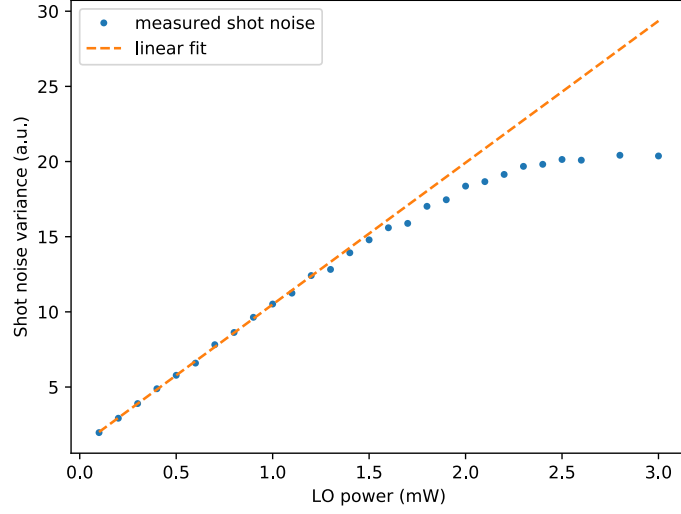


Fig. 8.3 Homodyne detection calibration: measured shot noise (corrected of dark noise) for various LO powers.

deviation) $\Delta\lambda$ centred at λ_0 . We also assume a Gaussian spatial profile of waist w_0 positioned on the grating. This assumption is reasonable as, just like with the pulse shaper (see section 5.3.1), the actual waist position will have little effect on the design. Our goal is to determine the repartition of this field on the photodiodes. The signal to be measured must have a comparable bandwidth to the LO beam we use if we want to be able to measure it properly. To simplify the problem we assume that the lenses of the microlens array (see Fig. 8.4) have no separation between them and will focus efficiently all the light they encapsulate into the corresponding photodiode. We also linearise the diffraction relation. Finally we consider that the diffraction plane is perfectly horizontal and limit the description to this plane.

Under all those conditions, the normalised intensity along the microlens array plane can be written:

$$I(x, \delta\lambda) = \frac{w_0}{f\lambda_0} \exp\left(-2\frac{(x - \alpha\delta\lambda)^2}{w'^2} - \frac{\delta\lambda^2}{2\Delta\lambda^2}\right) \quad \text{with} \quad w' = \frac{f\lambda_0}{\pi w_0} \quad (8.24)$$

where f is the focal length of the collimation lens, $\alpha = \frac{af}{\cos\theta_d^{(0)}}$ is the diffracting power of the grating, $\delta\lambda = \lambda - \lambda_0$ is the wavelength detuning (see Fig. 8.5). This expression is quite easy to understand, it has two contributions. The first term in the exponential corresponds to the spatial distribution of light along x . This term also depends on $\delta\lambda$ because of the diffracting elements that separate the frequency components spatially. Each frequency component keeps its spatial Gaussian shape so the spatial waist after the lens is just $w' = \frac{f\lambda_0}{\pi w_0}$. And, as we saw with the pulse shaper in section 5.2, each frequency component is shifted to the central position $\alpha\delta\lambda$ by the grating (Eq. (5.5)). The second term $e^{-\frac{\delta\lambda^2}{2\Delta\lambda^2}}$ just corresponds to the frequency distribution of the input Gaussian spectrum. Integrating

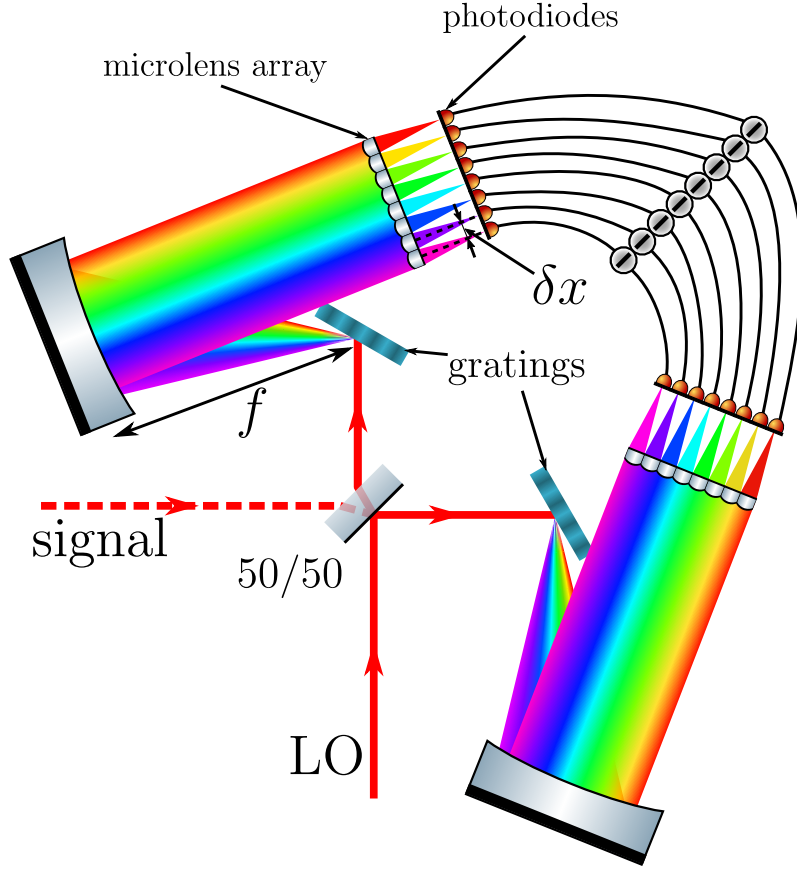


Fig. 8.4 The multipixel homodyne detection (MHD) scheme. After interference of the LO and signal beam on a balanced beam splitter, the different frequency components of both outputs are spatially separated using a grating. Each frequency band is measured separately with a photodiode, and the photocurrents are subtracted two by two for matching frequency bands.

Eq. (8.24) over $\delta\lambda$ we get the total intensity at transverse position x :

$$I(x) = \frac{1}{\sqrt{2\pi}\Delta x} e^{-\frac{x^2}{2\Delta x^2}} \quad \text{with} \quad \Delta x = \sqrt{\alpha^2 \Delta \lambda^2 + \left(\frac{w'}{2}\right)^2} \quad (8.25)$$

We see that the beam total intensity follows a Gaussian of width Δx . We can simplify this expression even further if we notice that in our conditions the second term in the square root in Δx is negligible compared to the first so that: $\Delta x \approx \alpha \Delta \lambda$. This simple expression allows us to choose a combination (a, f) that spreads the LO optimally on the photodiodes. For example if we require that the 8 photodiodes encapsulate 5 standard deviation of the input field¹ we get the condition:

$$8\delta x = 5\Delta x \quad (8.26)$$

$$\Rightarrow f \approx \frac{8\delta x \cos \theta_d^{(0)}}{5a\Delta \lambda} \quad (8.27)$$

¹This correspond to collecting $\sim 99\%$ of the input power.

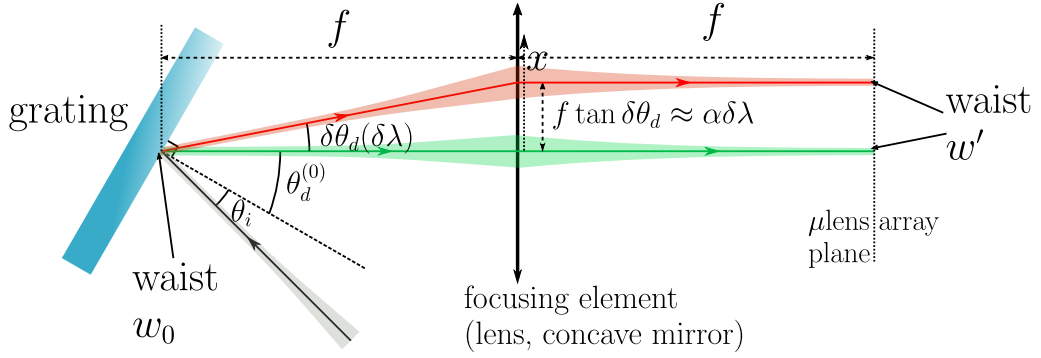


Fig. 8.5 Schematic representation of the effect of the grating in the multipixel homodyne detection scheme. Each frequency is shifted transversally relative to the central frequency by $\alpha\delta\lambda$. Each frequency component has a waist $w' = \frac{f\lambda_0}{\pi w_0}$ after the grating and focusing element.

Where δx is the microlens array pitch. In our experiment, we have a grating with $a = 1800$ gr/cm available and the microlens array has a $\delta x = 1$ mm pitch. For a 10 nm FWHM LO this gives $f \approx 129$ mm. This is a bit too small to achieve in practice as we need enough space between the different optical components to fit their mounts so we finally chose a focal length of 175 mm.

The normalised spectral intensity of light that is collected by each photodiode is easily determined with:

$$I_n(\delta\lambda) = \int_{n\delta x}^{(n+1)\delta x} dx I(x, \delta\lambda) \quad (8.28)$$

$$= \frac{1}{2\sqrt{2\pi}\Delta\lambda} e^{-\frac{\delta\lambda^2}{2\Delta\lambda^2}} \left(\operatorname{erf}\left(\frac{\sqrt{2}(\delta x(n+1) - \alpha\delta\lambda)}{w'}\right) - \operatorname{erf}\left(\frac{\sqrt{2}(\delta x n - \alpha\delta\lambda)}{w'}\right) \right) \quad (8.29)$$

Where the number $n \in [-4, 3]$ labels the photodiodes. Each photodiode collects a portion of the input spectrum. The spectral shape of the LO within this portion will determine the corresponding mode measured by homodyne detection (the frexel mode).

The power fraction of the input collected by photodiode n is then:

$$P_n = \int_{-\infty}^{\infty} d\delta\lambda I_n(\delta\lambda) \quad (8.30)$$

$$= \frac{1}{2} \left(\operatorname{erf}\left(\frac{\sqrt{2}\delta x(n+1)}{2\Delta x^2}\right) - \operatorname{erf}\left(\frac{\sqrt{2}\delta x n}{2\Delta x^2}\right) \right) \quad (8.31)$$

Fig. 8.6 shows the predicted light repartition on the photodiodes for our design. 93.5 % of the input light is collected, the overlap between neighbouring modes is below 4.5 %. Fig. 8.6 also shows the corresponding measured frexel modes (without PCF). The measurement was acquired by scanning a single diffraction column on the SLM while recording the intensity in each photodiodes.

8.2.3 Measurement details

The details of the electronic set-up used for multipixel homodyne acquisition is shown in Fig. 8.7. Our multipixel homodyne detector uses photodiode arrays model *S4111* from

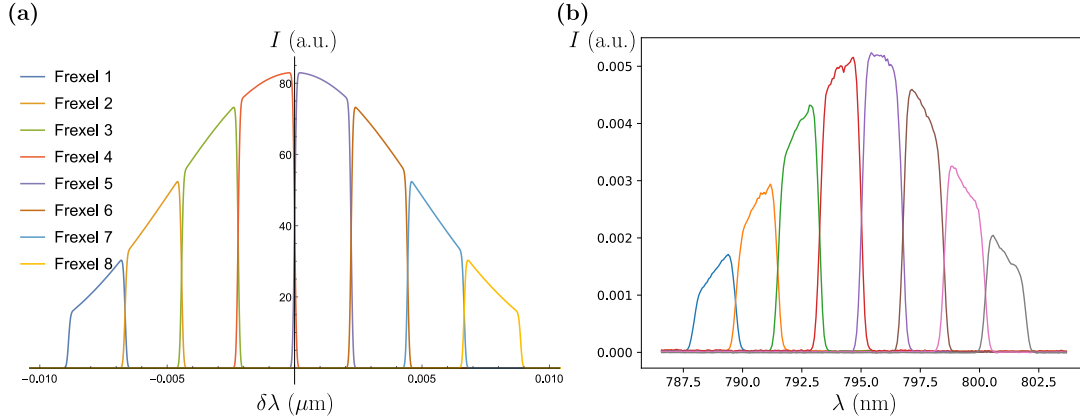


Fig. 8.6 (a) Predicted frexel mode spectral shape. (b) Measured frexel mode spectral shape.

hamamatsu [191] and home-made amplifier circuits designed by Cai Yin and Jon Roslund. The quantum efficiency of the photodiodes is around 80 %. The signal from each photodiode is amplified by this circuit before subtraction with its counterpart. The subtraction is done with a power splitter model *ZSC-2-1+* from minicircuit [192], the subtracted photocurrent is filtered with a 5 MHz low-pass filter model *BLP-5+* from minicircuit [188] and a home-made 25 kHz high pass filter. It is then amplified with 2 successive low noise amplifiers model *ZFL-500LN-BNC+* from minicircuit [189] and mixed down at 1 MHz using an electronic local oscillator, a doubled balanced mixer model *ZAD-3+* from minicircuit [193] and a 100 kHz home-made low pass filter. This signal is then digitised and acquired with a NI-PXI-5105 oscilloscope from National Instrument [194] with a 2 MHz sampling rate and 12-bit resolution. The acquisition time is set to 50 ms to span a few periods of the LO scan. We use 8 photodiodes and the LO power is set to ~ 15 mW which gives shot noise to dark noise clearances between ~ 10 dB for the central frexels and ~ 5 dB for the side frexels. For all measurements, the typical homodyne visibility is ~ 91 %.

8.3 Reconstruction from multipixel homodyne

8.3.1 Principle

As in section 8.1.1, the signal from photodiode i can be written as:

$$s_i(\theta) = \alpha_i(\cos \theta q_i + \sin \theta p_i) + e_i \quad (8.32)$$

Where α_i is a proportionality factor that depends on the LO power, θ is the LO phase, q_i and p_i are samples from the quadratures of the signal in the LO frexel mode i and e_i is the electronic noise. α_i is proportional to the LO power available on frexel i , the signal from photodiode i will only be relevant if the photodiode collects enough power from the LO, otherwise the electronic noise will dominate. A typical homodyne trace is shown in Fig. 8.8.

Assuming the sampling frequency f_s is fast enough compared to the LO phase scanning, we can compute variance and covariance of these signals over rolling windows, the size of this window determines the video bandwidth (VBW). Here, the demodulation bandwidth is $RBW = 100$ kHz, and we use a video bandwidth of $VBW = 1$ kHz.

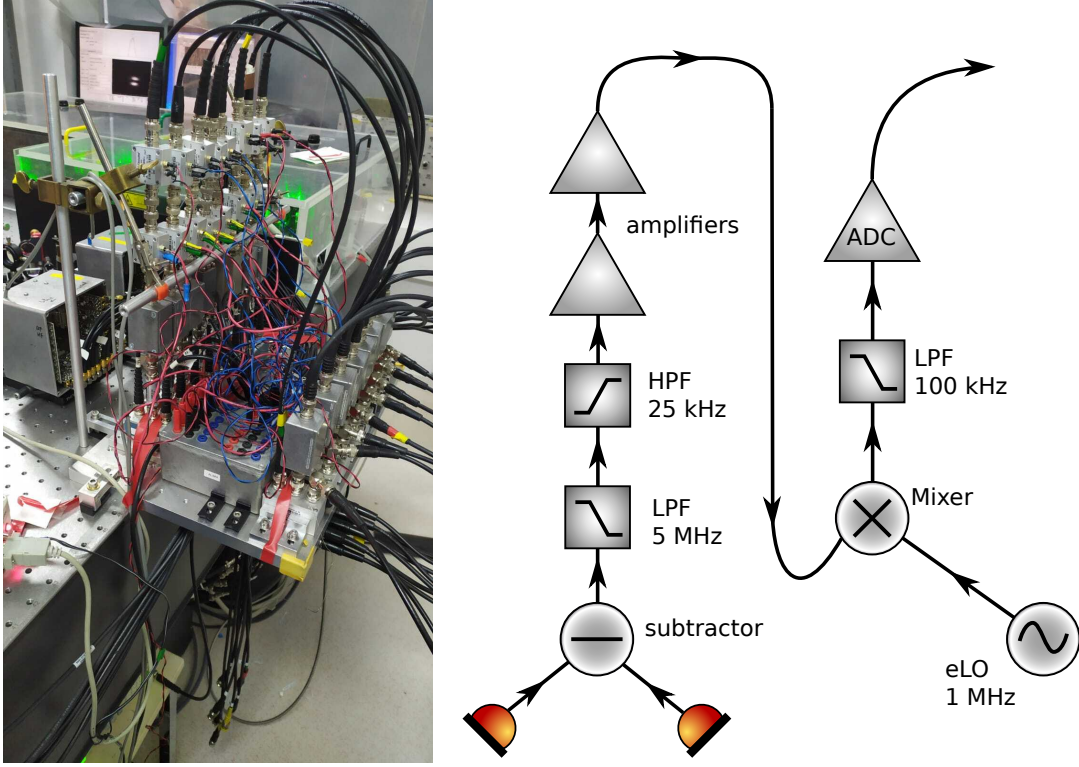


Fig. 8.7 Photo and scheme of the electronic modulation, filtering and amplification line used for multipixel homodyne detection.

Given the expression of s_i^θ (Eq. (8.32)), the covariance between two traces i, j is:

$$C_{ij}(\theta_1, \theta_2) := \text{Cov}(s_i(\theta_1), s_j(\theta_2)) \quad (8.33)$$

$$= \alpha_i \alpha_j (\cos(\theta_1) \cos(\theta_2) \langle q_i q_j \rangle + \sin(\theta_1) \sin(\theta_2) \langle p_i p_j \rangle) \quad (8.34)$$

$$+ \cos(\theta_1) \sin(\theta_2) \langle q_i p_j \rangle + \sin(\theta_1) \cos(\theta_2) \langle p_i q_j \rangle + \langle e_i e_j \rangle \quad (8.35)$$

When measuring shot noise, since for vacuum $\langle x^2 \rangle = \langle p^2 \rangle = 1$, we get the variance terms:

$$\text{Var}(s_i(\theta)) = \alpha_i^2 + \langle e_i^2 \rangle \quad (8.36)$$

So we can renormalise the covariances to:

$$\tilde{C}_{ij}(\theta_1, \theta_2) := \frac{C_{ij}(\theta_1, \theta_2) - \langle e_i e_j \rangle}{\sqrt{(\langle s_i(\theta_1)^2 \rangle - \langle e_i^2 \rangle) (\langle s_j(\theta_2)^2 \rangle - \langle e_j^2 \rangle)}} \quad (8.37)$$

Fig. 8.9 shows typical renormalised covariance traces obtained.

Using trigonometric relation this can be written given Eq. (8.33) as:

$$\tilde{C}_{ij}(\theta_1, \theta_2) = \frac{1}{2} \left((\cos(\theta_1 - \theta_2) + \cos(\theta_1 + \theta_2)) \langle q_i q_j \rangle \right. \quad (8.38)$$

$$\left. + (\cos(\theta_1 - \theta_2) - \cos(\theta_1 + \theta_2)) \langle p_i p_j \rangle \right) \quad (8.39)$$

$$+ (\sin(\theta_1 + \theta_2) - \sin(\theta_1 - \theta_2)) \langle q_i p_j \rangle \quad (8.40)$$

$$\left. + (\sin(\theta_1 + \theta_2) + \sin(\theta_1 - \theta_2)) \langle p_i q_j \rangle \right) \quad (8.41)$$

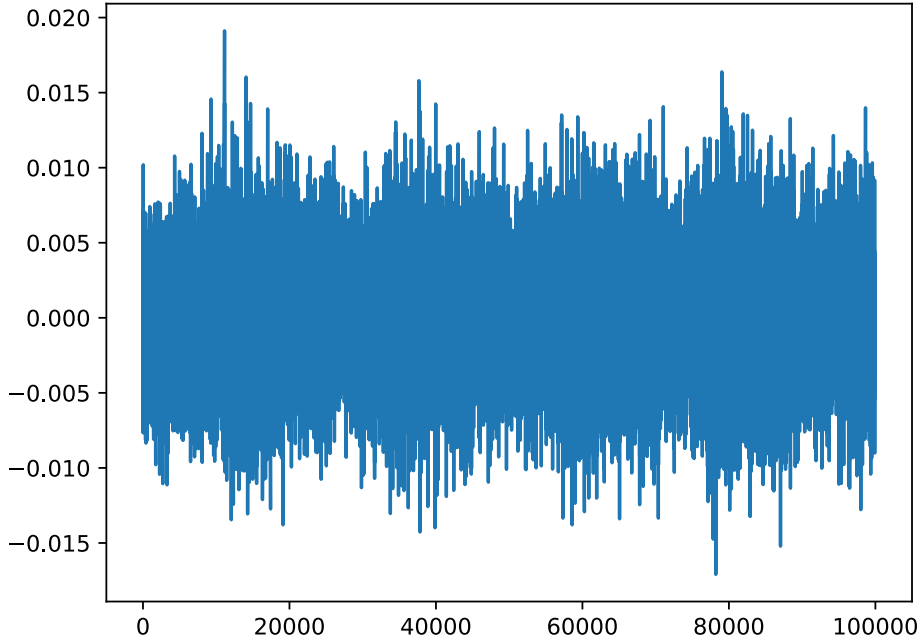


Fig. 8.8 Typical homodyne trace obtained from the multipixel homodyne detection.

We now show that from this expression, using only phase shaping on the LO beam we can recover each term of the covariance matrix. The covariance trace expression of Eq. 8.38 contains all terms of the covariance matrix for the frexel pair (i, j) . In order to isolate each term we just need two measurement: one with the same LO phase for both frexels ($\theta_1 = \theta_2$) and one with a $\pi/2$ phase shift between the two frexels ($\theta_1 = \theta_2 \pm \frac{\pi}{2}$). We will therefore take several acquisition with different phase shifts imprinted on certain frexels of the LO beam using the pulse shaper. In order to get for all frexel pairs, one acquisition with $\theta_1 = \theta_2$ and one acquisition with $\theta_1 = \theta_2 \pm \frac{\pi}{2}$, we implement a sequence of phase shaping on the LO with the following frexel phase values:

- $(0 \ 0 \ 0 \ 0 \ 0 \ 0 \ 0 \ 0 \ 0)$
- $(\frac{\pi}{2} \ \frac{\pi}{2} \ \frac{\pi}{2} \ \frac{\pi}{2} \ 0 \ 0 \ 0 \ 0 \ 0)$
- $(\frac{\pi}{2} \ \frac{\pi}{2} \ 0 \ 0 \ \frac{\pi}{2} \ \frac{\pi}{2} \ 0 \ 0 \ 0)$
- $(\frac{\pi}{2} \ 0 \ \frac{\pi}{2} \ 0 \ \frac{\pi}{2} \ 0 \ \frac{\pi}{2} \ 0 \ 0)$

For a given frexel pair (i, j) there are 4 different possible cases:

- The trace with no LO phase shift for either frexel i, j : $\theta_1 = \theta_2 = \theta$.
- The trace with $\pi/2$ LO phase shift for both frexel i, j : $\theta_1 = \theta_2 = \theta + \pi/2$.
- The trace with a $\pi/2$ phase shift in the LO for frexel i : $\theta_1 = \theta + \pi/2, \theta_2 = \theta$.
- The trace with a $\pi/2$ phase shift in the LO for frexel j : $\theta_1 = \theta, \theta_2 = \theta + \pi/2$.

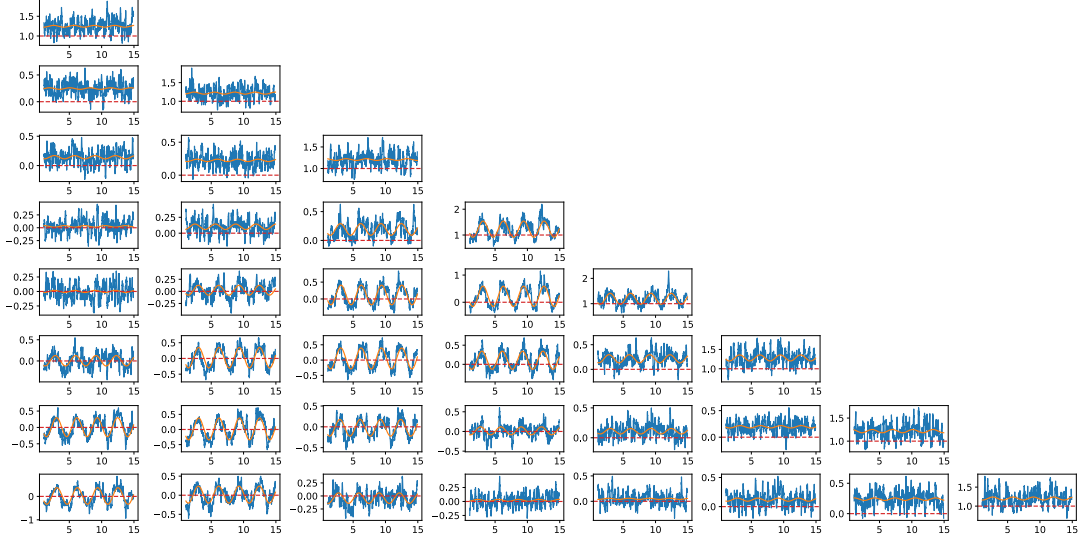


Fig. 8.9 Typical covariance traces obtained from multipixel homodyne detection. The graph in row i and column j corresponds to the covariance trace between the signals from frexel i and j .

When the LO phase is the same for frexels i and j , we get:

$$\tilde{C}_{ij}(\theta, \theta) = \underbrace{\frac{\langle q_i q_j \rangle + \langle p_i p_j \rangle}{2}}_{a_{ij}} + \underbrace{\frac{\langle q_i p_j \rangle + \langle p_i q_j \rangle}{2}}_{b_{ij}} \sin 2\theta + \underbrace{\frac{\langle q_i q_j \rangle - \langle p_i p_j \rangle}{2}}_{c_{ij}} \cos 2\theta \quad (8.42)$$

$$\tilde{C}_{ij}(\theta + \pi/2, \theta + \pi/2) = \underbrace{\frac{\langle q_i q_j \rangle + \langle p_i p_j \rangle}{2}}_{a_{ij}} + \underbrace{\frac{-\langle q_i p_j \rangle - \langle p_i q_j \rangle}{2}}_{-b_{ij}} \sin 2\theta + \underbrace{\frac{-\langle q_i q_j \rangle + \langle p_i p_j \rangle}{2}}_{-c_{ij}} \cos 2\theta \quad (8.43)$$

When there is a $\pi/2$ phase shift between frexel i and j , we get:

$$\tilde{C}_{ij}(\theta, \theta + \pi/2) = \underbrace{\frac{\langle q_i p_j \rangle - \langle p_i q_j \rangle}{2}}_{a_{ij}^{\pi/2}} + \underbrace{\frac{\langle p_i p_j \rangle - \langle q_i q_j \rangle}{2}}_{b_{ij}^{\pi/2}} \sin 2\theta + \underbrace{\frac{\langle q_i p_j \rangle + \langle p_i q_j \rangle}{2}}_{c_{ij}^{\pi/2}} \cos 2\theta \quad (8.44)$$

$$\tilde{C}_{ij}(\theta + \pi/2, \theta) = \underbrace{\frac{-\langle q_i p_j \rangle + \langle p_i q_j \rangle}{2}}_{-a_{ij}^{\pi/2}} + \underbrace{\frac{\langle p_i p_j \rangle - \langle q_i q_j \rangle}{2}}_{b_{ij}^{\pi/2}} \sin 2\theta + \underbrace{\frac{\langle q_i p_j \rangle + \langle p_i q_j \rangle}{2}}_{c_{ij}^{\pi/2}} \cos 2\theta \quad (8.45)$$

If we know the phase θ (details of phase determination are given in the next section 8.3.2) we can then fit the function $f(\theta) := a + b \sin \theta + c \cos \theta$ to those covariance traces to recover the terms $a_{ij}, b_{ij}, c_{ij}, a_{ij}^{\pi/2}, b_{ij}^{\pi/2}, c_{ij}^{\pi/2}$.

And finally we can reconstruct the covariance matrix terms with:

$$\langle q_i q_j \rangle = a_{ij} + c_{ij} = a_{ij} - b_{ij}^{\pi/2} \quad (8.46)$$

$$\langle p_i p_j \rangle = a_{ij} - c_{ij} = a_{ij} + b_{ij}^{\pi/2} \quad (8.47)$$

$$\langle q_i p_i \rangle = \langle p_i x_i \rangle = b_{ii} \quad (8.48)$$

$$\langle q_i p_j \rangle = a_{ij}^{\pi/2} + c_{ij}^{\pi/2} = a_{ij}^{\pi/2} + b_{ij} \quad (8.49)$$

$$\langle p_i q_j \rangle = -a_{ij}^{\pi/2} + c_{ij}^{\pi/2} = -a_{ij}^{\pi/2} + b_{ij} \quad (8.50)$$

Note we have $c_{ij} = -b_{ij}^{\pi/2}$ and $b_{ij} = c_{ij}^{\pi/2}$. This system is overdetermined and we can either use the a , b or a , c terms to reconstruct the covariance matrix. The two methods give similar results.

Once the covariance matrix is reconstructed we can use the decomposition we presented in section 2.2.3 to find the supermodes.

8.3.2 Phase reconstruction

To apply the reconstruction technique we just described we have to know the value of θ (LO phase) for all the variance and covariance traces we obtained. In order to do so we will use the variance trace of a single frexel, here we use the 4th frexel (one of the central frexels). This trace will show oscillation in the variance that will allow us to recover θ . We saw the (normalised) variance trace could be written:

$$V_i(\theta) = \cos^2(\theta) \langle q_i^2 \rangle + \sin^2(\theta) \langle p_i^2 \rangle + \cos(\theta) \sin(\theta) (\langle q_i p_i \rangle + \langle p_i q_i \rangle) \quad (8.51)$$

$$= \frac{\langle q_i^2 \rangle + \langle p_i^2 \rangle}{2} + \frac{\langle q_i p_i \rangle + \langle p_i q_i \rangle}{2} \sin 2\theta + \frac{\langle q_i^2 \rangle - \langle p_i^2 \rangle}{2} \cos 2\theta \quad (8.52)$$

Since the single mode quantum state corresponding to this pixel mode is Gaussian, we can just set $\langle q_i p_i \rangle = \langle p_i q_i \rangle = 0$. This just amounts to a particular choice of quadrature definition (or LO reference phase) where the squeezed and anti-squeezed quadrature are along q_i and p_i . We will also consider that the squeezed quadrature is p_i and q_i is anti-squeezed. In other words, we set the LO phase convention so that $\theta = 0$ corresponds to measuring the anti-squeezed quadrature of the phase reference frexel mode. We finally have:

$$V_i(\theta) = \frac{\langle q_i^2 \rangle + \langle p_i^2 \rangle}{2} + \underbrace{\frac{\langle q_i^2 \rangle - \langle p_i^2 \rangle}{2}}_{\geq 0} \cos 2\theta \quad (8.53)$$

We then fit the function $g(t) := a \cos(2\pi f t + \phi_0) + b$ to this trace and recover the LO phase with:

$$\theta = \frac{2\pi f t + \phi_0}{2} \quad (8.54)$$

The initial guesses for the fit are calculated using the fast Fourier transform (FFT) of the trace. Note that with our phase convention $a \geq 0$ but the fit might converge to a negative value for a in which case we need to add/subtract $\pi/2$ to θ .

There is an additional subtlety to consider here. When using Eqs. (8.42), (8.44) and (8.45), we implicitly consider that the phase of the LO on the 4th frexel we use for phase reconstruction is not shifted by the pulse shaper. If it is, then all other shifted frexels can

be considered as not shifted, since all phases are referenced to the 4th frexel. Likewise all the unshifted frexel can be considered shifted by $-\pi/2$. In other word, for all measurement where the phase reconstruction frexel is shifted by $\pi/2$, we have the 3 alternative cases:

- No phase shift on the LO for frexel i and j : $\theta_1 = \theta_2 = \theta - \pi/2$.
- $\pi/2$ phase shift on the LO for both frexel i and j : $\theta_1 = \theta_2 = \theta$.
- $\pi/2$ phase shift on the LO for frexel i : $\theta_1 = \theta$, $\theta_2 = \theta - \pi/2$.
- $\pi/2$ phase shift on the LO for frexel j : $\theta_1 = \theta - \pi/2$, $\theta_2 = \theta$.

In those cases we get traces given by:

$$\tilde{C}_{ij}(\theta - \pi/2, \theta - \pi/2) = \underbrace{\frac{\langle q_i q_j \rangle + \langle p_i p_j \rangle}{2}}_{a_{ij}} + \underbrace{\frac{-\langle q_i p_j \rangle - \langle p_i q_j \rangle}{2}}_{-b_{ij}} \sin 2\theta + \underbrace{\frac{\langle p_i p_j \rangle - \langle q_i q_j \rangle}{2}}_{-c_{ij}} \cos 2\theta \quad (8.55)$$

$$\tilde{C}_{ij}(\theta, \theta) = \underbrace{\frac{\langle q_i q_j \rangle + \langle p_i p_j \rangle}{2}}_{a_{ij}} + \underbrace{\frac{\langle q_i p_j \rangle + \langle p_i q_j \rangle}{2}}_{b_{ij}} \sin 2\theta + \underbrace{\frac{\langle q_i q_j \rangle - \langle p_i p_j \rangle}{2}}_{c_{ij}} \cos 2\theta \quad (8.56)$$

$$\tilde{C}_{ij}(\theta - \pi/2, \theta) = \underbrace{\frac{\langle q_i p_j \rangle - \langle p_i q_j \rangle}{2}}_{a_{ij}^{\pi/2}} + \underbrace{\frac{\langle q_i q_j \rangle - \langle p_i p_j \rangle}{2}}_{-b_{ij}^{\pi/2}} \sin 2\theta + \underbrace{\frac{-\langle q_i p_j \rangle - \langle p_i q_j \rangle}{2}}_{-c_{ij}^{\pi/2}} \cos 2\theta \quad (8.57)$$

$$\tilde{C}_{ij}(\theta, \theta - \pi/2) = \underbrace{\frac{\langle p_i q_j \rangle - \langle q_i p_j \rangle}{2}}_{-a_{ij}^{\pi/2}} + \underbrace{\frac{\langle q_i q_j \rangle - \langle p_i p_j \rangle}{2}}_{-b_{ij}^{\pi/2}} \sin 2\theta + \underbrace{\frac{-\langle q_i p_j \rangle - \langle p_i q_j \rangle}{2}}_{-c_{ij}^{\pi/2}} \cos 2\theta \quad (8.58)$$

Chapter 9

Experimental optimization of the pulse shaper

Contents

9.1 Flat pump	137
9.2 Optimising maximum squeezing	143
9.2.1 With amplitude shaping	143
9.2.2 With phase shaping	147
9.3 Optimising degenerate squeezing	150

In this chapter we present the measurement results of the SPOPO output using the techniques described in chapter 8 for the various optimal pump profiles $(\bar{f}_2^{(a)}, \bar{f}_2^{(\phi)}, \bar{f}_1^{(\phi)})$ obtained in chapter 7. We first measure the SPOPO output with the original Gaussian spectrum of our pump (no shaping). This gives us a reference of the SPOPO supermodes and squeezing levels in the absence of pump shaping. We then implement the pump shapes obtained in chapter 7, and measure significant changes in the supermodes shapes and squeezing levels.

These changes are in good qualitative agreements with the simulations of chapter 7. However, the purity of the measured quantum state is limited due to losses and to the finite spectral range and resolution of our multipixel detection. This is particularly limiting for one of the pump shape $(\bar{f}_1^{(\phi)})$ which gives supermodes with particularly complex spectral shapes.

9.1 Flat pump

In all measurements of this chapter the pump power was set to 20 mW. We first present the measurement without pump shaping. This gives us a reference of the SPOPO supermodes and squeezing levels in the absence of squeezing. We use 3 types of measurements that are complementary:

- Covariance matrix measurement with the multipixel homodyne detection technique (MHD) described in section 8.2. This measurement allows a full covariance matrix recovery but has a limited bandwidth and frequency resolution.
- Covariance matrix measurement with the standard homodyne detection technique

(SHD) described in section 8.1. This measurement has a larger bandwidth and double the frequency resolution of MHD, but does not work for all quantum states.

- Direct supermode quadrature measurement with standard homodyne detection. This measurement has better efficiency and lower losses compared to MHD, and SHD but does not recover the full quantum state and require knowledge of the supermodes spectral shape. We present the results of this measurement in section 9.2.

Fig. 9.1(a) shows the mean covariance matrix reconstructed from multipixel homodyne detection (MHD) over 100 acquisitions with the technique of section 8.3. Fig. 9.1(b), (c)

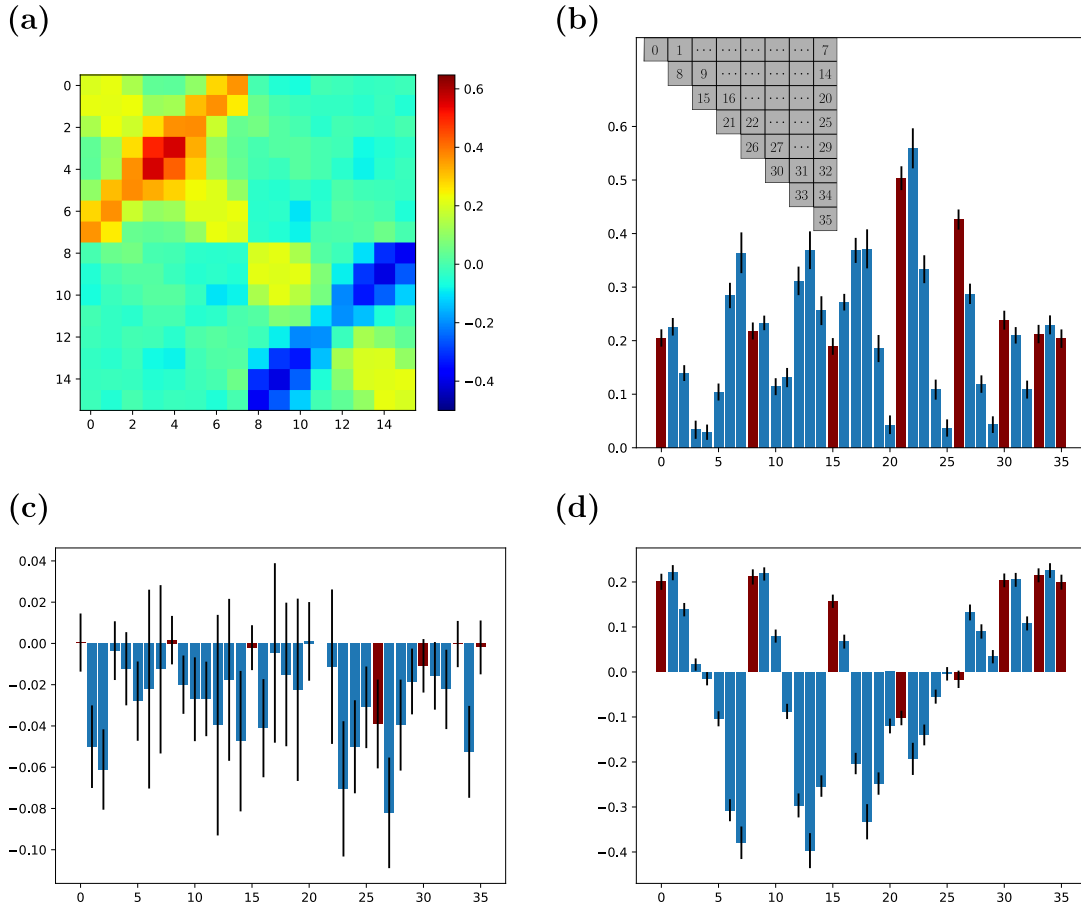


Fig. 9.1 Covariance matrix reconstructed from multipixel homodyne measurements without pump shaping. 100 acquisitions were taken. (a) shows the mean covariance matrix coefficients. (b), (c) and (d) show the mean coefficients and errors bars of the \mathbf{V}_{qq} , \mathbf{V}_{qp} and \mathbf{V}_{pp} blocks respectively. Since the covariance matrix is symmetric, (b), (c) and (d) only represents the coefficients of the upper triangular part. The coefficients are plotted row by row according to the lookup table in (b). Red bars correspond to the diagonal coefficients. 1 has been subtracted to the diagonal coefficients of the covariance matrix to highlight the variations in the off-diagonal terms.

and (d) show the mean coefficients and error bars (1 standard deviation) of the \mathbf{V}_{qq} , \mathbf{V}_{qp} and \mathbf{V}_{pp} blocks respectively. Since the covariance matrix is symmetric we only represent

its upper triangular part. They are represented in a 1D fashion (flattened) in the order given by the lookup table of Fig. 9.1(b) (reading row by row). All the coefficients of the \mathbf{V}_{qp} and \mathbf{V}_{pq} blocks are close to 0. As we saw in section 8.1.1, this is consistent with the pump being real.

We then recover the supermodes and squeezing levels from this covariance matrix using the decomposition presented in section 2.2.3. The first eigenvectors and squeezing levels are presented in Fig 9.2. The reconstructed estimates for the squeezing levels are

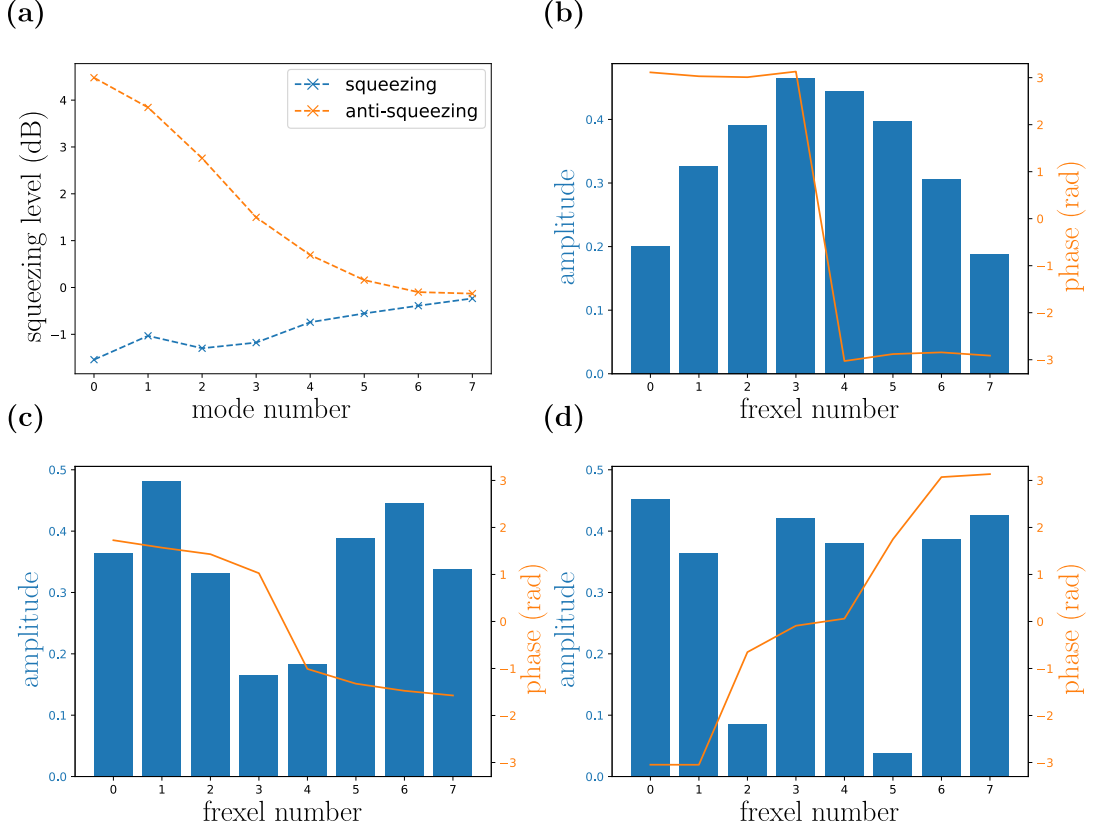


Fig. 9.2 Squeezing levels (a) and spectral shapes (b), (c), (d) of the first supermodes reconstructed from the multipixel homodyne measurement of the SPOPO output without pump shaping.

quite low (maximum ~ 1.5 dB). The higher anti-squeezing level indicates impurity in the reconstructed supermodes. The limited values of squeezing are caused by various loss sources:

- Intra-cavity losses in the SPOPO causes some intrinsic impurity in the output quantum state. This impurity increases with pump power (see Eq. (6.79)).
- Optical losses in the path from the SPOPO output to the multipixel detection. They are mostly due to the limited efficiency of the MHD gratings ($\sim 90\%$).
- Losses from homodyne detection visibility ($\mathcal{V} = 91\%$).
- Losses from the limited quantum efficiency ($\sim 80\%$) of the detectors.

- Even with no losses, some impurity will always appear as the exact supermodes can only be so well approximated by combinations of the frexel modes due to finite spectral resolution and range.

The eigenvectors are mostly real with flat phases or π phase shifts between frexels. Again this is consistent with the fact that our pump has no spectral phase. The frexel modes of the MHD technique are portion of the Gaussian spectrum of the LO beam and don't have a rectangular spectral shape (see Fig. 8.6). So in order to reconstruct a faithful estimates of the SPOPO supermodes we need to multiply the eigenvectors of Fig. 9.2 with the frexel mode shapes of Fig. 8.6. Doing so, we recover the supermode spectral shapes shown in Fig. 9.3. Note the reconstructed supermodes are not smooth because they are piecewise functions so there can be sharp edges at the interface between frexels. The supermode spectral shapes are close to Hermite-Gauss functions as expected from the results of section 6.3.2. We fit them with such functions to get an estimate of their width and central wavelength.

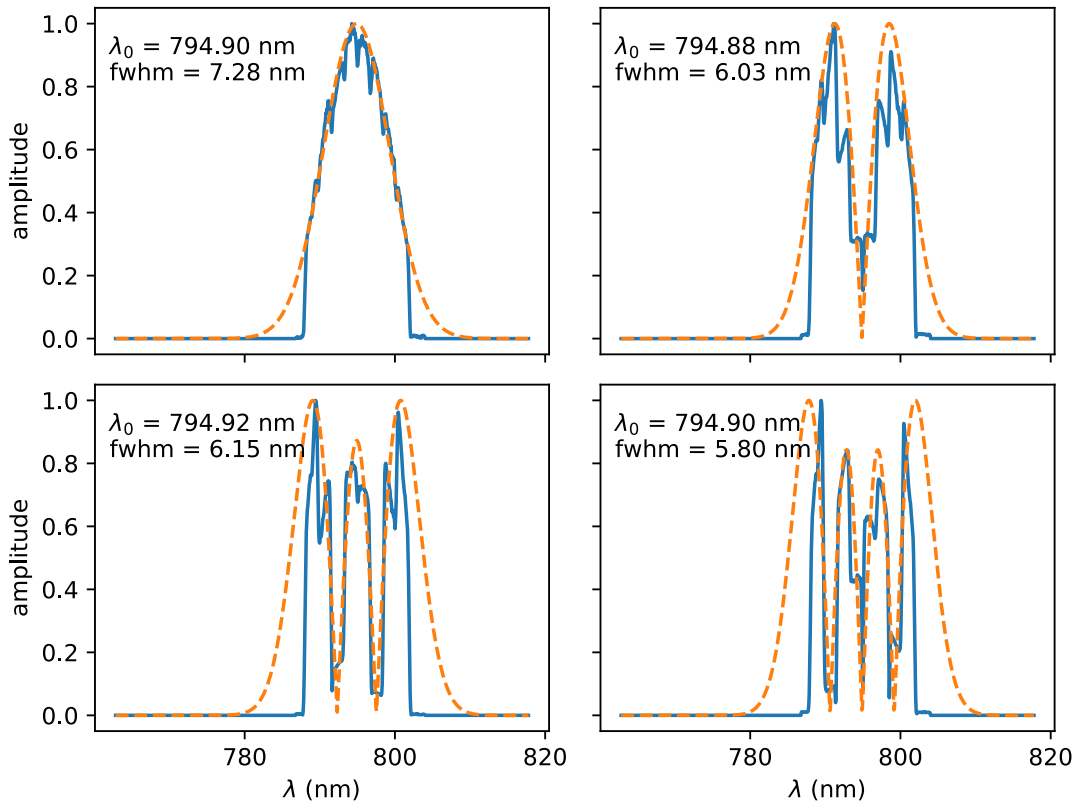


Fig. 9.3 Absolute amplitude of the supermodes reconstructed from multipixel measurement without pump shaping (in blue solid line) and fit by Hermite-Gauss functions (in orange dotted line). The central wavelength and FWHM of the fits are shown on each plot.

It is obvious from Fig. 9.3 that the multipixel homodyne detection is not broadband enough to encapsulate the whole supermodes, the 3rd supermode is already well outside the measurement range. We could change the design of the MHD to get a broader detection bandwidth. However, this would be at the cost of spectral resolution because we are

ultimately limited by the number of frequency bands of detection (8 in this case). Going to a broader spectral width would mean having a lower frequency resolution and we may not be able to resolve the spectral variations of higher order supermodes. In the current design, we are already at the limit of the necessary resolution to capture the spectral variations of the 4th supermode (see Fig. 9.3).

For this pump setting (no pump shaping), since the qp blocks of the covariance matrix are close to zero, we can use the standard homodyne measurement technique presented in section 8.1. This allows to perform a more broadband measurement, and also have a better resolution. We use 16 frexel modes and the LO spectrum broadened with the PCF fibre. Our detection spans a range from ~ 783 nm to ~ 807 nm. The qq and pp blocks of the covariance matrix measured using this technique are shown in Fig 9.4.

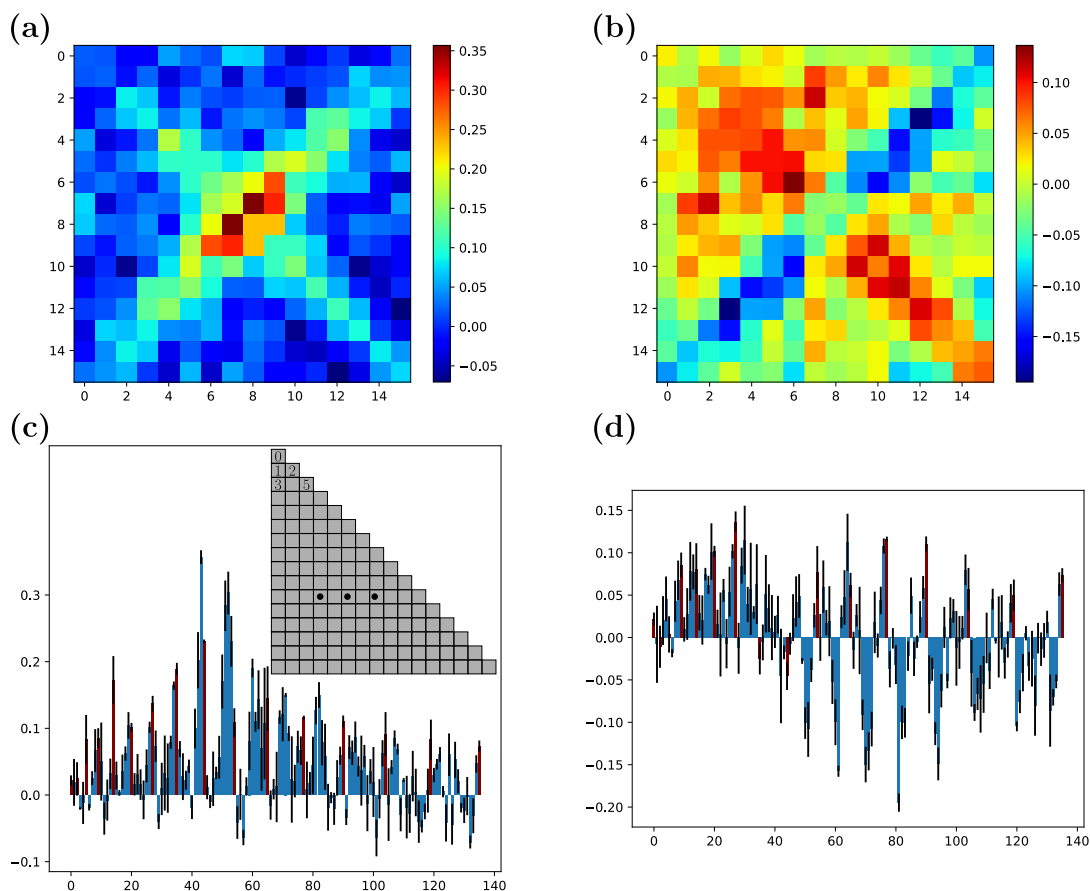


Fig. 9.4 V_{qq} (a), (c) and V_{pp} (b), (d) blocks of the covariance matrix of the SPOPO output, measured using the standard homodyne detection technique, without pump shaping. The second row shows the values and standard deviation of the matrix elements. Since the covariance matrix is symmetric, (c) and (d) only represents the coefficients of the lower triangular parts of V_{qq} and V_{pp} . The plotting order of the coefficients is given by the lookup table in (c). Red bars correspond to the diagonal coefficients. 1 has been subtracted to the diagonal coefficients to highlight the variations in the off-diagonal terms

The reconstructed \mathbf{V}_{qq} and \mathbf{V}_{pp} have similar shapes to the ones from MHD measurements (Fig. 9.1). \mathbf{V}_{qq} has significant positive anti-diagonal terms. This shows there are

qq correlations between symmetric pairs of frequencies around the central frequency. And \mathbf{V}_{pp} has significant negative anti-diagonal terms, showing pp anti-correlations between the same frequency band pairs. Note the scale of the coefficient here (Fig 9.4) is different to the one of the MHD measurements (Fig. 9.1). This is not surprising since the dimensionality of the covariance matrix is different (different frexel numbers).

From \mathbf{V}_{qq} and \mathbf{V}_{pp} , using the matrix decomposition introduced section 2.2.3, we reconstruct the supermodes spectral shape and their squeezing levels. Fig. 9.5 shows those squeezing/anti-squeezing levels and the corresponding supermodes. Again, as with the

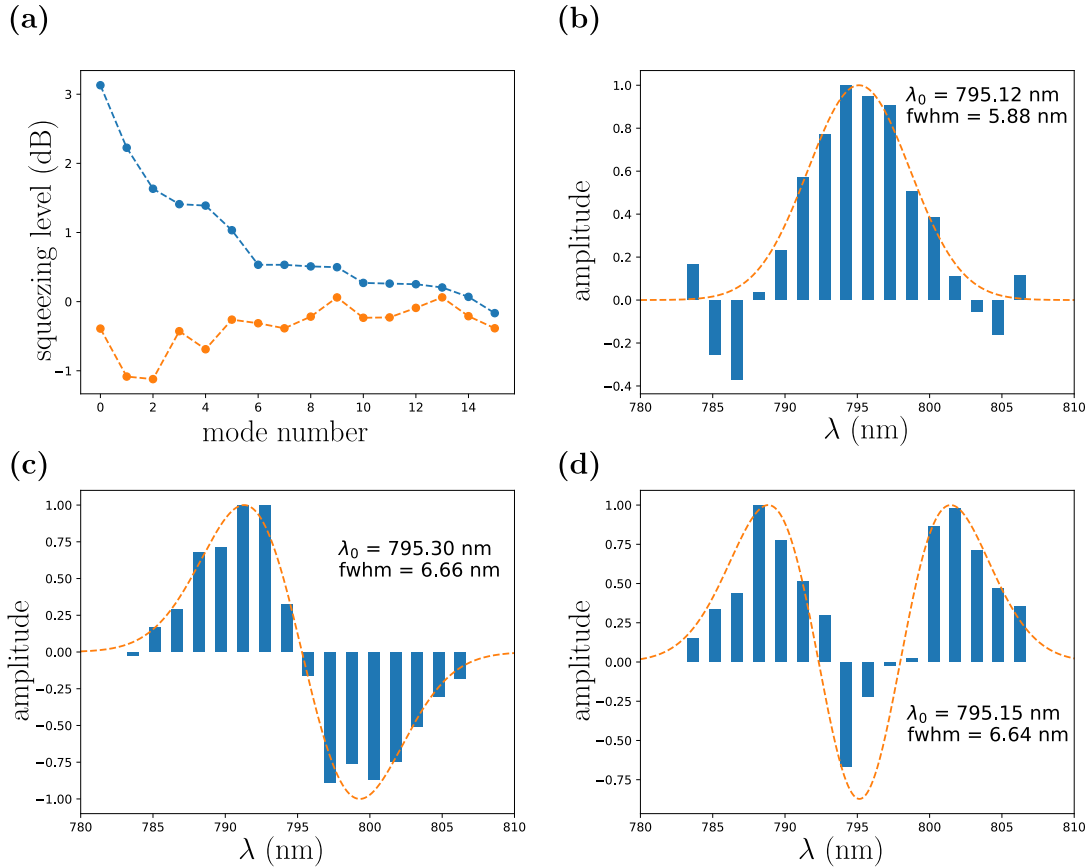


Fig. 9.5 (a) Squeezing levels and first supermodes (b), (c), (d) reconstructed from standard homodyne measurement without pump shaping. The mode are shown in order of decreasing anti-squeezing value. In (b), (c) and (d), the blue bars represent the eigenvector coefficients and the orange dotted lines are fit by Hermite-Gauss functions. The central wavelength and FWHM of the fits are reported each graphs.

MHD measurements, the squeezing values, and purity of the supermodes is limited by losses and the finite resolution and range of the measurement. Here, unlike with the MHD measurements, the frexel modes are essentially rectangular functions (see Fig. 8.2 b). Therefore we do not need to multiply the eigenvectors with the frexel modes. The eigenvectors already give a faithful representations of the supermodes. Since the SHD technique assumes $\mathbf{V}_{qp} = \mathbf{V}_{pq} = 0$, the supermodes are real functions. We also fitted the supermode with Hermite-Gauss function to determine their typical width.

The supermodes are quite well described by Hermite-Gauss functions as expected from the simulations of section 6.3.2. Actually, the first supermode shows some oscillations on the sides around 785 nm and 805 nm, where it becomes negative. This deviation from the Hermite-Gauss shape is also present in the numerical results from simulations (see Fig. 6.5). Indeed the supermodes are well described by Hermite-Gauss functions for large phase matching functions (short crystals). When the width of the phase matching and the width of the pump spectrum are comparable, we start seeing these oscillations in the supermodes. They are a residue of the sinc function of phase matching (see Eq. 6.44).

There is a discrepancy between the supermode widths obtained by MHD and SHD, especially for the first supermode. The supermodes obtained by SHD are more accurate because of the better spectral range and resolution. Still the supermode widths obtained by SHD (5.9 nm) are larger than the one predicted by the numerical simulations of Fig. 6.5 (4.2 nm). This cannot be an effect of intra-cavity dispersion as it tends to narrow the mode bandwidth, simulation taking dispersion into account predicted an even smaller width of ~ 3.2 nm (see Fig. 6.8). A possible explanation could be a spatial mismatch between the SPOPO cavity mode and the pump beam, due to walk off of the pump in the crystal for example. As a result the effective crystal length for PDC interaction would be smaller which would give broader supermodes.

Ultimately, to have a more accurate measurement of the supermodes squeezing levels, we need to do a direct homodyne measurement where the LO is shaped into the supermodes. For that we can use the estimate of the supermode shapes we have reconstructed from MHD and SHD measurements. We also did this measurement. The results are shown in Table. 9.1 of the following section, when we analyse the effect of amplitude pump shaping and compare it to the unshaped measurements of this section.

The measurements of this section validates both the multipixel and standard homodyne detection scheme to measure the SPOPO output. Both these technique are in good qualitative agreement between themselves and with the theoretical results of section 6.3.2.

9.2 Optimising maximum squeezing

We now look at the SPOPO output for various pump shaping profiles designed to maximise the squeezing level of the first supermode. We test two pump profiles (shown in Fig. 9.6): one with amplitude shaping only (profile $\bar{f}_2^{(a)}$) and one with phase shaping only (profile $\bar{f}_2^{(\phi)}$). It turns out that even the phase shaping profile corresponds to a real pump spectrum as the frexel phase values are either 0 or π . This means the qp terms of the covariance matrix should be null and we can use the SHD technique to reconstruct the covariance matrix.

9.2.1 With amplitude shaping

In this section, we use the optimal pump profile $\bar{f}_2^{(a)}$ found in section 7.3.1 (see Fig. 9.6(a)) that corresponds to maximising squeezing in the first supermode using amplitude shaping only.

Fig. 9.7 shows the covariance matrix reconstructed from multipixel homodyne measurement for 100 acquisitions. The covariance matrix obtained is qualitatively similar to the one in the previous section. The \mathbf{V}_{qp} blocks are close to 0 as expected (real pump). The anti-diagonal terms of \mathbf{V}_{qq} and \mathbf{V}_{pp} have a larger magnitude than the one obtained

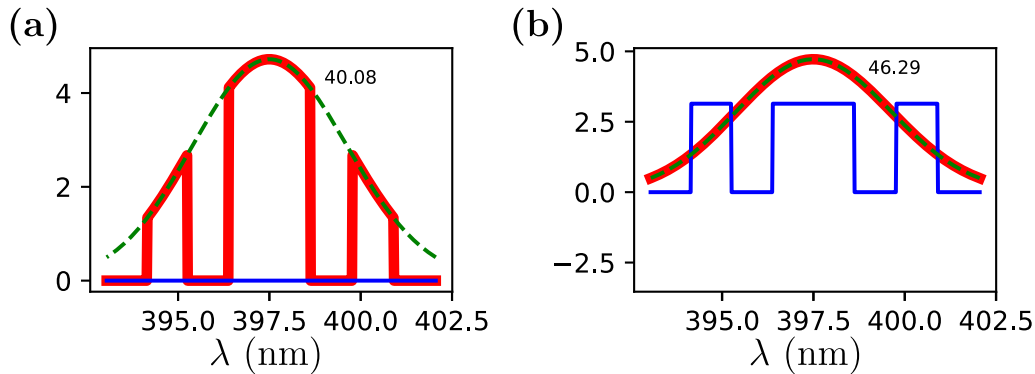


Fig. 9.6 (a) $\bar{f}_2^{(a)}$: pump profile that maximises squeezing in one mode with amplitude shaping. (b) $\bar{f}_2^{(\phi)}$: pump profile that maximises squeezing in one mode with phase shaping. The red line shows the amplitude (in a.u.), the blue line shows the phase (in rad) and the green dotted line represents the unshaped pump profile.

without pump shaping (see Fig. 9.1). So the qq correlations and pp anti-correlations of the symmetric frequency bands have been increased by the pump shaping.

Fig. 9.8 shows the reconstructed squeezing levels and eigenvectors. Again the eigenvectors are mostly real with flat phases or pi phase shifts between frexels elements. The squeezing levels do not seem to be improved by pump shaping, in fact they are slightly worse compared to the one of Fig. 9.2. The anti-squeezing level of the first few modes is significantly increased however. Based only on these observations, it is difficult to give a precise interpretation of the efficiency of pump shaping to maximise the squeezing level of the first mode. The increased anti-squeezing could be a sign that more squeezing is present in the first supermodes but is not visible in the noisy MHD measurements. To make sure the squeezing in the first mode is improved by pump shaping we will need to measure it directly.

Multiplying the eigenvectors of Fig. 9.8 by the frexels modes of Fig. 8.6 we obtain the supermodes of Fig. 9.9. The first supermode seems to be broadened by pump shaping as predicted by the simulation of section 7.3.1 (Fig. 7.13) but we reach the bandwidth limit of the multipixel homodyne detection.

To get a better estimate of the supermode spectrum we perform the covariance measurement with the SHD technique. Fig. 9.10 shows the qq and pp blocks of the covariance matrix measured using this technique. The increase in the magnitude of the anti-diagonal coefficients is confirmed by this measure.

Fig. 9.11 shows the reconstructed supermodes from the SHD measurements. There is no significant difference here in the squeezing and anti-squeezing levels compared with Fig. 9.5. Unlike with the MHD measurement we do not observe an increase in the first supermode anti-squeezing level.

The first supermode is significantly broadened by the pump shaping as expected from the simulations of section 7.3.1 (see Fig. 7.13). It goes from a 5.88 nm FWHM to a 8.44 nm FWHM (intensity). However this broadening seems to be limited to the first supermode in apparent contradiction with the simulation results. This is probably an effect of the limited measurement range. As higher order modes are broader they are more sensitive

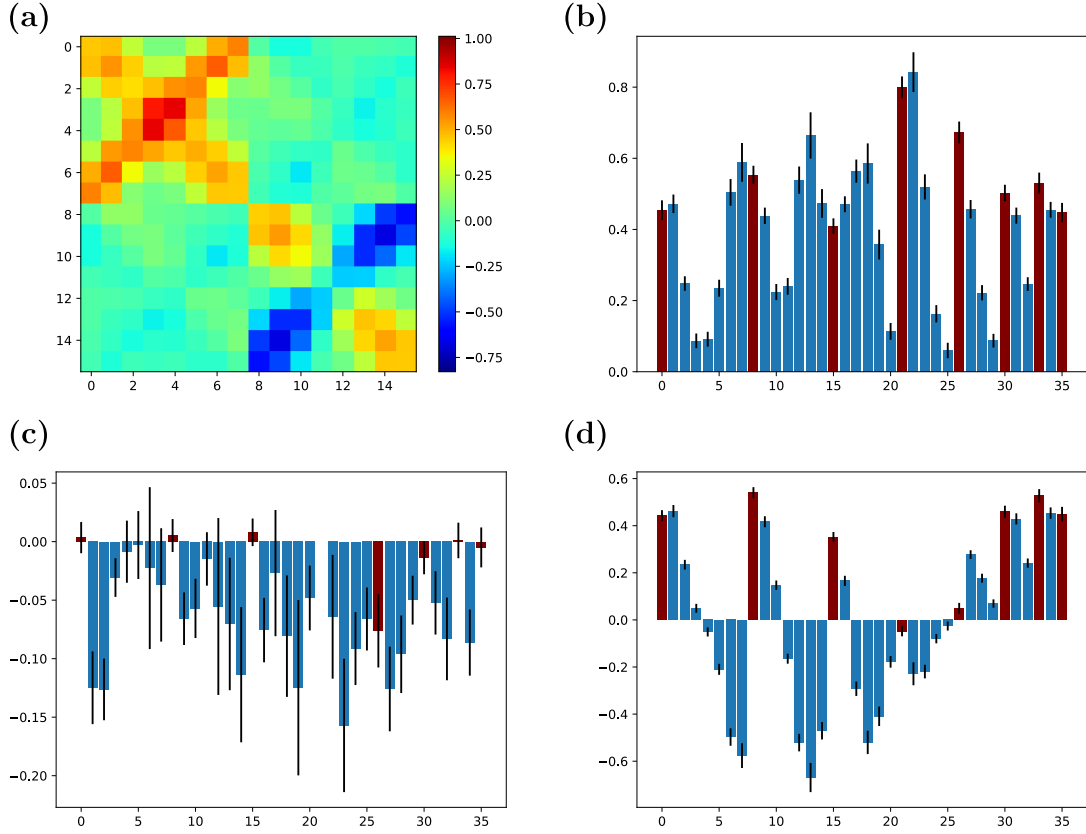


Fig. 9.7 Covariance matrix reconstructed from multipixel homodyne measurements with pump shape $\bar{f}_2^{(a)}$. 100 acquisitions were taken. (a) shows the mean covariance matrix coefficients. (b), (c) and (d) show the mean coefficients and errors bars of the \mathbf{V}_{qq} , \mathbf{V}_{qp} and \mathbf{V}_{pp} blocks respectively. Since the covariance matrix is symmetric, (b), (c) and (d) only represents the coefficients of the upper triangular part. The coefficients are plotted row by row according to the lookup table in (b). Red bars correspond to the diagonal coefficients. 1 has been subtracted to the diagonal coefficients of the covariance matrix to highlight the variations in the off-diagonal terms.

to this effect.

Note the 3rd mode shown in Fig 9.11 follows a 3rd order Hermite-Gauss function, when we would expect it to be a 2nd order Hermite-Gauss function. This is just a mode ordering issue. Here we order modes by decreasing anti-squeezing level. Mode number 4 is not shown in Fig. 9.11 but it follows a 2nd order Hermite-Gauss function. It actually correspond to the 3rd supermode and if we look at the squeezing level we see that it is more squeezed than mode number 3. In other word, classical noise (from measurement, losses, ...) is not equal for all the supermodes. So the reconstructed squeezing levels of Fig. 9.11 are each affected differently by noise. As a result the reconstructed squeezing and anti-squeezing level do not necessarily decrease as mode order increase, as would be expected for the theoretical supermodes.

To determine whether pump shaping did improve squeezing in the supermode, we measure squeezing directly with and without amplitude pump shaping. To do that we

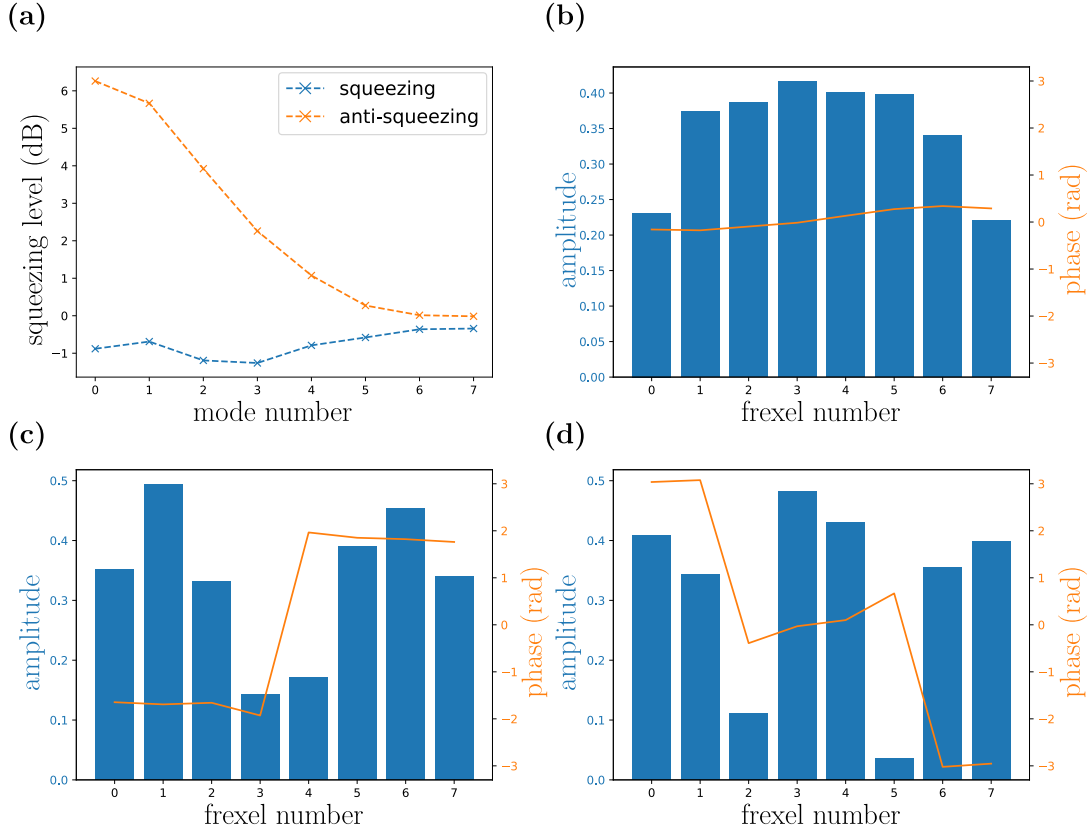


Fig. 9.8 Squeezing levels (a) and spectral shapes (b), (c), (d) of the first supermodes reconstructed from the multipixel homodyne measurement of the SPOPO output with pump shape $\bar{f}_2^{(a)}$.

shape the LO into the first 4 modes of an Hermite-Gauss basis. The squeezing and anti-squeezing levels are then directly determined from the signal variance minima and maxima (respectively) when scanning the LO phase. For measurements without pump shaping we use a HG basis with a ~ 6 nm FWHM, (this correspond to the width of the first supermode reconstructed in Fig. 9.5). For measurements without pump shaping we use a HG basis with a ~ 8.5 nm FWHM, (this correspond to the width of the first supermode reconstructed in Fig. 9.11). Results are shown in Table 9.1.

mode	Squeezing level (dB)		Anti-squeezing level (dB)	
	no pump shaping	pump shaping	no pump shaping	pump shaping
HG ₀	3.79 (4.43)	3.78 (4.42)	4.32 (4.58)	4.55 (4.82)
HG ₁	1.30 (1.45)	1.81 (2.04)	3.14 (3.36)	4.06 (4.31)
HG ₂	0.70 (0.78)	0.16 (0.18)	2.81 (3.01)	3.06 (3.27)
HG ₃	0.63 (0.70)	0.53 (0.59)	1.83 (1.98)	2.72 (2.92)

Table 9.1 – Results of direct squeezing measurement with and without amplitude pump shaping. Squeezing values are corrected for dark noise and the value in parenthesis indicate the estimated value of squeezing corrected from losses (visibility). We model losses as vacuum noise coupling.

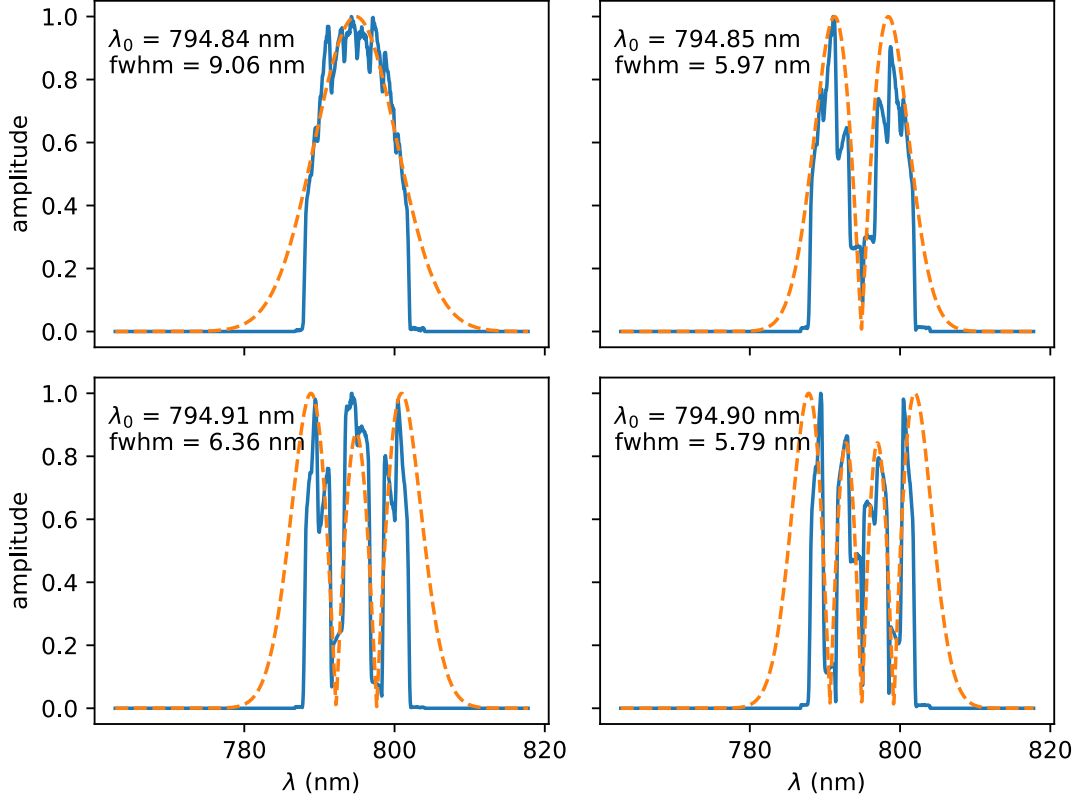


Fig. 9.9 Absolute amplitude of the supermodes reconstructed from multipixel homodyne detection measurement for amplitude pump shaping.

When using pump shaping, there is an increase of ~ 0.6 dB in the squeezing of the second supermode (if we look at the loss corrected values). Although there is no measurable increase in the squeezing of the first supermode, the increased anti-squeezing value does suggest that the pump shaping works as expected. There is also a decrease of the squeezing level of the other supermodes. So the pump shape $\bar{f}_2^{(a)}$ does affect the squeezing levels and the supermode shapes as predicted by the simulations (see Fig. 7.13). The effect is small however. It would need to be confirmed with other measurements. In particular, to make sure this is not an effect of the chosen measurement basis, we would need to perform the measurements for a range of HG bases of varying width. This is left for future work.

9.2.2 With phase shaping

We now use the pump phase shaping profile $\bar{f}_2^{(\phi)}$ obtained in section 7.3.1. We recall this pump profile in Fig. 9.6. This shape corresponds to maximising squeezing in the first supermode using phase shaping only (it is also the optimum when using full shaping of phase and amplitude).

Fig. 9.12 shows the covariance matrix reconstructed from multipixel homodyne measurement. The covariance matrix obtained is similar to the one in section 9.2.1 with amplitude shaping. But there are non negligible terms in the qp blocks.

Fig. 9.13 shows the reconstructed squeezing levels and eigenvectors. The pump shaping does not seem to change the squeezing values significantly. The anti-squeezing increases

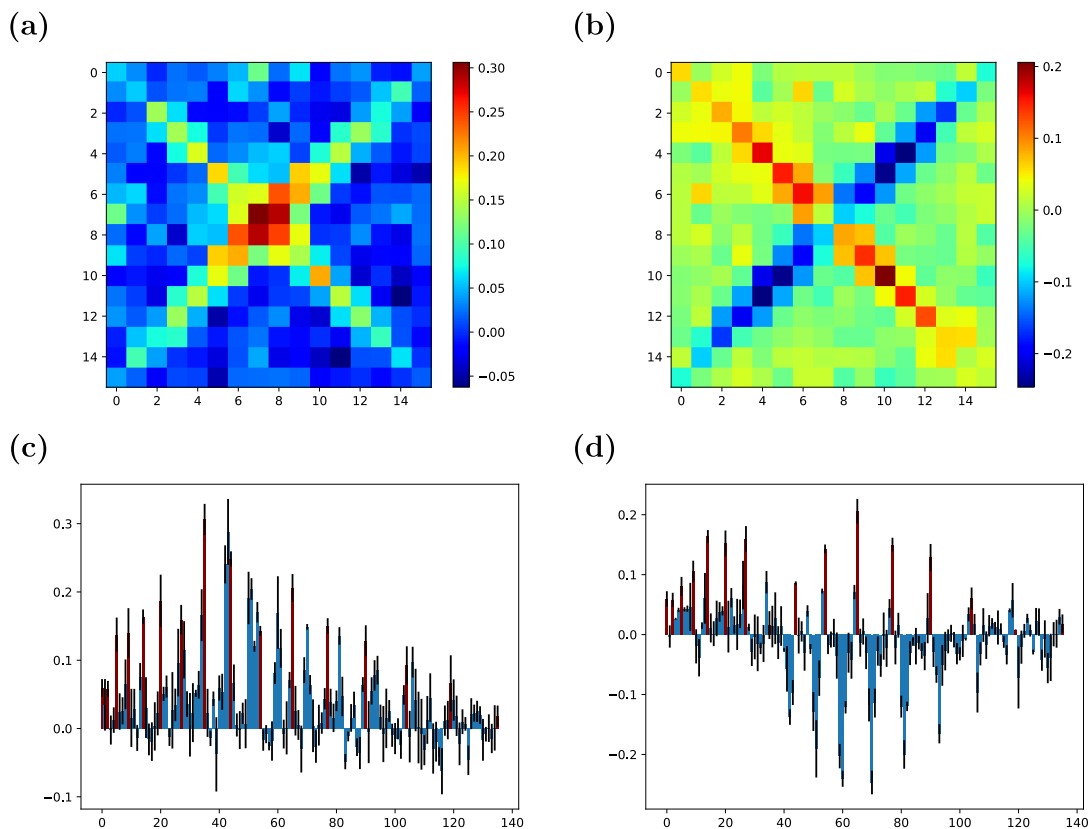


Fig. 9.10 V_{qq} (a), (c) and V_{pp} (b), (d) blocks of the covariance matrix of the SPOPO output, measured using the standard homodyne detection technique, with pump shape $\bar{f}_2^{(a)}$. The second row shows the values and standard deviation of the matrix elements. Since the covariance matrix is symmetric, (c) and (d) only represents the coefficients of the lower triangular parts of V_{qq} and V_{pp} . The plotting order of the coefficients is the same as in Fig. 9.4. Red bars correspond to the diagonal coefficients. 1 has been subtracted to the diagonal coefficients to highlight the variations in the off-diagonal terms.

slightly. Here, the second, and third eigenvectors are not real, they have a significant spectral phase. But it is a linear spectral phase and could be explained by a drift in the LO delay line. All the phases are referenced to the LO phase, if there is a mismatch of the optical delay between the LO beam and the signal beam paths, a contribution will appear in the qp terms of the covariance matrix. This contribution reflects the linear spectral phase between the frexel modes. The reconstructed supermodes show this linear spectral phase.

Multiplying the eigenvectors by the frexels modes of Fig. 8.6 we obtain the supermodes of Fig. 9.14. Unlike for amplitude pump shaping the first supermode is not significantly broadened. So for the MHD measurement, pump shaping seems to have a negligible effect on the SPOPO output.

To get a better estimate of the supermode spectrum we perform the covariance measurement with the standard homodyne measurement technique. Fig. 9.15 shows the qq and pp blocks of the covariance matrix measured using this technique and Fig. 9.16 shows

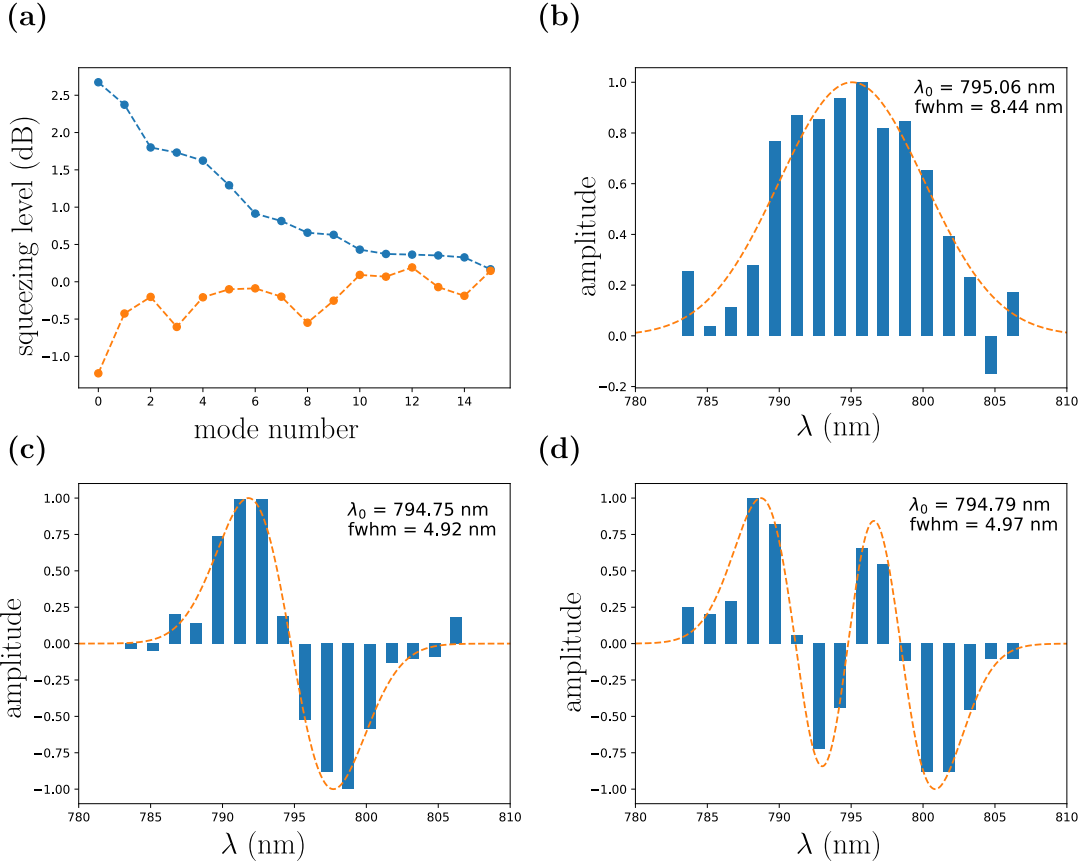


Fig. 9.11 Supermodes reconstructed from standard homodyne measurement and fit by Hermite-Gauss functions. The mode are shown in decreasing anti-squeezing value order.

the reconstructed supermodes. The covariance matrix obtained is similar to the one in section 9.2.1.

The order of the supermode is again affected by noise. The actual first supermode is the mode labelled in Fig. 9.16 as mode number 2. This is apparent in its higher squeezing level. The squeezing of the first supermode is slightly increased compared to the measurement without pump shaping (see Fig. 9.4). The first supermode (on the bottom right graph) is significantly broadened by the pump shaping as predicted by simulations, it goes from a 5.88 nm FWHM to a 8.20 nm FWHM (intensity).

To confirm the effects of the pump shape $\bar{f}_2^{(\phi)}$ on the squeezing levels we would need to measure the squeezing directly, by shaping the LO into the estimated supermode spectral shapes (as we did for $\bar{f}_2^{(a)}$). This is left for future work.

In conclusion, both pump shape designed to increase squeezing in the first supermode seem to work. This was confirmed in the case of amplitude pump shaping, by direct measurement of the supermode squeezing. Both pump shapes increase significantly the width of the first supermode as was predicted by simulations. The higher order supermode seem unaffected but this is probably just an effect of the finite measurement range. For the case of phase shaping, more measurement would be required to confirm the increase in squeezing. In particular the MHD measurement does not agree with the SHD measurement

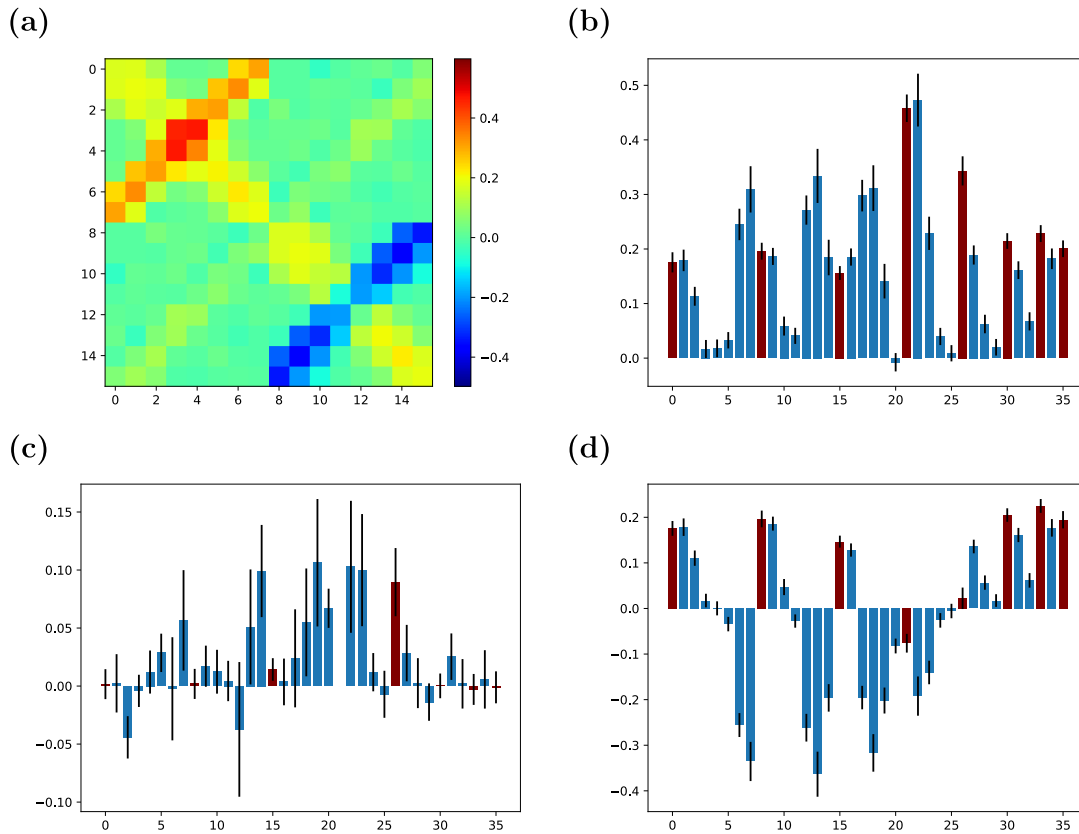


Fig. 9.12 Covariance matrix reconstructed from multipixel homodyne measurements with pump shape $\bar{f}_2^{(\phi)}$. 100 acquisitions were taken. (a) shows the mean covariance matrix coefficients. (b), (c) and (d) show the mean coefficients and errors bars of the \mathbf{V}_{qq} , \mathbf{V}_{qp} and \mathbf{V}_{pp} blocks respectively. Since the covariance matrix is symmetric, (b), (c) and (d) only represents the coefficients of the upper triangular part. The coefficients are plotted row by row according to the lookup table in (b). Red bars correspond to the diagonal coefficients. 1 has been subtracted to the diagonal coefficients of the covariance matrix to highlight the variations in the off-diagonal terms.

and shows no improvement in squeezing nor any change in supermode shape.

9.3 Optimising degenerate squeezing

The last pump shape we investigate is $\bar{f}_1^{(\phi)}$ (see Fig. 9.17). It is the shape that maximises the squeezing degeneracy according to the machine learning simulations.

Fig. 9.18 shows the covariance matrix reconstructed from multipixel homodyne measurement. The qp terms of the covariance matrix are close to 0 as the pump is real. The covariance matrix differs significantly from the one of sections 9.1 and 9.2. There are still significant off diagonal terms in the \mathbf{V}_{qq} and \mathbf{V}_{pp} blocks. But the structure of the qq and pp correlations is more complex than before. In particular the correlated/anti-correlated frexel are no longer distributed pairwise around the central frequency.

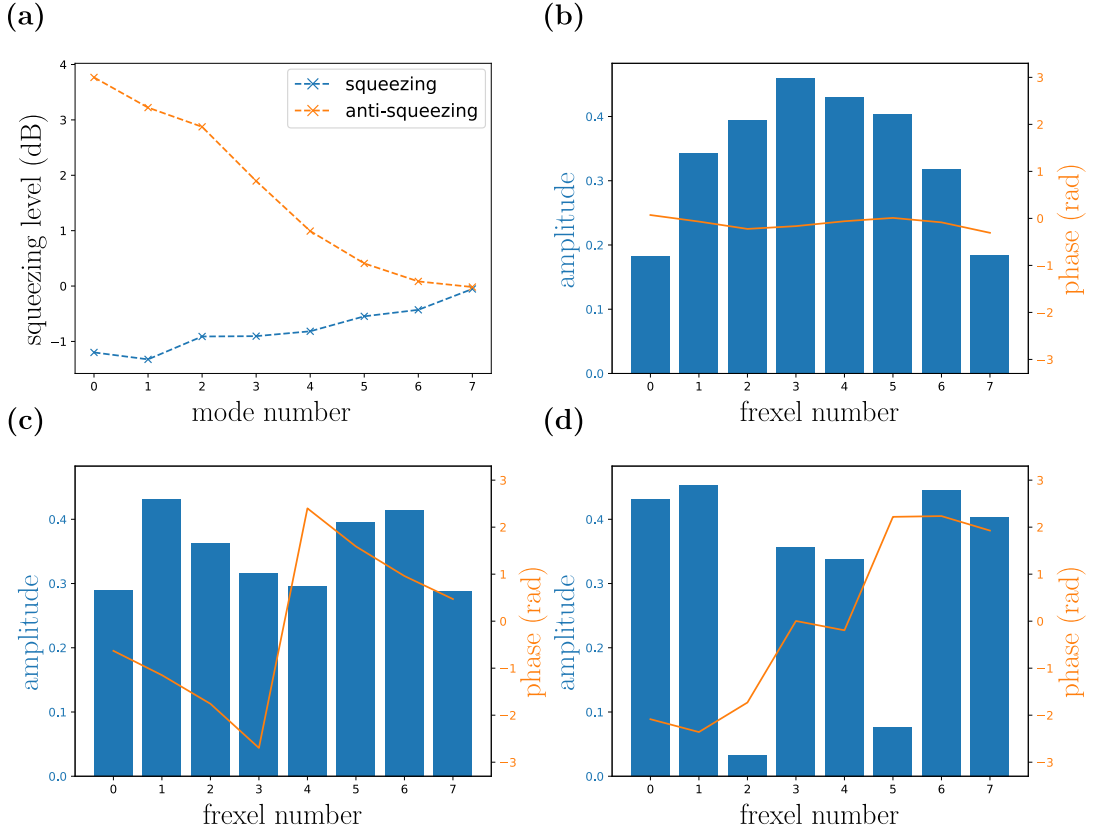


Fig. 9.13 Squeezing levels (a) and spectral shapes (b), (c), (d) of the first supermodes reconstructed from the multipixel homodyne measurement of the SPOPO output with pump shape $\bar{f}_2^{(\phi)}$.

Fig. 9.19 shows the corresponding squeezing levels and eigenvectors reconstructed with the usual technique. It is hard to affirm just from this measurement whether the squeezing degeneracy is increased by this pump shaping. The squeezing distribution among the first few supermodes does not seem to be significantly “flatter” than in the case without pump shaping (Fig. 9.2). There seem to be a flattening effect on the anti-squeezing level though. The anti-squeezing levels are also lower on the whole than in the results of Fig. 9.2.

The supermode shapes are significantly altered by the pump shaping. They are no longer close to Hermite-Gauss functions. Despite their complicated shapes, the supermode are still close to real functions. The frexel relative spectral phases are multiples of π (or close). This is consistent with the qp blocks of the covariance matrix being close to 0.

The shapes of the supermode were too complicated for us to measure the squeezing levels with a direct measurement. The frequency resolution of our LO pulse shaper is small enough in theory to imprint the supermode shapes on the LO. However, with shapes given by the eigenvectors of Fig. 9.19, a small error in the central frequency, is enough to obtain an entirely different mode. The accuracy of the LO pulse shaper to realise those shapes is therefore highly dependent on the pulse shaper frequency calibration. We did not manage to reproduce the supermode shapes with enough accuracy to successfully do a direct squeezing measurement.

We do not have any simulated shape to which we can compare those modes either.

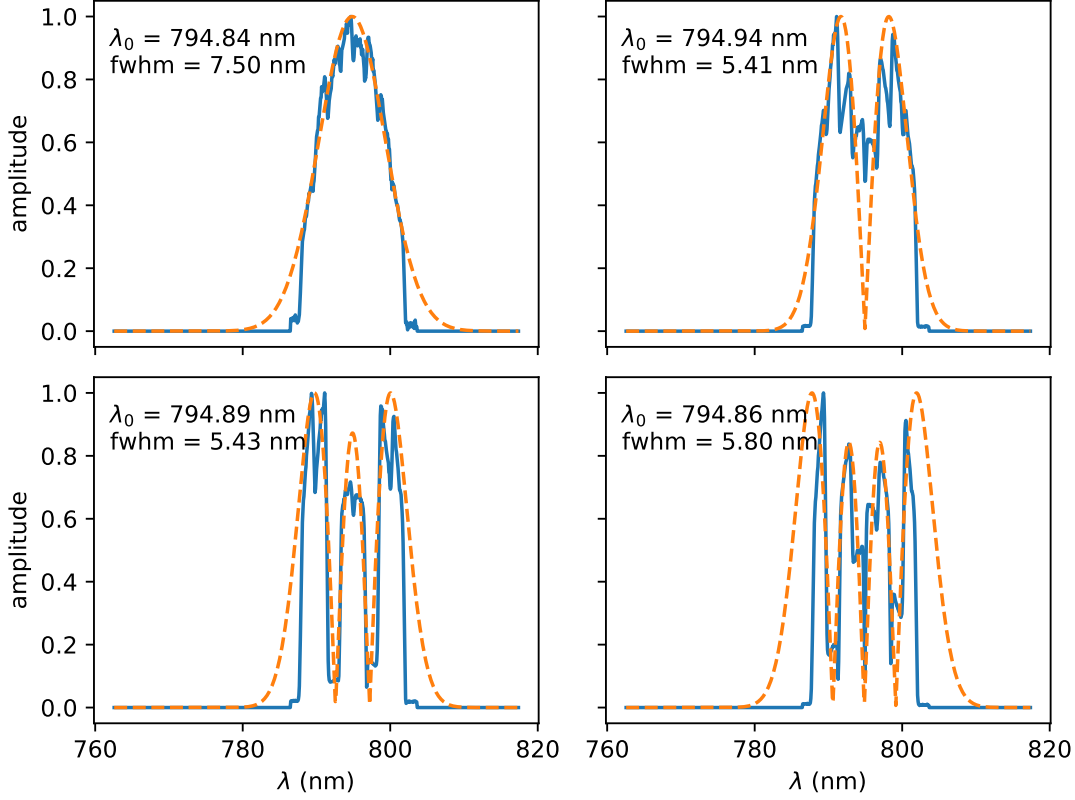


Fig. 9.14 Absolute amplitude of the supermodes reconstructed from multipixel measurement for the pump phase shaping profile that maximises squeezing in the first supermode.

Indeed our simulation model for pump shaping optimisation did not take into account intra-cavity dispersion. As we saw, the modes we obtained with the simulation for the pump shape $\bar{f}_1^{(\phi)}$ were way too broadband and would be filtered by the SPOPO cavity in a realistic setting where dispersion is present. Further work needs to be done to adapt the machine learning optimisation to include the effects of intra-cavity dispersion, so that realistic and measurable modes could be obtained from the simulations.

To conclude this chapter let us recall the important results we obtained here. We investigated the SPOPO output quantum state for three pump shapes: $\bar{f}_1^{(\phi)}$, $\bar{f}_2^{(a)}$ and $\bar{f}_2^{(\phi)}$ (see Fig. 9.17 and 9.6)). We used 3 measurement techniques: the MHD which allows full covariance matrix recovery even when the pump and the supermodes are not real. The SHD which has better frequency range and resolution but cannot recover the full covariance matrix and is limited to cases where the pump is real. And the direct squeezing measurement, which has reduced losses compared to the other two techniques but require knowledge of the supermodes to be measured.

For $\bar{f}_2^{(a)}$ and $\bar{f}_2^{(\phi)}$, we reconstructed the supermodes of the SPOPO output with MHD and SHD and confirmed the effects predicted by our simulation. The supermodes are real, they still have Hermite-Gaussian shapes and their bandwidths are increased by the pump shaping. For $\bar{f}_2^{(a)}$ we even confirmed the increase of squeezing in the second supermode

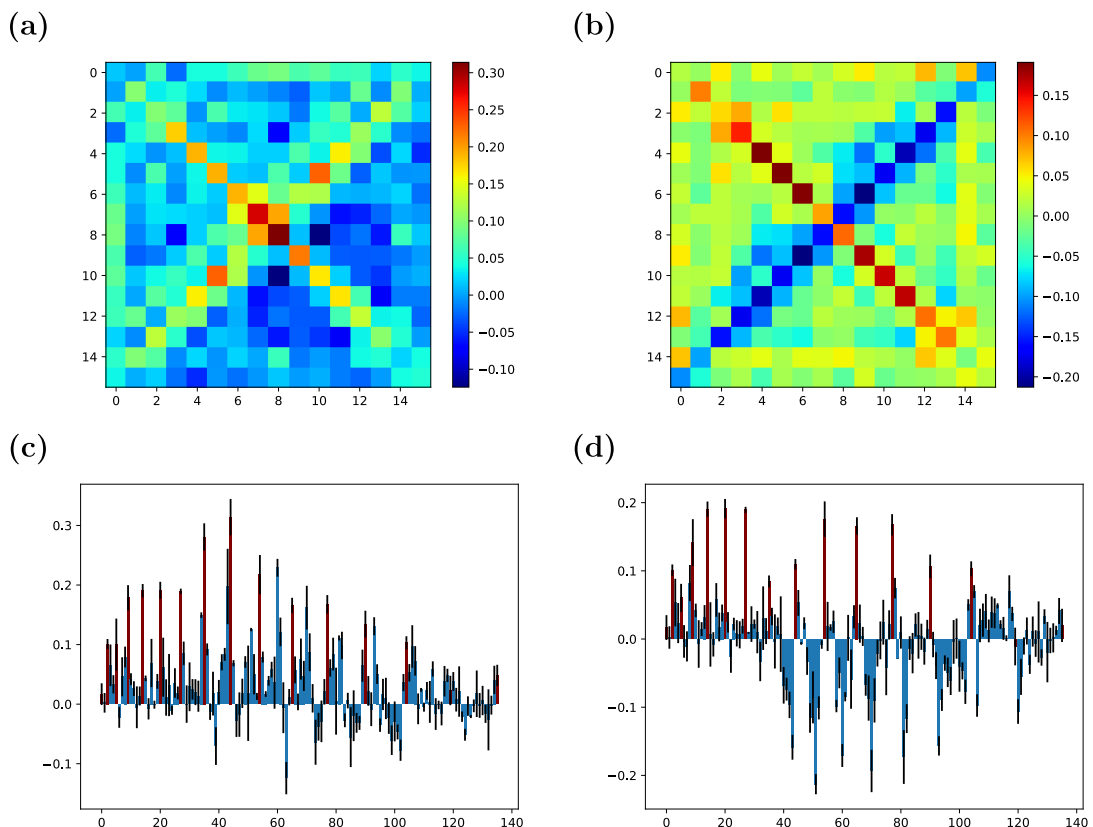


Fig. 9.15 V_{qq} (a), (c) and V_{pp} (b), (d) blocks of the covariance matrix of the SPOPO output, measured using the standard homodyne detection technique, with pump shape $\bar{f}_2^{(\phi)}$. The second row shows the values and standard deviation of the matrix elements. Since the covariance matrix is symmetric, (c) and (d) only represents the coefficients of the lower triangular parts of V_{qq} and V_{pp} . The plotting order of the coefficients is the same as in Fig. 9.4. Red bars correspond to the diagonal coefficients. 1 has been subtracted to the diagonal coefficients to highlight the variations in the off-diagonal terms.

with a direct measurement.

For $\bar{f}_1^{(\phi)}$, we only used MHD measurements. The covariance matrix was altered significantly by this pump shaping and the resulting supermodes have complicated shapes. The anti-squeezing levels do seem to be “flattened” by this pump shaping as predicted but further investigation is required. We were not able to successfully measure the squeezing level directly. The complex spectral shapes are hard to realise experimentally. Even if our pulse shaper resolution is sufficient, it is hard to guarantee that the different mode we shape the LO in will be orthogonal. This is due to the imperfect pulse shaper calibration in terms of frequency and phase mapping.

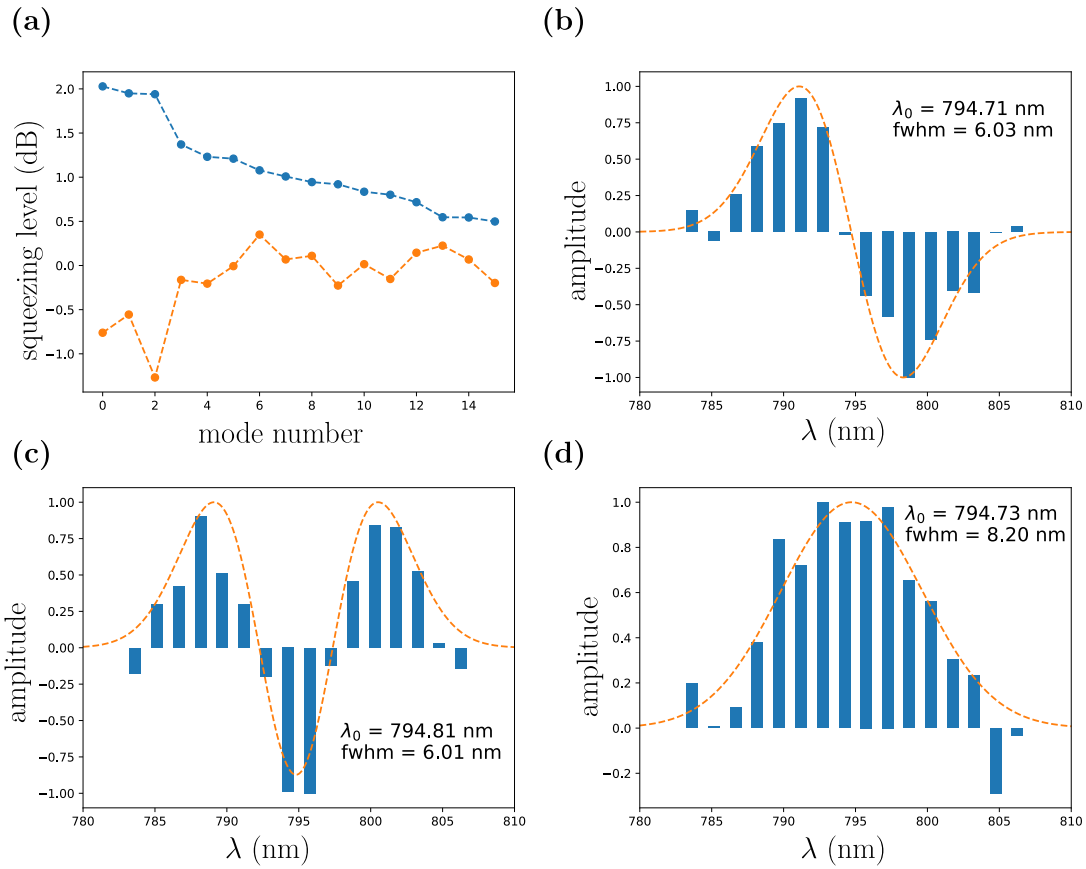


Fig. 9.16 Supermodes reconstructed from standard homodyne measurement and fit by Hermite-Gauss functions. The mode are shown in decreasing anti-squeezing value order.

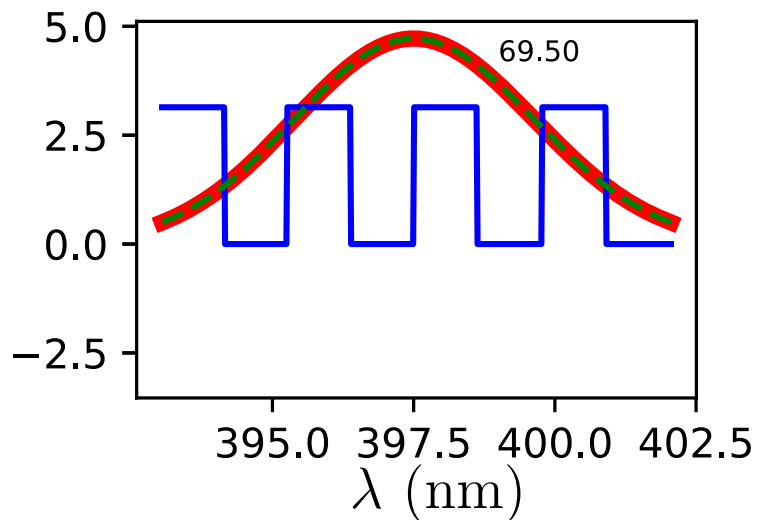


Fig. 9.17 $\bar{J}_1^{(\phi)}$: pump profile that maximises squeezing degeneracy with phase shaping. The red line shows the amplitude (in a.u.), the blue line shows the phase (in rad) and the green dotted line represents the unshaped pump profile.

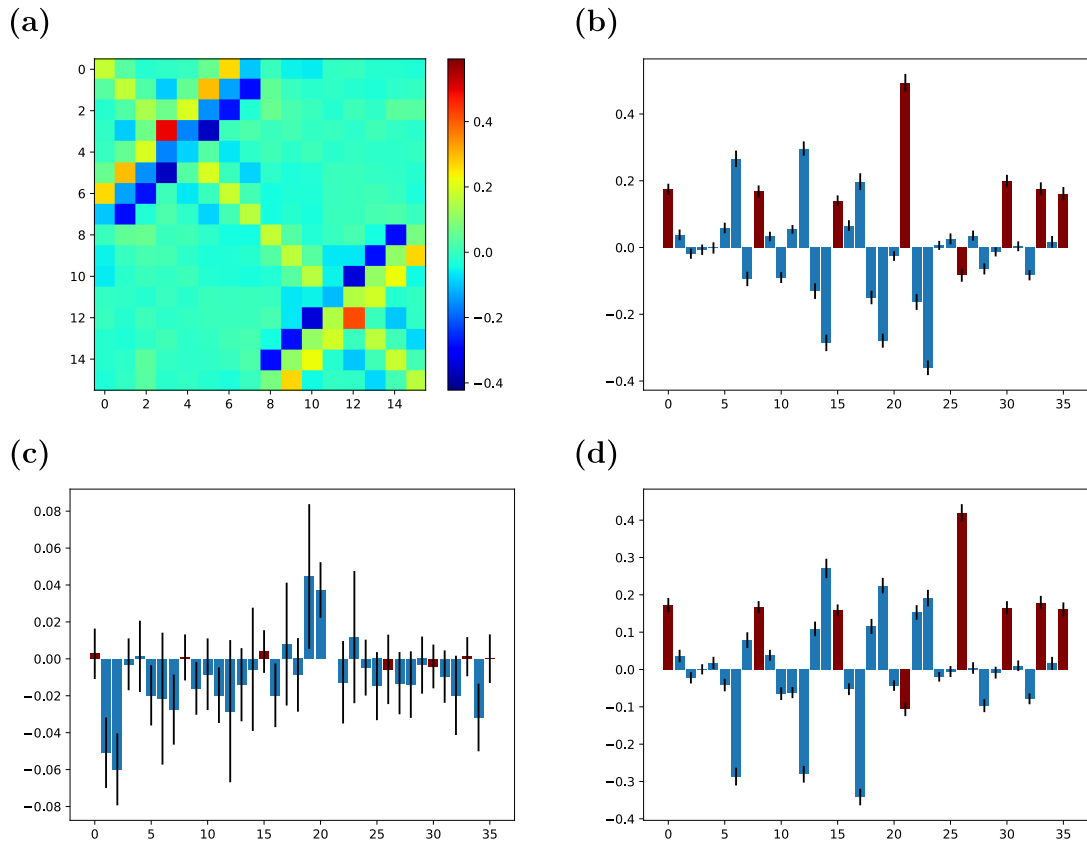


Fig. 9.18 Covariance matrix reconstructed from multipixel homodyne measurements with pump shape $\bar{f}_1^{(\phi)}$. 100 acquisitions were taken. (a) shows the mean covariance matrix coefficients. (b), (c) and (d) show the mean coefficients and errors bars of the \mathbf{V}_{qq} , \mathbf{V}_{qp} and \mathbf{V}_{pp} blocks respectively. Since the covariance matrix is symmetric, (b), (c) and (d) only represents the coefficients of the upper triangular part. The coefficients are plotted row by row according to the lookup table in (b). Red bars correspond to the diagonal coefficients of the covariance matrix to highlight the variations in the off-diagonal terms.

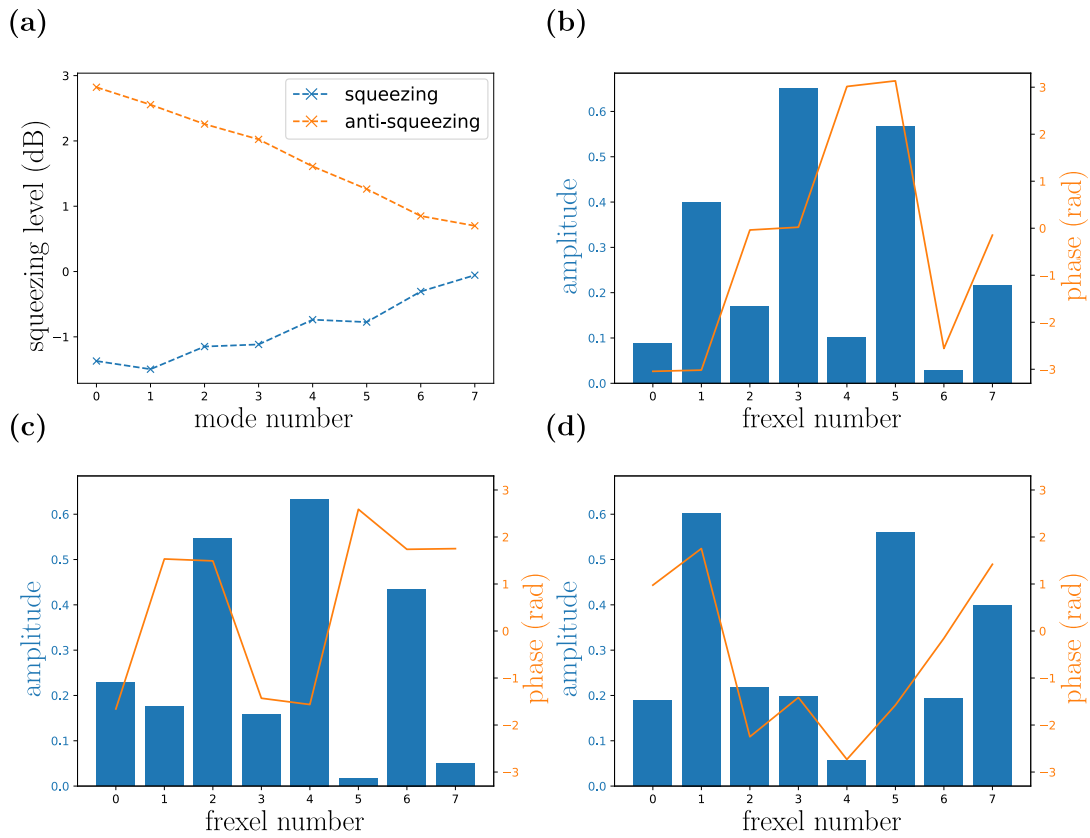


Fig. 9.19 Squeezing levels (a) and spectral shapes (b), (c), (d) of the first supermodes reconstructed from the multipixel homodyne measurement of the SPOPO output with pump shape $\bar{f}_1^{(\phi)}$.

Conclusion and outlook

In the course of this thesis, we engineered multimode entangled Gaussian states by tuning the spectral shape of a pulsed laser beam synchronously pumping an optical parametric oscillator (SPOPO). This work contains two significant advances. The first concerns the optimisation of the SPOPO pump using machine learning algorithm. The second concerns the study of the effect intra-cavity dispersion on the SPOPO output.

Using a pulse shaper, it is possible to tune the SPOPO pump spectrum and tailor the properties of the SPOPO output state. As long as intra-cavity dispersion is neglected, the pump spectral shape along with the phase matching properties of the non linear crystal fully determines the SPOPO output quantum state. But this relation between the pump shape and the SPOPO output is non trivial. One must therefore use an optimisation process in order to find a pump spectrum that produces a given desirable output quantum state. It is possible to estimate the SPOPO output using numerical calculations, so the pump shape can be optimised numerically. This has been initiated in the work of Francesco Arzani and Jonathan Roslung [164] who used evolutionary algorithm for pump optimisation. However, various experimental limitations like the finite resolution of the pulse shaper or the measurement losses meant that the optimal pump shape found could not be implemented nor the SPOPO output state measured. To obtain measurable quantum states with practically achievable pump shapes, we ran optimisations with a reduced number of pump parameters. For that we used machine learning algorithms. This was a way to confirm the previously obtained results in an independent way. A longer term goal was to adapt these algorithm to a live optimisation of the experimental set-up. This remains to be done but would be very interesting as any pump optimisation is ultimately limited by experimental factors (pulse shaper resolution, measurement losses, ...). A live optimisation would automatically include those detrimental effects to find practical pump shapes that achieve a desirable output quantum state.

In an effort towards the design of a fully automated set-up, a machine learning algorithm based on artificial neural network (ANN) was put to the task of pump shaping optimisation. This algorithm, designed by Aaron Tranter and Harry Slatyer, already proved to be efficient in the live optimisation of a complex experimental set-up and was tested on a “toy” set-up for the optimisation of a spatial light modulator. The (ANN) was implemented on the numerical simulations of pump shaping with a reduced number of parameters. Having less parameters ensured a faster optimisation but also the experimental feasibility of the obtained pump shapes. The first implementation on numerical calculations rather than directly on the experimental set-up was also due to the worldwide sanitary crisis. The results of the ANN were confirmed with a second machine learning algorithm: a reinforcement learning algorithm based on projective simulation.

The pump was optimised for two target states. The first state has the highest possible

squeezing level concentrated in one mode. This state is particularly relevant for metrology. Indeed, in single parameter estimation with a multimode Gaussian state, the best estimate can be obtained when all the squeezing resource is concentrated in one mode. The second state has degenerate squeezing levels among as many modes as possible. This state is more relevant for measurement based quantum computation (MBQC). Indeed this state can be used to construct a good approximation of a continuous variable cluster state.

The obtained optimal pump shapes were then implemented in the experiment. In order to measure the SPOPO output, a multipixel homodyne detection device was rebuilt. For the first target state, the measurement confirmed the efficiency of the proposed pump shapes in optimising squeezing in a single mode. The influence of pump shaping on the SPOPO supermode shapes was also in good qualitative agreement with what was predicted by the simulations. For the second target state, the measurements were not sufficient to confirm the effects of pump shaping on the squeezing degeneracy. Nevertheless the supermodes spectral shapes were successfully measured.

When we ran the pump numerical optimisation, we used a single pass PDC model to predict the SPOPO output, all cavity effects were neglected. But we showed that certain pump shapes can lead to a significant spectral broadening of the SPOPO output. This is the case for pump shapes optimised for the second target state, for example. In this case intra-cavity dispersion can no longer be neglected. Based on a previous modelling of the SPOPO [160] (without dispersion), we studied the effect of intra-cavity dispersion with numerical simulations. In the conditions of our experimental set-up, the main effect of intra-cavity dispersion is simply to limit the bandwidth of the SPOPO output. It also limits the number of supermodes with significant squeezing levels. In the cases we studied, the overall supermode shapes remained similar. A more complex effect on the shapes of the SPOPO supermodes is not excluded however. This could be the case for particular pump shaping conditions, when the SPOPO supermodes have complicated spectral shapes, but it remains to be studied.

Two main lines of research appear particularly relevant for extending the present work. On the simulation side, the intra-cavity modelling should be included in the pump shape numerical optimisation so that the SPOPO output can be predicted accurately, regardless of the pumping conditions. On the experimental side, the machine learning optimisation can be adapted to control and optimise the pump and LO beam pulse shapers in real time. The covariance matrix reconstruction can be improved by increasing the frequency range and resolution of the measurements and reducing losses. For reducing losses, more efficient grating and photodiodes with higher quantum efficiencies can be used. The frequency range and resolution can be improved if we have more frequency bands. For that the LO spectrum needs to be broadened even further, and more photodiodes need to be added to the multipixel homodyne detection.

Appendix A

Appendix

A.1 A squeezed state QRNG

Part of the work of my PhD concerns a subject that has no direct link with the work on SPOPO pump shape optimisation. This was mostly conducted during my first year at the Australian National University. The results were published in details in a paper. This paper is reproduced here.

The main idea of this work is to use a single mode squeezed vacuum (produce by an OPO) as a source of quantum random numbers. Using a particular measurement and randomness extraction protocol, it is possible to certify the security of the random numbers regardless of the trust we put in the quantum source.

Real-Time Source-Independent Quantum Random-Number Generator with Squeezed States


Thibault Michel^{1,2,†}, Jing Yan Haw,¹ Davide G. Marangon,³ Oliver Thearle,¹ Giuseppe Vallone,^{3,4} Paolo Villorosi,^{3,4} Ping Koy Lam,^{1,‡} and Syed M. Assad^{1,*}

¹*Centre for Quantum Computation and Communication Technology, Department of Quantum Science, The Australian National University, Canberra, ACT 0200, Australia*

²*Laboratoire Kastler Brossel, UPMC-Sorbonne Universités, CNRS, ENS-PSL Research University, Collège de France, 4 Place Jussieu, 75252 Paris, France*

³*Dipartimento di Ingegneria dell'Informazione, Università degli Studi di Padova, Via Gradenigo 6B, 35131 Padova, Italy*

⁴*Istituto di Fotonica e Nanotecnologie – CNR, Via Trasea 7, 35131 Padova, Italy*

 (Received 18 March 2019; revised manuscript received 3 July 2019; published 11 September 2019)

Random numbers are a fundamental ingredient in fields such as simulation, modeling, and cryptography. Good random numbers should be independent and uniformly distributed. Moreover, for cryptographic applications, they should also be unpredictable. A fundamental feature of quantum theory is that certain measurement outcomes are intrinsically random and unpredictable. These can be harnessed to provide unconditionally secure random numbers. We demonstrate a real-time self-testing source-independent quantum random-number generator (SI QRNG) that uses squeezed light as a source. We generate secure random numbers by measuring the quadratures of the electromagnetic field without making any assumptions about the source other than an energy bound; only the detection device is trusted. We use homodyne detection to measure alternately the \hat{Q} and \hat{P} conjugate quadratures of our source. \hat{P} measurements allow us to estimate a bound on any classical or quantum side information that a malicious eavesdropper may obtain. This bound gives the minimum number of secure bits we can extract from the \hat{Q} measurement. We discuss the performance of different estimators for this bound. We operate this QRNG with a squeezed-state source and compare its performance with a thermal-state source. This is a demonstration of a QRNG using a squeezed state, as well as an implementation of real-time quadrature switching for a SI QRNG.

DOI: [10.1103/PhysRevApplied.12.034017](https://doi.org/10.1103/PhysRevApplied.12.034017)

I. INTRODUCTION

Random numbers are used as a resource in many applications such as statistical analysis, numerical simulation, encryption, and communication protocols. Random numbers must satisfy three main requirements: they must be uniformly distributed, independent, and unpredictable. Pseudorandom numbers are generated by a computer via algorithmic routines from a seed. They have the advantage of being easy to implement and fast, but they are intrinsically not secure, due to their deterministic generation [1], and some commonly used pseudorandom-number generators (PRNGs) have been shown to be insecure [2]. Their randomness can also be flawed [3], which can lead to errors in simulations [4,5]. Physical random-number generators

use a stochastic physical process as the source of randomness [6,7]. They are slower than PRNGs but can still achieve a very high generation rate and have been used as a seed for PRNGs. In random-number generators based on classical systems, the randomness usually originates from a lack of knowledge of the initial state of the system, in which case the security relies on the assumption that no one has a better knowledge of this original state. On the other hand, quantum systems [8] offer an interesting alternative source of randomness, as the outcomes of measurements on such systems are intrinsically random, due to Born's rule [9]. This has been harnessed to create long-term-stable [10], fast quantum random-number generators (QRNGs) [11–14], which can operate in a self-testing fashion [15] or even on a mobile phone [16]. Full security is not guaranteed, however, as measurement outcomes may still be correlated with those of another party [17]. This is the case whenever the source of randomness is in a mixed state. To guarantee full security, it is possible to exploit nonlocal Bell-state measurements [18,19] and extract true

* thibault.michel@lkb.upmc.fr

† ping.lam@anu.edu.au

‡ cqtsma@gmail.com

random numbers without any assumptions about the source of randomness or the measurement device [20–24]. But these implementations are very slow, with bit rates of around a few tens of bits per second. In a similar fashion, generation protocols using light emitted from distant cosmic sources have been recently proposed and demonstrated [25–27]. As a faster alternative, one can implement a semi-device-independent QRNG by assuming that only either the source [28] or the detection device [29–33] is trusted. In a source-independent quantum random-number generator (SI QRNG), the source of randomness can be arbitrary and controlled by an adversarial party, yet it can still yield secure random numbers. One way to achieve source independence is to measure alternately and randomly two conjugate observables. Roughly speaking, by switching between different measurement bases, one is able to assess the purity of the source, which can in turn set a bound on its extractable randomness. This can be formalized rigorously using the entropic uncertainty relation [34], which was first introduced in Ref. [35].

SI QRNGs based on the entropic uncertainty relation have already been demonstrated for both discrete [29] and continuous variables (CV) [31]. However, in these proof-of-principle experiments, the randomness estimation was always done in postprocessing after collecting all the raw data. Moreover, in the previous CV work, no actual quadrature switching was implemented, as the source of entropy was the vacuum. Here we implement a continuous-variable SI QRNG where all processing is done in real time. Additionally, we dynamically switch between two measurement bases to alternate between a *check* measurement and a *random-data* measurement. The only assumption about the source that remains is that it has a bounded energy and falls within our measurement range. The SI QRNG is self-testing and changes its output secure bit rate depending on the check-measurement data. Although theoretical proposals for using squeezed states as sources of entropy for a QRNG have been made [31,36], we report an experimental use of squeezed states as an entropy source for a QRNG.

This paper is organized as follows. In Sec. II, we present the protocol and experimental details for generating random numbers. The protocol requires estimating a lower bound on the conditional min-entropy. In Sec. III, we present the real-time entropy-estimation procedure and the statistics of the random numbers generated. Because of the finite sample size, we find that the evaluated conditional min-entropy is positively biased, which can lead to an overestimation of the randomness rate. To mitigate this, we propose and discuss other more robust estimators in Sec. IV. Finally, we conclude in Sec. V with a discussion of several ways to extend the work presented in this paper, as well as a summary of our work. Various notation is used in the following; for convenience, we provide a glossary of this notation in Appendix A.

II. PROTOCOL AND EXPERIMENT

In a SI QRNG, we are attempting to generate secure random numbers without having to trust the source of entropy. This is possible by performing trusted measurements on two noncommuting observables. Our experiment is performed on continuous-variable light fields, and the observables measured are the field quadratures \hat{Q} and \hat{P} . By measuring the check quadrature \hat{P} , we put a bound on how much secure randomness can be extracted from the orthogonal random-data quadrature \hat{Q} . In the following, we provide details of how this bound can be calculated.

A. Randomness bound from conditional min-entropy

In our experiment, even though the quadrature observable has a continuous degree of freedom, the data that are recorded are ultimately discrete. The discretization size is determined by the finite resolution of the digitizer. This finite resolution implies that we do not measure the observables \hat{Q} and \hat{P} , but rather their discretized counterparts. Formally, we measure the positive-operator-valued measure (POVM) $\{\hat{Q}_{\delta q}^k\}_{k \in [-(m/2), m/2-1]}$, where

$$\hat{Q}_{\delta q}^k = \int_{I_{\delta q}^k} dq |q\rangle\langle q| \text{ and}$$

$$I_{\delta q}^k = \begin{cases} \left[-\infty, \left(k + \frac{1}{2}\right) \delta q \right] & \text{for } k = -\frac{m}{2}, \\ \left(\left(k - \frac{1}{2}\right) \delta q, \left(k + \frac{1}{2}\right) \delta q \right) & \text{for } -\frac{m}{2} < k < \frac{m}{2} - 1, \\ \left(\left(k - \frac{1}{2}\right) \delta q, \infty \right) & \text{for } k = \frac{m}{2} - 1. \end{cases} \quad (1)$$

The even integer m denotes the total number of bins, the index k enumerates the outcomes, and $\delta q > 0$ specifies the precision of the measurement. The measurement outcomes q_k on state ρ_A appear with probability $\mathfrak{p}(q_k) = \text{Tr}[\rho_A \hat{Q}_{\delta q}^k]$ and are stored in a classical register $Q_{\delta q}$. The POVM $\{\hat{P}_{\delta p}^k\}_{k \in [-(m/2), m/2-1]}$ corresponding to measurements of \hat{P} is defined in the same way, with precision δp .

As we do not trust the source of randomness, let us assume that ρ_A can be correlated with the state of a malicious party Eve (E), who will try to guess the QRNG output. This corresponds to ρ_A being mixed and $\rho_A = \text{Tr}_E(\rho_{AE})$, where ρ_{AE} is the collective state. After a measurement on system A with outcome k , Eve's state collapses to ρ_E^k . So, the total collective state is now a classical-quantum state,

$$\rho_{QE} = \sum_k \mathfrak{p}(q_k) |k\rangle\langle k|_A \otimes \rho_E^k. \quad (2)$$

The maximum amount of secure extractable randomness from a single-shot measurement of $Q_{\delta q}$ is then given

by [17,37–41]

$$r_{\text{sec}}^{\epsilon}(Q_{\delta q}|E) = H_{\min}(Q_{\delta q}|E) - 2 \log_2 \frac{1}{\epsilon}, \quad (3)$$

where ϵ is the security parameter and $H_{\min}(Q_{\delta q}|E)$ is the conditional min-entropy of $Q_{\delta q}$ [37]. The protocol is then said to be ϵ -secure, which means that the probability of distinguishing the output from a truly uniform independent distribution is smaller than $\frac{1}{2}(1 + \epsilon)$ [41]. The conditional min-entropy $H_{\min}(Q_{\delta q}|E)$ is defined as [38,39,42]

$$H_{\min}(Q_{\delta q}|E) = -\log_2 \max_{\{\hat{E}_k\}} \underbrace{\sum_k \mathbf{p}(q_k) \text{Tr}[\hat{E}_k \rho_E^k]}_{p_{\text{guess}}(\{\hat{E}_k\})}, \quad (4)$$

where $\{\hat{E}_k\}$ is a POVM on the system E . The quantity $p_{\text{guess}}(\{\hat{E}_k\})$ is the average probability for the adversary Eve to correctly guess the index k using a measurement strategy $\{\hat{E}_k\}$. The maximization of the POVM $\{\hat{E}_k\}$ corresponds to finding the best measurement strategy Eve might apply to guess the index k of the postmeasurement state ρ_{QE} . The amount of secure randomness is then the smallest conditional min-entropy for states ρ_{QE} consistent with Alice's state ρ_A . If the state ρ_A is pure, this implies that A and E are independent, $\rho_{AE} = \rho_A \otimes \rho_E$, in which case the conditional min-entropy reduces to the classical unconditional min-entropy

$$H_{\min}(Q_{\delta q}) = -\log_2 \max_k \{\mathbf{p}(q_k)\}. \quad (5)$$

Here Eve's best guessing strategy is to guess the most likely index k every time. For any state, $H_{\min}(Q_{\delta q}) \geq H_{\min}(Q_{\delta q}|E)$ and the difference can be seen as the amount of side information accessible to Eve. To compute the exact value of $H_{\min}(Q_{\delta q}|E)$ in Eq. (4), one needs to know ρ_{QE} . Since Alice does not have access to E , she would need to perform a complete tomography of ρ_A to find all compatible states ρ_{QE} . This is tedious for an infinite-dimensional system. Instead, one can bound $H_{\min}(Q_{\delta q}|E)$ by the max-entropy of the conjugate quadrature $H_{\max}(P_{\delta p})$ using the *entropic uncertainty relation* (EUR), [34,35,43–48]:

$$H_{\min}(Q_{\delta q}|E) + H_{\max}(P_{\delta p}) \geq -\log_2 c(\delta q, \delta p), \quad (6)$$

where the max-entropy is defined as

$$H_{\max}(P_{\delta p}) = 2 \log_2 \sum_k \sqrt{\mathbf{p}(p_k)}, \quad (7)$$

and $\mathbf{p}(p_k) = \text{Tr}[\rho_A \hat{P}_{\delta p}^k]$ is the probability of outcome p_k . The classical unconditional max- and min-entropies are equivalent to the Rényi entropies [49] of order $\frac{1}{2}$ and ∞ ,

respectively. The EUR can be seen as a generalization of the Heisenberg uncertainty relation. Additionally,

$$c(\delta q, \delta p) = \frac{1}{4\pi} \delta q \delta p S_0^{(1)} \left(1, \frac{\delta q \delta p}{8}\right)^2 \quad (8)$$

is a measure of the incompatibility between the two measurements, where $S_0^{(1)}$ is the zeroth radial prolate spheroidal wave function of the first kind [50]. This is a constant that depends only on the discretization sizes δq and δp . The wave function comes about by considering the maximum overlap between the eigenstates of $\hat{Q}_{\delta q}$ and $\hat{P}_{\delta p}$. Because of the Heisenberg uncertainty relation, a quantum state with zero extension in \hat{P} has an infinite extension in the conjugate variable \hat{Q} . However, when considering a discretized observable, this is no longer true. Because of the finite bin size, a quantum state which would yield a single value p_0 for $P_{\delta p}$ with probability 1 could still have a finite \hat{Q} extension. The constant $c(\delta q, \delta p)$ characterizes this fact. Note that Eq. (8) is written in accordance with the convention that the vacuum state has a quadrature variance of 1.

A complete description of the EUR is outside the scope of this paper, but one can easily get an intuitive understanding of this relation from a simple example. Consider a P -squeezed state; as the squeezing increases, the $P_{\delta p}$ measurement will be less spread out, and therefore $H_{\max}(P_{\delta p})$ decreases. To respect the EUR, $H_{\min}(Q_{\delta q}|E)$ has to increase with the amount of squeezing. So, measuring squeezing on \hat{P} indicates a certain amount of purity of the state, which means reduced correlations with Eve. Conversely, if Eve's side information is high [$H_{\min}(Q_{\delta q}|E)$ small], the state measured on Alice's side is highly mixed and the $P_{\delta p}$ measurement is very spread out, and so $H_{\max}(P_{\delta p})$ is high, in agreement with the EUR.

As illustrated by this simple example, the EUR provides a bound on $H_{\min}(Q_{\delta q}|E)$ and the amount of side information accessible to Eve. This bound is obtained by measuring the orthogonal quadrature \hat{P} and evaluating $H_{\max}(P_{\delta p})$. We will call this bound $H_{\text{low}}(P_{\delta p})$. From Eq. (6), we have

$$H_{\min}(Q_{\delta q}|E) \geq \underbrace{-H_{\max}(P_{\delta p}) - \log_2 c(\delta q, \delta p)}_{H_{\text{low}}(P_{\delta p})}. \quad (9)$$

Note that this bound depends only on the outcome of the measurement of $P_{\delta p}$, not $Q_{\delta q}$, as underlined by the notation $H_{\text{low}}(P_{\delta p})$. It is also independent of E , in other words, unconditional.

The above relation (and the EUR) holds for a POVM $\{\hat{Q}_{\delta q}^k\}, \{\hat{P}_{\delta p}^k\}$ that spans the entire phase space (from $-\infty$ to ∞) with a constant bin size $\delta p, \delta q$. In practice, however, our detection has a finite range, so we assume that the input states ρ_A are limited in phase space and have no support in the two extreme bins. These extreme bins,

defined in Eq. (1), have infinite width. This requirement corresponds to bounding the energy of the input state. Here we assume that this requirement is satisfied. Even though this assumption is reasonable, it is important to stress that, strictly speaking, the QRNG is not fully source-independent, as some assumption is made about the source [51]. This assumption would need to be checked in order to fully claim source-independence. The assumption can be verified by including an energy test as part of the protocol [52–54]. A different approach was followed in Ref. [31], where the effect of the finite range was taken into account by evaluating how the finite range impacts the estimation of the max-entropy in the worst-case scenario, corresponding to out-of-range measurements all belonging to different bins of the discretized P quadrature.

B. Experimental details

As shown in Fig. 1, the experimental setup has two parts. The first part is an untrusted entropy source, which consists of a quantum state ρ_A that may be mixed and correlated with that of a malicious party E : $\rho_A = \text{Tr}_E(\rho_{AE})$. We operate the device with two sources, a squeezed state and a thermal state. A shot-noise-limited 1064-nm Nd:YAG continuous-wave laser provides the laser source for this experiment. A portion of the 1064-nm light is frequency-doubled to provide a pump field at 532 nm. The thermal state is generated with amplitude and phase electro-optic modulators, to which we send a white-noise electronic signal from two independent function generators. By varying

the amplitudes of the noise sent to the modulators, we change the variance of this thermal state to see the effect on the secure bit rate. A squeezed state with around 3 dB of squeezing is generated with a seeded doubly resonant optical parametric amplifier (OPA) in a bow-tie geometry. Details of the squeezed-state generation can be found in the Supplemental Material [55] and in Ref. [56].

The second part of the setup is a trusted measurement device, which consists of a homodyne detector that can measure one of two conjugate quadratures \hat{Q} and \hat{P} on the state ρ_A by locking the phase of a local oscillator (LO) using amplitude or phase modulation. The ac component of the signal field is obtained from the subtracted current by mixing it down to 15 MHz and filtering with a 2 MHz-cutoff-frequency low-pass filter. It is then digitized over $m = 2^{12}$ bins. The acquisition rate is set at 200 kHz, well below the Nyquist frequency of the low-pass filter to avoid any time correlation in the signal. Note that the overall speed of the QRNG is not limited by the acquisition time but by the quadrature-switching and data-hashing time. More details of the acquisition are given in the Supplemental Material [55].

The measurement device switches randomly between two measurement states: check measurements and random-data measurements. Check measurements are performed to evaluate the amount of true random numbers that we may extract using our bound from Eq. (9), and random-data measurements are performed to get the data from which the random numbers are extracted. On average, a check measurement is performed once every ten measurement cycles.

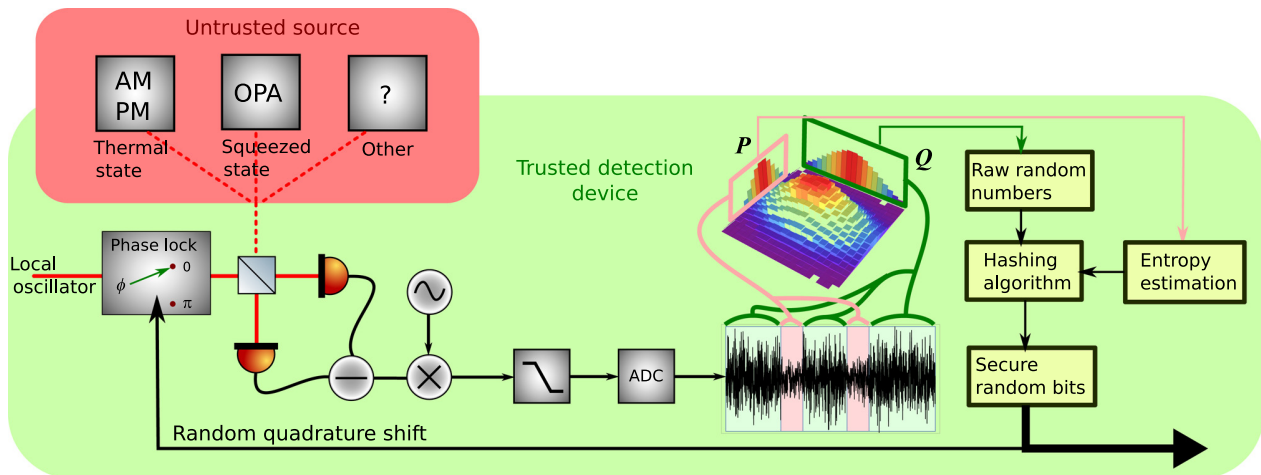


FIG. 1. Scheme and protocol of the SI QRNG. A local oscillator whose phase is locked to measure the check quadrature is interfered with an untrusted entropy source, which can be a squeezed, thermal, or unknown state. The two output beams are detected, and the resulting photocurrents are subtracted. From this homodyne measurement, the min-entropy of the random-data quadrature is estimated. The phase lock then switches to the orthogonal random-data quadrature, and the same homodyne measurement is performed. The raw random numbers are hashed according to the previous min-entropy estimation. Some of the secure random bits obtained in this way are used to determine when the next lock switch will happen. The check quadrature is measured randomly, on average once every ten runs.

In the check measurement state, three measurement steps are performed. In the first step, the LO and signal beams are blocked using servo-controlled beam blocks, and the electronic dark noise is recorded. In the second step, the signal beam is blocked, while the LO is unblocked. This allows us to record the vacuum shot noise. In the third step, both the signal and the LO beams are unblocked; the LO is locked to \hat{P} , and the check data are recorded. The data are then normalized according to the shot noise corrected for dark noise: $\sigma_{\text{shot, cor}}^2 = \sigma_{\text{shot}}^2 - \sigma_{\text{dark}}^2$. In this way, all electronic noise is accounted for as impurity in ρ_A .

From the check data, we evaluate the probabilities $p(p_k)$ using the frequentist estimator and $H_{\text{max}}(P_{\delta p})$ from Eq. (7). For each evaluation, the bin size δp is recalculated, in units of shot noise, using the corrected shot-noise measurement. The corresponding value of $c(\delta q, \delta p)$ is then evaluated using a precalculated polynomial approximation. In the experiment, we have averages $\delta q = (14.45 \pm 0.09) \times 10^{-3}$ and $\delta q = (15.56 \pm 0.09) \times 10^{-3}$ for the thermal-state and squeezed-state runs, respectively. The bound $H_{\text{low}}(P_{\delta p})$ is then estimated using Eq. (9) and stored in the computer for use in the random-data measurement stage. The variance of $P_{\delta p}$ is also recorded.

In the random-data measurement state, both the signal and the LO beams are unblocked. The LO phase is locked to \hat{Q} , and the raw data are recorded. The data are then normalized according to the shot noise corrected for dark noise taken from the previous check measurement. In order to eliminate Eve's information, we apply the Toeplitz-matrix hashing algorithm [57] to the raw data to obtain the secure random data. The length of the Toeplitz matrix is determined by the randomness bound evaluated in the check stage. A few bits of the hashed random numbers are used to determine whether the next stage will be a check or random-data measurement stage.

For each check and random-data measurement, we collect $n = 16000$ points, and so the data are hashed in blocks of size n . This number is chosen as a trade-off between accurate bound estimation and hashing time. Collecting data blocks larger than this means better precision in our bound estimation but a longer hashing time. In our implementation, to avoid slowing down the protocol, the random Toeplitz matrix is generated once at the start of the experiment using a trusted QRNG source [13]. However, for the hashing to be fully secure, a new hashing function randomly chosen from a family of two-universal hashing functions should be used every time [41, 58, 59]. This is so that Eve does not have knowledge of the hash function prior to preparing the state, so that she cannot implement deception strategies tailored to the hashing function. For monitoring purposes, we also evaluate the unconditional min-entropy $H_{\text{min}}(Q_{\delta q})$ using the frequentist estimator. Appendix B shows a flow-chart representation of the protocol.

III. RESULTS AND ESTIMATION-ERROR ANALYSIS

As mentioned before, the QRNG is operated with two different sources: a \hat{P} -squeezed state and a thermal state. In order to generate secure randomness, we use the bound provided by $H_{\text{low}}(P_{\delta p})$ in Eq. (9). To apply this bound, we need to know the value of $H_{\text{max}}(P_{\delta p})$. In Sec. III A, we present a real-time experimental result where the frequentist estimator for $H_{\text{max}}(P_{\delta p})$ is used. In Sec. III B, we show that this estimator is biased, which may compromise the security of the QRNG.

A. Real-time entropy estimation

In the experiment, the entropies are calculated in real time using the frequentist estimator. After measuring $n = 16000$ data points and binning the outcomes into $m = 2^{12}$ bins, the probabilities are estimated by

$$p_k^{\text{freq}} = \frac{n_k}{n},$$

where n_k denotes the number of outcomes in the k th bin. The frequentist estimators are then given by

$$H_{\text{min}}^{\text{freq}}(\vec{n}) = -\log_2 \frac{\max_k \{n_k\}}{n}, \quad (10)$$

$$H_{\text{max}}^{\text{freq}}(\vec{n}) = 2 \log_2 \sum_{k=1}^m \sqrt{\frac{n_k}{n}}, \quad (11)$$

where $\vec{n} = (n_1, n_2, \dots, n_m)$. The entropy bounds $H_{\text{low}}^{\text{freq}}(P_{\delta p})$ and the unconditional classical entropy $H_{\text{min}}^{\text{freq}}(Q_{\delta q})$ from the experiments are recorded for the thermal and the squeezed state. These are presented as points in Figs. 2(a) and 2(b) as a function of the check-data variance. In the same figure, we also plot simulation results $H_{\text{low}}^{\text{sim}}(P_{\delta p})$ and $H_{\text{min}}^{\text{sim}}(Q_{\delta q})$ obtained by sampling n points from a perfect Gaussian distribution. These simulations are repeated 1000 times to estimate the mean and standard deviation of the estimated entropy bound. Finally, the theoretical values we would expect for a perfect discretized Gaussian distribution,

$$p(p_k) = \frac{1}{2} \operatorname{erf} \left(\frac{p_k + \delta p/2}{\sqrt{2}\sigma} \right) - \frac{1}{2} \operatorname{erf} \left(\frac{p_k - \delta p/2}{\sqrt{2}\sigma} \right), \quad (12)$$

are plotted as the solid lines $H_{\text{low}}^{\text{th}}(P_{\delta p})$ and $H_{\text{min}}^{\text{th}}(Q_{\delta q})$. As one can see from Eqs. (5) and (7), the min- and max-entropies are in the range $[0, \log_2 m = 12]$ and depend on the number of bins used. To analyze the entropy independently of the number of bins, we therefore plot entropy rates, that is, the entropy per bit, $H/12$. Note that the *unconditional* min-entropy $H_{\text{min}}(Q_{\delta q})$ would be the extractable randomness if we trusted the source entirely.

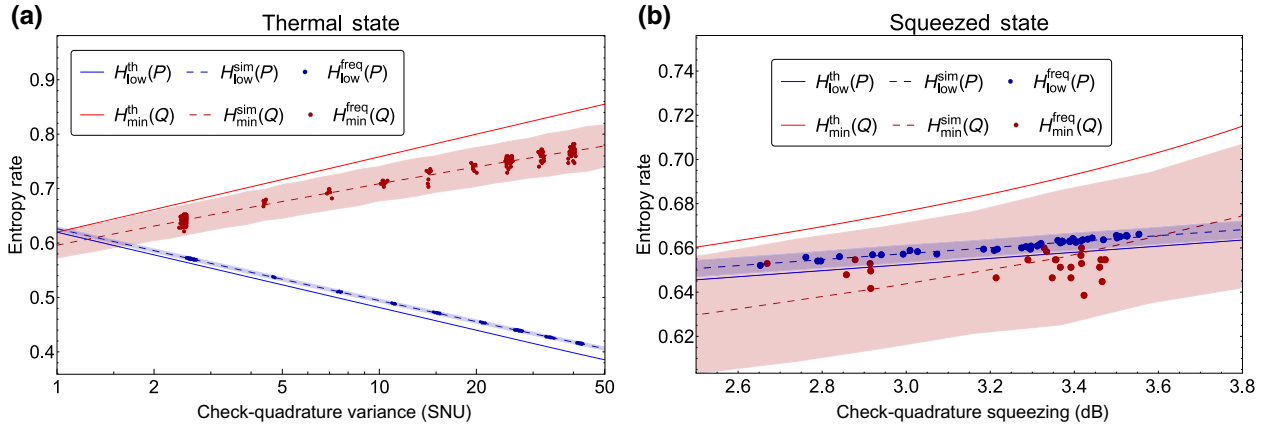


FIG. 2. Entropy bound and classical min-entropy for (a) a thermal state with different values of noise and (b) a \hat{P} -squeezed state with 33% loss. SNU, shot-noise units. The red solid lines show the theoretical unconditional min-entropy of the random-data quadrature \hat{Q} . This gives the extractable randomness if the source is trusted. The blue solid lines show the theoretical bound on the conditional min-entropy $H_{\min}(Q|E)$ obtained from the entropic uncertainty relation. This gives the secure extractable randomness for an untrusted source. The blue and red points show the corresponding experimental data calculated in real time using a frequentist estimator on data samples of length $n = 16\,000$. For most values of squeezing, we find that $H_{\text{low}}^{\text{freq}} > H_{\min}^{\text{freq}}$, which appears to be in violation of the EUR, Eq. (9). This apparent violation arises due to a bias in the frequentist estimators. The dashed lines show the corresponding simulation results, and the shaded area corresponds to a 5-standard-deviation uncertainty region.

However, if the source is untrusted, the secure extractable randomness is given by the *conditional* min-entropy $H_{\min}(Q_{\delta q}|E)$. As we explain in Sec. II A, $H_{\text{low}}(P_{\delta p})$ is a bound on the extractable randomness, so its value in Figs. 2(a) and 2(b) (blue points) corresponds to the secure hashing rate that we use. For example, if $H_{\text{low}}(P_{\delta p}) = 0.5$, then blocks of raw random numbers from $Q_{\delta q}$ measurements are hashed down to half their size.

The thermal-state results in Fig. 2(a) illustrate the difference between the conditional and unconditional min-entropy. Indeed, a thermal state can be purified by a two-mode squeezed state such that the outcome of a measurement on that state may well be correlated with a mode obtained by Eve. This amount of quantum or classical side information is the difference between the unconditional min-entropy, which quantifies the entropy of the measurement distribution, and the conditional min-entropy, which quantifies the entropy given any possible side information. For a thermal state, the higher the variance, the higher the min-entropy, which reflects the apparent random noise in the quadrature measurement, yet the conditional min-entropy is lower because the state could be a two-mode squeezed state with higher correlations.

The data points in Fig. 2(a) appear in clusters; each of these clusters corresponds to a different noise amplitude sent to the modulators, that is, a different input thermal state. For input states with low variance, the unconditional min-entropy $H_{\min}(Q_{\delta q})$ and the bound $H_{\text{low}}(P_{\delta q})$ on the conditional min-entropy are close. This corresponds to a low amount of side information, as the state has low impurity. For example, if a pure vacuum state or

a coherent state were used as a source of randomness, the unconditional min-entropy $H_{\min}(Q_{\delta q})$ and the bound $H_{\text{low}}(P_{\delta q})$ would be approximately equal. For noisier inputs, the unconditional min-entropy increases; however, the bound $H_{\text{low}}(P_{\delta q})$ decreases, which corresponds to a higher amount of side information. Indeed, even if the state is noisier and appears more random, it is also more mixed, and potentially more correlated with that of Eve, which is why $H_{\min}(Q_{\delta q}|E)$ decreases, and so does $H_{\text{low}}(P_{\delta q})$. For the thermal-state run, the secure bit rate varies between 7.2 kb/s for the state with lower variance to 5.2 kb/s for the state with higher variance.

The experimental results for the squeezed states are plotted in Fig. 2(b). This shows that higher squeezing gives rise to more extractable randomness. Indeed, measuring squeezing on one quadrature guarantees increased noise in the conjugate antisqueezed quadrature. Unlike in the thermal-noise case, this noise is not correlated with another system. For example, having 5 dB squeezing on the source increases the entropy rate by around 10% compared with the vacuum. Therefore using a squeezed state as an entropy source can improve the QRNG bit rate, especially with broadband squeezing. For the squeezed-state run, the bit rate was 8.2 kb/s. In the simulation results, the impurity of the squeezed state is accounted for by inferring the amount of loss in the state from the two-quadrature variance measurement. This is estimated to be 33%. This is the reason why the min-entropy and the bound are not equal; they can only be equal for a pure state.

As we mentioned in Sec. II A, the unconditional min-entropy is always larger than the conditional min-entropy.

So, regardless of the input state, we must have

$$H_{\min}(Q_{\delta q}) \geq H_{\min}(Q_{\delta q}|E) \geq H_{\text{low}}(P_{\delta q}), \quad (13)$$

where the second inequality comes from the definition of $H_{\text{low}}(P_{\delta q})$ [Eq. (9)]. In particular, we should have $H_{\min}(Q_{\delta q}) \geq H_{\text{low}}(P_{\delta q})$. The theoretical curves indeed show this behavior, and the only point in Fig. 2(a) where $H_{\min}^{\text{th}}(Q_{\delta q}) = H_{\text{low}}^{\text{th}}(P_{\delta q})$ is for a variance of 1, which corresponds to a pure vacuum or coherent state. On the other hand, the simulation curves and experimental points do not always respect this inequality. This is a problem, as this observation appears to violate the EUR. This indicates that our live evaluation of the bound $H_{\text{low}}^{\text{freq}}(P_{\delta p})$ might be higher than the true conditional min-entropy, which would compromise security.

We will investigate and explain this bias in the next subsection and find solutions in Sec. IV.

B. Bias of the frequentist estimator

We see in Figs. 2(a) and 2(b) that there is a discrepancy between the theoretical bound $H_{\text{low}}^{\text{th}}(P_{\delta p})$, $H_{\min}^{\text{th}}(Q_{\delta q})$ calculated for a Gaussian state, and the experimental data. To analyze this, we run a simulation by sampling a pure Gaussian distribution for different sample sizes n . Each simulation is repeated 1000 times. As shown in Figs. 3(a) and 3(b), we find that the frequentist estimators $H_{\text{low}}^{\text{freq}}(P_{\delta p})$ and $H_{\min}^{\text{freq}}(Q_{\delta q})$ are both biased. The means of the frequentist estimators do not match the true values $H_{\text{low}}^{\text{th}}(P_{\delta p})$ and $H_{\min}^{\text{th}}(Q_{\delta q})$. This leads to an apparent violation of the EUR, as $H_{\text{low}}^{\text{freq}}(P_{\delta p})$ is positively biased, while $H_{\min}^{\text{freq}}(Q_{\delta q})$ is negatively biased. This bias becomes smaller as the sample size increases. It is significant in Figs. 2(a) and 2(b), where the

entropies are estimated with only 16 000 samples. But even for very large sample sizes this problem might be present; it depends on the source state considered, as we show in Appendix D. Moreover, if Eve's state is maximally correlated with ours, then any overestimation of the bound will compromise the security of the random numbers. One may try to correct this by using a different estimator for the max-entropy.

IV. OTHER ESTIMATORS FOR THE ENTROPY BOUND

Having learned that the frequentist estimator can be biased, in this section we investigate and compare three different estimators. These estimators come with their own natural confidence intervals that we can set.

A. Bayesian estimators

Another class of possible estimators for H_{max} are the Bayesian estimators. To calculate a Bayesian estimator of an unknown parameter, one has to specify a prior probability density. This represents our initial belief about the distribution of the unknown parameter. Here we analyze two estimators for H_{max} based on two different priors. The first is an uninformative prior which makes no assumption about the underlying probability distribution. The second assumes the worst-case scenario by choosing a prior peaked around the uniform probability. Deciding which prior to use is a matter of the experimentalist's degree of paranoia. We note that using Bayesian estimators brings with it the additional advantage of having the posterior estimate as a natural confidence interval.

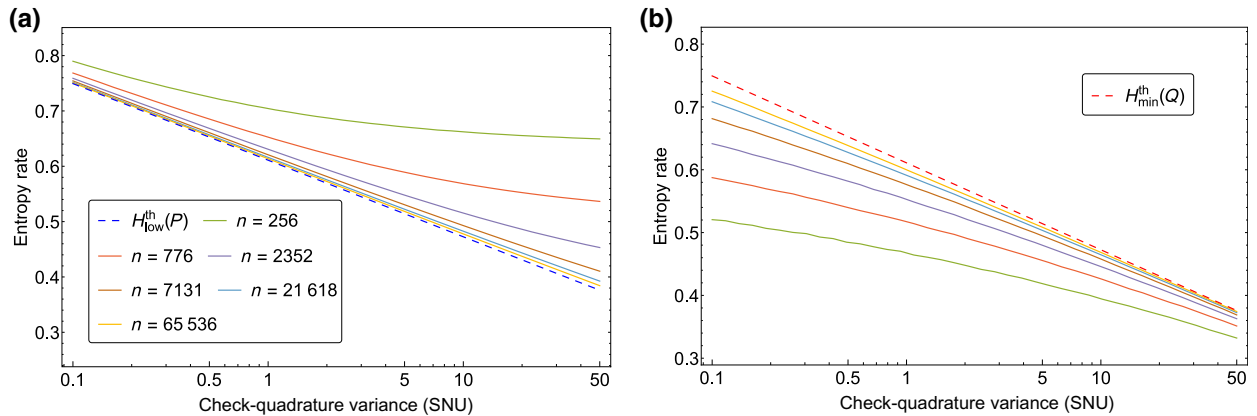


FIG. 3. (a) Simulation of the frequentist estimator of the entropy bound for a pure Gaussian state. We set $\delta q = 0.015\,560\,7$, which is the mean value of δq for the squeezed-state runs, and run the simulation for different sample sizes. The dashed line shows the theoretical value of H_{low} , which gives a lower bound on the conditional min-entropy. Because of the finite sample size, this estimator is positively biased, which may lead to erroneously extracting more keys than are secure. (b) Simulation of the frequentist estimator of the unconditional min-entropy with the same parameters. Because of the finite sample size, this estimator is negatively biased, which leads to instances where $H_{\min}^{\text{freq}} < H_{\text{low}}^{\text{freq}}$.

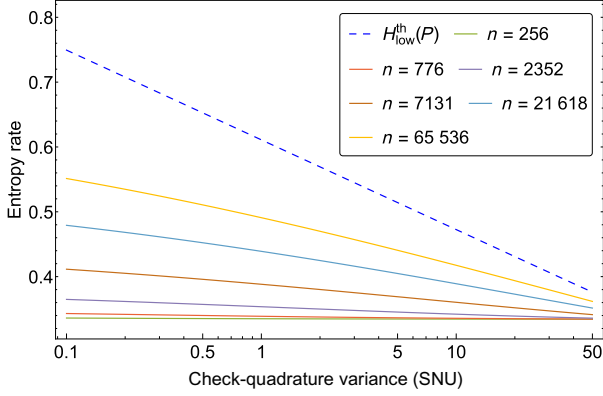


FIG. 4. Simulation of the uniform-prior Bayesian estimator for the entropy bound of a pure Gaussian state with the same parameters as in Fig. 3. The estimator is negatively biased, which does not compromise security.

1. Bayesian estimator for max-entropy with a completely uninformative prior

The indirect Bayesian estimator with a completely uninformative uniform prior was developed in Refs. [60] and [61] and proposed for source-device-independent QRNGs in Ref. [29]. It is given by

$$H_{\max}^{\text{UP}}(\vec{n}) = 2 \log_2 \left(\frac{\Gamma(n+m)}{\Gamma(n+m+\frac{1}{2})} \sum_{k=1}^m \frac{\Gamma(n_k + \frac{3}{2})}{\Gamma(n_k + 1)} \right). \quad (14)$$

Using this estimator in a simulation for a Gaussian state under our experimental conditions, we find that it has a negative bias, which does not lead to a violation of the EUR (see Fig. 4). If one can check that the distribution is Gaussian, it is then justifiable to use this Bayesian estimator. In fact, one can go a step further and remove the bias from the estimator. Otherwise, this negative bias will lead to a severe underestimation of the secure bit rate. But, *a priori*, the distribution might not be Gaussian, and the bias will then depend on the distribution and on experimental conditions such as the bin size. We show in Appendix D that in some extreme cases this bias can still be positive.

2. Bayesian estimator for max-entropy with a prior peaked around the uniform distribution

The Bayesian estimator depends on the chosen prior. The natural choice of prior is the Dirichlet distribution, since this is the conjugate prior to the multinomial distribution. The Dirichlet distribution with concentration parameter $\vec{\alpha}$ is given by

$$\mathcal{D}[\vec{p}; \vec{\alpha}] = \frac{\Gamma(\sum_{k=1}^m \alpha_k)}{\prod_{k=1}^m \Gamma(\alpha_k)} \prod_{k=1}^m p_k^{\alpha_k - 1},$$

where $p_k = \mathbb{p}(p_k)$. In order to prevent an underestimation of H_{\max} , it is prudent to assume the worst-case scenario by choosing a prior that is sharply peaked around the uniform distribution. This is because the uniform distribution is the distribution with the maximum possible H_{\max} . We subsequently adjust our belief when presented with the measured data. Such a prior can be constructed by choosing $\alpha_k = K$ for all k :

$$\pi(\vec{p}) = \mathcal{D}[\vec{p}; K] \quad (15)$$

$$= \frac{\Gamma(mK)}{\Gamma(K)^m} (p_1 \cdots p_m)^{K-1}. \quad (16)$$

Here K characterizes the peakedness of the prior distribution. A large value of K corresponds to a distribution peaked around the uniform distribution, while $K = 0$ corresponds to the frequentist estimator. The Bayes posterior estimator given the measurement outcomes \vec{n} is the Dirichlet distribution with parameters $\vec{\alpha} = \vec{n} + K$ [62],

$$f(\vec{p}|\vec{n}) = \mathcal{D}[\vec{p}; \vec{n} + K]. \quad (17)$$

From this posterior distribution, we can arrive at a Bayesian estimator for H_{\max} . Alternatively, an indirect estimator for H_{\max} , which we denote by H_{\max}^{PP} , can be obtained by substituting the Bayesian posterior mean for the probabilities \vec{p} ,

$$p_k^{\text{PP}} = \mathbb{E}[p_k|\vec{n}] \quad (18)$$

$$= \frac{n_k + K}{n + mK}, \quad (19)$$

into Eq. (7). As we shall see in Sec. IV C, with a large K , this estimator tends to be very conservative.

B. Extremal variance-based estimator

Another way to estimate H_{\max} is by estimating the variance of the distribution. Instead of estimating $H_{\max}(P_{\delta p})$ from the sampled distribution, we can try to bound it. We first estimate V_P , the variance of $P_{\delta p}$, with the unbiased estimator $V_P = 1/(n-1) \sum_{k=1}^n (p_k - \bar{p})^2$. We can then find the distribution that maximizes H_{\max} for this given variance. This is similar to the method used in Ref. [30] for bounding the Shannon entropy [63,64].

We show in Appendix C that, given a variance V_P , the corresponding extremal distribution is given by

$$p(p_k) = C \frac{1}{[1 + (p_k/s)^2]^2}, \quad (20)$$

where

$$C = \left(\sum_j \frac{1}{[1 + (p_j/s)^2]^2} \right)^{-1} \quad (21)$$

is a normalization constant,

$$s = \sqrt{\frac{1 - \gamma V_P}{\gamma}}, \quad (22)$$

and γ is the solution to the equation

$$\sum_k \frac{p_k^2 - V_P}{[1 + \gamma(p_k^2 - V_P)]^2} = 0. \quad (23)$$

This distribution is a discretized Student's t -distribution with 3 degrees of freedom. Although Eq. (23) does not have a closed-form solution for γ , one may calculate a solution numerically. We can then calculate the extremal variance-based (EVB) estimator $H_{\max}^{\text{EVB}}(V_P)$. This is the extremal max-entropy consistent with the variance V_P . From this, we get an estimate for $H_{\text{low}}^{\text{EVB}}$ from Eq. (9). This is plotted in Fig. 5 for a Gaussian state with parameters similar to those in our experiment.

Under these conditions, we see that the EVB estimator shows no bias, and the mean value does not change with the sample size. Moreover, by construction, the mean of the EVB estimator for $H_{\text{low}}^{\text{EVB}}$ is always smaller than $H_{\text{low}}^{\text{th}}(P_{\delta p})$. Unlike the frequentist estimators, the EVB estimator does not overestimate $H_{\text{low}}^{\text{th}}$. However, because the EVB estimator uses only the variance instead of the whole distribution, it does not converge to $H_{\text{low}}^{\text{th}}$ even when the sample size is large. It only converges to $H_{\text{low}}^{\text{th}}$ if the check-quadrature distribution happens to be the discretized Student's t -distribution [Eq. (20)].

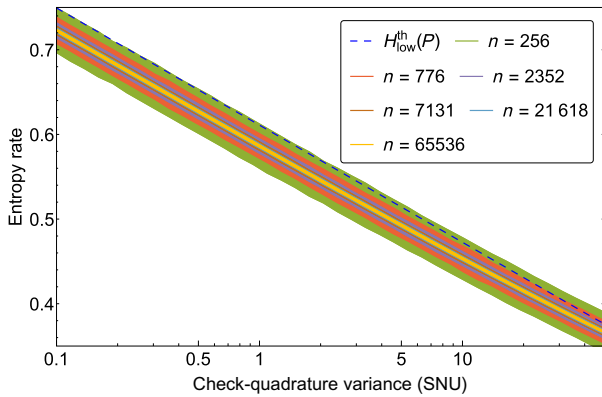


FIG. 5. Extremal variance-based estimator $H_{\text{low}}^{\text{EVB}}$ obtained by estimating the variance of the check quadrature. The shaded area shows 5 standard deviations. This estimator shows no bias. The dashed lines show the theoretical bound for a Gaussian distribution. The estimator is lower because the extremal distribution for the EVB estimator assumes a discretized Student's t -distribution [Eq. (20)]. For sample sizes above 1000, the variance of this estimator becomes small enough that the probability of a single-shot estimation being above $H_{\text{low}}^{\text{th}}$ becomes negligible.

We note that here the theoretical $H_{\text{low}}^{\text{th}}(P_{\delta p})$ and simulations are computed for Gaussian states. The results for the bias will differ for other input states, and in some cases the EVB estimator can still be positively biased. Indeed, even though the variance estimator is unbiased, the max-entropy is a concave function of the variance. This means that it has a negative bias. This is illustrated in Appendix D. However, we can get a confidence interval for the variance from the sampled data, and from this we can arrive at a confident estimate for the max-entropy.

C. Comparison of performance of the different estimators

A comparison of how the different estimators perform with increasing sample size for a vacuum-state input is shown in Fig. 6. The frequentist estimator has a positive bias, leading to an overestimation of the secure randomness rate, which can compromise the security of the random numbers. In contrast, the EVB estimator and both Bayes estimators have a negative bias, which leads to an underestimation of the secure randomness rate. Of all the estimators, the Bayesian peaked-prior estimator is the most conservative; it will significantly underestimate the bound even for large sample sizes.

Finally, we note that even with an unbiased estimator for H_{\max} , one should not take its mean value as a point estimate. Doing so will lead to a 50% probability of overestimating H_{\max} . Instead, one should obtain a point estimate based on its confidence interval and a required failure rate.

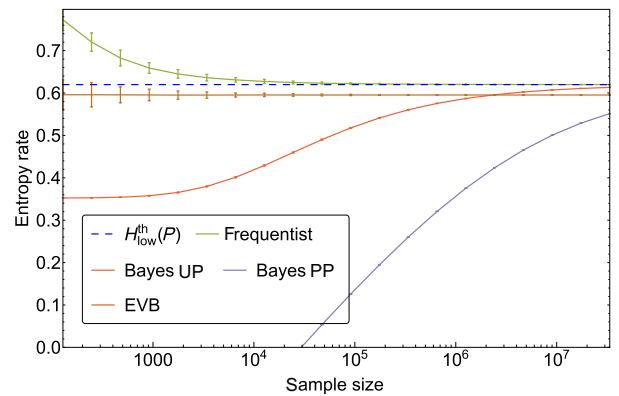


FIG. 6. Simulations of H_{low} for a vacuum state with finite sample size for various estimators. We compare four estimators: the frequentist estimator, the Bayesian estimator with a uniform prior (UP), the Bayesian estimator with a peaked prior (PP), and the EVB estimator. For the Bayesian estimator with a peaked prior, K is set to 100 [see Eq. (15)]. Each simulation is repeated 100 times to obtain the mean and standard deviation of the estimator. The error bars show 5 standard deviations. We also plot the theoretical value of H_{low} .

V. CONCLUSION AND OUTLOOK

We demonstrate a real-time SI QRNG incorporating measurement-basis switching and hashing using a squeezed state of light as a source of entropy. The only assumption required about the source is an energy bound. The protocol is validated on different thermal states. In the real-time demonstration, the sample size is limited by finite computational resources. A valuable lesson learned from this demonstration is that due to finite-size effects, the frequentist estimator can lead to an underestimation of the max-entropy due to its biased nature. This can lead to an underestimation of the adversary's knowledge about the measured data. To mitigate this potential problem, we propose three different ways of estimating the max-entropy. Which of these estimators the experimenter picks will depend on the experimenter's level of paranoia.

We note that this estimation problem does not arise with a trusted-source QRNG, where a confidence interval for the entropy estimator can be calculated from knowledge of the source. Nor does it appear in asymptotic CV quantum-key-distribution protocols, where the measured distribution can be assumed to be Gaussian due to the optimality of Gaussian attacks [65,66]. For Gaussian distributions, it is then easy to construct a confidence interval for the max-entropy. However, in a source-independent protocol, we see that a Gaussian distribution is not the best that the adversary can use. Hence, assuming a Gaussian distribution might lead to an underestimation of her knowledge.

In our experimental demonstration, the bit rate is limited by three main factors: first, the slow real-time hashing of the raw bits, which is done on a desktop computer; second, the mechanical beam blocking in the check measurement; and third, the limited squeezing bandwidth. The first limitation can be circumvented using fast hashing codes [17,57] on graphics cards or field-programmable gate arrays (FPGA). We foresee that implementing the hashing on an FPGA would allow us to reach the GHz regime [67]. The second limitation is less stringent, since the beam blocking happens only during the check measurement. In our setup, the check measurement is performed with a 10% probability, and the data measurement is not limited by the slow mechanical beam blocks. Furthermore, one may use faster nonmechanical ways to block the beam, for example by using acoustic-optical modulators to deflect the beams. The third limitation in this experiment is the squeezing bandwidth, which is imposed by the bandwidth of the OPA squeezing cavity. Hence, using a squeezed-state source may limit the bit rate through bandwidth limitation more than it improves it through the higher security rate. This limitation can be circumvented by using a single-pass OPA, which would offer squeezing over much larger bandwidths [68].

ACKNOWLEDGMENTS

This work is funded by the Australian Research Council Centre of Excellence and Laureate Fellowship schemes (Grants No. CE110001027 and No. FL150100019). Our research is also supported by the Defence Industry and Innovation Next Generation Technologies Fund.

We thank Nathan Walk for useful discussions and comments on this work.

APPENDIX A: GLOSSARY OF NOTATION

\hat{Q} Random-data quadrature, from which random numbers are extracted.

\hat{P} Check quadrature, used to estimate the secure randomness.

$\{\hat{Q}_{\delta q}^k\}$ POVM corresponding to the discretized measurement of \hat{Q} .

$\{\hat{P}_{\delta p}^k\}$ POVM corresponding to the discretized measurement of \hat{P} .

$\delta q, \delta p$ Precision, in shot-noise units, of the discretized \hat{Q} and \hat{P} measurements.

m Number of bins in the discrete quadrature measurement. Set to $2^{12} = 4096$ in our experiment.

$H_{\min}(Q_{\delta q})$ Min-entropy of $Q_{\delta q}$, given by Eq. (5). This quantity gives the amount of secure random numbers if we trust the source of entropy.

$H_{\min}(Q_{\delta q}|E)$ Min-entropy of $Q_{\delta q}$ conditioned on E , given by Eq. (4). This quantity gives the amount of secure random numbers if we do not trust the source of entropy.

$H_{\text{low}}(P_{\delta p})$ Bound on $H_{\min}(Q_{\delta q}|E)$, given by Eq. (9). This allows us to bound the secure randomness when we do not trust the source, without having to do a full tomography of the input state. It depends solely on measurements of the check quadrature \hat{P} and precision $\delta q, \delta p$.

$H_{\max}(P_{\delta p})$ Max-entropy of $P_{\delta p}$, given by Eq. (7). Required for calculating $H_{\text{low}}(P_{\delta p})$; see the entropic uncertainty relation, Eq. (9).

$c(\delta q, \delta p)$ Constant term appearing in the entropic uncertainty relation. Defined by Eq. (8). Quantifies the incompatibility of $\{\hat{Q}_{\delta q}^k\}$ and $\{\hat{P}_{\delta p}^k\}$.

n Number of samples acquired in each measurement cycle. One cycle can be either a check or a random-data measurement. Set to 16 000 in the experiment.

$H_{\min}^{\text{freq}}(\vec{n})$ Frequentist estimator for the unconditional min-entropy based on measurement outcome \vec{n} , given by Eq. (10).

$H_{\max}^{\text{freq}}(\vec{n})$ Frequentist estimator for the max-entropy based on measurement outcome \vec{n} , given by Eq. (11)

$H_{\text{low}}^{\text{freq}}(\vec{n})$ Frequentist estimator for the bound $H_{\text{low}}(P_{\delta p})$. Calculated from Eq. (9) using the values of $H_{\max}^{\text{freq}}(\vec{n})$ and $c(\delta q, \delta p)$.

$H_{\min}^{\text{th}}(Q_{\delta q})$ Theoretical value of the unconditional min-entropy for a Gaussian-state input. Calculated using Eqs. (5) and (12).

$H_{\text{low}}^{\text{th}}(P_{\delta p})$ Theoretical value of the bound $H_{\text{low}}(P_{\delta p})$ for a Gaussian-state input. Calculated using Eqs. (9), (7), and (12).

$H_{\min}^{\text{sim}}(P_{\delta p})$ Simulated value of the unconditional min-entropy. Obtained by numerically sampling a Gaussian distribution n times and using Eq. (10).

$H_{\text{low}}^{\text{sim}}(P_{\delta p})$ Simulated value of the bound $H_{\text{low}}(P_{\delta p})$. Obtained by numerically sampling a Gaussian distribution n times and using Eqs. (9) and (11).

APPENDIX B: FLOW CHART OF THE PROTOCOL

A flow chart of the protocol for measurement and random-number extraction is shown in Fig. 7.

APPENDIX C: EXTREMAL DISTRIBUTION FOR MAX-ENTROPY WITH A FIXED VARIANCE

Suppose we experimentally observe a discrete distribution with a finite support. From the variance of this distribution, we can upper-bound its entropy. To do this, we derive the probability distribution that maximizes the entropy for a fixed variance. We note that the entropy does not depend on the labels of the bins; to have a tighter bound, we can rearrange the bins to minimize the variance.

Here we derive the probability distribution that maximizes the max-entropy for a fixed variance in a finite-support setting. We want to find the extremal distribution $\mathcal{P} = \{p_k\}$ that maximizes the max-entropy

$$H_{\max}(\vec{p}) = 2 \log_2 \sum_k \sqrt{p_k} \quad (\text{C1})$$

over the finite support $x_k = k \delta x$ for integer values $k \in [-m, m]$ subject to the normalization constraint $\sum_k p_k = 1$ and the fixed-variance condition

$$\sum_k p_k x_k^2 - \left(\sum_k p_k x_k \right)^2 = V. \quad (\text{C2})$$

We first show that the extremal distribution must be symmetric, with $p_k = p_{-k}$. From an arbitrary distribution $\mathcal{Q} = \{q_k\}$, we can construct a symmetrized distribution $\mathcal{P} = \{p_k\}$ with

$$p_k = \frac{q_k + q_{-k}}{2}.$$

This distribution has a smaller variance, $\text{var}(\mathcal{P}) \leq \text{var}(\mathcal{Q})$, but a higher max-entropy, $H_{\max}(\mathcal{P}) \geq H_{\max}(\mathcal{Q})$. The first statement holds due to $\langle \mathcal{Q} \rangle^2 = \langle \mathcal{P} \rangle^2$ and $\langle \mathcal{Q} \rangle^2 \geq \langle \mathcal{P} \rangle^2 = 0$. The second statement follows from the concavity of the

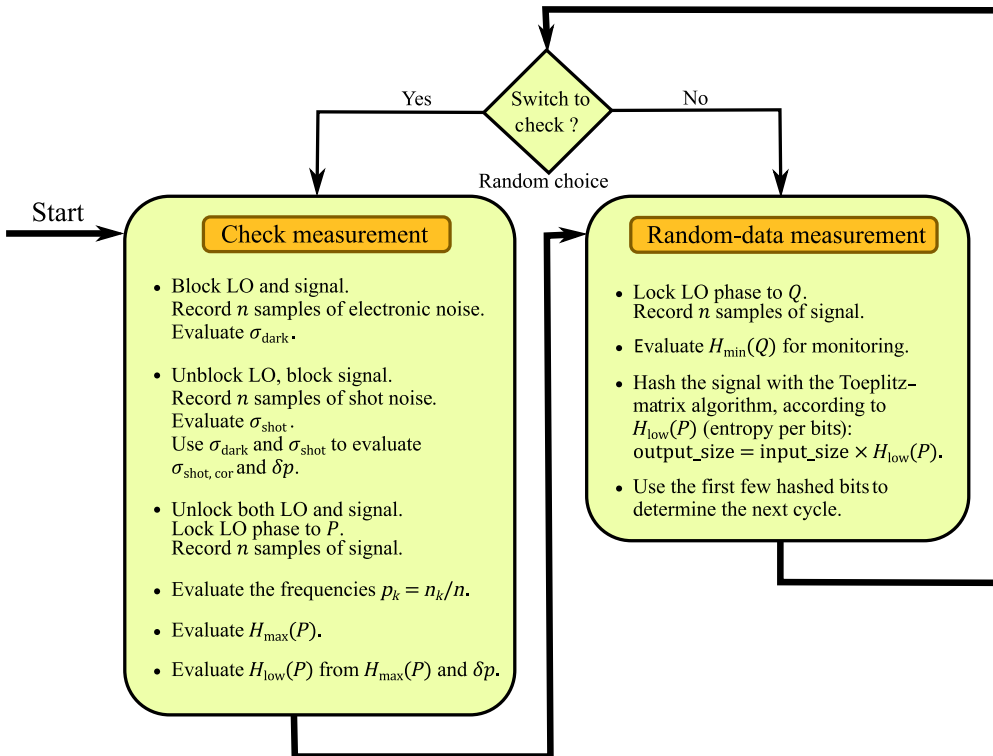


FIG. 7. Flow chart of the measurement and random-number-extraction protocol. First, the amount of secure randomness is evaluated in the check step. The random-data step follows, where data are measured and random numbers are extracted. This last step is repeated until the protocol randomly switches back to the check step, to reevaluate the secure randomness of the source.

entropy function:

$$\begin{aligned}
 H_{\max}(\mathcal{P}) &= 2 \log_2 \sum_k \sqrt{p_k} \\
 &= 2 \log_2 \sum_k \sqrt{\frac{q_k + q_{-k}}{2}} \\
 &\geq 2 \log_2 \sum_k \left(\frac{1}{2} \sqrt{q_k} + \frac{1}{2} \sqrt{q_{-k}} \right) \\
 &= H_{\max}(\mathcal{Q}).
 \end{aligned}$$

Hence, the extremal distribution is symmetric and has zero mean.

To find the extremal distribution \mathcal{P} , we write the Lagrangian as

$$\begin{aligned}
 L(\mathcal{P}, \alpha, \gamma) &= 2 \log_2 \sum_k \sqrt{p_k} \\
 &+ \frac{\alpha}{\ln 2} \left(1 - \sum_k p_k \right) + \frac{\gamma}{\ln 2} \left(V - \sum_k p_k x_k^2 \right).
 \end{aligned}$$

L attains a stationary point when

$$\begin{aligned}
 \frac{\partial L}{\partial p_k} &= 0 \\
 \Rightarrow \frac{1}{\sqrt{p_k}} \frac{1}{\sum_j \sqrt{p_j}} - \alpha - \gamma x_k^2 &= 0 \\
 \Rightarrow \frac{1}{\sqrt{p_k}} &= (\alpha + \gamma x_k^2) \sum_j \sqrt{p_j}.
 \end{aligned}$$

Multiplying both sides by p_k and summing over k , we obtain the relation

$$\alpha + \gamma V = 1.$$

This, together with the constraint $\partial L / \partial \alpha = 0$, allows us to write

$$p_k = \frac{1/[1 + \gamma(x_k^2 - V)]^2}{\sum_j \left\{ 1/[1 + \gamma(x_j^2 - V)]^2 \right\}}.$$

We recognize this as a discretized version of the nonstandardized Student's t -distribution with 3 degrees of freedom

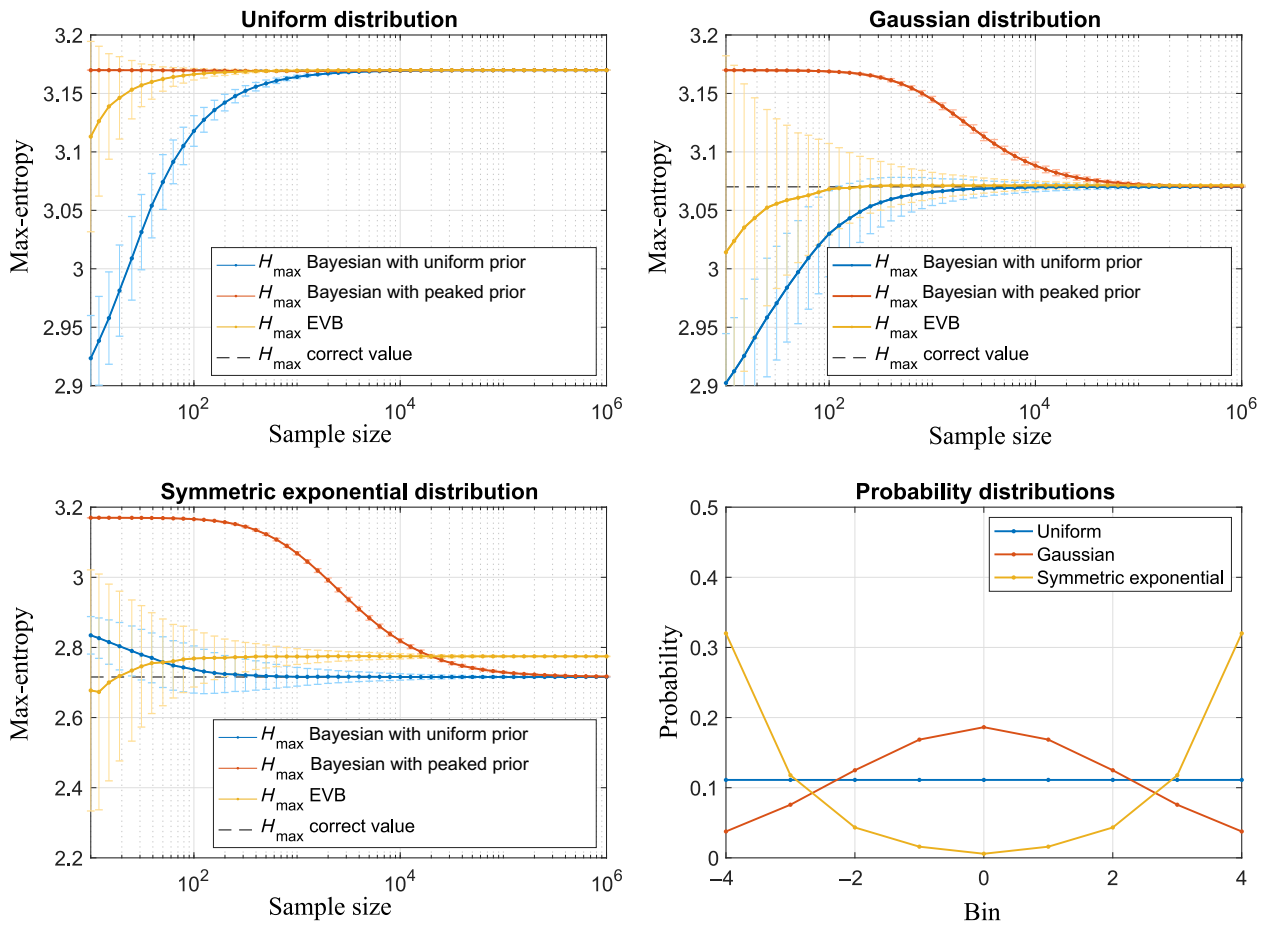


FIG. 8. Comparison of estimators for H_{\max} on three probability distributions with just nine bins. A negative bias in H_{\max} translates to a positive bias in H_{low} . For the Bayesian estimator with a peaked prior, K is set to 100.

and standard deviation s ,

$$S_3(x; s) = \frac{2}{\pi s (1 + x^2/s^2)^2}.$$

When $\delta q \rightarrow 0$ and $m \delta q \rightarrow \infty$, we retrieve the continuous limit, $\gamma \rightarrow \frac{1}{2}$ and $s^2 \rightarrow V$. This is consistent with the known result that the Student's t -distribution is the extremal continuous distribution for H_{\max} [69].

A necessary condition for the Lagrange multiplier γ is obtained from the constraint $\partial L/\partial \gamma = 0$, which gives an implicit equation

$$\begin{aligned} \sum_k \frac{x_k^2}{[1 + \gamma(x_k^2 - V)]^2} &= \sum_j \frac{V}{[1 + \gamma(x_j^2 - V)]^2} \\ \Rightarrow \sum_k \frac{x_k^2 - V}{[1 + \gamma(x_k^2 - V)]^2} &= 0. \end{aligned}$$

Numerically, we see that there can be more than one real solution for γ . The extremal H_{\max} is given by the solution that is closest to zero.

APPENDIX D: EXAMPLE OF SMALL NUMBER OF BINS

In this Appendix, we show that in extreme cases, when the number of bins is very small, when the number of samples is very small, or when the input state saturates the extreme bins, some of the estimators for H_{\max} proposed in the main text may still be negatively biased, which leads to a positive bias in H_{low} . To illustrate this, we consider three different distributions with only nine bins, as shown in Fig. 8. The only estimator that shows no negative bias is the peaked-prior Bayes estimator.

-
- [1] P. Hellekalek, Good random number generators are (not so) easy to find, *Math. Comput. Simul.* **46**, 485 (1998).
- [2] Y. Dodis, D. Pointcheval, S. Ruhault, D. Vergniaud, and D. Wichs, in *Proceedings of the 2013, ACM SIGSAC Conference on Computer and Communications Security – CCS'13* (ACM Press, Berlin, Germany, 2013), p. 647.
- [3] M. Herrero-Collantes and J. C. Garcia-Escartin, Quantum random number generators, *Rev. Mod. Phys.* **89**, 015004 (2017).
- [4] G. Marsaglia, Random numbers fall mainly in the planes, *Proc. Natl. Acad. Sci. U.S.A.* **61**, 25 (1968).
- [5] A. M. Ferrenberg, D. P. Landau, and Y. J. Wong, Monte Carlo Simulations: Hidden Errors from “Good” Random Number Generators, *Phys. Rev. Lett.* **69**, 3382 (1992).
- [6] A. Uchida, K. Amano, M. Inoue, K. Hirano, S. Naito, H. Someya, I. Oowada, T. Kurashige, M. Shiki, S. Yoshimori, K. Yoshimura, and P. Davis, Fast physical random bit generation with chaotic semiconductor lasers, *Nat. Photonics* **2**, 728 (2008).
- [7] D. G. Marangon, G. Vallone, and P. Villoresi, Random bits, true and unbiased, from atmospheric turbulence, *Sci. Rep.* **4**, 5490 (2015).
- [8] X. Ma, X. Yuan, Z. Cao, B. Qi, and Z. Zhang, Quantum random number generation, *npj Quantum Inf.* **2**, 16021 (2016).
- [9] J. Rarity, P. Owens, and P. Tapster, Quantum random-number generation and key sharing, *J. Mod. Opt.* **41**, 2435 (1994).
- [10] D. G. Marangon, A. Plews, M. Lucamarini, J. F. Dynes, A. W. Sharpe, Z. Yuan, and A. J. Shields, Long-term test of a fast and compact quantum random number generator, *J. Lightwave Technol.* **JLT 36**, 3778 (2018).
- [11] A. Trifonov and H. Vig, Quantum noise random number generator U.S. Patent No. 7,284,024 (2007).
- [12] T. Symul, S. M. Assad, and P. K. Lam, Real time demonstration of high bitrate quantum random number generation with coherent laser light, *Appl. Phys. Lett.* **98**, 231103 (2011).
- [13] J. Y. Haw, S. M. Assad, A. M. Lance, N. H. Y. Ng, V. Sharma, P. K. Lam, and T. Symul, Maximization of Extractable Randomness in a Quantum Random-Number Generator, *Phys. Rev. Appl.* **3**, 054004 (2015).
- [14] Q. Zhang, X. Deng, C. Tian, and X. Su, Quantum random number generator based on twin beams, *Opt. Lett.* **42**, 895 (2017).
- [15] T. Lunghi, J. B. Brask, C. C. W. Lim, Q. Lavigne, J. Bowles, A. Martin, H. Zbinden, and N. Brunner, Self-Testing Quantum Random Number Generator, *Phys. Rev. Lett.* **114**, 150501 (2015).
- [16] B. Sanguinetti, A. Martin, H. Zbinden, and N. Gisin, Quantum Random Number Generation on a Mobile Phone, *Phys. Rev. X* **4**, 031056 (2014).
- [17] D. Frauchiger, R. Renner, and M. Troyer, True randomness from realistic quantum devices, arXiv:1311.4547 [quant-ph] (2013).
- [18] J. S. Bell, On the einstein podolsky rosen paradox, *Phys. Phys. Fiz.* **1**, 195 (1964).
- [19] N. Brunner, D. Cavalcanti, S. Pironio, V. Scarani, and S. Wehner, Bell nonlocality, *Rev. Mod. Phys.* **86**, 419 (2014).
- [20] S. Pironio, A. Acín, S. Massar, A. B. de la Giroday, D. N. Matsukevich, P. Maunz, S. Olmschenk, D. Hayes, L. Luo, T. A. Manning, and C. Monroe, Random numbers certified by Bell's theorem, *Nature* **464**, 1021 (2010).
- [21] B. G. Christensen, K. T. McCusker, J. B. Altepeter, B. Calkins, T. Gerrits, A. E. Lita, A. Miller, L. K. Shalm, Y. Zhang, S. W. Nam, N. Brunner, C. C. W. Lim, N. Gisin, and P. G. Kwiat, Detection-loophole-free Test of Quantum Nonlocality and Applications, *Phys. Rev. Lett.* **111**, 130406 (2013).
- [22] M. Pivoluska and M. Plesch, Device independent random number generation, *Acta Phys. Slovaca* **64**, 601 (2014).
- [23] Y. Liu, X. Yuan, M.-H. Li, W. Zhang, Q. Zhao, J. Zhong, Y. Cao, Y.-H. Li, L.-K. Chen, H. Li, T. Peng, Y.-A. Chen, C.-Z. Peng, S.-C. Shi, Z. Wang, L. You, X. Ma, J. Fan, Q. Zhang, and J.-W. Pan, High-speed Device-independent Quantum Random Number Generation Without a Detection Loophole, *Phys. Rev. Lett.* **120**, 010503 (2018).
- [24] P. Bierhorst, E. Knill, S. Glancy, Y. Zhang, A. Mink, S. Jordan, A. Rommal, Y.-K. Liu, B. Christensen, S. W. Nam, M. J. Stevens, and L. K. Shalm, Experimentally generated

- randomness certified by the impossibility of superluminal signals, *Nature* **556**, 223 (2018).
- [25] C. Wu, B. Bai, Y. Liu, X. Zhang, M. Yang, Y. Cao, J. Wang, S. Zhang, H. Zhou, X. Shi, X. Ma, J.-G. Ren, J. Zhang, C.-Z. Peng, J. Fan, Q. Zhang, and J.-W. Pan, Random Number Generation with Cosmic Photons, *Phys. Rev. Lett.* **118**, 140402 (2017).
- [26] J. Handsteiner, A. S. Friedman, D. Rauch, J. Gallicchio, B. Liu, H. Hosp, J. Kofler, D. Bricher, M. Fink, C. Leung, A. Mark, H. T. Nguyen, I. Sanders, F. Steinlechner, R. Ursin, S. Wengerowsky, A. H. Guth, D. I. Kaiser, T. Scheidl, and A. Zeilinger, Cosmic Bell Test: Measurement Settings from Milky way Stars, *Phys. Rev. Lett.* **118**, 060401 (2017).
- [27] C. Leung, A. Brown, H. Nguyen, A. S. Friedman, D. I. Kaiser, and J. Gallicchio, Astronomical random numbers for quantum foundations experiments, *Phys. Rev. A* **97**, 042120 (2018).
- [28] Y.-Q. Nie, J.-Y. Guan, H. Zhou, Q. Zhang, X. Ma, J. Zhang, and J.-W. Pan, Experimental measurement-device-independent quantum random-number generation, *Phys. Rev. A* **94**, 060301 (2016).
- [29] G. Vallone, D. G. Marangon, M. Tomasin, and P. Villoresi, Quantum randomness certified by the uncertainty principle, *Phys. Rev. A* **90**, 052327 (2014).
- [30] B. Xu, Z. Chen, Z. Li, J. Yang, Q. Su, W. Huang, Y. Zhang, and H. Guo, High speed continuous variable source-independent quantum random number generation, *Quantum Sci. Technol.* **4**, 025013 (2019).
- [31] D. G. Marangon, G. Vallone, and P. Villoresi, Source-device-independent Ultra-fast Quantum Random Number Generation, *Phys. Rev. Lett.* **118**, 060503 (2017).
- [32] J. Ma, A. Hakande, X. Yuan, and X. Ma, Coherence as a resource for source-independent quantum random-number generation, *Phys. Rev. A* **99**, 022328 (2019).
- [33] M. Avesani, D. G. Marangon, G. Vallone, and P. Villoresi, Source-device-independent heterodyne-based quantum random number generator at 17 Gbps, *Nat. Commun.* **9**, 5365 (2018).
- [34] F. Furrer, M. Berta, M. Tomamichel, V. B. Scholz, and M. Christandl, Position-momentum uncertainty relations in the presence of quantum memory, *J. Math. Phys.* **55**, 122205 (2014).
- [35] I. Białynicki-Birula and J. Mycielski, Uncertainty relations for information entropy in wave mechanics, *Commun. Math. Phys.* **44**, 129 (1975).
- [36] Y. Zhu, G. He, and G. Zeng, Unbiased quantum random number generation based on squeezed vacuum state, *Int. J. Quantum Inf.* **10**, 1250012 (2012).
- [37] R. Renner, Security of quantum key distribution, *Int. J. Quantum Inf.* **6**, 1 (2008).
- [38] R. König, R. Renner, and C. Schaffner, The operational meaning of min- and max-entropy, *IEEE Trans. Inf. Theory* **55**, 4337 (2009).
- [39] R. König and R. Renner, Sampling of min-entropy relative to quantum knowledge, *IEEE Trans. Inf. Theory* **57**, 4760 (2011).
- [40] M. Tomamichel and M. Hayashi, A hierarchy of information quantities for finite block length analysis of quantum tasks, *IEEE Trans. Inf. Theory* **59**, 7693 (2013).
- [41] M. Tomamichel, *Quantum Information Processing with Finite Resources: Mathematical Foundations* (Springer, 2015), Vol. 5.
- [42] M. Tomamichel, R. Colbeck, and R. Renner, A fully quantum asymptotic equipartition property, *IEEE Trans. Inf. Theory* **55**, 5840 (2009).
- [43] M. Berta, M. Christandl, R. Colbeck, J. M. Renes, and R. Renner, The uncertainty principle in the presence of quantum memory, *Nat. Phys.* **6**, 659 (2010).
- [44] A. E. Rastegin, Entropic uncertainty relations for extremal unravelings of super-operators, *J. Phys. A: Math. Theor.* **44**, 095303 (2011).
- [45] M. Tomamichel and R. Renner, The Uncertainty Relation for Smooth Entropies, *Phys. Rev. Lett.* **106**, 110506 (2011).
- [46] P. J. Coles, R. Colbeck, L. Yu, and M. Zwozak, Uncertainty Relations from Simple Entropic Properties, *Phys. Rev. Lett.* **108**, 210405 (2012).
- [47] J. Zhang, Y. Zhang, and C.-S. Yu, Rényi entropy uncertainty relation for successive projective measurements, *Quantum Inf. Process.* **14**, 2239 (2015).
- [48] P. J. Coles, M. Berta, M. Tomamichel, and S. Wehner, Entropic uncertainty relations and their applications, *Rev. Mod. Phys.* **89**, 015002 (2017).
- [49] A. Rényi, in *Proceedings of the Fourth Berkeley Symposium on Mathematical Statistics and Probability, Volume 1: Contributions to the Theory of Statistics* (The Regents of the University of California, Berkeley, Los Angeles, 1961).
- [50] H. J. Landau and H. O. Pollak, Prolate spheroidal wave functions, Fourier analysis and uncertainty – II, *Bell Syst. Tech. J.* **40**, 65 (1961).
- [51] T. Van Himbeek, E. Woodhead, N. J. Cerf, R. García-Patrón, and S. Pironio, Semi-device-independent framework based on natural physical assumptions, *Quantum* **1**, 33 (2017).
- [52] F. Furrer, Reverse-reconciliation continuous-variable quantum key distribution based on the uncertainty principle, *Phys. Rev. A* **90**, 042325 (2014).
- [53] Y.-C. Zhang, Z. Chen, C. Weedbrook, S. Yu, and H. Guo, Continuous-variable source-device-independent quantum key distribution against general attacks, arXiv:1811.11973 [quant-ph] (2018).
- [54] D. Drahı, N. Walk, M. J. Hoban, W. S. Kolthammer, J. Nunn, J. Barrett, and I. A. Walmsley, Certified quantum randomness from untrusted light, arXiv:1905.09665v2 [quant-ph] (2019).
- [55] See Supplemental Material at <http://link.aps.org/supplemental/10.1103/PhysRevApplied.12.034017> for details of the experimental setup and the data acquisition and processing.
- [56] H. M. Chrzanowski, S. M. Assad, J. Bernu, B. Hage, A. P. Lund, T. C. Ralph, P. K. Lam, and T. Symul, Reconstruction of photon number conditioned states using phase randomized homodyne measurements, *J. Phys. B: At. Mol. Opt. Phys.* **46**, 104009 (2013).
- [57] X. Ma, F. Xu, H. Xu, X. Tan, B. Qi, and H.-K. Lo, Postprocessing for quantum random-number generators: Entropy evaluation and randomness extraction, *Phys. Rev. A* **87**, 062327 (2013).
- [58] C. H. Bennett, G. Brassard, C. Crépeau, and U. M. Maurer, Generalized privacy amplification, *IEEE Trans. Inf. Theory* **41**, 1915 (1995).

- [59] R. Renner and R. König, in *Theory of Cryptography*, edited by J. Kilian (Springer Berlin Heidelberg, Berlin, Heidelberg, 2005), p. 407.
- [60] D. H. Wolpert and D. R. Wolf, Estimating functions of probability distributions from a finite set of samples, *Phys. Rev. E* **52**, 6841 (1995).
- [61] D. Holste, I. Große, and H. Herzel, Bayes' estimators of generalized entropies, *J. Phys. A: Math. Gen.* **31**, 2551 (1998).
- [62] T. Leonard, A Bayesian approach to some multinomial estimation and pretesting problems, *J. Am. Stat. Assoc.* **72**, 869 (1977).
- [63] C. E. Shannon, A mathematical theory of communication, *Bell Syst. Tech. J.* **27**, 379 (1948).
- [64] M. M. Wolf, G. Giedke, and J. I. Cirac, Extremality of Gaussian Quantum States, *Phys. Rev. Lett.* **96**, 080502 (2006).
- [65] R. García-Patrón and N. J. Cerf, Unconditional Optimality of Gaussian Attacks against Continuous-Variable Quantum Key Distribution, *Phys. Rev. Lett.* **97**, 190503 (2006).
- [66] M. Navascués, F. Grosshans, and A. Acín, Optimality of Gaussian Attacks in Continuous-Variable Quantum Cryptography, *Phys. Rev. Lett.* **97**, 190502 (2006).
- [67] X.-G. Zhang, Y.-Q. Nie, H. Zhou, H. Liang, X. Ma, J. Zhang, and J.-W. Pan, Note: Fully integrated 3.2 Gbps quantum random number generator with real-time extraction, *Rev. Sci. Instrum.* **87**, 076102 (2016).
- [68] S. Ast, M. Mehmet, and R. Schnabel, High-bandwidth squeezed light at 1550 nm from a compact monolithic PPKTP cavity, *Opt. Express* **21**, 13572 (2013).
- [69] O. Johnson and C. Vignat, Some results concerning maximum Rényi entropy distributions, *Ann. Inst. Henri Poincaré (B) Probab. Stat.* **43**, 339 (2007).

A.2 Gaussian unitaries

Here we give the proof of relations (2.34). In creation/annihilation space the BM decomposition reads:

$$\mathbf{E} = \mathbf{U}\mathbf{\Lambda}_E\mathbf{V}^\dagger \quad (\text{A.1})$$

$$\mathbf{F} = \mathbf{U}\mathbf{\Lambda}_F\mathbf{V}^T \quad (\text{A.2})$$

In quadrature space it reads:

$$\mathbf{S} = \mathbf{O}_1 \begin{pmatrix} \mathbf{K} & 0 \\ 0 & \mathbf{K}^{-1} \end{pmatrix} \mathbf{O}_2 \quad (\text{A.3})$$

Where \mathbf{S} is related to \mathbf{E} and \mathbf{F} via:

$$\mathbf{S} = \mathbf{W} \begin{pmatrix} \mathbf{E} & \mathbf{F} \\ \mathbf{F}^* & \mathbf{E}^* \end{pmatrix} \mathbf{W}^{-1} \quad (\text{A.4})$$

With $\mathbf{W} = \begin{pmatrix} 1 & 1 \\ -i & i \end{pmatrix}$ and $\mathbf{W}^{-1} = \frac{1}{2} \begin{pmatrix} 1 & i \\ 1 & -i \end{pmatrix}$.

We want to find the relation between \mathbf{O}_1 , \mathbf{O}_2 , \mathbf{K} and \mathbf{U} , \mathbf{V} , $\mathbf{\Lambda}_E$, $\mathbf{\Lambda}_F$.

First let us explicitly calculate \mathbf{S} in terms of \mathbf{E} , \mathbf{F} , we find:

$$\mathbf{S} = \frac{1}{2} \begin{pmatrix} \mathbf{E}^* + \mathbf{E} + \mathbf{F}^* + \mathbf{F} & -i(\mathbf{E}^* - \mathbf{E}) + i(\mathbf{F}^* - \mathbf{F}) \\ i(\mathbf{E}^* - \mathbf{E}) + i(\mathbf{F}^* - \mathbf{F}) & \mathbf{E}^* + \mathbf{E} - (\mathbf{F}^* + \mathbf{F}) \end{pmatrix} \quad (\text{A.5})$$

$$= \begin{pmatrix} \text{Re}(\mathbf{E}) + \text{Re}(\mathbf{F}) & \text{Im}(\mathbf{F}) - \text{Im}(\mathbf{E}) \\ \text{Im}(\mathbf{E}) + \text{Im}(\mathbf{F}) & \text{Re}(\mathbf{E}) - \text{Re}(\mathbf{F}) \end{pmatrix} \quad (\text{A.6})$$

Let us define $\mathbf{X}_{U/V}$ and $\mathbf{Y}_{U/V}$ as the real and imaginary part of \mathbf{U}/\mathbf{V} . From the BM decomposition we get:

$$\mathbf{E} = (\mathbf{X}_U + i\mathbf{Y}_U)\mathbf{\Lambda}_E(\mathbf{X}_V + i\mathbf{Y}_V)^\dagger \quad (\text{A.7})$$

$$= (\mathbf{X}_U\mathbf{\Lambda}_E\mathbf{X}_V^T + \mathbf{Y}_U\mathbf{\Lambda}_E\mathbf{Y}_V^T) + i(-\mathbf{X}_U\mathbf{\Lambda}_E\mathbf{Y}_V^T + \mathbf{Y}_U\mathbf{\Lambda}_E\mathbf{X}_V^T) \quad (\text{A.8})$$

$$\mathbf{F} = (\mathbf{X}_U + i\mathbf{Y}_U)\mathbf{\Lambda}_F(\mathbf{X}_V + i\mathbf{Y}_V)^T \quad (\text{A.9})$$

$$= (\mathbf{X}_U\mathbf{\Lambda}_F\mathbf{X}_V^T - \mathbf{Y}_U\mathbf{\Lambda}_F\mathbf{Y}_V^T) + i(\mathbf{X}_U\mathbf{\Lambda}_F\mathbf{Y}_V^T + \mathbf{Y}_U\mathbf{\Lambda}_F\mathbf{X}_V^T) \quad (\text{A.10})$$

So that \mathbf{S} can now be written:

$$\mathbf{S} = \begin{pmatrix} \mathbf{X}_U(\mathbf{\Lambda}_E + \mathbf{\Lambda}_F)\mathbf{X}_V^T + \mathbf{Y}_U(\mathbf{\Lambda}_E - \mathbf{\Lambda}_F)\mathbf{Y}_V^T & \mathbf{X}_U(\mathbf{\Lambda}_E + \mathbf{\Lambda}_F)\mathbf{Y}_V^T - \mathbf{Y}_U(\mathbf{\Lambda}_E - \mathbf{\Lambda}_F)\mathbf{X}_V^T \\ -\mathbf{X}_U(\mathbf{\Lambda}_E - \mathbf{\Lambda}_F)\mathbf{Y}_V^T + \mathbf{Y}_U(\mathbf{\Lambda}_E + \mathbf{\Lambda}_F)\mathbf{X}_V^T & \mathbf{X}_U(\mathbf{\Lambda}_E - \mathbf{\Lambda}_F)\mathbf{X}_V^T + \mathbf{Y}_U(\mathbf{\Lambda}_E + \mathbf{\Lambda}_F)\mathbf{Y}_V^T \end{pmatrix} \quad (\text{A.11})$$

Let us write \mathbf{O}_1 and \mathbf{O}_2 from Eq. A.3 as:

$$\mathbf{O}_1 = \begin{pmatrix} \mathbf{X}_1 & \mathbf{Y}_1 \\ -\mathbf{Y}_1 & \mathbf{X}_1 \end{pmatrix} \quad (\text{A.12})$$

$$\mathbf{O}_2 = \begin{pmatrix} \mathbf{X}_2 & \mathbf{Y}_2 \\ -\mathbf{Y}_2 & \mathbf{X}_2 \end{pmatrix} \quad (\text{A.13})$$

We can then develop:

$$\mathbf{S} = \mathbf{O}_1 \begin{pmatrix} \mathbf{K} & 0 \\ 0 & \mathbf{K}^{-1} \end{pmatrix} \mathbf{O}_2 \quad (\text{A.14})$$

$$= \begin{pmatrix} \mathbf{X}_1 \mathbf{K} \mathbf{X}_2 - \mathbf{Y}_1 \mathbf{K}^{-1} \mathbf{Y}_2 & \mathbf{X}_1 \mathbf{K} \mathbf{Y}_2 + \mathbf{Y}_1 \mathbf{K}^{-1} \mathbf{X}_2 \\ -\mathbf{Y}_1 \mathbf{K} \mathbf{X}_2 - \mathbf{X}_1 \mathbf{K}^{-1} \mathbf{Y}_2 & -\mathbf{Y}_1 \mathbf{K} \mathbf{Y}_2 + \mathbf{X}_1 \mathbf{K}^{-1} \mathbf{X}_2 \end{pmatrix} \quad (\text{A.15})$$

This expression can be identified with Eq. A.11 if we set:

$$\mathbf{K} = \mathbf{\Lambda}_E + \mathbf{\Lambda}_F \quad (\text{A.16})$$

$$\mathbf{K}^{-1} = \mathbf{\Lambda}_E - \mathbf{\Lambda}_F \quad (\text{A.17})$$

and

$$\mathbf{X}_1 = \mathbf{X}_U \quad (\text{A.18})$$

$$\mathbf{Y}_1 = -\mathbf{Y}_U \quad (\text{A.19})$$

$$\mathbf{X}_2 = \mathbf{X}_V^T \quad (\text{A.20})$$

$$\mathbf{Y}_2 = \mathbf{Y}_V^T \quad (\text{A.21})$$

In other words:

$$\mathbf{O}_1 = \begin{pmatrix} \text{Re}(\mathbf{U}) & -\text{Im}(\mathbf{U}) \\ \text{Im}(\mathbf{U}) & \text{Re}(\mathbf{U}) \end{pmatrix} \quad (\text{A.22})$$

$$\mathbf{O}_2 = \begin{pmatrix} \text{Re}(\mathbf{V}) & -\text{Im}(\mathbf{V}) \\ \text{Im}(\mathbf{V}) & \text{Re}(\mathbf{V}) \end{pmatrix}^T \quad (\text{A.23})$$

Table A.1 shows the common Gaussian unitaries and their properties.

Transformation \hat{H}	Unitary $\hat{U} = \exp(-i\hat{H})$	Mode transformation $\hat{U}^\dagger \hat{a} \hat{U}$	Quadrature transformation
Phase rotation θ	$\hat{R}(\theta) = e^{-i\theta \hat{a}^\dagger \hat{a}}$	$e^{-i\theta} \hat{a}$	$\mathbf{d} = \mathbf{0}$ $\mathbf{S} = \mathbf{R}(\theta) = \begin{pmatrix} \cos \theta & \sin \theta \\ -\sin \theta & \cos \theta \end{pmatrix}$
Displacement α	$\hat{D}(\alpha) = e^{\alpha \hat{a}^\dagger - \alpha^* \hat{a}}$	$\hat{a} + \alpha$	$\mathbf{d} = \begin{pmatrix} 2\text{Re}(\alpha) \\ 2\text{Im}(\alpha) \end{pmatrix}$ $\mathbf{S} = \mathbf{1}$
Single mode squeezing $\zeta = r e^{i\theta}$	$\hat{S}(\zeta) = e^{(\zeta \hat{a}^{\dagger 2} - \zeta^* \hat{a}^2)/2}$	$\hat{a} \rightarrow \cosh r \hat{a} + e^{i\theta} \sinh r \hat{a}^\dagger$	$\mathbf{d} = \mathbf{0}$ $\mathbf{S} = \mathbf{R}(-\frac{\theta}{2}) \begin{pmatrix} e^r & 0 \\ 0 & e^{-r} \end{pmatrix} \mathbf{R}(\frac{\theta}{2})$
Beam splitter $\eta = \cos^2(\theta)$	$\hat{B}(\theta) = e^{\theta(\hat{a}_1^\dagger \hat{a}_2 - \hat{a}_1 \hat{a}_2^\dagger)}$	$\begin{pmatrix} \hat{a}_1 \\ \hat{a}_2 \end{pmatrix} \rightarrow \mathbf{R}(\theta) \begin{pmatrix} \hat{a}_1 \\ \hat{a}_2 \end{pmatrix}$	$\mathbf{d} = \mathbf{0}$ $\mathbf{S} = \mathbf{R}_2(\theta) = \begin{pmatrix} \mathbf{R}(\theta) & \mathbf{0} \\ \mathbf{0} & \mathbf{R}(\theta) \end{pmatrix}$
Two-mode squeezing $\zeta = r e^{i\theta}$	$\hat{S}_2(\zeta) = e^{(\zeta \hat{a}_1^\dagger \hat{a}_2^\dagger - \zeta^* \hat{a}_1 \hat{a}_2)}$	$\hat{a}_{1/2} \rightarrow \cosh r \hat{a}_{1/2} + e^{i\theta} \sinh r \hat{a}_{2/1}^\dagger$	$\mathbf{d} = \mathbf{0}$ $\mathbf{S} = \begin{pmatrix} \cosh r \sinh r & 0 & 0 \\ \sinh r \cosh r & 0 & 0 \\ 0 & \cosh r \sinh r & 0 \\ 0 & \sinh r \cosh r & 0 \end{pmatrix} \cdot (\mathbf{R}(\theta) \otimes \mathbf{1})$

Table A.1 – Common Gaussian unitary transformations and their properties. “QQPP” convention is used for symplectic space.

A.3 Fourier transform definition and useful properties

Throughout this thesis we will use the following definitions of the 1D-Fourier transform and its inverse:

$$\tilde{f}(\omega) := \mathcal{F}[f](\omega) = \int_{\mathbb{R}} \frac{dt}{\sqrt{2\pi}} f(t) e^{i\omega t} \quad (\text{A.24})$$

$$f(t) := \mathcal{F}^{-1}[\tilde{f}](t) = \int_{\mathbb{R}} \frac{d\omega}{\sqrt{2\pi}} \tilde{f}(\omega) e^{-i\omega t} \quad (\text{A.25})$$

With these convention the Fourier transform is unitary. Note the sign in the exponential is opposite to the most standard convention, this is to be consistent with the definition of the analytical field of chapter 1 in which the positive frequency components oscillate with a $e^{-i\omega t}$ factor.

Useful properties of the Fourier transform are given in Table A.2.

$f \text{ real} \Rightarrow \tilde{f}(-\omega) = \tilde{f}(\omega)^*$ $\mathcal{F}[f(t - t_0)](\omega) = e^{i\omega t_0} \tilde{f}(\omega)$ $\mathcal{F}^{-1}[\tilde{f}(\omega - \omega_0)](t) = e^{-i\omega_0 t} f(t)$ $\mathcal{F}[f(t) e^{-i\omega_0 t}](\omega) = \tilde{f}(\omega - \omega_0)$ $\mathcal{F}^{-1}[\tilde{f}(\omega) e^{-i\omega t_0}](t) = f(t + t_0)$ $\mathcal{F}[f \times g] = \frac{1}{\sqrt{2\pi}} \mathcal{F}[f] \otimes \mathcal{F}[g]$ $\mathcal{F}[f \otimes g] = \sqrt{2\pi} \mathcal{F}[f] \times \mathcal{F}[g]$
--

Table A.2 – Fourier transform properties.

Fourier transforms of commonly used functions and distributions are given in table A.3

$\mathcal{F}[e^{-\alpha t^2}](\omega) = \frac{1}{\sqrt{2\alpha}} e^{-\frac{\omega^2}{4\alpha}} \quad \text{with} \quad \text{Re}\{\alpha\} > 0$ $\mathcal{F}[\Pi_T(t)](\omega) = \frac{T}{\sqrt{2\pi}} \text{sinc}\left(\frac{\omega T}{2}\right)$ $\mathcal{F}[1](\omega) = \sqrt{2\pi} \delta(\omega)$ $\mathcal{F}[e^{-i\omega_0 t}](\omega) = \sqrt{2\pi} \delta(\omega - \omega_0)$ $\mathcal{F}[\text{III}_T(t)](\omega) = \frac{\sqrt{2\pi}}{T} \text{III}_{\Omega=\frac{2\pi}{T}}(\omega)$
--

Table A.3 – Common Fourier transforms.

A.4 Derivation of the non linear interaction equation from Maxwell's equations

Given an electric charge density $\rho(\mathbf{r}, t)$ (in C m^{-3}) and an electric current density $\mathbf{j}(\mathbf{r}, t)$ (in A m^{-3}), the electric vector field $\mathbf{E}(\mathbf{r}, t)$ (in V m^{-1}) and the magnetic pseudo-vector field $\mathbf{B}(\mathbf{r}, t)$ (in T or $\text{kg s}^{-2} \text{A}^{-1}$) are governed by Maxwell's equations, which read (in the

Si units convention):

$$\nabla \cdot \mathbf{E} = \frac{\rho}{\varepsilon_0} \quad \boxed{\text{Gauss electric}} \quad (\text{A.26})$$

$$\nabla \cdot \mathbf{B} = 0 \quad \boxed{\text{Gauss magnetic}} \quad (\text{A.27})$$

$$\nabla \times \mathbf{E} = -\frac{\partial \mathbf{B}}{\partial t} \quad \boxed{\text{Maxwell-Faraday}} \quad (\text{A.28})$$

$$\nabla \times \mathbf{B} = \mu_0(\mathbf{j} + \varepsilon_0 \frac{\partial \mathbf{E}}{\partial t}) \quad \boxed{\text{Maxwell-Ampère}} \quad (\text{A.29})$$

where the two constant ε_0 (in F m^{-1} or $\text{C}^2 \text{N}^{-1} \text{m}^{-2}$) and μ_0 (in H m^{-1} or N A^{-2}) are respectively, the permittivity/dielectric constant and the permeability/magnetic constant of vacuum. They are linked to the speed of light in vacuum by $c = \frac{1}{\sqrt{\varepsilon_0 \mu_0}}$. These equations are sometimes referred to as the microscopic Maxwell's equations because they relate fundamental microscopic quantities.

Inside matter, on the other end, Maxwell's equations can be modified to describe mesoscopic quantities. The fields and charge/current densities are then described as mesoscopic averages. This allows to neglect the inhomogeneities at the atom level, to have a more bulk description of a material. The effects of bound charges and current densities ρ_b and \mathbf{j}_b are considered separately from the free ones ρ_f and \mathbf{j}_f . The mesoscopic displacement field \mathbf{D} and magnetising field \mathbf{H} include the effect of bound charges and currents:

$$\mathbf{D}(\mathbf{r}, t) = \varepsilon_0 \mathbf{E}(\mathbf{r}, t) + \mathbf{P}(\mathbf{r}, t) \quad (\text{A.30})$$

$$\mathbf{H}(\mathbf{r}, t) = \frac{1}{\mu_0} \mathbf{B}(\mathbf{r}, t) - \mathbf{M}(\mathbf{r}, t) \quad (\text{A.31})$$

where \mathbf{P} and \mathbf{M} are the electric and magnetic polarisation field induced by bound charges and currents:

$$\nabla \cdot \mathbf{P} = -\rho_b \quad (\text{A.32})$$

$$\nabla \times \mathbf{M} = \mathbf{j}_b - \frac{\partial \mathbf{P}}{\partial t} \quad (\text{A.33})$$

With these quantities Maxwell's equation read:

$$\nabla \cdot \mathbf{D} = \rho_f \quad (\text{A.34})$$

$$\nabla \cdot \mathbf{B} = 0 \quad (\text{A.35})$$

$$\nabla \times \mathbf{E} = -\frac{\partial \mathbf{B}}{\partial t} \quad (\text{A.36})$$

$$\nabla \times \mathbf{H} = \mathbf{j}_f + \frac{\partial \mathbf{D}}{\partial t} \quad (\text{A.37})$$

Let us now consider a homogeneous dielectric material, by definition it's an insulating material which means it contains no free charges or current $\rho_f = 0$ and $\mathbf{j}_f = \mathbf{0}$. It has also no magnetisation $\mathbf{M} = \mathbf{0}$ so $\mathbf{B} = \mu_0 \mathbf{H}$. Let us now take the curl of equation A.36 and use the identity $\nabla \times \nabla \times \mathbf{A} = \nabla(\nabla \cdot \mathbf{A}) - \nabla^2 \mathbf{A}$. We get

$$\nabla(\nabla \cdot \mathbf{E}) - \nabla^2 \mathbf{E} = -\frac{\partial \nabla \times \mathbf{B}}{\partial t} \quad (\text{A.38})$$

Where we have swapped the two linear operator, curl and time derivative in the second member. Substituting Eq. A.37 and A.30 we now get:

$$-\frac{1}{\varepsilon_0}\nabla(\nabla\cdot\mathbf{P})-\nabla^2\mathbf{E}=-\mu_0\frac{\partial^2 D}{\partial t^2} \quad (\text{A.39})$$

Now using eq A.32 and A.30 we obtain:

$$-\frac{1}{\varepsilon_0}\nabla(-\rho_b)-\nabla^2\mathbf{E}=-\mu_0(\varepsilon_0\frac{\partial^2 E}{\partial t^2}+\frac{\partial^2 P}{\partial t^2}) \quad (\text{A.40})$$

The first term vanishes because the media is homogeneous so ρ_b does not depend on the position \mathbf{r} . We therefore obtain the equation:

$$\nabla^2\mathbf{E}-\frac{1}{c^2}\frac{\partial^2 E}{\partial t^2}=\frac{1}{\varepsilon_0 c^2}\frac{\partial^2 P}{\partial t^2} \quad (\text{A.41})$$

A.5 Units, normalization and discretization

This section deals with making sure our units are coherent so that the proper SHG efficiencies η_{SHG} coupling factor χ gain g are obtained in chapter 6. This is relevant to obtain a properly scaled \mathcal{S}_0 and allow us to obtain the absolute values of squeezing for a given pump power as well as the pump threshold. Moreover, it is important when taking into account intra-cavity dispersion effect, in order to have the right scaling between \mathcal{U}_0 and \mathcal{S}_0 . An electric field is defined in units of V m^{-1} so we can write the electric field as follow:

$$\mathbf{E}^{(+)}(\rho, t) = E_0 s(t) u(\rho) e^{i\omega_0 t} \quad (\text{A.42})$$

Where $s(t)$ is a (unitless) function giving the temporal envelope of $\mathbf{E}^{(+)}(\rho, t)$, $u(\rho)$ is a (unitless) function giving the transverse spatial shape of $\mathbf{E}^{(+)}(\rho, t)$ and E_0 is the field amplitude in V m^{-1} . Here we will consider $s(t)$ to be a train of pulse, so we will introduce τ the effective temporal width of $\mathbf{E}^{(+)}(\rho, t)$ defined as

$$\tau = \int_{\text{pulse}} |s(t)|^2 dt \quad (\text{A.43})$$

for a Gaussian envelope of temporal width Δt (intensity standard deviation) we therefore have $\tau = \sqrt{2\pi}\Delta t$. And S the typical area of $\mathbf{E}^{(+)}(\rho, t)$ defined as

$$S = \int_{\mathbb{R}^2} u(\rho)^2 d^2\rho \quad (\text{A.44})$$

for a Gaussian beam of waist w we therefore have $S = \frac{\pi w^2}{2}$.

Let's derive how we can recover the field amplitude E_0 from variables we know (beam power, repetition rate etc.) The field intensity is usually defined as the average of the Poynting vector (average being taken over a time long compared to an optical cycle), it can then be determined from the analytical field as

$$I(\mathbf{r}, t) = 2nc\varepsilon_0 \left\| \mathbf{E}^{(+)}(\mathbf{r}, t) \right\|^2 \quad (\text{A.45})$$

The power can be defined by integrating the intensity over transverse coordinates:

$$P(z, t) = \int_{\mathbb{R}^2} I(\mathbf{r}, t) d^2r \quad (\text{A.46})$$

The energy in one pulse of light is then

$$U_{pulse} = \int_{pulse} P(t) dt \quad (\text{A.47})$$

So using Eqs. A.43 and A.44 we get

$$U_{pulse} = 2nc\varepsilon_0 E_0^2 \int_{pulse} |s(t)|^2 dt \int_{\mathbb{R}^2} |u(\rho)|^2 d^2\rho \quad (\text{A.48})$$

$$= 2nc\varepsilon_0 E_0^2 S\tau \quad (\text{A.49})$$

For a frequency comb laser with a repetition rate f_{rep} , the average power is given by the energy in a single pulse times the number of pulses per second:

$$P_0 = U_{pulse} f_{rep} \quad (\text{A.50})$$

So that we have finally

$$E_0 = \sqrt{\frac{P_0}{2n\varepsilon_0 c S \tau f_{rep}}} \quad (\text{A.51})$$

In the following we will develop $E^{(+)}(\rho, t)$ as an infinite train of Gaussian pulses with repetition rate $f_{rep} = \frac{1}{T_{rep}}$:

$$E^{(+)}(\rho, t) = E_0 s(t) u(\rho) e^{-i\omega_0 t} \quad (\text{A.52})$$

$$s(t) = \sum_{k=-\infty}^{+\infty} e^{-\frac{(t-kT_{rep})^2}{4\Delta t^2}} \quad (\text{A.53})$$

In the expression of \mathcal{S}_0 we have the pump field E_p in the Fourier domain.

$$E_p^{(+)}(\omega) = \mathcal{F}[E_p^{(+)}(\rho = 0, t)](\omega) := \int_{\mathbb{R}} \frac{dt}{\sqrt{2\pi}} E_p^{(+)}(t) e^{i\omega t} \quad (\text{A.54})$$

$$= E_0 \sum_{k=-\infty}^{+\infty} \mathcal{F}[s(t) \times e^{-i\omega_0 t}] \quad (\text{A.55})$$

$$= E_0 \sum_{k=-\infty}^{+\infty} \frac{1}{\sqrt{2\pi}} \mathcal{F}[e^{-\frac{(t-kT_{rep})^2}{4\Delta t^2}}] \otimes \mathcal{F}[e^{i\omega_0 t}] \quad (\text{A.56})$$

And

$$\mathcal{F}[e^{-\frac{(t-kT_{rep})^2}{4\Delta t^2}}] = \sqrt{2\Delta t} e^{-\Delta t^2 \omega^2} e^{ikT_{rep}\omega} \quad (\text{A.57})$$

$$\mathcal{F}[e^{-i\omega_0 t}] = \sqrt{2\pi} \delta(\omega - \omega_0) \quad (\text{A.58})$$

So that

$$E_p^{(+)}(\omega) = E_0 \sqrt{2\Delta t} e^{-\Delta t^2 (\omega - \omega_0)^2} \sum_{k=-\infty}^{+\infty} e^{ikT_{rep}(\omega - \omega_0)} \quad (\text{A.59})$$

$$= \mathcal{E}_p e^{-\frac{(\omega - \omega_0)^2}{4\Delta\omega^2}} \text{III}_1\left(\frac{\omega - \omega_0}{\omega_{rep}}\right) \quad (\text{A.60})$$

with $\mathcal{E}_p = E_0 \sqrt{2\Delta t} = \frac{1}{\sqrt{\pi}} E_0 \tau$.

Bibliography

- [1] T. H. MAIMAN; “Stimulated Optical Radiation in Ruby”; *Nature* **187**, pp. 493–494 (1960). ISSN 1476-4687. <http://www.nature.com/articles/187493a0>; number: 4736 Publisher: Nature Publishing Group. 2
- [2] S. HAROCHE; “Nobel Lecture: Controlling photons in a box and exploring the quantum to classical boundary”; *Reviews of Modern Physics* **85**, pp. 1083–1102 (2013). <https://link.aps.org/doi/10.1103/RevModPhys.85.1083>; publisher: American Physical Society. 2
- [3] L. GILDER; *The age of entanglement: when quantum physics was reborn* (Vintage) (2009). 2
- [4] N. GISIN; *Quantum Chance: Nonlocality, Teleportation and Other Quantum Marvels* (Springer) (2014); ISBN 978-3-319-05473-5. 2
- [5] A. EINSTEIN, B. PODOLSKY & N. ROSEN; “Can Quantum-Mechanical Description of Physical Reality Be Considered Complete?” p. 4. 2, 24
- [6] J. S. BELL; “ON THE EINSTEIN PODOLSKY ROSEN PARADOX”; *Physics Physique Fizika* **1**, p. 6 (1964). 2
- [7] J. F. CLAUSER, M. A. HORNE, A. SHIMONY & R. A. HOLT; “Proposed Experiment to Test Local Hidden-Variable Theories”; *Physical Review Letters* **23**, pp. 880–884 (1969). <https://link.aps.org/doi/10.1103/PhysRevLett.23.880>; publisher: American Physical Society. 2
- [8] S. J. FREEDMAN & J. F. CLAUSER; “Experimental test of local hidden-variable theories”; *Physical Review Letters* **28**, p. 938 (1972). 2
- [9] A. ASPECT, P. GRANGIER & G. ROGER; “Experimental Realization of Einstein-Podolsky-Rosen-Bohm Gedankenexperiment: A New Violation of Bell’s Inequalities”; *Physical Review Letters* **49**, pp. 91–94 (1982). <https://link.aps.org/doi/10.1103/PhysRevLett.49.91>; publisher: American Physical Society. 2
- [10] B. HENSEN, H. BERNIEN, A. E. DRÉAU, A. REISERER, N. KALB, M. S. BLOK, J. RUITENBERG, R. F. L. VERMEULEN, R. N. SCHOUTEN, C. ABELLÁN, W. AMAYA, V. PRUNERI, M. W. MITCHELL, M. MARKHAM, D. J. TWITCHEN, D. ELKOUSS, S. WEHNER, T. H. TAMINIAU & R. HANSON; “Loophole-free Bell inequality violation using electron spins separated by 1.3 kilometres”; *Nature* **526**, pp. 682–686 (2015). ISSN 1476-4687. <http://www.nature.com/articles/nature15759/>; number: 7575 Publisher: Nature Publishing Group. 2

- [11] M. GIUSTINA, M. A. VERSTEEGH, S. WENGEROWSKY, J. HANDSTEINER, A. HOCHRAINER, K. PHELAN, F. STEINLECHNER, J. KOFLER, J.-K. LARSSON, C. ABELLÁN, W. AMAYA, V. PRUNERI, M. W. MITCHELL, J. BEYER, T. GER-RITS, A. E. LITA, L. K. SHALM, S. W. NAM, T. SCHEIDL, R. URSIN, B. WITTMANN & A. ZEILINGER; “Significant-Loophole-Free Test of Bell’s Theorem with Entangled Photons”; *Physical Review Letters* **115**, p. 250401 (2015). <https://link.aps.org/doi/10.1103/PhysRevLett.115.250401>; publisher: American Physical Society. 2
- [12] A. ASPECT; “Closing the Door on Einstein and Bohr’s Quantum Debate”; *Physics* **8** (2015) <https://physics.aps.org/articles/v8/123?from=singlemessage&isappinstalled;=0>; publisher: American Physical Society. 2
- [13] C. H. BENNETT, G. BRASSARD, C. CRÉPEAU, R. JOZSA, A. PERES & W. K. WOOT-TERS; “Teleporting an unknown quantum state via dual classical and Einstein-Podolsky-Rosen channels”; *Physical Review Letters* **70**, pp. 1895–1899 (1993). <https://link.aps.org/doi/10.1103/PhysRevLett.70.1895>; publisher: American Physical Society. 2
- [14] L. VAIDMAN; “Teleportation of quantum states”; *Physical Review A* **49**, pp. 1473–1476 (1994). <https://link.aps.org/doi/10.1103/PhysRevA.49.1473>; publisher: American Physical Society. 2
- [15] D. BOUWMEESTER, J.-W. PAN, K. MATTLE, M. EIBL, H. WEINFURTER & A. ZEILINGER; “Experimental quantum teleportation”; *Nature* **390**, pp. 575–579 (1997). ISSN 1476-4687. <http://www.nature.com/articles/37539>; number: 6660 Publisher: Nature Publishing Group. 2
- [16] S. L. BRAUNSTEIN & H. J. KIMBLE; “Teleportation of Continuous Quantum Variables”; *Physical Review Letters* **80**, pp. 869–872 (1998). <https://link.aps.org/doi/10.1103/PhysRevLett.80.869>; publisher: American Physical Society. 2
- [17] A. FURUSAWA, J. L. SØRENSEN, S. L. BRAUNSTEIN, C. A. FUCHS, H. J. KIMBLE & E. S. POLZIK; “Unconditional Quantum Teleportation”; *Science* **282**, pp. 706–709 (1998). ISSN 0036-8075, 1095-9203. <http://science.sciencemag.org/content/282/5389/706>; publisher: American Association for the Advancement of Science Section: Research Article. 2
- [18] S. PIRANDOLA, J. EISERT, C. WEEDBROOK, A. FURUSAWA & S. L. BRAUNSTEIN; “Advances in quantum teleportation”; *Nature Photonics* **9**, pp. 641–652 (2015). ISSN 1749-4893. <http://www.nature.com/articles/nphoton.2015.154>; number: 10 Publisher: Nature Publishing Group. 2
- [19] J.-G. REN, P. XU, H.-L. YONG, L. ZHANG, S.-K. LIAO, J. YIN, W.-Y. LIU, W.-Q. CAI, M. YANG, L. LI, K.-X. YANG, X. HAN, Y.-Q. YAO, J. LI, H.-Y. WU, S. WAN, L. LIU, D.-Q. LIU, Y.-W. KUANG, Z.-P. HE, P. SHANG, C. GUO, R.-H. ZHENG, K. TIAN, Z.-C. ZHU, N.-L. LIU, C.-Y. LU, R. SHU, Y.-A. CHEN, C.-Z. PENG, J.-Y. WANG & J.-W. PAN; “Ground-to-satellite quantum teleportation”; *Nature* **549**, pp. 70–73 (2017). ISSN 1476-4687. <http://www.nature.com/articles/nature23675/>; number: 7670 Publisher: Nature Publishing Group. 2

- [20] H. J. KIMBLE; “The quantum internet”; *Nature* **453**, pp. 1023–1030 (2008). ISSN 1476-4687. <http://www.nature.com/articles/nature07127>; number: 7198 Publisher: Nature Publishing Group. 2
- [21] C. H. BENNETT & G. BRASSARD; “Proceedings of the IEEE International Conference on Computers, Systems and Signal Processing”; (1984). 2
- [22] A. K. EKERT; “Quantum cryptography based on Bell’s theorem”; *Physical Review Letters* **67**, pp. 661–663 (1991). <https://link.aps.org/doi/10.1103/PhysRevLett.67.661>; publisher: American Physical Society. 2
- [23] F. GROSSHANS & P. GRANGIER; “Continuous Variable Quantum Cryptography Using Coherent States”; *Physical Review Letters* **88**, p. 057902 (2002). <https://link.aps.org/doi/10.1103/PhysRevLett.88.057902>; publisher: American Physical Society. 2
- [24] S.-K. LIAO, W.-Q. CAI, W.-Y. LIU, L. ZHANG, Y. LI, J.-G. REN, J. YIN, Q. SHEN, Y. CAO, Z.-P. LI, F.-Z. LI, X.-W. CHEN, L.-H. SUN, J.-J. JIA, J.-C. WU, X.-J. JIANG, J.-F. WANG, Y.-M. HUANG, Q. WANG, Y.-L. ZHOU, L. DENG, T. XI, L. MA, T. HU, Q. ZHANG, Y.-A. CHEN, N.-L. LIU, X.-B. WANG, Z.-C. ZHU, C.-Y. LU, R. SHU, C.-Z. PENG, J.-Y. WANG & J.-W. PAN; “Satellite-to-ground quantum key distribution”; *Nature* **549**, pp. 43–47 (2017). ISSN 1476-4687. <http://www.nature.com/articles/nature23655/>; number: 7670 Publisher: Nature Publishing Group. 2
- [25] D. DEUTSCH & R. PENROSE; “Quantum theory, the Church–Turing principle and the universal quantum computer”; *Proceedings of the Royal Society of London. A. Mathematical and Physical Sciences* **400**, pp. 97–117 (1985). <https://royalsocietypublishing.org/doi/abs/10.1098/rspa.1985.0070>; publisher: Royal Society. 2
- [26] C. H. BENNETT & D. P. DIVINCENZO; “Quantum information and computation”; *Nature* **404**, pp. 247–255 (2000). ISSN 1476-4687. <http://www.nature.com/articles/35005001>; number: 6775 Publisher: Nature Publishing Group. 2
- [27] P. W. SHOR; “Algorithms for quantum computation: discrete logarithms and factoring”; in “Proceedings 35th Annual Symposium on Foundations of Computer Science,” pp. 124–134 (1994). 2
- [28] L. K. GROVER; “A fast quantum mechanical algorithm for database search”; in “Proceedings of the twenty-eighth annual ACM symposium on Theory of Computing,” STOC ’96; pp. 212–219 (Association for Computing Machinery, New York, NY, USA) (1996); ISBN 978-0-89791-785-8. <https://doi.org/10.1145/237814.237866>. 2
- [29] K. TEMME, S. BRAVYI & J. M. GAMBETTA; “Error Mitigation for Short-Depth Quantum Circuits”; *Physical Review Letters* **119**, p. 180509 (2017). <https://link.aps.org/doi/10.1103/PhysRevLett.119.180509>; publisher: American Physical Society. 2

- [30] F. ARUTE, K. ARYA, R. BABBUSH, D. BACON, J. C. BARDIN, R. BARENDS, R. BISWAS, S. BOIXO, F. G. S. L. BRANDAO, D. A. BUELL, B. BURKETT, Y. CHEN, Z. CHEN, B. CHIARO, R. COLLINS, W. COURTNEY, A. DUNSWORTH, E. FARHI, B. FOXEN, A. FOWLER, C. GIDNEY, M. GIUSTINA, R. GRAFF, K. GUERIN, S. HABEGGER, M. P. HARRIGAN, M. J. HARTMANN, A. HO, M. HOFFMANN, T. HUANG, T. S. HUMBLE, S. V. ISAKOV, E. JEFFREY, Z. JIANG, D. KAFRI, K. KECHEDZHI, J. KELLY, P. V. KLIMOV, S. KNYSH, A. KOROTKOV, F. KOSTRITSA, D. LANDHUIS, M. LINDMARK, E. LUCERO, D. LYAKH, S. MANDRÀ, J. R. MCCLEAN, M. MCEWEN, A. MEGRANT, X. MI, K. MICHELSEN, M. MOHSENI, J. MUTUS, O. NAAMAN, M. NEELEY, C. NEILL, M. Y. NIU, E. OSTBY, A. PETUKHOV, J. C. PLATT, C. QUINTANA, E. G. RIEFFEL, P. ROUSHAN, N. C. RUBIN, D. SANK, K. J. SATZINGER, V. SMELYANSKIY, K. J. SUNG, M. D. TREVITHICK, A. VAINSENER, B. VILLALONGA, T. WHITE, Z. J. YAO, P. YEH, A. ZALCMAN, H. NEVEN & J. M. MARTINIS; “Quantum supremacy using a programmable superconducting processor”; *Nature* **574**, pp. 505–510 (2019). ISSN 1476-4687. <http://www.nature.com/articles/s41586-019-1666-5>; number: 7779 Publisher: Nature Publishing Group. 2
- [31] H.-S. ZHONG, H. WANG, Y.-H. DENG, M.-C. CHEN, L.-C. PENG, Y.-H. LUO, J. QIN, D. WU, X. DING, Y. HU, P. HU, X.-Y. YANG, W.-J. ZHANG, H. LI, Y. LI, X. JIANG, L. GAN, G. YANG, L. YOU, Z. WANG, L. LI, N.-L. LIU, C.-Y. LU & J.-W. PAN; “Quantum computational advantage using photons”; *Science* **370**, pp. 1460–1463 (2020). ISSN 0036-8075, 1095-9203. <https://science.sciencemag.org/content/370/6523/1460>; publisher: American Association for the Advancement of Science Section: Report. 2
- [32] A. ASPURU-GUZI, A. D. DUTOI, P. J. LOVE & M. HEAD-GORDON; “Simulated Quantum Computation of Molecular Energies”; *Science* **309**, pp. 1704–1707 (2005). ISSN 0036-8075, 1095-9203. <http://science.sciencemag.org/content/309/5741/1704>; publisher: American Association for the Advancement of Science Section: Report. 3
- [33] R. D. SOMMA, S. BOIXO, H. BARNUM & E. KNILL; “Quantum Simulations of Classical Annealing Processes”; *Physical Review Letters* **101**, p. 130504 (2008). <https://link.aps.org/doi/10.1103/PhysRevLett.101.130504>; publisher: American Physical Society. 3
- [34] A. PERUZZO, J. MCCLEAN, P. SHADBOLT, M.-H. YUNG, X.-Q. ZHOU, P. J. LOVE, A. ASPURU-GUZI & J. L. O’BRIEN; “A variational eigenvalue solver on a photonic quantum processor”; *Nature Communications* **5**, p. 4213 (2014). ISSN 2041-1723. <http://www.nature.com/articles/ncomms5213>; number: 1 Publisher: Nature Publishing Group. 3
- [35] S. BRAVYI, D. GOSSET & R. KÖNIG; “Quantum advantage with shallow circuits”; *Science* **362**, pp. 308–311 (2018). ISSN 0036-8075, 1095-9203. <http://science.sciencemag.org/content/362/6412/308>; publisher: American Association for the Advancement of Science Section: Report. 3
- [36] I. CONG, S. CHOI & M. D. LUKIN; “Quantum convolutional neural networks”; *Nature Physics* **15**, pp. 1273–1278 (2019). ISSN 1745-2481. <http://www.nature.com/>

- [articles/s41567-019-0648-8](#); number: 12 Publisher: Nature Publishing Group. 3
- [37] G. BRASSARD, I. CHUANG, S. LLOYD & C. MONROE; “Quantum computing”; *Proceedings of the National Academy of Sciences* **95**, pp. 11032–11033 (1998). ISSN 0027-8424, 1091-6490. <https://www.pnas.org/content/95/19/11032>; publisher: National Academy of Sciences. 3
- [38] D. GOTTESMAN & I. L. CHUANG; “Demonstrating the viability of universal quantum computation using teleportation and single-qubit operations”; *Nature* **402**, pp. 390–393 (1999). ISSN 1476-4687. <http://www.nature.com/articles/46503/>; number: 6760 Publisher: Nature Publishing Group. 3
- [39] P. WALTHER, K. J. RESCH, T. RUDOLPH, E. SCHENCK, H. WEINFURTER, V. VEDRAL, M. ASPELMEYER & A. ZEILINGER; “Experimental one-way quantum computing”; *Nature* **434**, pp. 169–176 (2005). ISSN 1476-4687. <http://www.nature.com/articles/nature03347>; number: 7030 Publisher: Nature Publishing Group. 3
- [40] X. ZOU & W. MATHIS; “Generating a four-photon polarization-entangled cluster state”; *Physical Review A* **71**, p. 032308 (2005). <https://link.aps.org/doi/10.1103/PhysRevA.71.032308>; publisher: American Physical Society. 3
- [41] C.-Y. LU, X.-Q. ZHOU, O. GÜHNE, W.-B. GAO, J. ZHANG, Z.-S. YUAN, A. GOEBEL, T. YANG & J.-W. PAN; “Experimental entanglement of six photons in graph states”; *Nature Physics* **3**, pp. 91–95 (2007). ISSN 1745-2481. <http://www.nature.com/articles/nphys507>; number: 2 Publisher: Nature Publishing Group. 3
- [42] R. CECCARELLI, G. VALLONE, F. DE MARTINI, P. MATALONI & A. CABELLO; “Experimental Entanglement and Nonlocality of a Two-Photon Six-Qubit Cluster State”; *Physical Review Letters* **103**, p. 160401 (2009). <https://link.aps.org/doi/10.1103/PhysRevLett.103.160401>; publisher: American Physical Society. 3
- [43] H.-S. ZHONG, Y. LI, W. LI, L.-C. PENG, Z.-E. SU, Y. HU, Y.-M. HE, X. DING, W. ZHANG, H. LI, L. ZHANG, Z. WANG, L. YOU, X.-L. WANG, X. JIANG, L. LI, Y.-A. CHEN, N.-L. LIU, C.-Y. LU & J.-W. PAN; “12-Photon Entanglement and Scalable Scattershot Boson Sampling with Optimal Entangled-Photon Pairs from Parametric Down-Conversion”; *Physical Review Letters* **121**, p. 250505 (2018). <https://link.aps.org/doi/10.1103/PhysRevLett.121.250505>; publisher: American Physical Society. 3
- [44] X. MA, X. YUAN, Z. CAO, B. QI & Z. ZHANG; “Quantum random number generation”; *npj Quantum Information* **2** (2016). ISSN 2056-6387. <http://www.nature.com/articles/npjqi201621>. 3
- [45] C. M. CAVES; “Quantum-mechanical noise in an interferometer”; *Physical Review D* **23**, pp. 1693–1708 (1981). <https://link.aps.org/doi/10.1103/PhysRevD.23.1693>; publisher: American Physical Society. 3
- [46] R. E. SLUSHER, L. W. HOLLBERG, B. YURKE, J. C. MERTZ & J. F. VALLEY; “Observation of Squeezed States Generated by Four-Wave Mixing in an Optical

- Cavity”; *Physical Review Letters* **55**, pp. 2409–2412 (1985). <https://link.aps.org/doi/10.1103/PhysRevLett.55.2409>; publisher: American Physical Society. 3
- [47] E. S. POLZIK, J. CARRI & H. J. KIMBLE; “Spectroscopy with squeezed light”; *Physical Review Letters* **68**, pp. 3020–3023 (1992). <https://link.aps.org/doi/10.1103/PhysRevLett.68.3020>; publisher: American Physical Society. 3
- [48] J. AASI, J. ABADIE, B. ABBOTT, R. ABBOTT, T. ABBOTT, M. ABERNATHY, C. ADAMS, T. ADAMS, P. ADDESSO, R. ADHIKARI *et al.*; “Enhanced sensitivity of the LIGO gravitational wave detector by using squeezed states of light”; *Nature Photonics* **7**, pp. 613–619 (2013). ISSN 1749-4893. <http://www.nature.com/articles/nphoton.2013.177/>; number: 8 Publisher: Nature Publishing Group. 3
- [49] LIGO SCIENTIFIC COLLABORATION AND VIRGO COLLABORATION, B. P. ABBOTT, R. ABBOTT, T. ABBOTT, M. ABERNATHY, F. ACERNESE, K. ACKLEY, C. ADAMS, T. ADAMS, P. ADDESSO, R. ADHIKARI *et al.*; “Observation of Gravitational Waves from a Binary Black Hole Merger”; *Physical Review Letters* **116**, p. 061102 (2016). <https://link.aps.org/doi/10.1103/PhysRevLett.116.061102>; publisher: American Physical Society. 3
- [50] J. LAURAT, T. COUDREAU, N. TREPS, A. MAÎTRE & C. FABRE; “Conditional preparation of a nonclassical state in the continuous-variable regime: Theoretical study”; *Physical Review A* **69**, p. 033808 (2004). <https://link.aps.org/doi/10.1103/PhysRevA.69.033808>; publisher: American Physical Society. 3
- [51] S. LLOYD & S. L. BRAUNSTEIN; “Quantum Computation Over Continuous Variables”; in “Quantum Information with Continuous Variables,” , edited by S. L. BRAUNSTEIN & A. K. PATI; pp. 9–17 (Springer Netherlands, Dordrecht) (2003); ISBN 978-94-015-1258-9. https://doi.org/10.1007/978-94-015-1258-9_2. 3
- [52] N. J. CERF, G. LEUCHS & E. S. POLZIK; *Quantum Information With Continuous Variables Of Atoms And Light* (World Scientific) (2007); ISBN 978-1-908979-36-0; google-Books-ID: RWO7CgAAQBAJ. 3
- [53] N. C. MENICUCCI, P. VAN LOOCK, M. GU, C. WEEDBROOK, T. C. RALPH & M. A. NIELSEN; “Universal Quantum Computation with Continuous-Variable Cluster States”; *Physical Review Letters* **97**, p. 110501 (2006). <https://link.aps.org/doi/10.1103/PhysRevLett.97.110501>; publisher: American Physical Society. 3
- [54] J. ZHANG & S. L. BRAUNSTEIN; “Continuous-variable Gaussian analog of cluster states”; *Physical Review A* **73**, p. 032318 (2006). <https://link.aps.org/doi/10.1103/PhysRevA.73.032318>; publisher: American Physical Society. 3
- [55] J. LAURAT; “On-demand entanglement could lead to scalable quantum networks”; *Nature* **558**, pp. 192–193 (2018). <http://www.nature.com/articles/d41586-018-05336-1>; number: 7709 Publisher: Nature Publishing Group. 3
- [56] P. C. HUMPHREYS, N. KALB, J. P. J. MORITS, R. N. SCHOUTEN, R. F. L. VERMEULEN, D. J. TWITCHEN, M. MARKHAM & R. HANSON; “Deterministic delivery of remote entanglement on a quantum network”; *Nature* **558**, pp. 268–273 (2018). ISSN 1476-4687. <http://www.nature.com/articles/s41586-018-0200-5>; number: 7709 Publisher: Nature Publishing Group. 3

- [57] X. SU, A. TAN, X. JIA, J. ZHANG, C. XIE & K. PENG; “Experimental Preparation of Quadripartite Cluster and Greenberger-Horne-Zeilinger Entangled States for Continuous Variables”; *Physical Review Letters* **98**, p. 070502 (2007). <https://link.aps.org/doi/10.1103/PhysRevLett.98.070502>; publisher: American Physical Society. 3
- [58] M. YUKAWA, R. UKAI, P. VAN LOOCK & A. FURUSAWA; “Experimental generation of four-mode continuous-variable cluster states”; *Physical Review A* **78**, p. 012301 (2008). <https://link.aps.org/doi/10.1103/PhysRevA.78.012301>; publisher: American Physical Society. 3
- [59] J. L. O’BRIEN, A. FURUSAWA & J. VUČKOVIĆ; “Photonic quantum technologies”; *Nature Photonics* **3**, pp. 687–695 (2009). ISSN 1749-4893. <http://www.nature.com/articles/nphoton.2009.229>; number: 12 Publisher: Nature Publishing Group. 3
- [60] N. C. MENICUCCI, S. T. FLAMMIA & O. PFISTER; “One-Way Quantum Computing in the Optical Frequency Comb”; *Physical Review Letters* **101**, p. 130501 (2008). <https://link.aps.org/doi/10.1103/PhysRevLett.101.130501>; publisher: American Physical Society. 3
- [61] S. YOKOYAMA, R. UKAI, S. C. ARMSTRONG, C. SORNPHIPHATPHONG, T. KAJI, S. SUZUKI, J.-i. YOSHIKAWA, H. YONEZAWA, N. C. MENICUCCI & A. FURUSAWA; “Ultra-large-scale continuous-variable cluster states multiplexed in the time domain”; *Nature Photonics* **7**, pp. 982–986 (2013). ISSN 1749-4893. <http://www.nature.com/articles/nphoton.2013.287/>; number: 12 Publisher: Nature Publishing Group. 3
- [62] M. CHEN, N. C. MENICUCCI & O. PFISTER; “Experimental Realization of Multipartite Entanglement of 60 Modes of a Quantum Optical Frequency Comb”; *Physical Review Letters* **112**, p. 120505 (2014). <https://link.aps.org/doi/10.1103/PhysRevLett.112.120505>; publisher: American Physical Society. 3
- [63] W. ASAVANANT, Y. SHIOZAWA, S. YOKOYAMA, B. CHAROENSOMBUTAMON, H. EMURA, R. N. ALEXANDER, S. TAKEDA, J.-i. YOSHIKAWA, N. C. MENICUCCI, H. YONEZAWA & A. FURUSAWA; “Generation of time-domain-multiplexed two-dimensional cluster state”; *Science* **366**, pp. 373–376 (2019). ISSN 0036-8075, 1095-9203. <http://science.sciencemag.org/content/366/6463/373>; publisher: American Association for the Advancement of Science Section: Report. 3, 119
- [64] D. E. SPENCE, P. N. KEAN & W. SIBBETT; “60-fsec pulse generation from a self-mode-locked Ti:sapphire laser”; *Optics Letters* **16**, pp. 42–44 (1991). ISSN 1539-4794. <http://www.osapublishing.org/ol/abstract.cfm?uri=ol-16-1-42>; publisher: Optical Society of America. 3
- [65] S. A. DIDDAMS; “The evolving optical frequency comb [Invited]”; *JOSA B* **27**, pp. B51–B62 (2010). ISSN 1520-8540. <http://www.osapublishing.org/josab/abstract.cfm?uri=josab-27-11-B51>; publisher: Optical Society of America. 3, 45
- [66] U. MORGNER, F. X. KÄRTNER, S. H. CHO, Y. CHEN, H. A. HAUS, J. G. FUJIMOTO, E. P. IPPEN, V. SCHEUER, G. ANGELOW & T. TSCHUDI; “Sub-two-cycle pulses

- from a Kerr-lens mode-locked Ti:sapphire laser”; *Optics Letters* **24**, pp. 411–413 (1999). ISSN 1539-4794. <http://www.osapublishing.org/ol/abstract.cfm?uri=ol-24-6-411>; publisher: Optical Society of America. 3
- [67] P. B. CORKUM, N. H. BURNETT & M. Y. IVANOV; “Subfemtosecond pulses”; *Optics Letters* **19**, pp. 1870–1872 (1994). ISSN 1539-4794. <http://www.osapublishing.org/ol/abstract.cfm?uri=ol-19-22-1870>; publisher: Optical Society of America. 3
- [68] P. M. PAUL, E. S. TOMA, P. BREGER, G. MULLOT, F. AUGÉ, P. BALCOU, H. G. MULLER & P. AGOSTINI; “Observation of a Train of Attosecond Pulses from High Harmonic Generation”; *Science* **292**, pp. 1689–1692 (2001). ISSN 0036-8075, 1095-9203. <http://science.sciencemag.org/content/292/5522/1689>; publisher: American Association for the Advancement of Science Section: Report. 3
- [69] P. AGOSTINI & L. F. DIMAURO; “The physics of attosecond light pulses”; *Reports on Progress in Physics* **67**, pp. 813–855 (2004). ISSN 0034-4885. <https://doi.org/10.1088/0034-4885/67/6/r01>; publisher: IOP Publishing. 3
- [70] A. LINDINGER, J. HAGEN, L. D. SOCACIU, T. M. BERNHARDT, L. WÖSTE, D. DUFT & T. LEISNER; “Time-resolved explosion dynamics of H₂O droplets induced by femtosecond laser pulses”; *Applied Optics* **43**, pp. 5263–5269 (2004). ISSN 2155-3165. <http://www.osapublishing.org/ao/abstract.cfm?uri=ao-43-27-5263>; publisher: Optical Society of America. 3
- [71] N. PICQUÉ & T. W. HÄNSCH; “Frequency comb spectroscopy”; *Nature Photonics* **13**, pp. 146–157 (2019). ISSN 1749-4893. <http://www.nature.com/articles/s41566-018-0347-5>; number: 3 Publisher: Nature Publishing Group. 3
- [72] R. HOLZWARTH, T. UDEM, T. W. HÄNSCH, J. C. KNIGHT, W. J. WADSWORTH & P. S. J. RUSSELL; “Optical Frequency Synthesizer for Precision Spectroscopy”; *Physical Review Letters* **85**, pp. 2264–2267 (2000). <https://link.aps.org/doi/10.1103/PhysRevLett.85.2264>; publisher: American Physical Society. 3
- [73] T. UDEM, R. HOLZWARTH & T. W. HÄNSCH; “Optical frequency metrology”; *Nature* **416**, pp. 233–237 (2002). ISSN 1476-4687. <http://www.nature.com/articles/416233a>; number: 6877 Publisher: Nature Publishing Group. 3, 45
- [74] G. J. DE VALCÁRCEL, G. PATERA, N. TREPS & C. FABRE; “Multimode squeezing of frequency combs”; *Physical Review A* **74**, p. 061801 (2006). <https://link.aps.org/doi/10.1103/PhysRevA.74.061801>; publisher: American Physical Society. 3
- [75] G. PATERA, N. TREPS, C. FABRE & G. J. DE VALCÁRCEL; “Quantum theory of synchronously pumped type I optical parametricoscillators: characterization of the squeezed supermodes”; *The European Physical Journal D* **56**, p. 123 (2009). ISSN 1434-6079. <https://doi.org/10.1140/epjd/e2009-00299-9>. 3
- [76] J. ROSLUND, R. M. DE ARAÚJO, S. JIANG, C. FABRE & N. TREPS; “Wavelength-multiplexed quantum networks with ultrafast frequency combs”; *Nature Photonics* **8**, pp. 109–112 (2014). ISSN 1749-4893. <http://www.nature.com/articles/nphoton.2013.340>; number: 2 Publisher: Nature Publishing Group. 3

- [77] O. PINEL, J. FADE, D. BRAUN, P. JIAN, N. TREPS & C. FABRE; “Ultimate sensitivity of precision measurements with intense Gaussian quantum light: A multimodal approach”; *Physical Review A* **85** (2012). ISSN 1050-2947, 1094-1622. <https://link.aps.org/doi/10.1103/PhysRevA.85.010101>. 4
- [78] T. MICHEL, J. Y. HAW, D. G. MARANGON, O. THEARLE, G. VALLONE, P. VILLORESI, P. K. LAM & S. M. ASSAD; “Real-Time Source-Independent Quantum Random-Number Generator with Squeezed States”; *Physical Review Applied* **12**, p. 034017 (2019). <https://link.aps.org/doi/10.1103/PhysRevApplied.12.034017>. 5
- [79] G. GRYNBERG, A. ASPECT & C. FABRE; *Introduction to Quantum Optics: From the Semi-classical Approach to Quantized Light* (Cambridge University Press) (2010); ISBN 978-1-139-49084-9. 9, 11
- [80] J. C. MAXWELL; “VIII. A dynamical theory of the electromagnetic field”; *Philosophical transactions of the Royal Society of London* pp. 459–512 (1865). 9
- [81] J. C. MAXWELL; *A Dynamical Theory of the Electromagnetic Field* (Wipf and Stock Publishers) (1996); ISBN 978-1-57910-015-5; google-Books-ID: p1pKAwAAQBAJ. 9
- [82] D. J. GRIFFITHS; *Introduction to Electrodynamics* (Cambridge University Press) (2017); ISBN 978-1-108-35714-2; google-Books-ID: Kh4xDwAAQBAJ. 9
- [83] J. D. JACKSON; *CLASSICAL ELECTRODYNAMICS, 3RD ED* (Wiley India Pvt. Limited) (2007); ISBN 978-81-265-1094-8; google-Books-ID: 8qHCZjJHRUGC. 9
- [84] N. YOUNG; *An Introduction to Hilbert Space* (Cambridge University Press) (1988); ISBN 978-0-521-33717-5; google-Books-ID: _igwFHKwcyYC. 11
- [85] D. J. GRIFFITHS & D. F. SCHROETER; *Introduction to quantum mechanics* (Cambridge University Press) (2018). 13
- [86] G. LINDBLAD; “A General No-Cloning Theorem”; *Letters in Mathematical Physics* **47**, pp. 189–196 (1999). ISSN 1573-0530. <https://doi.org/10.1023/A:1007581027660>. 13
- [87] E. WIGNER; “Über die Operation der Zeitumkehr in der Quantenmechanik”; *Nachrichten von der Gesellschaft der Wissenschaften zu Göttingen, Mathematisch-Physikalische Klasse* **1932**, pp. 546–559 (1932). 15
- [88] E. P. WIGNER; “On the Quantum Correction for Thermodynamic Equilibrium”; in “Part I: Physical Chemistry. Part II: Solid State Physics,” , edited by A. S. WIGHTMAN; *The Collected Works of Eugene Paul Wigner*; pp. 110–120 (Springer, Berlin, Heidelberg) (1997); ISBN 978-3-642-59033-7. https://doi.org/10.1007/978-3-642-59033-7_9. 15
- [89] J. VILLE; “Theorie et application de la notion de signal analytique”; *Cables et Transmissions* **2**, pp. 61–74 (1948) <https://ci.nii.ac.jp/naid/10022496459/>. 15
- [90] Y. S. KIM & M. E. NOZ; *Phase Space Picture Of Quantum Mechanics: Group Theoretical Approach* (World Scientific) (1991); ISBN 978-981-4506-67-0; google-Books-ID: Pp3sCgAAQBAJ. 15

- [91] C. ZACHOS, D. FAIRLIE & T. CURTRIGHT; *Quantum Mechanics in Phase Space: An Overview with Selected Papers* (World Scientific) (2005); ISBN 978-981-238-384-6; google-Books-ID: NnVpDQAAQBAJ. 15
- [92] J. v. NEUMANN; *Mathematical Foundations of Quantum Mechanics: New Edition* (Princeton University Press) (2018); ISBN 978-0-691-17856-1; google-Books-ID: B3OYDwAAQBAJ. 16
- [93] C. FABRE & N. TREPS; “Modes and states in quantum optics”; *Reviews of Modern Physics* **92**, p. 035005 (2020). <https://link.aps.org/doi/10.1103/RevModPhys.92.035005>; publisher: American Physical Society. 17, 26
- [94] N. TREPS, V. DELAUBERT, A. MAÎTRE, J. M. COURTY & C. FABRE; “Quantum noise in multipixel image processing”; *Physical Review A* **71** (2005). ISSN 1050-2947, 1094-1622. <https://link.aps.org/doi/10.1103/PhysRevA.71.013820>. 18
- [95] E. SCHRÖDINGER; “Der stetige Übergang von der Mikro-zur Makromechanik”; *Naturwissenschaften* **14**, pp. 664–666 (1926)Publisher: Springer. 18
- [96] E. C. G. SUDARSHAN; “Equivalence of Semiclassical and Quantum Mechanical Descriptions of Statistical Light Beams”; *Physical Review Letters* **10**, pp. 277–279 (1963). <https://link.aps.org/doi/10.1103/PhysRevLett.10.277>; publisher: American Physical Society. 18
- [97] R. J. GLAUBER; “The Quantum Theory of Optical Coherence”; *Physical Review* **130**, pp. 2529–2539 (1963). <https://link.aps.org/doi/10.1103/PhysRev.130.2529>; publisher: American Physical Society. 18
- [98] J. R. KLAUDER, J. MCKENNA & D. G. CURRIE; “On “Diagonal” Coherent-State Representations for Quantum-Mechanical Density Matrices”; *Journal of Mathematical Physics* **6**, pp. 734–739 (1965). ISSN 0022-2488. <https://aip.scitation.org/doi/abs/10.1063/1.1704330>; publisher: American Institute of Physics. 18
- [99] M. WALSCHAERS, C. FABRE, V. PARIGI & N. TREPS; “Entanglement and Wigner Function Negativity of Multimode Non-Gaussian States”; *Physical Review Letters* **119**, p. 183601 (2017). <https://link.aps.org/doi/10.1103/PhysRevLett.119.183601>; publisher: American Physical Society. 25
- [100] M. WALSCHAERS, C. FABRE, V. PARIGI & N. TREPS; “Statistical signatures of multimode single-photon-added and -subtracted states of light”; *Physical Review A* **96**, p. 053835 (2017). <https://link.aps.org/doi/10.1103/PhysRevA.96.053835>; publisher: American Physical Society. 25
- [101] M. WALSCHAERS, S. SARKAR, V. PARIGI & N. TREPS; “Tailoring Non-Gaussian Continuous-Variable Graph States”; *Physical Review Letters* **121**, p. 220501 (2018). <https://link.aps.org/doi/10.1103/PhysRevLett.121.220501>; publisher: American Physical Society. 25
- [102] M. WALSCHAERS, Y.-S. RA & N. TREPS; “Mode-dependent-loss model for multimode photon-subtracted states”; *Physical Review A* **100**, p. 023828 (2019). <https://link.aps.org/doi/10.1103/PhysRevA.100.023828>; publisher: American Physical Society. 25

- [103] M. WALSCHAERS & N. TREPS; “Remote Generation of Wigner Negativity through Einstein-Podolsky-Rosen Steering”; *Physical Review Letters* **124**, p. 150501 (2020). <https://link.aps.org/doi/10.1103/PhysRevLett.124.150501>; publisher: American Physical Society. 25
- [104] M. WALSCHAERS, V. PARIGI & N. TREPS; “Practical Framework for Conditional Non-Gaussian Quantum State Preparation”; *PRX Quantum* **1**, p. 020305 (2020). <https://link.aps.org/doi/10.1103/PRXQuantum.1.020305>; publisher: American Physical Society. 25
- [105] Y.-S. RA, C. JACQUARD, A. DUFOUR, C. FABRE & N. TREPS; “Tomography of a Mode-Tunable Coherent Single-Photon Subtractor”; *Physical Review X* **7**, p. 031012 (2017). <https://link.aps.org/doi/10.1103/PhysRevX.7.031012>; publisher: American Physical Society. 25
- [106] Y.-S. RA, A. DUFOUR, M. WALSCHAERS, C. JACQUARD, T. MICHEL, C. FABRE & N. TREPS; “Non-Gaussian quantum states of a multimode light field”; *Nature Physics* **16**, pp. 144–147 (2020). ISSN 1745-2481. <https://www.nature.com/articles/s41567-019-0726-y>; number: 2 Publisher: Nature Publishing Group. 25
- [107] C. WEEDBROOK, S. PIRANDOLA, R. GARCÍA-PATRÓN, N. J. CERF, T. C. RALPH, J. H. SHAPIRO & S. LLOYD; “Gaussian quantum information”; *Reviews of Modern Physics* **84**, pp. 621–669 (2012). ISSN 0034-6861, 1539-0756. <https://link.aps.org/doi/10.1103/RevModPhys.84.621>. 26, 29
- [108] ARVIND, B. DUTTA, N. MUKUNDA & R. SIMON; “The real symplectic groups in quantum mechanics and optics”; *Pramana* **45**, pp. 471–497 (1995). ISSN 0304-4289, 0973-7111. <http://link.springer.com/10.1007/BF02848172>. 26
- [109] A. FERRARO, S. OLIVARES & M. G. PARIS; “Gaussian states in continuous variable quantum information”; arXiv preprint quant-ph/0503237 (2005). 27
- [110] N. BOGOLIUBOV; “On the theory of superfluidity”; *J. Phys* **11**, p. 23 (1947). 29
- [111] P. T. NAM, M. NAPIÓRKOWSKI & J. P. SOLOVEJ; “Diagonalization of bosonic quadratic Hamiltonians by Bogoliubov transformations”; *Journal of Functional Analysis* **270**, pp. 4340–4368 (2016). ISSN 0022-1236. <http://www.sciencedirect.com/science/article/pii/S0022123615004905>. 29
- [112] J. DEREZIŃSKI; “Bosonic quadratic Hamiltonians”; *Journal of Mathematical Physics* **58**, p. 121101 (2017). ISSN 0022-2488. <http://aip.scitation.org/doi/full/10.1063/1.5017931>; publisher: American Institute of Physics. 29
- [113] X. MA & W. RHODES; “Multimode squeeze operators and squeezed states”; *Physical Review A* **41**, pp. 4625–4631 (1990). <https://link.aps.org/doi/10.1103/PhysRevA.41.4625>; publisher: American Physical Society. 30
- [114] C. BLOCH & A. MESSIAH; “The canonical form of an antisymmetric tensor and its application to the theory of superconductivity”; *Nuclear Physics* **39**, pp. 95–106 (1962). 31

- [115] S. L. BRAUNSTEIN; “Squeezing as an irreducible resource”; *Physical Review A* **71** (2005). ISSN 1050-2947, 1094-1622. <https://link.aps.org/doi/10.1103/PhysRevA.71.055801>. 31
- [116] J. WILLIAMSON; “On the algebraic problem concerning the normal forms of linear dynamical systems”; *American journal of mathematics* **58**, pp. 141–163 (1936). 32
- [117] K. D. IKRAMOV; “On the Symplectic Eigenvalues of Positive Definite Matrices”; *Moscow University Computational Mathematics and Cybernetics* **42**, pp. 1–4 (2018). ISSN 1934-8428. <https://doi.org/10.3103/S0278641918010041>. 32
- [118] C. M. CAVES & B. L. SCHUMAKER; “New formalism for two-photon quantum optics. I. Quadrature phases and squeezed states”; *Physical Review A* **31**, pp. 3068–3092 (1985). <https://link.aps.org/doi/10.1103/PhysRevA.31.3068>. 33
- [119] B. L. SCHUMAKER & C. M. CAVES; “New formalism for two-photon quantum optics. II. Mathematical foundation and compact notation”; *Physical Review A* **31**, pp. 3093–3111 (1985). <https://link.aps.org/doi/10.1103/PhysRevA.31.3093>. 33
- [120] R. LOUDON; *The quantum theory of light*; Oxford science publications; 3rd edition (Oxford University Press, Oxford ; New York) (2000); ISBN 978-0-19-850177-0 978-0-19-850176-3. 34, 37
- [121] B. L. SCHUMAKER; “Noise in homodyne detection”; *Optics Letters* **9**, pp. 189–191 (1984). ISSN 1539-4794. <http://www.osapublishing.org/ol/abstract.cfm?uri=ol-9-5-189>; publisher: Optical Society of America. 39
- [122] H. P. YUEN & V. W. S. CHAN; “Noise in homodyne and heterodyne detection”; *Optics Letters* **8**, pp. 177–179 (1983). ISSN 1539-4794. <http://www.osapublishing.org/ol/abstract.cfm?uri=ol-8-3-177>; publisher: Optical Society of America. 40
- [123] G. L. ABBAS, V. W. S. CHAN & T. K. YEE; “Local-oscillator excess-noise suppression for homodyne and heterodyne detection”; *Optics Letters* **8**, pp. 419–421 (1983). ISSN 1539-4794. <http://www.osapublishing.org/ol/abstract.cfm?uri=ol-8-8-419>; publisher: Optical Society of America. 40
- [124] F. A. S. BARBOSA, A. S. COELHO, K. N. CASSEMIRO, P. NUSSENZVEIG, C. FABRE, A. S. VILLAR & M. MARTINELLI; “Quantum state reconstruction of spectral field modes: Homodyne and resonator detection schemes”; *Physical Review A* **88**, p. 052113 (2013). <https://link.aps.org/doi/10.1103/PhysRevA.88.052113>; publisher: American Physical Society. 41, 125
- [125] J. L. HALL; “Optical frequency measurement: 40 years of technology revolutions”; *IEEE Journal of Selected Topics in Quantum Electronics* **6**, pp. 1136–1144 (2000). ISSN 1558-4542; conference Name: IEEE Journal of Selected Topics in Quantum Electronics. 45
- [126] T. FORTIER & E. BAUMANN; “20 years of developments in optical frequency comb technology and applications”; *Communications Physics* **2**, pp. 1–16 (2019). ISSN 2399-3650. <http://www.nature.com/articles/s42005-019-0249-y>; number: 1 Publisher: Nature Publishing Group. 45

- [127] J. L. HALL; “Nobel Lecture: Defining and measuring optical frequencies”; *Reviews of Modern Physics* **78**, pp. 1279–1295 (2006). <https://link.aps.org/doi/10.1103/RevModPhys.78.1279>; publisher: American Physical Society. 45
- [128] T. W. HÄNSCH; “Nobel Lecture: Passion for precision”; *Reviews of Modern Physics* **78**, pp. 1297–1309 (2006). <https://link.aps.org/doi/10.1103/RevModPhys.78.1297>; publisher: American Physical Society. 45
- [129] “Mira 900 | Coherent”; <https://fr.coherent.com/lasers/laser/mira-900>. 46
- [130] “Verdi V-Series | Coherent”; <https://fr.coherent.com/lasers/laser/verdi-v-series>. 46
- [131] R. L. FORK, O. E. MARTINEZ & J. P. GORDON; “Negative dispersion using pairs of prisms”; *Optics Letters* **9**, pp. 150–152 (1984). ISSN 1539-4794. <http://www.osapublishing.org/ol/abstract.cfm?uri=ol-9-5-150>; publisher: Optical Society of America. 46
- [132] B. LYOT; “Optical apparatus with wide field using interference of polarized light”; *CR Acad. Sci. (Paris)* **197** (1933). 46
- [133] J. K. LL.D; “XL. A new relation between electricity and light: Dielectrified media birefringent”; *The London, Edinburgh, and Dublin Philosophical Magazine and Journal of Science* **50**, pp. 337–348 (1875). ISSN 1941-5982. <https://doi.org/10.1080/14786447508641302>; publisher: Taylor & Francis _eprint: <https://doi.org/10.1080/14786447508641302>. 46
- [134] J. K. LL.D; “LIV. A new relation between electricity and light: Dielectrified media birefringent (Second paper)”; *The London, Edinburgh, and Dublin Philosophical Magazine and Journal of Science* **50**, pp. 446–458 (1875). ISSN 1941-5982. <https://doi.org/10.1080/14786447508641319>; publisher: Taylor & Francis _eprint: <https://doi.org/10.1080/14786447508641319>. 46
- [135] T. BRABEC, C. SPIELMANN, P. F. CURLEY & F. KRAUSZ; “Kerr lens mode locking”; *Optics Letters* **17**, pp. 1292–1294 (1992). ISSN 1539-4794. <http://www.osapublishing.org/ol/abstract.cfm?uri=ol-17-18-1292>; publisher: Optical Society of America. 46
- [136] V. THIEL; *Modal analysis of an ultrafast frequency comb : from classical to quantum spectral correlations*; phdthesis; Université Pierre et Marie Curie - Paris VI (2015). <https://tel.archives-ouvertes.fr/tel-01367423>. 46
- [137] O. PINEL; *Optique quantique multimode avec des peignes de fréquence*; phdthesis; Université Pierre et Marie Curie - Paris VI (2010). <https://tel.archives-ouvertes.fr/tel-00654841>. 46
- [138] R. M. DE ARAUJO; *Génération et manipulation de peignes de fréquences quantiques multimodes*; Ph.D. thesis (2013). <https://tel.archives-ouvertes.fr/tel-00771444/document>. 46, 54, 91, 93

- [139] Y. CAI; *Quantum coherent control with an optical frequency comb*; phdthesis; Ecole normale supérieure - ENS PARIS ; Université normale de la Chine de l'Est (Shanghai) (2015). <https://tel.archives-ouvertes.fr/tel-01438382>. 46
- [140] M. PESSOT; “1000 times expansion/compression of optical pulses for chirped pulse amplification”; *Optics Communications* **62**, pp. 419–421 (1987). ISSN 0030-4018. <http://www.sciencedirect.com/science/article/pii/0030401887900113>; publisher: North-Holland. 50
- [141] P. MAINE, D. STRICKLAND, P. BADO, M. PESSOT & G. MOUROU; “Generation of ultrahigh peak power pulses by chirped pulse amplification”; *IEEE Journal of Quantum Electronics* **24**, pp. 398–403 (1988). ISSN 1558-1713; conference Name: IEEE Journal of Quantum Electronics. 50
- [142] J. P. HERITAGE, A. M. WEINER & R. N. THURSTON; “Picosecond pulse shaping by spectral phase and amplitude manipulation”; *Optics Letters* **10**, pp. 609–611 (1985). ISSN 1539-4794. <http://www.osapublishing.org/ol/abstract.cfm?uri=ol-10-12-609>; publisher: Optical Society of America. 67
- [143] A. M. WEINER, J. P. HERITAGE & E. M. KIRSCHNER; “High-resolution femtosecond pulse shaping”; *Journal of the Optical Society of America B* **5**, p. 1563 (1988). ISSN 0740-3224, 1520-8540. <https://www.osapublishing.org/abstract.cfm?URI=josab-5-8-1563>. 67
- [144] A. MONMAYRANT, S. WEBER & B. CHATEL; “A newcomer’s guide to ultrashort pulse shaping and characterization”; *Journal of Physics B: Atomic, Molecular and Optical Physics* **43**, p. 103001 (2010). ISSN 0953-4075, 1361-6455. <http://stacks.iop.org/0953-4075/43/i=10/a=103001?key=crossref.a3845bf6ff5ac8d2545d08312eb698>. 67
- [145] A. M. WEINER; “Ultrafast optical pulse shaping: A tutorial review”; *Optics Communications* **284**, pp. 3669–3692 (2011). ISSN 00304018. <http://linkinghub.elsevier.com/retrieve/pii/S0030401811003750>. 67
- [146] M. DANAILOV & I. CHRISTOV; “Time-space Shaping of Light Pulses by Fourier Optical Processing”; *Journal of Modern Optics* **36**, pp. 725–731 (1989). ISSN 0950-0340, 1362-3044. <http://www.tandfonline.com/doi/abs/10.1080/09500348914550811>. 67
- [147] “Richardson Gratings | Acal BFi FR”; <https://www.acalbfi.com/fr/search/RIC>. 69
- [148] “Products | Hamamatsu Photonics”; <http://www.hamamatsu.com.cn/UserFiles/DownFile/Product/20130920095320007.pdf>. 69
- [149] J. ALBERO, I. MORENO, J. A. DAVIS, D. M. COTTRELL & D. SAND; “Generalized phase diffraction gratings with tailored intensity”; *Optics Letters* **37**, pp. 4227–4229 (2012). ISSN 1539-4794. <https://www.osapublishing.org/ol/abstract.cfm?uri=ol-37-20-4227>; publisher: Optical Society of America. 70

- [150] C. JACQUARD; *A single-photon subtractor for spectrally multimode quantum states*; phdthesis; Université Pierre et Marie Curie - Paris VI (2017). <https://tel.archives-ouvertes.fr/tel-01646428>. 70, 93
- [151] A. MONMAYRANT; “FAÇONNAGE ET CARACTÉRISATION D’IMPULSIONS ULTRACOURTES.CONTRÔLE COHÉRENT DE SYSTÈMES SIMPLES.” p. 182. 74
- [152] A. M. WEINER; “Femtosecond pulse shaping using spatial light modulators”; *Review of Scientific Instruments* **71**, pp. 1929–1960 (2000). ISSN 0034-6748, 1089-7623. <http://aip.scitation.org/doi/10.1063/1.1150614>. 77
- [153] E. TREACY; “Optical pulse compression with diffraction gratings”; *IEEE Journal of Quantum Electronics* **5**, pp. 454–458 (1969). ISSN 1558-1713; conference Name: IEEE Journal of Quantum Electronics. 78
- [154] O. E. MARTINEZ, J. P. GORDON & R. L. FORK; “Negative group-velocity dispersion using refraction”; *Journal of the Optical Society of America A* **1**, p. 1003 (1984). ISSN 1084-7529, 1520-8532. <https://www.osapublishing.org/abstract.cfm?URI=josaa-1-10-1003>. 78
- [155] Z. BOR & B. RÁCZ; “Group velocity dispersion in prisms and its application to pulse compression and travelling-wave excitation”; *Optics Communications* **54**, pp. 165–170 (1985). ISSN 0030-4018. <http://www.sciencedirect.com/science/article/pii/0030401885902846>. 78
- [156] O. E. MARTINEZ; “Grating and prism compressors in the case of finite beam size”; *Journal of the Optical Society of America B* **3**, p. 929 (1986). ISSN 0740-3224, 1520-8540. <https://www.osapublishing.org/abstract.cfm?URI=josab-3-7-929>. 78
- [157] O. MARTINEZ; “3000 times grating compressor with positive group velocity dispersion: Application to fiber compensation in 1.3-1.6 μm region”; *IEEE Journal of Quantum Electronics* **23**, pp. 59–64 (1987). ISSN 1558-1713; conference Name: IEEE Journal of Quantum Electronics. 78
- [158] T. LIPFERT, D. HOROSHKO, G. PATERA & M. KOLOBOV; “Bloch-Messiah decomposition and Magnus expansion for parametric down-conversion with monochromatic pump”; *Physical Review A* **98**, p. 013815 (2018). ISSN 2469-9926, 2469-9934. <http://arxiv.org/abs/1806.09384>; arXiv: 1806.09384.

KEY: lipfert2018

ANNOTATION: Comment: 12 pages, 4 figures, 2 tables

87

- [159] G. CARIOLARO & G. PIEROBON; “Bloch-Messiah reduction of Gaussian unitaries by Takagi factorization”; *Physical Review A* **94**, p. 062109 (2016). ISSN 2469-9926, 2469-9934. <https://link.aps.org/doi/10.1103/PhysRevA.94.062109>. 89
- [160] S. JIANG, N. TREPS & C. FABRE; “A time/frequency quantum analysis of the light generated by synchronously pumped optical parametric oscillators”; *New Journal*

- of Physics **14**, p. 043006 (2012). ISSN 1367-2630. <https://doi.org/10.1088/1367-2630/14/4/043006>; publisher: IOP Publishing. 91, 158
- [161] B. EDLÉN; “The dispersion of standard air”; *Josa* **43**, pp. 339–344 (1953). 93
- [162] “sf.decompositions — Strawberry Fields 0.16.0 documentation”; https://strawberryfields.readthedocs.io/en/stable/code/sf_decompositions.html. 94
- [163] W. MCCUTCHEON; “Structure in Multimode Squeezing: A Generalised Bloch-Messiah Reduction”; arXiv:1809.02544 [quant-ph] (2018)<http://arxiv.org/abs/1809.02544>; arXiv: 1809.02544. 94
- [164] F. ARZANI, C. FABRE & N. TREPS; “Versatile engineering of multimode squeezed states by optimizing the pump spectral profile in spontaneous parametric down-conversion”; *Physical Review A* **97**, p. 033808 (2018). <https://link.aps.org/doi/10.1103/PhysRevA.97.033808>; publisher: American Physical Society. 99, 107, 108, 157
- [165] A. D. TRANTER, H. J. SLATYER, M. R. HUSH, A. C. LEUNG, J. L. EVERETT, K. V. PAUL, P. VERNAZ-GRIS, P. K. LAM, B. C. BUCHLER & G. T. CAMPBELL; “Multiparameter optimisation of a magneto-optical trap using deep learning”; *Nature Communications* **9**, pp. 1–8 (2018). ISSN 2041-1723. <https://www.nature.com/articles/s41467-018-06847-1>. 99, 103
- [166] F. ROSENBLATT; “The perceptron: a probabilistic model for information storage and organization in the brain.” *Psychological review* **65**, p. 386 (1958). 100
- [167] J. G. CARBONELL, R. S. MICHALSKI & T. M. MITCHELL; “Machine learning: a historical and methodological analysis”; *AI Magazine* **4**, pp. 69–69 (1983). 100
- [168] J. DENG, W. DONG, R. SOCHER, L. LI, KAI LI & LI FEI-FEI; “ImageNet: A large-scale hierarchical image database”; in “2009 IEEE Conference on Computer Vision and Pattern Recognition,” pp. 248–255 (2009). 100
- [169] T. B. BROWN, B. MANN, N. RYDER, M. SUBBIAH, J. KAPLAN, P. DHARIWAL, A. NEELAKANTAN, P. SHYAM, G. SASTRY, A. ASKELL *et al.*; “Language models are few-shot learners”; arXiv preprint arXiv:2005.14165 (2020). 100
- [170] D. SILVER, A. HUANG, C. J. MADDISON, A. GUEZ, L. SIFRE, G. VAN DEN DRIESSCHE, J. SCHRITTWIESER, I. ANTONOGLU, V. PANNEERSHELVAM, M. LANCTOT, S. DIELEMAN, D. GREWE, J. NHAM, N. KALCHBRENNER, I. SUTSKEVER, T. LILLCRAP, M. LEACH, K. KAVUKCUOGLU, T. GRAEPEL & D. HASSABIS; “Mastering the game of Go with deep neural networks and tree search”; *Nature* **529**, pp. 484–489 (2016). ISSN 1476-4687. <http://www.nature.com/articles/nature16961>; number: 7587 Publisher: Nature Publishing Group. 100
- [171] V. MNIH, K. KAVUKCUOGLU, D. SILVER, A. A. RUSU, J. VENESS, M. G. BELLEMARE, A. GRAVES, M. RIEDMILLER, A. K. FIDJELAND, G. OSTROVSKI, S. PETERSEN, C. BEATTIE, A. SADIK, I. ANTONOGLU, H. KING, D. KUMARAN,

- D. WIERSTRA, S. LEGG & D. HASSABIS; “Human-level control through deep reinforcement learning”; *Nature* **518**, pp. 529–533 (2015). ISSN 1476-4687. <http://www.nature.com/articles/nature14236>; number: 7540 Publisher: Nature Publishing Group. 100
- [172] “claptrap”; <http://clipart-library.com/clipart/152805.htm>. 101
- [173] H. J. BRIEGEL & G. D. I. CUEVAS; “Projective simulation for artificial intelligence”; *Scientific Reports* **2**, pp. 1–16 (2012). ISSN 2045-2322. <https://www.nature.com/articles/srep00400/>; number: 1 Publisher: Nature Publishing Group. 100
- [174] J. MAUTNER, A. MAKMAL, D. MANZANO, M. TIERSCH & H. J. BRIEGEL; “Projective Simulation for Classical Learning Agents: A Comprehensive Investigation”; *New Generation Computing* **33**, pp. 69–114 (2015). ISSN 0288-3635, 1882-7055. <http://link.springer.com/10.1007/s00354-015-0102-0>. 100
- [175] A. A. MELNIKOV, A. MAKMAL, V. DUNJKO & H. J. BRIEGEL; “Projective simulation with generalization”; *Scientific Reports* **7**, p. 14430 (2017). ISSN 2045-2322. <http://www.nature.com/articles/s41598-017-14740-y>. 101
- [176] A. A. MELNIKOV, H. P. NAUTRUP, M. KRENN, V. DUNJKO, M. TIERSCH, A. ZEILINGER & H. J. BRIEGEL; “Active learning machine learns to create new quantum experiments”; *Proceedings of the National Academy of Sciences* **115**, pp. 1221–1226 (2018). ISSN 0027-8424, 1091-6490. <https://www.pnas.org/content/115/6/1221>; publisher: National Academy of Sciences Section: Physical Sciences. 101
- [177] D. P. KINGMA & J. BA; “Adam: A Method for Stochastic Optimization”; arXiv:1412.6980 [cs] (2017) <http://arxiv.org/abs/1412.6980>; arXiv: 1412.6980.
- KEY: kingma2017
 ANNOTATION: Comment: Published as a conference paper at the 3rd International Conference for Learning Representations, San Diego, 2015
- 103
- [178] R. H. BYRD, P. LU, J. NOCEDAL & C. ZHU; “A Limited Memory Algorithm for Bound Constrained Optimization”; *SIAM Journal on Scientific Computing* **16**, pp. 1190–1208 (1995). ISSN 1064-8275. <https://epubs.siam.org/doi/abs/10.1137/0916069>; publisher: Society for Industrial and Applied Mathematics. 103
- [179] “Prometheus | Coherent”; <https://www.coherent.com/lasers/laser/prometheus>. 104
- [180] “Thorlabs - Z825B 25 mm Motorized Actuator with Ø3/8" Barrel (0.5 m Cable)”; <https://www.thorlabs.com/thorproduct.cfm?partnumber=Z825B>. 104
- [181] “SparkFun Motor Driver - Dual TB6612FNG (with Headers) - ROB-14450 - SparkFun Electronics”; <https://www.sparkfun.com/products/14450>. 104
- [182] “NI PXI-7813R - NI R Series Multifunction RIO Device Drivers Help - National Instruments”; <https://zone.ni.com/reference/en-XX/help/371508V-01/target2devicehelp/pxi-7813r/>. 104

- [183] “Standard Deformable Mirrors”; <http://bostonmicromachines.com/standard-deformable-mirrors/>. 105
- [184] F. ARZANI; *Measurement based quantum information with optical frequency combs*; Theses; PSL Research University (2018). <https://tel.archives-ouvertes.fr/tel-01876070>. 105
- [185] J. ROSLUND, O. M. SHIR, T. BÄCK & H. RABITZ; “Accelerated optimization and automated discovery with covariance matrix adaptation for experimental quantum control”; *Physical Review A* **80**, p. 043415 (2009). <https://link.aps.org/doi/10.1103/PhysRevA.80.043415>; publisher: American Physical Society. 105
- [186] D. B. HOROSHKO, L. LA VOLPE, F. ARZANI, N. TREPS, C. FABRE & M. I. KOLOBOV; “Bloch-Messiah reduction for twin beams of light”; *Physical Review A* **100**, p. 013837 (2019). <https://link.aps.org/doi/10.1103/PhysRevA.100.013837>; publisher: American Physical Society. 118
- [187] “Si PIN photodiode S3590-09”; <https://www.hamamatsu.com/eu/en/product/type/S3590-09/index.html>. 124
- [188] “Mini-Circuits”; <https://www.minicircuits.com/WebStore/dashboard.html?model=BLP-5%2B>. 125, 130
- [189] “Mini-Circuits”; <https://www.minicircuits.com/WebStore/dashboard.html?model=ZFL-500LN-BNC%2B>. 125, 130
- [190] H.-A. BACHOR, T. C. RALPH, S. LUCIA & T. C. RALPH; *A guide to experiments in quantum optics*; volume 1 (Wiley Online Library) (2004). 125
- [191] “Si photodiode array S4111-16R”; <https://www.hamamatsu.com/eu/en/product/type/S4111-16R/index.html>. 130
- [192] “Mini-Circuits”; <https://www.minicircuits.com/WebStore/dashboard.html?model=ZSC-2-1%2B>. 130
- [193] “Mini-Circuits”; <https://www.minicircuits.com/WebStore/dashboard.html?model=ZAD-3%2B>. 130
- [194] “PXI-5105”; <https://www.ni.com/fr-fr/support/model.pxi-5105.html>. 130

Sujet :

Optimization of the pump spectral shape in a parametric down conversion process to generate multimode entangled states.

Résumé : Dans cette thèse, nous utilisons un oscillateur paramétrique optique pompé en mode synchrone par un peigne de fréquence optique afin de créer des états intriqués fortement multimodes. Un tel montage expérimental bénéficie d'une grande ajustabilité. En changeant le spectre de la pompe grâce à un façonneur d'impulsion, nous pouvons moduler les propriétés de l'état quantique généré. Avec des algorithmes d'apprentissage machine, nous trouvons les formes spectrales optimales pour créer certains états quantiques aux propriétés désirables. Ces formes sont ensuite implémentées dans l'expérience et les états quantiques produits sont mesurés avec une détection homodyne multiple résolue en fréquence.

Mots clés : Optique quantique, variables continues, intrication, états comprimés, multimode, états Gaussiens, peigne de fréquences optiques, laser ultrarapide, laser femtoseconde, canevass quantiques, apprentissage automatique, conversion paramétrique descendante, oscillateur paramétrique optique, façonnage d'impulsion, optimisation spectrale

Subject : Optimisation of the pump spectral shape in a parametric down conversion process to generate multimode entangled states.

Abstract: In this thesis, we use an optical parametric oscillator pumped synchronously (SPOPO) with an optical frequency comb (OFC) to generate large entangled states. One of the advantages of this set-up is its tunability. By changing the spectrum of the pump with a pulse shaper, we can tailor the properties of the generated quantum state. In this work, we focus on the optimisation of the pump spectral shape to generate specific states. Using simulations based on Machine Learning Algorithms (MLA), we find optimal pump profile for typical target states. We then implement those shapes and measure the resulting quantum states using a multipixel homodyne detection.

Keywords : Quantum optics, continuous variables, entanglement, squeezed states, multimode, Gaussian states, optical frequency comb, ultra-fast laser, femtosecond laser, cluster state, machine learning, parametric down conversion, optical parametric oscillator, pulse shaping, spectral optimisation